MECHANISTIC INSIGHTS INTO MULTI-FUNCTIONAL CATALYSTS FOR BIOMASS CONVERSION TO BIO-DIESEL AND BIO-SURFACTANT

by

Huong (Hannah) Nguyen

A dissertation submitted to the Faculty of the University of Delaware in partial fulfillment of the requirements for the degree of Doctor of Philosophy in Chemical Engineering

Fall 2018

© 2018 Huong (Hannah) Nguyen
All Rights Reserved

MECHANISTIC INSIGHTS INTO MULTI-FUNCTIONAL CATALYSTS FOR BIOMASS CONVERSION TO BIO-DIESEL AND BIO-SURFACTANT

by

Huong (Hannah) Nguyen

Approved: _____

Eric M. Furst, Ph.D.
Chair of the Department of Chemical and Biomolecular Engineering

Approved: _____

Babatunde A. Ogunnaike, Ph.D.
Dean of the College of Engineering

Approved: _____

Douglas J. Doren, Ph.D.
Interim Vice Provost for Office of Graduate and Professional Education

I certify that I have read this dissertation and that in my opinion it meets the academic and professional standard required by the University as a dissertation for the degree of Doctor of Philosophy.

Signed: _____

Dionisios G. Vlachos, Ph.D.
Professor in charge of dissertation

I certify that I have read this dissertation and that in my opinion it meets the academic and professional standard required by the University as a dissertation for the degree of Doctor of Philosophy.

Signed: _____

Raul F. Lobo, Ph.D.
Professor in charge of dissertation

I certify that I have read this dissertation and that in my opinion it meets the academic and professional standard required by the University as a dissertation for the degree of Doctor of Philosophy.

Signed: _____

Marat Orazov, Ph.D.
Member of dissertation committee

I certify that I have read this dissertation and that in my opinion it meets the academic and professional standard required by the University as a dissertation for the degree of Doctor of Philosophy.

Signed: _____

Paul M. Witt, Ph.D.
Member of dissertation committee

I certify that I have read this dissertation and that in my opinion it meets the academic and professional standard required by the University as a dissertation for the degree of Doctor of Philosophy.

Signed: _____

Yushan Yan, Ph.D.
Member of dissertation committee

ACKNOWLEDGMENTS

I am truly grateful to my main advisor, Professor Dion Vlachos for his guidance and dedication over the years to help develop me to the researcher I am today. His passion and relentless commitment to high quality research have motivated me to push beyond my limit. I would also like to thank Professor Raul Lobo for his continued support and valuable feedback to my research and career decision. My thesis committee, Professor Marat Orazov, Professor Yushan Yan, and Dr. Paul Witt, have been very helpful with their insightful inputs to the thesis. I am thankful to the Department of Energy for providing the funding source to the Catalysis Center of Energy Innovation via the Office of Basic Science to make this work possible.

I appreciate the group of great researchers, who I have got the opportunities to collaborate with at various points during my Ph.D., including Dr. Dallas Swift for the kinetic modeling work of sugar conversion, Dr. Anatoly Frenkel and his group for the XAS spectroscopic measurements, Dr. Weiqing Zheng with XPS data analysis, and Nick Gould for the FTIR measurement. I would also like to acknowledge the tremendous help from the undergraduate researchers, Nick Xiao and Dave Moglia, whose diligent work has contributed to the success of this thesis.

I feel extremely fortunate to be in a nurturing research group with the past and present colleagues, who have mentored me along the way, shared their knowledge and wisdom, and made the late nights at lab enjoyable, including Dr. Marta Leon Garcia, Dr. Vlad Nikolakis, Dr. Nima Nikbin, Dr. Stavros Caratzoulas, Dr. Efterpi Vasileiadou, Dr. Kostas Goulas, Dr. Weiqing Zheng, Jiayi Fu and Lily Cheng. Special

thanks go out to my friends, Elisa, Amber, Megan, Efi, Cesar, Matt and Nima, who have walked alongside me through the intellectual and mental challenges of graduate school and made my stay at Delaware memorable. I also thank my friends from Oklahoma, Nhung, Yến, Uyên and Sơn. They have become my family away from home and I am grateful for their endearing friendship over the years.

Finally, I would like to express my sincerest thanks to my family, Mom, Dad, and my sisters, Hin, Bủm. Despite half of the Earth away, they have always been there for me, made sacrifices and supported my every life decision. My family is the reason I have come this far and will fearlessly continue my journey.

TABLE OF CONTENTS

LIST OF TABLES xii
LIST OF FIGURES xiii
ABSTRACT xxii

Chapter

1 INTRODUCTION 1

1.1 Biomass as the Renewable Source of Carbon 1
1.2 Acid-Base Catalysts 3
1.3 Target Chemicals and Chemistries 8

1.3.1 Platform chemical 5-hydroxymethyl furfural 8
1.3.2 Bio-diesel 2,5-bis(alkoxymethyl)furan 13
1.3.3 Production of 2-dodecanoyl furan, a bio-surfactant precursor 15

1.4 Thesis Motivation and Scope 18

2 MECHANISTIC INSIGHTS INTO LEWIS ACID METAL SALT-CATALYZED GLUCOSE CHEMISTRY IN AQUEOUS SOLUTION 21

2.1 Introduction 21
2.2 Experimental Methods 24
2.3 Results and Discussion 26

2.3.1 Active species of metal chlorides for glucose isomerization to fructose 26
2.3.2 Mechanism of metal chloride-catalyzed glucose isomerization to fructose 30
2.3.3 Mechanism of metal chloride-catalyzed glucose epimerization to mannose 32
2.3.4 Quantification of mannose produced from reverse C2-C1 hydride transfer and the Bilik reaction 37
2.3.5 Lewis acid metal salt-catalyzed glucose conversion to other hexoses 41

2.4 Conclusions 44

3 TANDEM LEWIS ACID /BRØNSTED ACID –CATALYZED CONVERSION OF CARBOHYDRATES TO 5-HYDROXYMETHYLFURFURAL USING ZEOLITE BETA 46

3.1 Introduction 46
3.2 Experimental Methods 50

3.2.1 Materials 50
3.2.2 Reaction kinetics 51
3.2.3 Adsorption isotherms 51
3.2.4 Brønsted site density measurements 52
3.2.5 Computational methods 53

3.2.5.1 Adsorption 53
3.2.5.2 Continuity equations 54
3.2.5.3 Homogeneous reaction network 55
3.2.5.4 Heterogeneous reaction network 56
3.2.5.5 Experimental data treatment 58
3.2.5.6 Parameter estimation procedure 59

3.3 Results and Discussion 59

3.3.1 Single-component isotherms 59
3.3.2 Model assessment 62
3.3.3 Kinetic parameters and comparison to other catalysts 66

3.3.3.1 Kinetic regimes 69
3.3.3.2 Optimizing HMF yield in single phase and biphasic systems 75
3.3.3.3 Identification of key materials' properties 77

3.4 Conclusions 80

4 ROLE OF LEWIS AND BRØNSTED ACIDITY IN METAL CHLORIDE CATALYSIS IN ORGANIC MEDIA: REDUCTIVE ETHERIFICATION OF FURANICS 82

4.1 Introduction 82
4.2 Experimental Methods 84

4.2.1 Materials 84
4.2.2 Reductive etherification experiments 85
4.2.3 Etherification kinetic experiments 85
4.2.4 Product analysis 85

4.2.5 pH measurement 86
4.2.6 Spectroscopy techniques 86

4.3 Results and Discussions 87

4.3.1 Catalytic activity of metal chlorides for reductive etherification of HMF 87
4.3.2 Furfuryl alcohol (FA) etherification 89

4.3.2.1 Reaction network 89
4.3.2.2 Kinetic model 92

4.3.3 Furfural reduction 96

4.3.3.1 Reaction mechanism 96
4.3.3.2 Determination of catalytically active species 98

4.4 Conclusions 101

5 SYNERGY OF ACID-BASE SITES OF SUPPORTED ZIRCONIA FOR REDUCTIVE ETHERIFICATION OF BIOMASS-DERIVED FURAN DERIVATIVES 103

5.1 Introduction 103
5.2 Experimental Methods 104

5.2.1 Catalyst synthesis and characterization 104
5.2.2 Catalytic reactions 105

5.3 Results and Discussion 107

5.3.1 Catalytic performance assessment 107
5.3.2 Catalyst structure-activity relationship 109
5.3.3 Effect of zirconia loading 113

5.4 Conclusions 115

6 PRODUCTION OF RENEWABLE OLEO-FURAN SURFACTANTS BY CROSS-KETONIZATION OF BIOMASS-DERIVED FURAN DERIVATIVES AND FATTY ACIDS 117

6.1 Introduction 117
6.2 Experimental Methods 120

6.2.1 Materials 120

6.2.2 Catalytic reaction and analysis 121
6.2.3 Catalyst characterization 122

6.3 Results and Discussion 122

6.3.1 Catalytic activity of metal oxides for cross-ketonization of 2-furoic acid and lauric acid 122
6.3.2 Determination of catalytic active sites from iron oxide characterization 125
6.3.3 Reaction mechanism: 132

6.4 Conclusion 133

7 CONCLUSIONS AND OUTLOOK 135

7.1 Thesis Summary 135
7.2 Outlook 140

7.2.1 Exploring synthesis methods to enhance the ZrO_2/SiO_2 catalyst activity for reductive etherification of HMF 140
7.2.2 Tailoring catalyst and process design towards 2-dodecanoyl furan production 141
7.2.3 Application of multi-functional acid-base catalysts toward the production of bio-fuels 142

REFERENCES 144

Appendix

A SUPPLEMENTARY INFORMATION FOR CHAPTER 2 MECHANISTIC INSIGHTS INTO LEWIS ACID METAL SALT-CATALYZED GLUCOSE CHEMISTRY IN AQUEOUS SOLUTION 160
B SUPPLEMENTARY INFORMATION FOR CHAPTER 3 TANDEM LEWIS ACID/BRØNSTED ACID-CATALYZED CONVERSION OF CARBOHYDRATES TO 5-HYDROXYMETHYLFURFURAL USING ZEOLITE BETA 165

B.1 Quantification of the Ratio of Lewis to Brønsted Acid Sites in H-BEa-25 165
B.2 Adsorption 167

B.2.1 Single-component adsorption isotherms 167
B.2.2 Ideal adsorbed solution theory (IAST) 168

B.3 Sensitivity of Estimated Parameters 169
B.4 Reaction Kinetics 175

B.4.1 Kinetic paramaters 175
B.4.2 Parity plot 175
B.4.3 Effect of catalyst loading 175
B.4.4 Prediction of fraction of reaction in the zeolite 177
B.4.5 Experimental data for model prediction 177
B.4.6 Arrhenius plot of apparent glucose consumption rates 180

C SUPPLEMENTARY INFORMATION FOR CHAPTER 4 ROLE OF LEWIS AND BRØNSTED ACIDITY IN METAL CHLORIDE CATALYSIS IN ORGANIC MEDIA: REDUCTIVE ETHERIFICATION OF FURANICS 182

C.1 Polyarc™ Calibration Curve 182
C.2 Furfuryl Alcohol Reactivity with Select Catalysts 183
C.3 GCMS Analysis of 4,5,5-Trialkoxypentan-2-one 183
C.4 OLI Prediction of Metal Salt Speciation 184
C.5 ESI-MS of Metal Chloride Solutions 186
C.6 Apparent Activation Energy Analysis of Furfural Reduction 188

D SUPPLEMENTARY INFORMATION FOR CHAPTER 5 ON THE SYNERGY OF ACID-BASE SITES OF SUPPORTED ZIRCONIA FOR REDUCTIVE ETHERIFICATION OF BIOMASS-DERIVED FURAN DERIVATIVES 189
E SUPPLEMENTARY INFORMATION FOR CHAPTER 6 PRODUCTION OF RENEWABLE OLEO-FURAN SURFACTANTS BY CROSS-KETONIZATION OF BIOMASS-DERIVED FURAN DERIVATES AND FATTY ACIDS 192
F PERMISSION 196

LIST OF TABLES

Table 2.1. Yields of different hexoses after ^{13}C-C1 glucose reaction in metal chlorides and ratio of mannose formed via 1,2 hydride transfer (^{13}C-C1) and via the Bilik reaction (^{13}C-C2). Reaction conditions: 10 wt% ^{13}C-C1 glucose, 17 mM MCl_3, T = 140 ºC. The reaction time varied in order to have similar conversion of glucose. 34

Table 2.2. Effective ionic radius of the studied metal aqua cations[200] and their metal-oxygen distance with water in the first hydration sphere.[213-216] 40

Table 3.1. Fitted adsorption isotherm parameters for solutes in H-BEA-25. 61

Table 3.2. Estimated parameters for the intrinsic reaction rates in zeolite beta. 67

Table 4.1: Predicted rate constants of furfuryl alcohol (FA) reactions in Figure 4.3. Reaction conditions: 1 wt% FA, 90 °C, 5-10 mM MCl_3, 5-20 mM HCl. 95

Table B.1. Quantification of the ratio of Lewis to Brønsted acid site density 166

Table B.2. Zeolite-induced pH change at different loadings. Procedure as implemented by Kruger et al.[141] 170

Table C.1. Coordination number (CN) and interatomic distance (R) obtained in fitting experimental XAS data of 20 mM YCl_3 and 20 mM $CrCl_3$ solution in 2-propanol. 188

Table D.1. Binding energies of Zr $3d_{5/2}$, Si 2p and O 1s on the bulk ZrO_2, SiO_2, and the synthesized ZrO_2/SiO_2 with various zirconia content from XPS spectra. 190

Table E.1. Fe content in pure dodecane and post-reaction filtrates of iron oxides measured by XRF 192

Table E.2. BET surface areas and mircropore volumes of iron oxide catalysts before and after cross-ketonization reactions. 194

LIST OF FIGURES

Figure 1.1.Thermocatalytic conversion of biomass to valuable chemicals. 3

Figure 2.1. Summary of the mechanism of glucose interconversions by Lewis acids known to date. 22

Figure 2.2. Dynamic light scattering spectra of 1.7 mM $CrCl_3$ solution preheated to 140 °C with (a) for 24 h without HCl, (b) for 24 h with 10 mM HCl, and (c) for 1 h with 10 mM HCl. 29

Figure 2.3. Effect of HCl addition on the rate of isomerization with catalyst preheating (▲), without catalyst preheating (□) and concentration of $CrOH^{2+}$ predicted by OLI (●). 29

Figure 2.4. Bottom: ^{13}C NMR spectra of (a) a standard mixture of glucose and fructose and (b) a standard mixture of D2 glucose and fructose, and (c) sugar fraction after reaction in $GaCl_3$. Left blue box at top: magnification of the spectra within the C2 glucose region bracketed with blue dashed lines. The two C2 glucose peaks are labeled with vertical blue dashes lines. Right green box at top: magnification of the spectra within the C1 fructose region bracketed with green dashed lines. The three C1 fructose peaks are labeled with vertical green dashed lines. 31

Figure 2.5. Left: ^{13}C NMR of (a) a standard mixture of ^{13}C-C1 glucose, fructose and mannose, and the sugar fraction after reaction using (b) NaOH, (c) $YbCl_3$, and (d) $CrCl_3$. Right: magnification of the spectra of the C1 mannose peaks in green, the C2 mannose peaks in blue, and the C1 fructose peaks in red. 34

Figure 2.6. Stepwise mechanism of the Bilik reaction for glucose epimerization to mannose by metal chlorides 38

Figure 2.7. ^{13}C NMR spectra of (a) unlabeled sorbose and of the sugar fraction after reaction by $CrCl_3$ starting with (b) unlabeled glucose, (c) D2-glucose, (d) ^{13}C-C1 glucose. Glucose peaks are black, sorbose peaks are red, and peaks of the unknown compound are blue. 43

Figure 3.1. Reaction network inside H-BEA-25. Solid (dashed) lines indicate Brønsted (Lewis)-acid catalyzed reactions 56

Figure 3.2. Comparison between model (solid lines) and experimental (closed symbols) concentration profiles of glucose, fructose, and HMF for experiments starting with 10 wt% glucose (a) or fructose (b) at 130 ºC with an H-BEA-25 loading of 125 g/l. Open symbols and dashed lines in (b) indicate experimental and predicted concentrations, respectively, for 10 wt% fructose dehydration using 125 g/L HCl-washed H-BEA-25. No glucose is formed in this case. 62

Figure 3.3. Measured concentration profiles in solution (closed symbols) and estimated total concentration (including aqueous and zeolite phase concentrations - see text; open symbols) starting with 10 wt% fructose at 140 ºC with 125 g/l of H-BEA-25. Accounting for the adsorbed amounts, especially for HMF and LA, is important for correct description of kinetics. 65

Figure 3.4. Aqueous species concentrations (closed symbols) and estimated total concentration (including aqueous and zeolite phase concentrations; open symbols) starting with 2 wt% HMF at 140 ºC with 125 g/l of H-BEA-25. 66

Figure 3.5. Apparent activation energy for glucose-fructose isomerization in Sn-BEA[68], Ti-BEA[68], homogeneous $CrCl_3$[106] and H-BEA (present work) based on glucose consumption at 110-130 ºC. 68

Figure 3.6.Turnover frequency (TOF), determined from experimental data after 30 min, of 10 wt% fructose (a) and 5 wt% HMF (b) in HCl (pH = 1.1) and H-BEA-25 (125 g/l) at 140 ºC. 69

Figure 3.7. Predicted concentration profiles (a-d) and net reaction rates (e-h) of (a, e) glucose, (b, f) fructose, (c, g) HMF, and (d,h) LA at different L:B ratios. Conditions: 130 ºC, 125 g/L H-BEA-25, 1.2 mmol/g total sites, 10 wt% glucose. 72

Figure 3.8. Predicted rate of HMF formation (forward) as a function of (a) Lewis to Brønsted acid site ratio (holding the total number of sites constant at 1.2 mmol/g) after 6, 12, and 24 hours and (b) Brønsted site density with Lewis site density held constant at 0.3, 0.6, and 1.2 mmol/g after 6 hours. Reaction starts with 10 wt% glucose at 130 ºC with 125 g/l of H-BEA. 74

Figure 3.9. Normalized sensitivity coefficient of the forward HMF production rate for different L:B ratios after (a) 6 hours, (b) 12 hours, and (c) 24 hours.

Conditions: 130 ºC, 125 g/L H-BEA-25, 1.2 mmol/g total sites, 10 wt% glucose. 75

Figure 3.10. (a) HMF yield as a function of Lewis to Brønsted acid sites (L:B) ratio after 6, 12, and 24 hours and (b) corresponding normalized sensitivity coefficient of HMF yield for L:B = 1. Conditions: 130 ºC, 125 g/L H-BEA-25, 1.2 mmol/g total sites, 10 wt% glucose. 76

Figure 3.11. Predicted HMF yield in (a) aqueous single-phase solution, (b) a biphasic reactor (partition coefficient = 2, $Vorg/Vaq = 5$) , and (c) an ideal biphasic reactor (all HMF extracted) at different L:B ratios. Conditions: 130 ºC, 125 g/L H-BEA-25, 1.2 mmol/g total sites, 10 wt% glucose. 77

Figure 3.12. Predicted maximum HMF yield from glucose in (a) single phase and (b) biphasic (partition coefficient = 2, $Vorg/Vaq = 5$) systems along with the time to reach that yield. Catalysts include the actual H-BEA, H-BEA with modified adsorption (H-BEA' has low HMF loadings, H-BEA'' has high glucose/fructose loadings, and H-BEA''' has increased glucose/fructose loading and lower HMF loadings), BEA-L10 combined with H-BEA or HCl. 80

Figure 4.1: HMF conversion and product yields in 2-propanol catalyzed by variety of metal chlorides. Reaction conditions: 1 wt % HMF, 3 mM catalyst, 150 °C, 1 h reaction time. R represents an isopropyl group. 88

Figure 4.2. Proposed reaction network of HMF reactions by MCl_3 in 2-propanol. OR = $OCH(CH_3)_2$ 89

Figure 4.3. Proposed reaction network of furfural reductive etherification in 2-propanol. Furfuryl alcohol reaction network in blue arrows 92

Figure 4.4: Selectivity to isopropyl furfuryl ether (iPFE) over isopropy levulinate (iPL) in $CrCl_3$, YCl_3, and HCl. Reaction conditions: 1 wt % furfuryl alcohol, 90 °C, 10 mM catalyst. 92

Figure 4.5: Experimental (symbols) and modeling (lines) concentration profiles of furfuryl alcohol (FA), isorpropyl furfuryl ether (iPFE) and isopropyl levulinate (iPL) in HCl (a), YCl_3 (b) and $CrCl_3$ (c). Reaction conditions: 1 wt % FA, 10 mM catalyst, 90 °C 95

Figure 4.6: Apparent rate constant of furfuryl alcohol etherification $k_{1app} = k_1[catalyst]$ of 10 mM $CrCl_3$ and YCl_3. 95

Figure 4.7: GCMS spectra of furfuryl alcohol product. Reaction conditions: 1 wt% furfural, 150 °C, 3 mM YCl_3, in 2-propanol-d0 (t= 30 min), 2-propanol-OD (t= 30 min), and 2-propanol-d8 (t= 1 h). 97

Figure 4.8: ^{1}H NMR spectra of furfuryl alcohol standard (a) and post reaction mixture of furfural reduction by YCl_3 in 2-propanol-d0 (b), 2-propanol-OD (c), 2-propanol-d8 (d) and 1:1 mixture of 2-propanol-d0 and 2-propanol-d8 (e). 98

Figure 4.9: Effect of HCl addition on furfural conversion and product yields by YCl_3 (a) and $CrCl_3$ (b). Reaction conditions: 1 wt % furfural, 150 °C, 3 mM MCl_3, t= 30 min (YCl_3), t= 180 min ($CrCl_3$). 100

Figure 5.1. Comparison of product distribution of HMF reaction in 2-propanol between YCl_3 (data from previous work[285]) (gray), commercial ZrO_2 (black), and the synthesized 7.5 wt% ZrO_2/SiO_2 (orange). Reaction conditions: 1 wt% HMF, HMF: metal molar ratio = 100:3 (100:10 in case of commercial ZrO_2, 150 °C, t= 3 h (1 h for YCl_3), 20 bar N_2. 108

Figure 5.2. Concentration profile of HMF and major products in a continuous flow reactor containing 7.5 wt % ZrO_2/SiO_2. Reaction conditions: 1 wt % HMF in 2-propanol feed stream, 0.1 mL/min flow rate, 0.2 g catalyst, 150 °C, 20 bar. 109

Figure 5.3. FTIR spectra on 7.5 wt% ZrO_2/SiO_2 before (black) and after pyridine adsorption (blue) and evacuated at different temperatures. (B): Brønsted acid peak, (L): Lewis acid peak. 111

Figure 5.4. TPD of CO_2 on pure silica (red) and 7.5 wt% ZrO_2/SiO_2 samples. 111

Figure 5.5. Effect of various titrants on the rate of furfural hydrogenation (a) and furfuryl alcohol etherification (b). Reaction conditions: 1 wt % furfural (or furfuryl alcohol), 7.5 wt % ZrO_2/SiO_2, reactant: metal molar ratio = 100:3, reactant: titrant molar ratio = 1:1, 110 °C for furfural (or 150 °C for furfuryl alcohol), 20 bar N_2 113

Figure 5.6. Effect of zirconia loading of ZrO_2/SiO_2 on the rate constant of furfural hydrogenation (■) and fufuryl alcohol etherification (▲). 115

Figure 5.7. Comparison of the theoretical (---) and XPS-measured (■) ZrO_2 content on the surface and in the bulk of ZrO_2/SiO_2 vs. zirconia loading. 115

Figure 6.1. Various proposed pathways to produce oleo-furan sulfonate as bio-surfactant. R represents the n-$C_{11}H_{23}$ chain. Path C is the one developed herein. 119

Figure 6.2. Activity of various commercial metal oxides for reaction of 2-furoic acid with lauric acid in n-dodecane. Reaction conditions: 0.05 M lauric acid, 0.25 M 2-furoic acid, 0.2 g catalyst, 316 °C, 90 min, 20 bar N_2. 124

Figure 6.3. Proposed reaction network for reaction of 2-furoic acid and lauric acid in n-dodecane by iron oxide catalyst. R represents n-$C_{11}H_{23}$ group. 124

Figure 6.4. Lauric acid conversion (a) and 2-dodecanoyl furan yield (b) after three catalyst recycles in dodecane. Reaction conditions: 0.05 M lauric acid, 0.25 M 2-furoic acid, 0.2 g catalyst, 316 °C, 90 mins, 20 bar N_2 125

Figure 6.5. XRD pattern of the fresh and spent iron oxides FeO (a), Fe_3O_4(b), Fe_2O_3 (c) with assigned diffraction peaks for FeO (■), Fe_3O_4 or γ-Fe_2O_3 (*), and additional octahedral Fe cation peaks (♦). 126

Figure 6.6. XPS spectra of Fe 2p on the iron oxide catalyst surfaces (a) before and (b) after cross-ketonization reaction..... 131

Figure 6.7. Comparison of cross-ketonization activity of Fe_3O_4 catalysts exposed to different pretreatment conditions: the catalyst was used as received (a) or was pre-treated in a dodecane solution of pure dodecane (b), 0.05 M lauric acid (c), 0.25 M 2-furoic acid (d), and 5 bar of H_2 (e). Pretreatment conditions: 316 °C, 30 mins, 0.2 g fresh Fe_3O_4. Reaction conditions: 0.05 M lauric acid, 0.25 M 2-furoic acid, 316 °C, 20 mins, 20 bars of N_2, 0.2 g pretreated Fe_3O_4..... 131

Figure 6.8. Postulated reaction mechanism of cross-ketonization of 2-furoic acid and lauric acid on Fe_3O_4. 133

Figure 7.1. Proposed roadmap for converting biomass to bio-fuels. Adapted from Shylesh *et al.*[325] 143

Figure A.1. Comparison of glucose conversion profile by $CrCl_3$ (●), $CrCl_3$ and NaCl (▲) and $CrCl_3$ and HCl (■). Reaction conditions: 1wt % glucose, 1.7 mM $CrCl_3$, 100 mM NaCl, 100 mM HCl, 140 °C..... 160

Figure A.2. The effect of HCl addition on the rate of isomerization with catalyst preheating (▲), without catalyst preheating (□) and concentration of

MOH^{2+} predicted by OLI (●) for 5 mM $AlCl_3$ (a) and 20 mM $DyCl_3$ (b). Reaction conditions: 1 wt % glucose, MCl_3, 140 °C, [0-44 mM] HCl. 160

Figure A.3. Dynamic light scattering spectra of 5mM $AlCl_3$ and 20 mM $DyCl_3$ after heated up to 140 °C for 24 h. 161

Figure A.4. Bottom: ^{13}C NMR spectra of sugar fraction after reaction from D2 glucose in (a) $GaCl_3$, (b) $InCl_3$, (c) $DyCl_3$, (d) $YbCl_3$, and (e) $LaCl_3$. Left blue box at top: magnification of the spectra in the C2 glucose region. Right green box at top: magnification of the spectra within the C1 fructose region. 162

Figure A.5. Left: ^1H NMR of (a) a standard mixture of glucose and fructose, and sugar fraction after reaction from D2 glucose in (b) $GaCl_3$, (c) $InCl_3$, (d) $DyCl_3$, (e) $YbCl_3$, and (f) $LaCl_3$. Right: Magnification of the spectra in the region δ= 3.2-3.7 ppm. 162

Figure A.6. Left: ^{13}C NMR spectra of the sugar fraction after reaction from ^{13}C-C1 glucose using (a) $LaCl_3$, (b) $DyCl_3$, (c) $GaCl_3$, (d) $InCl_3$, and (e) $AlCl_3$. Right: magnification of the spectra of the C1 mannose peaks (green box), the C2 mannose peaks (blue box), the C1 fructose peaks (red box), and the C6 sorbose peak (purple box). 163

Figure A.7. ^{13}C NMR spectrum of an unlabeled mannose using quantitative ^{13}C NMR method. 163

Figure A.8. Correlation between glucose isomerization rate with concentration of $Al(OH)_x^{m+}$ predicted by OLI. Reaction condition: 1wt % glucose, glucose: Al =11:1 molar ratio, 140 °C. Catalysts are $AlCl_3$ (●), $Al(NO_3)_3$ (▲) and $Al_2(SO_4)_3$ (■). 164

Figure B.1. ^{27}Al NMR spectrum of H-BEA-25 catalyst. 165

Figure B.2. FTIR spectra of pyridine adsorption of H-BEA-25. 166

Figure B.3. Adsorption isotherms of fructose dehydration products in water on H-BEA-25. Experimental (points) and model predictions (lines) based on parameters shown in Table 3.1. 167

Figure B.4. Adsorption isotherm of LA on H-BEA-25 at various temperatures. Experimental (points) and model prediction (line) shown. Agreement between model predictions and observed isotherms indicates that the temperature-dependence of adsorption is captured by the model 168

Figure B.5.Estimated parameters using different assumptions for homogeneous solution pH. Activation energies are in general agreement, indicating that the model is not sensitive to assumptions about the solution pH at reaction temperature. 171

Figure B.6. Estimated parameters assuming additional humin formation reactions. The parameters associated with the non-humin formation reactions are rather insensitive to including these additional paths. 172

Figure B.7. $\boldsymbol{CS/C}$ vs $\boldsymbol{\tau}$ for different values of $\boldsymbol{\alpha}$. As $\boldsymbol{\alpha}$ approaches the value used in the present work, $\boldsymbol{CS/C \rightarrow 1}$ at very short times. 174

Figure B.8. Parity plot of model predictions and experimental observations indicating the quality of estimated kinetic parameters on both a linear (a) and logarithmic (b) scale. 175

Figure B.9. Conversion of glucose (a) and yield of fructose (b), HMF (c) for reaction of 10 wt% glucose at 130 °C and zeolite loadings of 12.5 g/L (■), 50 g/L (◆) and 12.5 g/L (▲). Symbols are experimental data and lines are model predictions. 176

Figure B.10. Estimated fraction of reactions that occur in the zeolite starting with 10 %w/v fructose, 125 g/l H-BEA-25, at 130°C. pH estimated at 3.46. Fractions determined by the ratio: $\mathbf{rBEArBEA + rH2O}$, where $\boldsymbol{r}$ is the rate normalized by reactor volume. 177

Figure B.11. Experimentally measured concentration profiles of HMF degradation in 125 g/l of H-BEA-25. Replicates shown as separate data points. 178

Figure B.12. Experimentally measured concentration profiles observed after fructose reaction in 125 g/l H-BEA-25 at different temperatures. 179

Figure B.13. . Experimentally measured concentration profiles observed after fructose reaction in HCl-washed 125 g/l H-BEA-25 at different temperatures. . 179

Figure B.14. Experimental observed concentration profiles after reaction of glucose with 125 g/l H-BEA-25 at various temperatures. 180

Figure B.15. Arrhenius plot based on apparent rates of glucose consumption. 181

Figure C.1. Universal calibration curve of various compounds on the GC equipped with the PolyArc™. 182

Figure C.2. Catalytic activity of $CrCl_3$ and YCl_3 in furfuryl alcohol reaction in 2-propanol. Reaction conditions: 1 wt % furfuryl alcohol, 90 °C, 10 mM MCl_3, t = 8 h. 183

Figure C.3. GCMS spectra of 4,5,5-triethoxypentan-2-one (a) and 4,5,5-tripropoxypentane-2-one (b) produced from reaction of furfuryl alcohol in ethanol and 1-propanol respectively. Reaction conditions: 1 wt % furfuryl alcohol, 90 °C, t= 4 h. 183

Figure C.4. Induced HCl concentration predicted by OLI for [5-10 mM] MCl_3 in aqueous solution at 100 °C showing a linear correlation between [HCl] and [MCl_3]. 184

Figure C.5. Predicted induced HCl concentration of $CrCl_3$ and YCl_3 in 2-propanol using [5-10] mM MCl_3 at 90 °C. 184

Figure C.6. GCMS spectra of furfuryl alcohol product over $CrCl_3$. Reaction conditions: 1 wt% furfural, 150 °C, 3 mM $CrCl_3$, in 2-propanol-d0 (t= 30 min), 2-propanol-OD (t= 30 min), 2-propanol-d8 (t= 1 h). 185

Figure C.7. : GCMS spectra of furfuryl alcohol product of furfural reduction by YCl_3 (a) and $CrCl_3$ (b) in 1:1 mixture of 2-propanol-d0 and 2-propanol-d8. Reaction conditions: 1 wt % furfural, 150 °C, t= 1 h. 185

Figure C.8. Catalytic activity of $CrCl_3$ and YCl_3 for furfural reduction in 2-propanol. Reaction conditions: 1 wt % furfural, 150 °C, 3 mM MCl_3, t= 1 h..... 186

Figure C.9. ESI-MS spectra of 20 mM YCl_3 (a) and 20 mM $CrCl_3$ (b) in 2-propanol. 187

Figure C.10. Arrhenius graphs of furfural reduction in 2-propanol by YCl_3 (a) and $CrCl_3$ (b). Reaction conditions: 1 wt % furfural, 3 mM MCl_3. 188

Figure D.1. Proposed reaction network of HMF reaction in 2-propanol by zirconia coated silica ZrO_2/SiO_2. R represents $(CH_3)_2CH$ group. 189

Figure D.2. Proposed reaction network of HMF reaction in 2-propanol by commercial bulk zirconia. R represents $(CH_3)_2CH$ group. 189

Figure D.3. Thermogravimetric analysis (TGA) of the spent 7.5 % ZrO_2/SiO_2 after stability experiment. 190

Figure D.4. XRD spectra of pure silica (a) and ZrO_2/SiO_2 with various zirconia content of 2.5 wt% (b), 5 wt% (b), 7.5 wt% (c), 10 wt% (d), 15 wt% (f). 191

Figure D.5. BET surface area of ZrO_2/SiO_2 with various zirconia content. 191

Figure E.1. Comparison of activity for cross-ketonization between FeO, its filtrate after reaction, and homogeneous ferrocene ($FeCp_2$). Reaction conditions: 0.05 M lauric acid, 0.25 M 2-furoic acid, 0.2 g FeO or $FeCp_2$, 316 °C, 90 mins. 192

Figure E.2. H_2 TPR-TGA profiles of iron oxides: FeO (a), Fe_3O_4 (b), and Fe_2O_3 (c). 193

Figure E.3. Time evolution of 2-dodecanoyl furan formation by Fe_3O_4. Reaction conditions: 0.05 M lauric acid, 0.25 M 2-furoic acid, 0.2 g Fe_3O_4, 316 °C, 90 mins. 193

Figure E.4. XPS spectra of Fe $2p_{3/}$ of Fe_3O_4 catalyst pretreated in H_2 (a), pure dodecane (b), 0.05 M lauric acid in dodecane (c), and 0.25 M furoic acid in dodecane (d). Reaction conditions: 0.2 g Fe_3O_4, 316 °C, 30 mins.... 193

Figure E.5. GCMS spectra of (a) 12-tricosanone from reaction starting with unlabeled lauric, (b) 12-tricosanone from reaction starting with ^{13}C-C1 lauric acid, and (c) 2-dodecanoyl furan from reaction starting with ^{13}C-C1 lauric acid. 194

Figure F.1. Permission for Chapter 2 197

Figure F.2. Permission for Chapter 3 198

Figure F.3. Permission for Chapter 4 199

ABSTRACT

With increasing concerns about CO_2 emissions and energy supply, research on renewable production of fuels and chemicals from biomass has surged. Although significant progress has been made, realizing a commercial bio-refinery is still challenging due to technological difficulties associated with the over functionalization of biomass-derived oxygenates. Developing effective catalytic processes to selectively tailor desired products requires deep mechanistic understandings of catalysis and process conditions. This thesis sheds lights on the catalytic roles of acid and base sites of multi-functional catalysts and their synergy in the production of the potential bio-diesel and bio-surfactants.

We undertake a comprehensive mechanistic and kinetic investigation of the multi-step conversion of biomass-derived glucose to 2,5-bis(alkoxymethyl)furan (di-ether), a potential bio-diesel product. To reduce the number of reaction steps and increase efficiency, we aim to develop two tandem catalytic processes with multi-functional acid-base catalysts to effectively facilitate each process. In the first process, glucose is isomerized to fructose, which undergoes dehydration to 5-hydroxymethylfurfural (HMF) in water by homogeneous metal chlorides. Using catalyst characterization, structure-activity relationships, and isotopic labeling experiments, we reveal that the metal salts, owning to their hydrolysis, induce Lewis acidity with an adjacent base site, and Brønsted acid as active species for isomerization and dehydration, respectively. In light of the findings, H-BEA zeolite is employed as the multi-functional solid acid catalyst for glucose conversion to HMF. A

robust kinetic model is developed to optimize the reaction conditions and identify key limitations of zeolite catalysts.

Next, the multi-functionality of metal chlorides is explored for the second tandem process of reductive etherification of HMF to di-ether in 2-propanol. We report for the first time reactivity of metal chlorides for HMF reduction (transfer hydrogenation). Key catalytic design features are elucidated. Specifically, a Lewis acid-base pair is necessary for HMF transfer hydrogenation, and a Brønsted/Lewis acid can enable subsequent etherification. Supported zirconia on silica is identified as a potentially desirable heterogeneous catalyst. The catalyst is synthesized, characterized, and assessed for activity and stability. The di-ether yield is improved by more than two-fold compared to the metal salts.

Besides bio-diesel, biomass-derived furanics are promising intermediates for other valuable chemicals, including oleo furan sulfonates (OFS), which recently emerged as excellent bio-surfactants. An original method is proposed to synthesize 2-dodecanoyl furan as OFS precursor from cross-ketonization of biomass-derived 2-furoic acid and vegetable oil's C_{12} fatty acid (lauric acid). The Earth abundant iron oxides exhibit high activity and selectivity towards 2-dodecanoyl furan formation. Extensive catalyst characterization, active site elucidation and reaction mechanism investigation are conducted to provide mechanistic insights into the relatively unexplored cross-ketonization reaction, and pave ways for future research direction to optimize the catalyst and process design.

Chapter 1

INTRODUCTION

This chapter describes the motivation of research presented in the thesis and provides relevant background. Section 1.1 discusses the potential of lignocellulosic biomass as an alternative feedstock to crude oil for production of fuels and chemicals. Section 1.2 provides an overview of acid-base catalysts and their various applications to biomass processes. Section 1.3 defines the target chemicals in this thesis and the strategic roadmaps for their production. Finally, the structure of the thesis is presented in Section 1.4.

1.1 Biomass as the Renewable Source of Carbon

In recent years, carbon dioxide emissions have become one of the most critical environmental concerns[1]. The rising accumulation of CO_2 in the atmosphere causes climate changes, including global warming, sea level rise, and ocean acidification, threatening sustainability of human population.[1-3] As the result, the increasing quest for production of renewable fuels and chemicals has become the center of scientific research. Non-edible lignocellulose biomass, such as switchgass, cornstover, or agricultural waste, is a promising alternative since it is naturally abundant and does not interfere with the food supply of the growing population.[4-6].

Though promising, the full potential of lignocellulose has not been materialized and the feedstock has primarily been used for energy supply as a heating

and power source.[7] Lignocellulosic biomass contains three major components, cellulose, a polymer of glucose (C6 sugar), hemicellulose, a polymer of glucose and xylose (C6 and C5 sugars), and lignin composed of highly cross-linked substituted phenols. The high oxygen content lowers the energy density of biomass, making it less efficient as a heating source compared to coal[4, 8]. Therefore, efforts to upgrade lignocellulose to high energy content fuels and functionalized chemicals has been strategic for future sustainability[9-11]. The US National Renewable Energy Laboratory proposed an integrated bio-refinery that utilizes biological, physical and thermochemical processes to convert biomass to valuable intermediates and final bio-products in an energy efficient and economically driven fashion [12]. Compared to other proposed thermochemical methods, such as gasification, liquefaction, and pyrolysis, thermocatalytic routes on biomass-derived carbohydrates have gained significant attention since they operate at mild conditions and are less energy intensive and more selective toward targeted molecules. This can be achieved by leveraging various catalytic technologies, as illustrated in Figure 1.1. In this approach, the (hemi)cellulose-rich woody lignocellulose, which is fractionated from the raw biomass in pulp processing[13], is hydrolyzed to monosaccharides and subsequently upgraded to furan derivatives[14-15]. Upon increasing the hydrogen density (e.g., hydrogenation, hydrogenolysis[16,17-19] and/or lengthening the carbon chain (e.g., via aldol condensation, etherification, ketonization)[20-22], the sugar-derived furanics can be converted into a wide range of valuable chemicals. However, unlike the well-developed petroleum refinery, biomass-related processes still face grand technological challenges stemming from the chemically complex feedstock[23-25]. The diverse

chemical functionality of biomass-derived building blocks, while brings potential for new chemistries, also drives competing side reactions. Therefore, realizing biomass valorization needs not only novel reaction pathways but also active and selective catalysts. Understanding the catalysis and the reaction mechanism is critical to improve process efficiency. Depending on the chemistry, desirable catalytic features include but are not limit to acid sites, base sites, redox properties and shape selectivities[26-33]. Catalysts with acid and/or base properties are most commonly used due to their applicability and tunability to a wide range of targeted chemistries.[26, 28, 34] The following section discusses the characteristics of acid-base catalysts and their potential application to the selected biomass-related reactions.

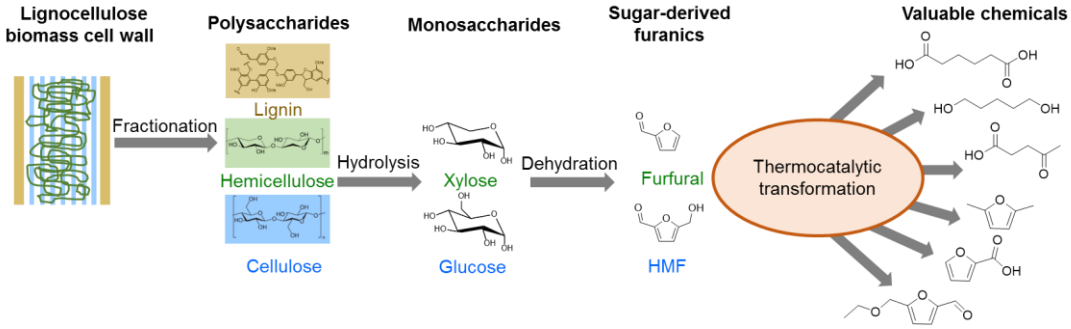

Figure 1.1.Thermocatalytic conversion of biomass to valuable chemicals.

1.2 Acid-Base Catalysts

An acid or base can be defined in term of Brønsted-Lowry concept or Lewis concept. A Brønsted acid/base catalyst transfers/receives proton to/from the reactant[35] while a Lewis acid/base catalyst accepts/donates electrons from/to the reactant[36]. Their applications can be found in numerous chemical production and oil refinery processes such as cracking, isomerization, and aromatization [37]. Herein, we will focus on the most common inorganic acid/base catalysts encountered in biomass conversion.

Brønsted acids vary from homogenous mineral acids[38-39], such as hydrochloric, sulfuric acids, to solid acids such as mesoporous and miroporous aluminosilicates[40-41], heteropoly acids[42-43], and (sulfated) metal oxides[44-45]. Lewis acids often contain electron deficient transition metal centers that coordinately bind to the reactants. Examples include homogeneous transition metal ions[46-47], high energy lattice metal oxides[48-49], and metal-substituted and cation exchanged zeotype catalysts[50-51]. On the other hand, amines, carbonates and hydroxides can act as homogeneous Brønsted bases in solution [52-54], while Lewis bases are less common and usually form on ligands in transition metal catalysis[55]. The most common solid base catalysts are metal oxides, especially of alkali and alkaline earth and rare earth metals[56-58]. The surface hydroxyl groups have strong proton affinity and possess Brønsted basicity while the surface oxygen atoms (O^{2-}) act as Lewis bases to donate a lone pair of electrons[59]. Brønsted acids are employed as catalysts for various biomass conversion processes, such as sugar dehydration[14], etherification/esterification of biomass derived-carboxylic acids for C-O coupling[26, 60-61], acylation[62-63] and Diels-Alder reaction of furan for C-C bond formation[64-65]. Lewis acids catalysts have also widely been used to facilitate (hemi)cellulose hydrolysis[66-67], sugars interconversions[48, 68-71], and catalytic transfer hydrogenation[19, 72]. Chemistries requiring base catalysts include, but are not limit to, lignin depolymerization[73-74], aldol condensation of furanic derivatives[20, 75], and transesterification of vegetable oils[56, 58]. Heterogeneous catalysts are generally preferred over the conventional homogeneous catalysts, which are often corrosive and difficult to separate and reuse. On the other hand, homogeneous catalysts with well-defined structures can provide information of the true catalytic activity, which is often

challenging to deconvolute from adsorption/desorption and transport limitations within solid catalysts. Therefore, mechanistic understanding over homogeneous catalysts can provide insights into heterogeneous catalyst design.

The strength of an acid/base greatly affects reactivity. It can be determined from various established, experimental methods. Homogenous Brønsted acidity/basicity in aqueous solution is measured directly from the pH value, and is associated with the activity of the corresponding dissociated proton or hydroxide ion, respectively (a_{H^+} and a_{OH^-}); see Eq. (1.1 and Eq. (1.2. The proton activity is a thermodynamic function of its concentration, temperature and ionic strength of the solution, and is frequently equated to the H^+ concentration in dilute solution[76].

$$pH_{acid} = -log_{10}(a_{H^+}) \qquad (1.1)$$

$$pH_{base} = 14 + log_{10}(a_{OH^-}) \qquad (1.2)$$

Since many biomass related reactions take place in an organic phase, where it is challenging to determine the activity coefficient of proton and hydroxide ions, experimental pH values do not correspond to the intrinsic acidity/basicity[77]. In those cases, the Hammett acidity (H_o) measurement, a titration method, is an alternative. In principle, H_o is determined from the dissociation constant (K_B) of a base indicator (B) and the ratio of the concentration of the base with the conjugate acid (BH^+) as follows[78]:

$$H_o = log_{10}(K_{B)} - log_{10}(\frac{[BH^+]}{[B]}) \qquad (1.3)$$

The Hammett acidity method can also be applied to super acids outside the pH range and to solid acid catalysts [79-80]. Acidity/basicity of solid catalysts is often quantified

based on the adsorption/desorption of probe molecules onto the materials[81-82]. In general, a base/acid molecule adsorbs on the surface of the catalyst for an extended amount of time at room temperature before removal of physically adsorbed components with inert gas flushing. After evacuation as the temperature is ramped up, chemisorbed molecules are detected. In a typical temperature-programed desorption (TPD) profile, the integrated area under the peak is used to quantify the acid/basic site density. Higher desorption temperatures are associated with a stronger acid/basic strength. Common probe molecules are ammonia, pyridine, and n-propanol for acidity, and carbon dioxide, sulfur dioxide and pyrrole for basicity[59, 83-84]. Although insightful, interpretation of acid/basic site density and strength from TPD profiles should be done carefully since probe molecules with strong affinity like ammonia may re-adsorb onto the catalyst surface during temperature ramping resulting in overestimation of the acidity[85-86]. In addition, it is challenging to differentiate Brønsted and Lewis sites from TPD of the aforementioned inert probes. Alternatively, TPD of reactive compounds like propyl amines, which decompose to propylene and ammonia over Brønsted acid sites in a well-defined range of temperature via the Hoffman elimination reaction, can be used to measure the Brønsted acid density[87-88]. Vibrational spectroscopic techniques of the adsorbed probe molecules are also powerful to identify and quantify the surface acidity/basicity of the catalytic materials[83]. Fourier-transformed infrared spectroscopy (FTIR) of pyridine adsorption is the most widely used method for acidity characterization. Pyridine adsorbs on solid acids in three modes with well-defined characteristic absorbance bands, that is hydrogen-bonded (physisorption), coordinatively bonded (on Lewis acid sites) and pyridinium ion (on Brønsted acid

sites). Combination of the peak areas with carefully measured extinction coefficients can provide quantitative information on the density of each type of sites. The change in intensity and wavenumber shift of the bands with increasing temperature during pyridine desorption can also be used to determine the relative acid strength[89-91]. Besides pyridine, other probe molecules such as substituted pyridine, (deuterated) acetonitrile, and CO can also be used selectively to probe Brønsted acid sites, stronger acid sites, and acid sites with potential steric hindrance, respectively[92-94]. Regarding basicity, IR of CO_2 adsorption is a common technique to characterize the nature and strength of surface basic sites, such as hydroxyl groups (Brønsted base) or surface oxygen (Lewis base). CO_2 adsorption on OH group forms bicarbonates, and on Lewis basic O^{2-} carbonates in either bidentate or unidentate mode, depending whether the metal cation is involved[95-96]. Bulk carbonate species in polydentate adsorption mode are also detected with much less defined structures[97]. Therefore, interpretation of CO_2 adsorption needs to be handled with care. Similar to acidity measurement, other acidic molecules (e.g., pyrrole, SO_2) can also be effective probes for surface basicity of solid catalysts[98-99]. Overall, the selection of probe molecules is not universal and depends significantly on the nature and strength of the catalyst sites, as well as size exclusion effects. While characterization techniques offer insightful details on acid/basic properties of catalysts, the correlation of different acid/base sites to their observed reactivity should be analyzed very critically. Interaction between the catalyst surfaces with probe molecules can be very different from that with the reactants[59, 83]. In addition, most of the acid/base measurements are conducted ex-situ and do not account for surface modification under reaction conditions, as well as solvation effects

in liquid phase reactions. Given all these challenges, titrations that selectively poison the acid/base sites and affect reaction rates can be effective in elucidating the true catalytic sites/species[100-101]. The active site density can also be determined from the minimum concentration of titrants to completely shut down the reactions[102-103]. In short, various basic and advanced techniques have been developed to characterize acidity/basicity of catalysts and should be complimentarily utilized to critically assess their contribution to surface reactions.

Due to the high functionality of biomass-derived oxygenates, processes typically consist of several reaction steps carried simultaneously but catalyzed by different catalyst sites[104-105]. Therefore, research on multifunctional catalysts and the cooperativity of multiple catalyst sites have gained significant attention. Cascade reactions increase process intensification[71, 105-108]. Since many biomass processes involve either acid or base catalysts, materials bearing acid-base pairs are attractive and can facilitate some of the main backbone transformations, such as aldol condensation, transfer hydrogenation, and dehydration[20, 109-110]. The following section discusses multifunctional acid-base catalysts and their application to the production of the bio-chemicals targeted in this thesis.

1.3 Target Chemicals and Chemistries

1.3.1 Platform chemical 5-hydroxymethyl furfural

The U.S. Department of Energy identified a list of top value-added chemicals from bio-refinery carbohydrates based on their potential markets[111]. Among these, 5-hydroxymethyl furfural (HMF) is considered as a platform intermediate for future

production of fuels and polymer precursors. Since the first reported synthesis of HMF from carbohydrates by fructose dehydration, a growing number of reports has focused on improving the isolated yield of HMF from biomass hexoses (C6 sugars)[112-113]. Key technological challenges to address include selective catalyst, cheaper sugar feedstock, optimal reaction conditions, and effective separation processes[113-114]. Despite the significant scientific advances in HMF production, further improvements are still needed for an economically viable HMF production.

Although fructose dehydration to HMF has been extensively studied over various Brønsted acid catalysts and produces up to 80% isolated HMF yield[115-117], the high cost of fructose renders the whole process uneconomical[114, 116, 118]. In the search for cheaper feedstock, glucose, which is the monomer of cellulose, became attractive as it costs only half of the price of fructose[119] However, glucose dehydration with Brønsted acid resulted in much lower HMF yield of maximum 20 %[113]. A two-step glucose production to HMF is envisioned, consisting of glucose isomerization to fructose, followed by fructose dehydration to HMF. However, since glucose isomerization is slightly endothermic with the equilibrium constant of 1 at 298 K, separation of the sugar mixture and glucose recycle are required, reducing the process efficiency. Therefore, a one-pot reaction for isomerization-dehydration is proposed to shift the equilibrium and maximize glucose conversion[109, 120]. While the tandem approach reduces the number of reactors and increases efficiency of unit operation, it also introduces new technological challenges, specifically with the catalyst and process design. Due to the differences in catalyst active site and reaction conditions between isomerization and dehydration, it is necessary to design multi-functional

catalysts to facilitate each reaction step selectively and optimize operating condition for both isomerization and dehydration that maximize the rate to HMF formation and minimize side reactions.

While mechanistic and kinetics insights are available for fructose dehydration[121-124], knowledge about glucose isomerization has been limited. Glucose conversion to fructose is an aldose-ketose isomerization[125]. The low solubility of sugars in most organic solvents limit the choice of solvent to aqueous solution, aprotic polar solvents like dimethyl suloxide (DMSO), dimethyl formamide (DMF), and ionic liquids (ILs)[126-127]. The low volatility of the aforementioned organic solvents makes them economically and ecologically unattractive, and thus, water is the green solvent choice. Historically, isomerization is facilitated by base catalysts, such as sodium and calcium hydroxide, via the Lobry de Bruyn–van Ekenstein reaction (LdB_AvE) with a tautomeric enediol as the intermediate. The enediol can be reprotonated back to glucose or mannose, which is an epimer of glucose due to the loss of the stereochemical configuration in the enol form[128]. Besides fructose and mannose, glucose conversion in base produces a handful of other sugars along with degradation products, leading to very low selectivity[129-130]. Weaker bases such as pyridine and amines have been shown to slow down side reactions and increase the yield to fructose[52, 131]. However, the basic solution neutralizes the acidic environment of fructose dehydration and prevents the cascade reaction of glucose conversion to HMF. Solid bases such as hydrotalcites and sodium-exchanged zeolites give similar activity to those of homogeneous weak bases but suffer from severe deactivation due to metal leaching and loss of active surface hydroxyls during reaction, respectively[132-133].

Currently, the high-fructose corn syrup industrial production utilizes xylose isomerase enzyme to selectively generate a product stream of 42 wt% fructose, 50 wt% glucose and 8 wt % saccharides[134]. Though selective, operation of the enzymatic isomerization is restricted to narrow ranges of pH and reaction temperatures, making it incompatible with the subsequent fructose dehydration[134]. Therefore, developing novel isomerization processes with high selectivity and compatibility to dehydration is critical. Recent breakthroughs on Lewis-acid catalyzed glucose isomerization encourage the prospect of HMF commercialization from biomass in aqueous solution[106, 126, 135-137]. Davis and co-workers introduced Lewis acid metal-substituted zeolites, most commonly Sn-BEA, as effective catalyst for isomerization and produced a mixture of 31 wt% fructose, 46 wt% of glucose and 9 wt% of mannose in aqueous solution. Homogeneous metal salts, such as $CrCl_3$ and $AlCl_3$ have also been shown to be active for glucose isomerization. These Lewis acids are hypothesized to facilitate isomerization via an intramolecular hydride transfer from C2 to C1 of glucose with a six-membered ring transition state at the metal center by isotopic labeling experiments coupled with NMR measurement[69, 135, 138]. Reactivity of the Lewis acids in aqueous solution was surprising since water molecules tend to coordinate to the metal centers and deactivate the catalysts. As the result, research focused intensively on investigating the nature of the catalytic active sites. An "open site" of tin, which is partially hydrolyzed from its closed conformation, is hypothesized to be active for glucose isomerization based on spectroscopic and computational work[135, 138]. The Lewis acidic metal site and the Brønsted basic adjacent hydroxyl group cooperatively mediate the hydride transfer. Although heterogeneous

catalysts are generally preferred due to the ease of separation, the synthesis of Sn-BEA is lengthy and complex, posing challenges for catalyst scale-up. Additionally, the structural environments of the metal center are not well-defined and are dynamically modified during reaction, leading to uncertainty on quantification of active sites and the comparison of intrinsic activity among metals. In contrast, metal chlorides are commercially available and inexpensive. The isomerization active species of $CrCl_3$ is hypothesized to be a partially hydrolyzed metal cation with similar structure to that of the open Sn site[69, 106]. However, a mechanistic study is still limited to $CrCl_3$ and there are still open questions about metal chloride catalysis, reaction mechanisms, and the dependence of activity on the metals. Mechanistic insights from the metal chloride-catalyzed glucose transformation can provide desirable features for new solid catalyst design. In light of Lewis acids as a new catalyst class for isomerization, a single catalyst with both Lewis and Brønsted sites can be promising to couple glucose isomerization and fructose dehydration to HMF in one pot. Zeolites, which contain Brønsted acid sites at framework aluminum[139-140], show activity for isomerization owing to their Lewis acid sites at extra-framework aluminums[141-142] and can be potential bi-functional catalyst for the cascade glucose conversion to HMF.

Besides the desirable glucose isomerization and fructose dehydration, other side reactions occur to significantly reduce HMF selectivity due to the high functionality of the sugars and HMF. The most unwanted pathways are HMF rehydration to levulinic acid (LA) and formic acid (FA), sugars and HMF oligomerization to heavy polymeric molecules (humins), as well as epimerization of glucose to mannose[38, 136, 143-144]. Mechanistic understandings of the side reactions are

necessary to mitigate carbon loss. Ring-opening of HMF to LA and FA in the presence of water by acid catalysts has been studied thoroughly [145]. Research on humin formation found the aldol addition/condensation of furanic compounds, derived from acid-dehydration of sugars, as a dominant reaction path; humin structures vary with process conditions[146-147]. The mannose formation follows intramolecular hydride transfer from fructose in Sn-BEA, or intramolecular carbon shift from C2 to C1 of glucose (Bilik pathway) when either alkali or borate salts are incorporated to the Sn sites[138]. However, the epimerization mechanism is still limited to zeolites and not known for other Lewis acid catalysts (e.g., metal salts). Overall, given the complexity of the reaction network of the one-pot glucose conversion to HMF and of multifunctional catalysis, optimization of HMF rate of formation and selectivity should consider not only catalyst design but also operating conditions.

1.3.2 Bio-diesel 2,5-bis(alkoxymethyl)furan

Commercial bio-fuels, such as ethanol from corn starch, and esters of methanol and triglycerides from vegetable oil, interfere with the food chain and the availability of feedstock is limited. In contrast, fuels from lignocellulose have the potential to replace transportation fuels in heavy duty vehicles, jet engines and other applications[4]. The U.S. National Renewable Energy Laboratory leads efforts to evaluate potential bio-fuels based on their energy density, combustion performance, and compatibility with the current vehicle infrastructure[148]. Biomass-derived furan derivatives are identified as such a class of molecules. While alkylated furans, i.e., methyl furan and 2,5 dimethylfuran, are considered as candidates for spark ignition engines[149], furanyl ethers, such as 5-alkoxymethyl furfural and 2,5-bis(alkoxymethyl) furan (BAMF),

show potential as alternatives to diesel[60, 150]. The representative ether molecule, 5-ethoxymethyl furfural (EMF), has energy density of 8.7 $kWhL^{-1}$, comparable to that of diesel fuel (9.7 $kWhL^{-1}$) and proven performance when was blended with diesel by Avantium Technologies[150]. Compared to EMF, BAMF is deemed to be a higher-grade diesel owing to its higher energy density, miscibility and lower crystallinity temperature[151-152]. Therefore, an effective catalytic process to produce this di-ether molecule is another thesis' research target.

A two-step process for BAMF production, including HMF hydrogenation (reduction) by H_2 gas over a noble metal catalyst, followed by the Brønsted acid catalyzed etherification in alcohol solvent was proposed. Balakrishnan *et al*. carried out both sequential and one-pot reaction of HMF reductive etherification under H_2 pressure using Pt/C and Amberlyst 15 to yield up to 65 % of HMF[60]. While the result is promising, the use of H_2 and noble metal catalyst increases the cost. In addition, the physical mixture of metal and acid catalysts can be cumbersome to separate and regenerate. Alternatively, transfer hydrogenation, which utilizes an organic solvent as a hydrogen donor can reduce the carbonyl group of furan to its corresponding alcohol, while eliminating the need for H_2 gas and noble metal and being selective by avoiding chemistry on the furan ring[153]. The mechanism is proposed to follow the Meerwein-Ponndorf-Verley (MPV) reduction, where the H atom at α-C of the alcohol donor is transferred to the α-C of furfural to yield the corresponding alcohol. Effective catalysts for MPV reduction of furfurals can be Lewis acids or bases such as metal substituted microporous/mesoporous aluminosilicates, metal oxides and metal hydroxides[154]. Etherification of furanyl alcohols has also been studied extensively with both

homogeneous and heterogeneous catalysts that exhibit Brønsted acidity[60, 155-156]. The structure of the substitution at C5 position of the furan ring and polarity of the alcohol solvents significantly affect the rate of furanyl ether formation. Etherification is proposed to proceed via nucleophilic substitution S_N 1 mechanism[155]. Lewis acids such as Sn-BEA zeolites, metal salts and transition metal oxides have also been reported to be active for etherification[151, 157-160]. However, the mechanism is not well understood, and the active species remains inconclusive. The silanol group in Sn-BEA zeolite was speculated to acts as weak Brønsted acid to facilitate etherification[152]. In the case of metal salts, several studies proposed that the induced Brønsted acid from metal salt alcoholysis is responsible for etherification[161-162]. However, there is no quantitative correlation between the concentration of the induced hydrogen ions and the rate of etherification. Understanding the nature of active sites and the mechanism of the MPV reduction and etherification will be insightful in designing multifunctional catalysts for the cascade reaction of reductive etherification of HMF to BAMF. The one-pot strategy utilizes an alcohol solvent not only as hydrogen donor for the transfer hydrogenation step, but also as the reactant for etherification.

1.3.3 Production of 2-dodecanoyl furan, a bio-surfactant precursor

With the incentive to pioneering chemical production from biomass, Catalysis Center for Energy Innovation (CCEI), led by research at University of Minnesota, has recently introduced oleo furan sulfonate as a new class of surfactants. Molecule structures consist of a furan ring, a hydrophobic long chain hydrocarbon at the C1 position, and a hydrophilic sulfonate group at the C5 position[63]. The compounds have been tested for detergency using several criteria, including critical micelle

concentration (CMC), defined as the minimum surfactant concentration for micelle formation, Kraft point (T_{Kraft}), below which surfactant forms solid crystals, and their stability in hard water conditions. Most of the furan-based molecules with modified hydrocarbon chain structures showed comparable or superior surfactant properties to the equivalent petroleum-derived surfactant alkylbenzenesulfonate[63].

The first and crucial step in the synthesis of oleo furan sulfonate is C-C coupling between the furan with a fatty acid-derived anhydride Park *et al.* employed Friedel Crafts acylation of furan and lauric anhydride under mild condition (180 °C) with a hierarchical porous Brønsted acid zeolite (Al-SPP) to achieve up to 89 % yield of 2-dodecanoyl furan as the acylated product[63]. However, the synthesis route also produces equimolar amount of lauric acid. The separation of the lauric acid from the reaction mixture is hard due to its high boiling point (299 °C) and its subsequent conversion to lauric anhydride via dehydration is energy intensive. Alternatively, a homogeneous route, where trifluoroacetic anhydride is used with a mixture of furan and lauric acid, could produce 2-dodecanoyl furan quantitatively at room temperature[63]. The limitation is that the method also generates a stream of corrosive trifluoroacetic acid, which cannot be recycled easily. In this thesis, a new synthesis method for 2-dodecanoyl furan using cross ketonization of furoic acid and lauric acid is proposed for the first time. Compared to acylation routes, in ketonization byproducts such as carbon dioxide and water are trivially separated, leading to increased process efficiency.

Ketonization is one of the oldest organic chemistry reactions and historically used for acetone production from acetic acids[163]. With the potential application to

grow the carbon chain of biomass-derived oxygenates, the chemistry has recently attracted growing interest[164]. Extensive studies on the reaction mechanism for alkyl carboxylic acids are available[164-165]. Various catalysts were shown to be effective for ketonization, including metal oxides, doped metal/metal oxides, and H-zeolites[166-170]. Effective (metal doped) metal oxides possess acid-base properties as well as reducible metal sites, and their mechanisms involve the formation of surface carboxylates prior to their C-C coupling[171-174]. The catalysis by H-zeolites leverages their strong acidity to form the highly reactive surface acyl species, which either reacts with another carboxylic acid to generate the final ketone or rehydrates back to the parent carboxylic acid. The competing rehydration makes H-zeolites inefficient as a catalyst, especially under abundant presence of water, which is often encountered in biomass processes[169]. It should be noted that most ketonization studies were conducted on small molecules in gas phase. Due to low volatility of both reagents lauric acid and 2-furoic acid, their cross-ketonization is performed herein in liquid phase where solvent effect needs to be accounted for. In addition, literature on cross-ketonization, especially with the involvement of cyclic compounds, is extremely limited compared to the more favorable self-ketonization of two identical carboxylic acids. Research on ketonization of furanic compounds is non-existent. Our strategy is to leverage previous knowledge on ketonization and explore the catalytic and mechanistic characteristics of cross-ketonization of furoic and lauric acid to selectively produce 2-dodecanoyl furan as the bio-surfactant precursor.

1.4 Thesis Motivation and Scope

While lignocellulosic biomass is great feedstock for fuels and chemicals, there still exist technological challenges that prevent commercialization. The aim of this thesis is to develop fundamental understandings of the thermochemical-catalytic processes to convert (1) lignocellulose biomass-derived sugars to the platform chemical 5-hydroxymethal furfural (HMF), (2) HMF to the potential biodiesel 2,5 bis-(alkoxymethyl) furan (BAMF), and (3) biomass-derived 2-furoic acid and lauric acid from vegetable oil to 2-dodecanoyl furan as a bio-surfactant precursor. Our intellectual focus is on elucidating the mechanistic interplay of multifunctional acid-base catalysts on these chemistries, as well as unraveling the kinetic details of the complex reaction networks. The insights gained herein can assist future research on multifunctional catalysts for other biomass processes.

Chapter 2 methodologically investigates the active species and mechanism of metal chloride-catalyzed glucose interconversion in aqueous phase as the first step in the one-pot HMF synthesis. Correlation between the effect of reaction parameters on metal chloride hydrolysis and glucose isomerization rate revealed a partially hydrolyzed metal cation as the isomerization active species. The mechanisms of isomerization, epimerization and other sugar interconversion by various metal chlorides were studied by isotopic labeling experiments.

Chapter 3 begins with examining H-BEA zeolite as the potential multifunctional catalyst for the cascade glucose conversion to HMF, based on the desirable catalyst design unveiled in Chapter 2. Its unexpectedly low activity necessitates deeper understanding of the catalyst and process. A first-of-its-kind kinetic model was developed by combining catalyst characterization, adsorption

isotherms, and experimental kinetics to reveal the key limitation of the catalyst and guide future research on HMF production.

Chapter 4 extends the previously learned bi-functionality of metal chloride catalysts in aqueous solution to the tandem reductive etherification of HMF to BAMF in 2-propanol. The dependence of product selectivity on the metals was correlated with the degree of alcoholysis/hydrolysis of the metal chloride catalysts. The role of the Lewis/Brønsted acidity for transfer hydrogenation and etherification was elucidated using experimental and a kinetic model in conjunction with the salt speciation.

Chapter 5 presents ZrO_2 supported on silica as a potential multifunctional solid acid-base catalyst for reductive etherification of HMF. The catalyst was synthesized, characterized and tested for HMF conversion to BAMF in 2-propanol. The synthesized ZrO_2/SiO_2 exhibits superior reductive etherification activity and stability compared to the homogeneous metal salts and the commercial bulk ZrO_2.

In chapter 6, a novel strategy is proposed to produce 2-dodecanoyl furan as a bio-surfactant precursor via cross ketonization of biomass-derived furoic acid and vegetable oil derived lauric acid. Earth abundant iron oxides display high activity and selectivity towards cross-ketonization. X-ray photoelectron spectra, in combination with other characterization techniques, showed the transformation of all the iron oxides to Fe_3O_4 post-reaction. The Fe^{2+} site and the surface oxygen are proposed to cooperatively facilitate the ketonization via a β-ketoacid intermediate pathway, which is verified by isotopic labeling experiments.

Finally, chapter 7 summarizes the key findings of this thesis and lays out some directions for future research for further improvement of the bio-diesel and bio-surfactant molecules, as well as on multifunctional acid-base catalysts for biomass conversion.

Chapter 2

MECHANISTIC INSIGHTS INTO LEWIS ACID METAL SALT-CATALYZED GLUCOSE CHEMISTRY IN AQUEOUS SOLUTION

2.1 Introduction

Renewable production of chemicals and fuels from biomass has drawn considerable attention due to increasing concerns about CO_2 emissions. Among the top platform chemicals produced from biomass, 5-hydroxymethyl furfural (HMF) has been a major target for the formation of polymer precursors, fuel additives and pharmaceuticals.[4] HMF can be produced from cellulose via cellulose hydrolysis to glucose, glucose isomerization to fructose, and fructose dehydration to HMF.[113] Currently, HMF production is not commercial partly due to the cost and the equilibrium limitation of the commercial enzymatic glucose isomerization to fructose.[134] To overcome these challenges, research has turned to thermochemical catalysts to carry out glucose isomerization. Such catalysts are compatible with Brønsted-acid catalyzed fructose dehydration and can enable integration of the three aforementioned steps in one-pot.[106, 136-137, 175]

A key development in this direction was made by Davis and co-workers who introduced for the first time substituted BEA zeolites (Sn-BEA, Ti-BEA) as effective Lewis acid catalysts for the glucose isomerization to fructose.[106, 135-136, 176-177] Aside from fructose, these Lewis acid BEA zeolites also convert glucose to other monosaccharides, such as mannose and sorbose.[138, 177] The catalytic activity,

selectivity, and mechanism of glucose interconversion vary with catalyst and reaction media. While both Sn-BEA and Ti-BEA isomerize glucose to fructose via a C2-C1 intramolecular hydride transfer (1,2 hydride transfer), the former catalyst is more active.[135] These Lewis acid BEA zeolites also catalyze the conversion of fructose to mannose via a subsequent reverse 1,2 hydride transfer, with faster rate in methanol than in water.[138] Interestingly, when the reaction occurs in the presence of borate salt or when sodium is incorporated into the active site (Na-Sn-BEA), a C2-C1 intramolecular carbon shift, known as the Bilik reaction,[178] occurs to directly form mannose as the major product.[138, 179] Unlike Sn-BEA, the Ti^{4+} center in Ti-BEA also facilitates a parallel path to convert glucose to sorbose through a C5-C1 hydride transfer (1,5 hydride transfer).[177] The different glucose interconversion mechanisms are summarized in Figure 2.1. In all cases, it is believed that the active sites around the metal (Sn, Ti) center are partially hydrolyzed, forming the so called "open site" structure. [176, 180-181]

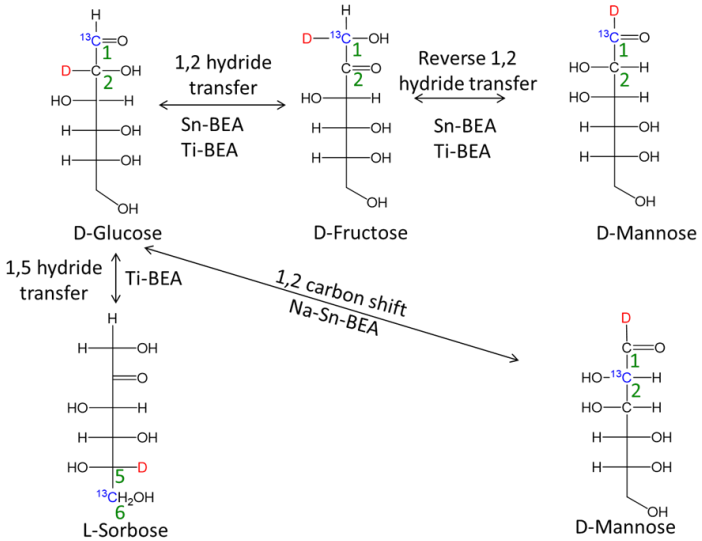

Figure 2.1. Summary of the mechanism of glucose interconversions by Lewis acids known to date.

Another class of Lewis acids effective for the glucose isomerization entails metal halides. Specifically, Zhao and co-workers introduced chromium chloride in ionic liquid to carry out glucose conversion to HMF.[126] Subsequently, several other groups implemented one pot synthesis of HMF from glucose using metal chlorides in different solvents, such as ionic liquids,[182-183] organic solvents[184-185] and water.[106, 137, 186] The rather unexpected tandem catalysis of Lewis acid isomerization of glucose to fructose followed by Brønsted acid catalyzed dehydration of fructose to HMF in the absence of external acid was rationalized by realizing that metal salt hydrolysis produces Brønsted acidity.[106] Our mechanistic studies of glucose isomerization by $CrCl_3$ and $AlCl_3$ showed striking analogy to the mechanism of glucose isomerization to fructose by Sn-BEA.[69] In all cases, the reaction proceeds through 1,2 hydride transfer and exhibits a kinetic isotope effect, indicating that the hydride transfer is the rate limiting step.[69, 135] Studies on the kinetics and speciation of metal chlorides in aqueous solution identified partially hydrolyzed metal aqua ions (i.e., $[CrOH]^{2+}$ and $[Al(OH)_2]^+$ for $CrCl_3$ and $AlCl_3$, respectively)[106, 187] and have been hypothesized to be to the active species. These species possess a Lewis acid center and OH group(s) as a Brønsted base to cooperatively facilitate the isomerization mechanism, and as such, they resemble the structure of open sites of Sn-BEA and Ti-BEA. These analogies open an opportunity to leverage the fundamental knowledge on homogeneous metal salts to better understand and improve heterogeneous Lewis acid catalysts, whose synthesis is often challenging.[69, 106, 188]

Despite recent work on metal salts for sugar conversion, there is still open questions about nature of the active metal species for glucose isomerization. In

addition, mechanistic studies on glucose epimerization by homogeneous Lewis acids is still limited. In this work, we will expand on the preceding $CrCl_3$ work to other metal chlorides and provide much stronger evidence for the previously hypothesized active species. Moreover, the mechanism of mannose formation from glucose in aqueous solution using various metal (III) chlorides will be examined for the first time. We also report the formation of hexoses other than fructose and mannose from glucose. We show that metal chlorides not only display a wide range of catalytic activity but also have different selectivity. Our study further delineates the mechanistic similarities and differences between homogeneous and heterogeneous Lewis acid catalysts.

2.2 Experimental Methods

The catalysts, including the hydrated form of $CrCl_3$, $AlCl_3$, $InCl_3$, $GaCl_3$, $LaCl_3$, $DyCl_3$ and $YbCl_3$, were purchased from Sigma Aldrich and used without further modification. A typical kinetic experiment was carried out in a 5 mL glass vial containing 2 mL of aqueous solution of glucose and a metal (III) chloride catalyst (MCl_3). The reactors were heated in a temperature controlled aluminum block, consisting of different oil wells, on a stirring hot plate. After a certain time, the glass vials were quenched immediately in an ice bath and the post reaction solutions were filtered and analyzed using high performance liquid chromatography (HPLC) consisting of Waters Alliance System (an e2695 HPLC), with a refractive index (RI) detector, photodiode array (PDA) detector, and a fraction collector. Post reaction mixtures were analyzed and separated using a Biorad HPX 87C column or a Biorad HPX 87P column. HPLC grade water was flowed at a rate of 0.5 mL/min as a mobile

phase; the column temperature was 75 ºC and the RI detector temperature was 35ºC. Calibration curves to correlate the integrated peaks with the compounds' concentration were prepared from standard solutions. The carbon loss due to humins formation is less than 10% for most of the catalysts (20% for $LaCl_3$).

In some experiments, the catalyst solutions were preheated to reaction temperature for 24 h prior to the catalytic reactions. The presence of nanoparticles in the catalyst solutions were detected with dynamic light scattering (DLS) spectrometer (Wyatt Mobius).

In the isotopic labeled experiments, reactions were conducted at 140ºC using 10 wt% glucose labeled with ^{13}C at C1 position ($^{13}C1$ glucose) or 10 wt % glucose labeled with ^{2}H at C2 position (D2 glucose) purchased from Cambridge Isotope, and 17 mM of MCl_3. The reaction time was varied in order to obtain adequate conversion. The monosaccharide sugars in post reaction solutions were separated and collected using a fraction collector. The collected samples were evaporated in a vacuum oven (30 ºC, 30 in Hg) before dissolved in D_2O for Nuclear magnetic resonance (NMR) measurements. ^{1}H NMR and ^{13}C NMR spectra were recorded using a Bruker 400 MHz NMR spectrometer. Unlike ^{1}H NMR spectroscopy, ^{13}C NMR spectroscopy is usually not quantitative due to low abundance of ^{13}C nuclei. In order to quantify the species concentration using ^{13}C NMR, we employed an inverse gated decoupling methodology. With this method, proton decoupling is only applied during acquisition time resulting in no polarization from ^{1}H to ^{13}C via the Nuclear Overhauser Effect (NOE).[189] Therefore, the obtained spectra can be quantitative.[190]

2.3 Results and Discussion

2.3.1 Active species of metal chlorides for glucose isomerization to fructose

Previous work on metal chloride-catalyzed glucose isomerization has shed some light on the active species either by coupling a kinetic study with speciation or spectroscopic techniques. Specifically, Choudhary *et al*. proposed that the partially hydrolyzed $CrOH^{2+}$ and $AlOH^{2+}$ species are the active ones for glucose isomerization by $CrCl_3$ and $AlCl_3$, respectively, based on the observed decreasing rate of isomerization with addition of HCl.[106] However, addition of HCl introduces both protons and chloride ion to the solution, and thus, perturbs not only the hydrolysis but also the thermodynamics of the formation of Cl^- containing species, as well as the solution's ionic strength. In addition, there are likely several hydrolyzed metal ions generated from hydrolysis, and their oligomerization to metal clusters should be considered (Eq. 2.1-2.5). Tang et al. showed the evidence for coordination of glucose and $Al(OH)_2^+$ species in the electrospray ionization mass spectra (ESI-MS) and concluded that $Al(OH)_2^+$ was the isomerization active species.[187] It should be noted that species can be easily hydrolyzed/altered during ESI-MS sample analysis due to charge reduction, ligand loss, and condensation.[191] Therefore, ESI-MS alone is not adequate to conclude the active species. Herein, we combined a kinetic study with a thermodynamic model and spectroscopy to provide stronger evidence for the active species hypothesis. The speciation from hydrolysis is

$$M^{3+} + H_2O \leftrightarrow M(OH)^{2+} + H^+ \qquad (2.1)$$

$$M(OH)^{2+} + H_2O \leftrightarrow M(OH)_2{}^+ + H^+ \qquad (2.2)$$

$$M(OH)_2{}^+ + H_2O \leftrightarrow M(OH)_3\downarrow + H^+ \qquad (2.3)$$

$$-MOH + -MOH \leftrightarrow M_2O + H_2O \qquad (2.4)$$

To investigate the effect of Cl^- and ionic strength, NaCl and HCl with the same concentration were added to a $CrCl_3$ solution to study their effect on isomerization rate. As illustrated in Figure A.1, glucose conversion significantly slows down with HCl addition but remains unchanged with NaCl. Consequently, the inhibitive effect of HCl can be attributed to the H^+ ion and its perturbation on the hydrolysis equilibrium of $CrCl_3$ solution rather than the change in the ionic strength. In addition to shifting the catalyst solution by Le Chatelier's principle, we preheated the salt solutions to reaction temperature for 24 h prior to reaction and observed a significant drop in isomerization rate. Visible solid precipitation was detected in the 24 h-preheated $CrCl_3$ solution. In contrast, the $CrCl_3$ solution heated to the operating temperature for 1 h (within reaction timeframe) showed no precipitation. Its DLS spectrum exhibited an exponential decay, indicating the presence of nanoparticle suspension (Figure 2.2). The nanoparticles and solid precipitate were likely to be hydroxide $Cr(OH)_3$ and metal clusters formed by oligomerization and aggregation, respectively. Since the formation of solid precipitate reduced the isomerization rate, we hypothesized that the metal clusters are not the catalytically active species. The change in isomerization rate was closely monitored with stepwise addition of HCl. Interestingly, enhancement on isomerization rate was observed for the first time with low concentration of added HCl (Figure 2.3). Higher concentration of HCl eventually resulted in decreasing isomerization rate, consistent with literature reports. At the peak of the isomerization rate (10 mM HCl), nanoparticles were no longer detected in the catalyst solution, indicating that the hydroxide is not the active species and the reaction is catalyzed

homogeneously. The commercial thermodynamics package OLI, which models the electrolyte speciation, predicts that the concentrations of the partially hydrolyzed metal ions $Cr(OH)^{2+}$ and $Cr(OH)_2^{+}$ follow the same trend with the isomerization rate and reaches a maximum at an intermediate concentration of HCl. This is consistent with the fact that HCl addition shifts the hydrolysis from the hydroxides and metal oligomers to the intermediate hydrolyzed metal ions, but too much HCl pushes the equilibrium all the way to the parent Cr^{3+} ion. The correlation between isomerization rate and $Cr(OH)_x^{n+}$ concentration strongly suggests that the partially hydrolyzed metal ions are the active species for glucose isomerization. The same volcano dependence of isomerization rate on HCl concentration was also observed for $AlCl_3$ (Figure A.2a). A solid suspension was also detected in the preheated $AlCl_3$ solution and reported in another publication from our group[192] (Figure A.3). In the case of lanthanide chlorides with $DyCl_3$ as representative, however, the glucose conversion rate decreases monotonically with increasing HCl addition (Figure A.2b). DLS spectra of the $DyCl_3$ catalyst solutions showed no sign of nanoparticles suspension (Figure A.3). Since lanthanide salt is considered as water tolerant with a much higher first hydrolysis constant ([7.6-8.5]) compared to $CrCl_3$ (4) and $AlCl_3$ (4.97), its hydrolysis under the reaction conditions does not produce solid. Therefore, HCl titrant only shifts $DyCl_3$ hydrolysis away from the partially hydrolyzed $Dy(OH)_y^{m+}$ active species and reduces the isomerization rate. The observed linear relationship between the rate of isomerization by $DyCl_3$ and $[DyOH^{2+}]$ predicted by OLI reinforces the hypothesis that the partially hydrolyzed metal ion is responsible for isomerization. The same quantitative correlation was not established for $CrCl_3$ and $AlCl_3$ probably because OLI

does not incorporate oligomerization of metal ions, leading to uncertainty in quantification of the hydrolyzed ions. The correlation between isomerization rate and OLI-predicted concentration of $Al(OH)_x^{n+}$ by aluminum salts with various anions also further supported the catalytically role of the partially hydrolyzed metal ions (Figure A.8).

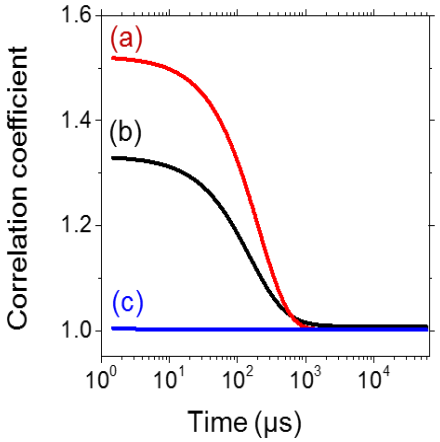

Figure 2.2. Dynamic light scattering spectra of 1.7 mM $CrCl_3$ solution preheated to 140 °C with (a) for 24 h without HCl, (b) for 24 h with 10 mM HCl, and (c) for 1 h with 10 mM HCl.

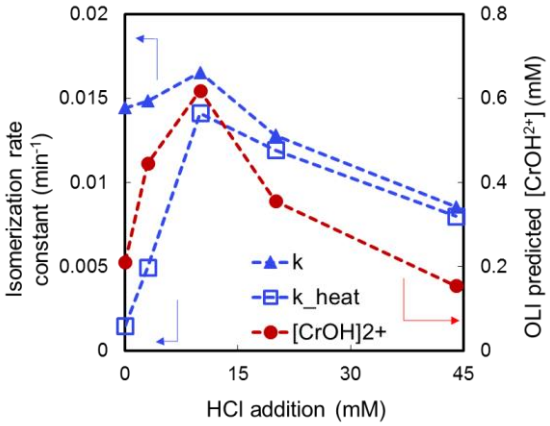

Figure 2.3. Effect of HCl addition on the rate of isomerization with catalyst preheating (▲), without catalyst preheating (□) and concentration of $CrOH^{2+}$ predicted by OLI (●).

2.3.2 Mechanism of metal chloride-catalyzed glucose isomerization to fructose

Various MCl_3 were tested for glucose isomerization in aqueous phase and exhibited different catalytic activity[137, 187, 193]. Accordingly, $CrCl_3$ and the Al group salts ($AlCl_3$, $InCl_3$, $GaCl_3$) show significantly higher glucose conversion than the lanthanide salts ($LaCl_3$, $DyCl_3$ and $YbCl_3$). In this study, we show that even though the MCl_3 salts catalyze glucose conversion to different extents, they follow the same 1,2 hydride transfer reaction pathway to form fructose.

The glucose isomerization mechanism was studied using isotope labeled experiments with glucose deuterated at C2 position (D2 glucose) as the starting substrate. In these experiments, ^{13}C NMR spectra of the sugar fractions after reaction were measured and compared with the ^{13}C NMR spectra of control samples, a mixture of D2 glucose and unlabeled fructose and a mixture of unlabeled glucose and unlabeled fructose (Figure 2.4). Here we only show a representative case using $GaCl_3$ as the catalyst. The C2 glucose peaks at δ = 74.1 ppm (β-pyranose) and 71.3 ppm (α-pyranose) in the unlabeled glucose appear as low intensity triplets in the D2 glucose spectrum due to C-D bonds at the C2 glucose position according to the NOE.[189] The C2 glucose region of the sugar fraction after reaction shows the same absence of NOE, indicating that there is no H/D exchange during the course of the reaction. By the same principle, the low intensity triplets in fructose product replace C1 fructose peaks at δ = 63.8 ppm (α-pyranose) and 62.4 ppm (β-furanose) in unlabeled fructose. This provides evidence for the formation of a C-D bond at the C1 position of fructose and suggests that the deuterium at C2 of glucose has shifted to C1 of fructose through an intramolecular hydride shift. ^{13}C NMR spectra of fructose fraction after reaction by other MCl_3 salts ($InCl_3$, $DyCl_3$, $YbCl_3$, $LaCl_3$) resemble those in $GaCl_3$ (Figure A.4).

The ^{1}H NMR spectrum of the sugar fractions after reaction further support this hypothesis by the disappearance of $\delta = 3.45$ ppm peak corresponding to the proton bonded to C1 of fructose (α-pyranose), as shown in Figure A.5. These results confirm that MCl_3 catalyze glucose to fructose through 1,2 hydride transfer, analogous to the isomerization mechanism in Sn-BEA[135] despite significant differences in their reactivity.

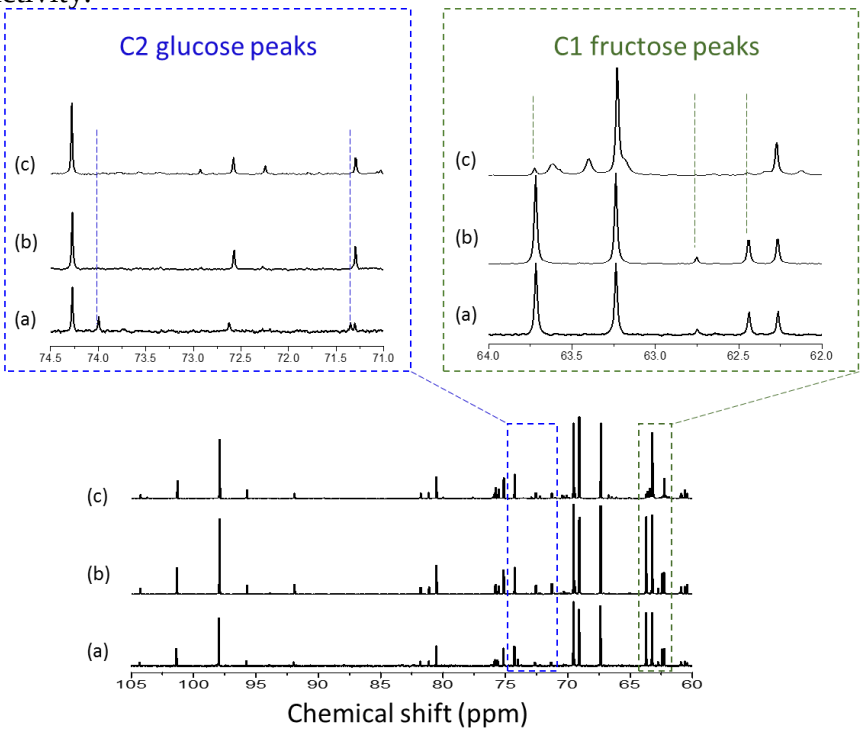

Figure 2.4. Bottom: ^{13}C NMR spectra of (a) a standard mixture of glucose and fructose and (b) a standard mixture of D2 glucose and fructose, and (c) sugar fraction after reaction in $GaCl_3$. Left blue box at top: magnification of the spectra within the C2 glucose region bracketed with blue dashed lines. The two C2 glucose peaks are labeled with vertical blue dashes lines. Right green box at top: magnification of the spectra within the C1 fructose region bracketed with green dashed lines. The three C1 fructose peaks are labeled with vertical green dashed lines.

2.3.3 Mechanism of metal chloride-catalyzed glucose epimerization to mannose

Besides fructose, mannose can be another main product reported for glucose epimerization using xylose isomerase,[194] base catalysts,[195] and Sn-BEA.[136] Herein, we investigate the mechanism of glucose epimerization to mannose by MCl_3 for the first time. In these experiments, we use glucose labeled ^{13}C at C1 position ($^{13}C1$ glucose) as the substrate and measure the ^{13}C NMR spectra of sugar fractions after reaction. A comparison of the ^{13}C NMR spectrum of a standard solution containing a mixture of $^{13}C1$ glucose, mannose, and fructose (Figure 2.5a) with the sugar fractions of product spectra (see Figure 2.5c, d for representative cases of $CrCl_3$ and $YbCl_3$ respectively) clearly shows evidence for rearrangement of the enriched C atom within the molecules. All three mentioned spectra exhibit enhanced C1 glucose peaks at δ = 95.8 ppm (β -pyranose) and 92 ppm (α-pyranose). Due to significant fraction of unreacted glucose at low conversion, the spectra were magnified in the interesting regions of fructose and mannose (Figure 2.5, right). Fructose products show enhancement of C1 fructose peaks at δ = 63.8 ppm (β-pyranose), 62.8 ppm (α-furanose), and 62.6 ppm (β-furanose) as expected for 1,2 hydride transfer from glucose. Interestingly, in $CrCl_3$ and $YbCl_3$, we observe chemical shifts corresponding to both C1 mannose and C2 mannose. Specifically, there are intensifications of C1 mannose peaks at δ = 93.9 ppm (α -pyranose) and 93.5 ppm (β-pyranose), and C2 mannose peak at δ = 71.1 ppm (β-pyranose) and 70.5 ppm (α–pyranose). No other mannose carbon peaks were detected. Therefore, the C1 and C2 mannose resonances arise from the enriched ^{13}C instead of natural abundant sources. These results suggest that there are two different isotopic

labeled mannose species formed via either reverse 1,2 hydride transfer or the Bilik reaction.

In order to compare mannose formation using Lewis acid and Brønsted base catalysts, we followed the same procedure using 10 mM NaOH as catalyst. The ^{13}C NMR spectrum after reaction (Figure 2.5b) shows resonances for C1 glucose (δ = 95.8 ppm, 92 ppm), C1 fructose (δ = 63.8 ppm, 62.8 ppm, 62.6 ppm), and C1 mannose (δ = 93.9 ppm, 93.5 ppm). This result confirms the Lobry de Bruyn–van Ekenstein reaction (LdB_AvE) of aldose-ketose transformation via enediol intermediates catalyzed by a base (NaOH).[195] We did not detect any other mannose carbon peaks as in metal salts, indicating there was no backbone carbon rearrangement. Therefore, glucose epimerization to mannose via the Bilik reaction was solely facilitated by the Lewis acid salts. The ^{13}C NMR spectra of product mixtures from reactions catalyzed by other MCl_3 also exhibit labeled ^{13}C at C1 fructose, and C1 and C2 mannose peaks (Figure A.6), except for the case of $InCl_3$, which is discussed in the following section. Based on these observations, we propose that the MCl_3 salts catalyze glucose epimerization to mannose through two competing pathways, 1,2 hydride transfer and the Bilik reaction. This result differs from the heterogeneous catalysts, where mannose forms via 1,2 hydride transfer using the Sn-BEA zeolite or via the Bilik reaction using the Na-Sn-BEA zeolite.[138]

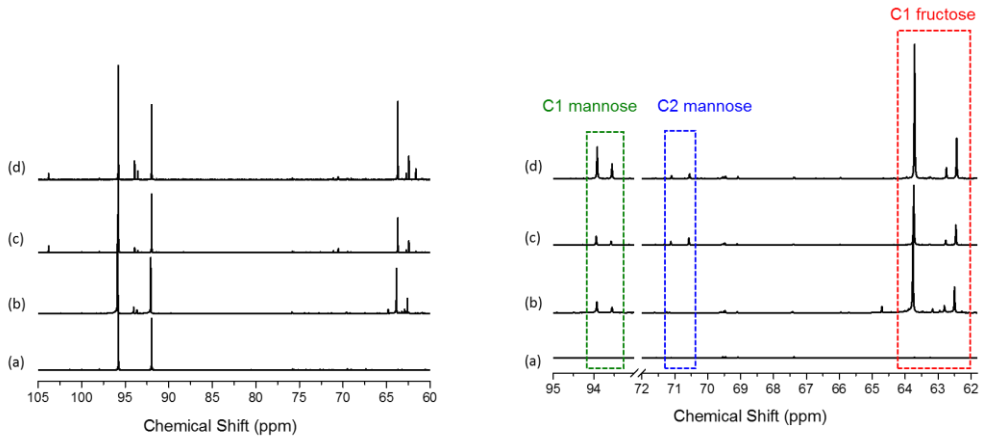

Figure 2.5. Left: ^{13}C NMR of (a) a standard mixture of ^{13}C-C1 glucose, fructose and mannose, and the sugar fraction after reaction using (b) NaOH, (c) $YbCl_3$, and (d) $CrCl_3$. Right: magnification of the spectra of the C1 mannose peaks in green, the C2 mannose peaks in blue, and the C1 fructose peaks in red.

Table 2.1. Yields of different hexoses after ^{13}C-C1 glucose reaction in metal chlorides and ratio of mannose formed via 1,2 hydride transfer (^{13}C-C1) and via the Bilik reaction (^{13}C-C2). Reaction conditions: 10 wt% ^{13}C-C1 glucose, 17 mM MCl_3, T = 140 °C. The reaction time varied in order to have similar conversion of glucose.

Catalyst		$CrCl_3$	$AlCl_3$	$GaCl_3$	$InCl_3$	$DyCl_3$	$YbCl_3$	$LaCl_3$
Reaction time (min)		5	13	7	12	60	60	240
Hexose Yield (%)	Glucose	76.5	77.2	77.6	77.9	76.6	78	77.1
	Fructose	12.8	15.7	17.6	16.5	9.1	10.1	2.4
	Mannose	2.3	1.5	2.4	2.7	1.1	1.3	0.6
	^{13}C-C1 mannose	1.9	1.3	2.0	2.7	0.7	0.7	0.3
	^{13}C-C2 mannose	0.4	0.2	0.4	0	0.4	0.6	0.3
	Sorbose	1.05	0.03	0.02	0.02	0.05	0.05	0.02
	Unknown[a]	0.01	0.1	0.25	0.2	0.12	0.15	0.19

^{13}C-C1/ ^{13}C-C2 mannose ratio	5.2	6.4	4.7	26.6[b]	1.8	1.2	1.2

[a]The unknown product was quantified assuming it has the same response factor with sorbose.
[b]We believe that the C2 mannose peaks using $InCl_3$ are unlabeled (see text).

The ability of the MCl_3 to facilitate a carbon skeletal rearrangement of aldohexoses parallels that of molybdic acid, which was discovered to catalyze the Bilik reaction in 1972 and has been a milestone in the synthesis of rare sugars.[178] Unlike intensive study of molybdate catalysts, the metal ion-aldose epimerization studies are rather limited. Kusin *et al*. reported the formation of mannose as major product (instead of fructose) via the Bilik reaction when treating glucose in an $Ca(OH)_2$ solution with glucose:Ca ratio of 1:1.[196] On the other hand, at the same conditions in NaOH, fructose forms as the main product via the LdB_AvE reaction.[196] Almost 60 years later, Yanagihara *et al*. confirmed Kusin's results by reporting a change in glucose conversion mechanism from the LdB_AvE to the Bilik reaction in $Ca(OH)_2$.[197] Various hydroxides were tested and $Sr(OH)_2$ and $La(OH)_3$ were found to catalyze the Bilik reaction (to a less extent than $Ca(OH)_2$). Interestingly, when they used $CaCl_2$ in a basic solution, the rate of epimerization to mannose increased with Ca^{2+} concentration and pH. Those observations suggest that while the hydroxide group catalyzes glucose to fructose via the LdB_AvE reaction, suitable metal ions and hydroxide cooperatively facilitate the Bilik reaction to mannose.[197-198] Our system, on the other hand, is acidic and only contains the Lewis acid metal cations catalyzing both the 1,2 hydride transfer to fructose and the Bilik reaction to mannose. Since more fructose forms than mannose in all MCl_3 salts (Table 2.1), hydride transfer is evidently the dominant pathway of glucose conversion.

It has been proposed that the active species for hydride transfer is a partially hydrolyzed metal aqua cation in the form of $[M(OH)_x(H_2O)_{n-x}]^{(3-x)+}$.[69, 106, 187] These species resemble the metal center Lewis acid and the Brønsted base OH^- group of the heterogeneous Sn-BEA zeolite. The bi-functionality of these active complexes is strikingly analogous to cooperative effect between the Ca^{2+} and OH^- group reported in ref [31]. Therefore, we hypothesize that the partially hydrolyzed metal cations are also responsible for the carbon skeletal rearrangement of glucose to the epimer mannose. Epimerization using the calcium complex was shown for glucose and xylose but not for galactose, ribose, talose and arabinose.[198-199] Angyal concluded that epimerization by the metal complex only happened with sugars possessing threo configuration of hydroxyl groups on C3 and C4, and postulated a complex of Ca with four oxygens O1, O2, O3, O4 of glucose.[198] Due to our main interest in glucose interconversion, we did not test the MCl_3 for epimerization of other aldoses for steric effect. In addition, our reaction medium is slightly acidic with glucose to metal molar ratio of 300:1, whereas the calcium hydroxide experiment was in basic solution with equimolar ratio of glucose and calcium. In basic solution, oxygens in hydroxyl groups of glucose are more likely to get deprotonated to form a highly coordinated complex with the metal. The high concentration of Ca^{2+} (66.7 M) also increased the possibility of forming a binuclear metal complex,[200] which might help to stabilize the tetra-coordination. Since the OH group in the Lewis acid active species is a much weaker Brønsted base, we hypothesize that it only locally removes the hydrogen bonded to O2, and coordinates with O1 and O2 in bidentate mode. We postulate a stepwise pathway of the Bilik reaction from glucose to mannose catalyzed by MCl_3 (Figure 2.6). The mechanism,

similar to the hydride transfer[69], consists of three steps: deprotonation, carbon shift, and reprotonation, with ring opening and closing steps being omitted.

2.3.4 Quantification of mannose produced from reverse C2-C1 hydride transfer and the Bilik reaction

The metal ions in our experiments differ from the ones tested by Yanagihara *et al.*[197] (except for aluminum). Their hydroxides have so low solubility in water that similar experiments to those with calcium hydroxide are not practical. Nevertheless, the occurrence of the Bilik reaction in metal chloride catalysts but not in alkali solutions suggests that some metal ion may be more suitable for carbon rearrangement than others. We investigated the extent to which the MCl_3 catalyze the Bilik reaction by quantifying the amounts of labeled ^{13}C mannose at C1 position (^{13}C-C1) and C2 position (^{13}C-C2) formed at the same glucose conversion. Mannose concentrations were analyzed using HPLC, and the ratio of ^{13}C-C1 mannose (reverse 1,2 hydride transfer product) to ^{13}C-C2 mannose (the Bilik product) was determined using the inverse gated decoupling ^{13}C NMR method (CIG). The ratio of intensity of C1 to C2 mannose peaks in the CIG spectrum of an unlabeled mannose sample is 1 (within 3% error), illustrating that the CIG method is quantitative (Figure A.7). Applying the same method to sugars spectra after reaction, we quantify the amount of ^{13}C-C1 mannose and ^{13}C-C2 mannose formed using the salts at similar glucose conversion (Table 2.1). The amounts of mannose formed from the reverse 1,2 hydride transfer and the Bilik reaction are comparable in lanthanide chlorides. However, when $CrCl_3$ or an aluminum group metal is used, mannose forms mainly via hydride transfer. In indium chloride, the intensities of C2 mannose peaks were extremely low, indicating that they

might be from the naturally abundant source of ^{13}C instead of the enriched one. The difference in the relative amount of ^{13}C-C1 mannose and ^{13}C-C2 mannose products shows that even though the Bilik reaction is a minor pathway in all MCl_3, it is still more favorable in lanthanides than in chromium and aluminum group salts.

The differences in carbon rearrangement in sugar reaction using various catalysts has been attributed to metal-sugar complex stability, steric effect, and ligand coordination/chirality or the combination of those effects.[201] Intensive studies on epimerization of aldoses via a carbon shift by nickel (II) diamine complex showed that the reaction was governed by the stability of the ternary nickel/sugar/diamine complex.[202-204] The structure of the diamine ligand influences the steric interaction between the sugar and the ligand in the complex. For example, nickel –N, N'-dialkylethylenediamine catalyzed glucose-mannose epimerization to a high degree,

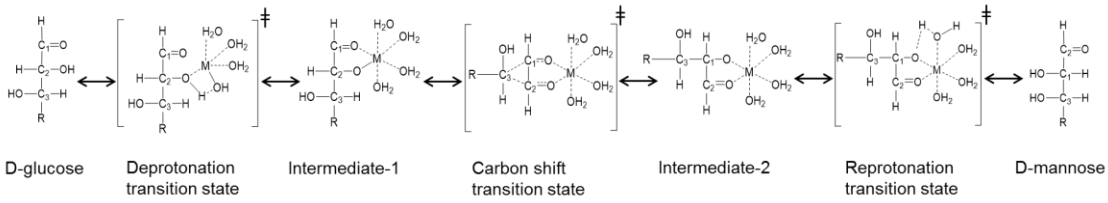

Figure 2.6. Stepwise mechanism of the Bilik reaction for glucose epimerization to mannose by metal chlorides

whereas the catalytic activity for the same reaction of nickel-N, N-dialkylethylenediamine was negligible.[205] Angyal also correlated metal-sugar complex stability of metal hydroxide with their catalytic activity for the Bilik reaction.[198] Studies on metal coordination with polyhydroxy alcohols and carbohydrates showed that the metal affinity to sugars generally increased in the order of univalent, divalent, and trivalent metals.[206-208] Alkali metals bind sugars very weakly, while some alkaline

earth metals, especially calcium, readily form complexes with neutral sugars.[208-209] Rare earth metals were shown to have even stronger affinity to sugars.[210-211] The reported relative stability constant for complexes between glucose with (similar sized) Ca^{2+}, La^{3+}, and Sm^{3+} are comparable.[211] Those studies may help explain why no Bilik reaction was observed using NaOH. Angyal hypothesized that $Ca(OH)_2$ and $La(OH)_3$ catalyzed glucose epimerization effectively since Ca^{2+} and La^{3+} have an optimum ionic radius (0.99 Å and 1.05 Å, respectively) that was required to form a stable complex with the sugar substrate, while the inactive metal hydroxides had either too small or too big cation size.[198] Mushrif and co-workers have conducted a theoretical study on molybdenum complex-catalyzed epimerization of glucose via the Bilik reaction and observed that the ligand coordination affects the flexibility/rigidity of oxygen atom (O2), which connects to C2 and metal center, and in turn plays a key role in the structural rearrangement of the carbon backbone.[212] Accordingly, the more flexible O2 pulls C2 away from C1 and C3, and eventually elongates the C2-C3 bond while shortens the C1-C3 bond to form the three carbon structure in the carbon shift transition state.

Based on the literature, the metal ionic radius and ligand coordination may also affect their ability to catalyze the Bilik reaction in our system. While Cr^{3+}, Al^{3+}, Ga^{3+}, and In^{3+} regularly exist as octahedral aqua ions with ionic radii in the range of 0.54-0.8 Å, the lanthanides have larger ionic radii around 1 Å and their ions' hydration number can vary, with a coordination number of eight being commonly observed.[200] As a result, compared to chromium and aluminum group, the lanthanides have longer metal-oxygen bond distance in the first hydration sphere[213-216], which may give more

freedom to the bridging oxygen in the metal-sugar complex (Table 2.2). Therefore, we hypothesize that the lanthanides' larger metal ionic radii and the associated metal-sugar complex stability/flexibility could be responsible for their ability to catalyze the Bilk reaction more effectively compared to chlorides of chromium (III) and other aluminum group metals.

Table 2.2. Effective ionic radius of the studied metal aqua cations[200] and their metal-oxygen distance with water in the first hydration sphere.[213-216]

Metal cation	Common hydration number	Effective ionic radius (Å)	Metal-oxygen distance (Å)
Cr^{3+}	6	0.62	1.97
Al^{3+}	6	0.54	1.91
Ga^{3+}	6	0.62	1.96
In^{3+}	6	0.8	2.13
Dv^{3+}	8	1.03	2.39
Yb^{3+}	8	0.99	2.98
La^{3+}	8	0.116	2.56

Recently, in order to understand the structure-activity relationship of the active sites in metal-substituted BEA, Davis and co-workers have studied glucose interconversion using the two homogeneous tin silsesquioxanes cubes in a mixed organic solvent. These catalysts resemble the open site structures of the zeolites with and without adjacent silanol group (corresponding to Sn-BEA and Na-Sn-BEA,

respectively).[217] The cubes were found to favor the same mechanism as their heterogeneous counterparts. However, unlike the zeolites, the homogeneous zeotypes are less selective and catalyzed both 1,2 hydride transfer and the Bilik reaction with the dominant path depending on the nearby site. These results suggested that the adjacent silanol group and the structural flexibility of the active sites can substantially affect the selectivity of glucose interconversion. The homogeneous metal salts catalysts studied herein are the most flexible and produce more fructose than mannose, with the latter forming via both 1,2 hydride transfer and 1,2 carbon shift. Taken all findings together, we believe that site flexibility and solvent and ligand effects around the active site are decisive factors controlling the preferred reaction pathways.

2.3.5 Lewis acid metal salt-catalyzed glucose conversion to other hexoses

Fructose and mannose are the primary hexoses products of glucose conversion.[106, 135, 176, 179] Recently, Ti-BEA was found to catalyze the glucose stereospecific isomerization to sorbose.[177] To our knowledge, formation of other hexoses from glucose by homogeneous Lewis acids has not been reported before. Here we report for the first time a similar isomerization of glucose to sorbose by the Lewis acid MCl_3 using a combination of HPLC and NMR spectroscopy. ^{13}C NMR spectra of sugars after reaction (Figure 2.5) contained resonances at δ= 61.7 ppm and δ= 103.8 ppm that do not belong to glucose, mannose, or fructose. Yet, chromatograms using the Biorad-87C column showed only responses for glucose, mannose, and fructose. In order to explore if small amounts of other products overlap with glucose, mannose, and fructose peaks, we used a Biorad-87P column and detected two other products eluting between glucose (12.7 min) and mannose (16.7 min); one of them matched the

retention time of sorbose (14.7 min). Since the sorbose in post reaction solutions using various salts was minimal except in $CrCl_3$, we used $CrCl_3$ as the catalyst in isotopic labeled experiments (Figure 2.7) to confirm the formation of sorbose and elucidate the mechanism. Sorbose in aqueous solution tautomerizes to an equilibrium mixture of 98% α-pyranose and 2% α-furanose[218]; hence, only α-pyranose carbon peaks were observed in the NMR spectrum at low concentration. The ^{13}C NMR spectrum after reaction of unlabeled glucose by $CrCl_3$, consisting of glucose, sorbose, and an unknown product, gave rise to all of six sorbose peaks, confirming its formation. When ^{13}C-C1 glucose was used as reactant, the sugar fraction contained glucose, sorbose, and an unknown product and exhibited enhanced peaks at δ = 95.8 ppm and 92 ppm (C1 glucose), δ = 103.8 ppm (unidentified), and δ = 61.7 ppm, which was assigned to C6 α-sorbopyranose. Additionally, when we started the experiment with D2-glucose, all α-sorbopyranose carbon peaks were detected except for the C5 peak (δ = 73.7 ppm). The suppression of the C5 α-sorbopyranose peak indicates that a C-D bond formed at the C5 position eliminates the NOE. These observations in $CrCl_3$ are reminiscent of those in Ti-BEA[177], suggesting the two catalysts mediate sorbose formation from glucose via the same 1,5 hydride transfer (Figure 2.1). Although a detailed mechanistic study was not done for other salts, the presence of very low sorbose peaks in LC chromatograms in conjunction with the detected C5 sorbose peak at δ = 61.7 ppm for some MCl_3 starting from labeled ^{13}C-C1 glucose indicate that other salts might follow the same mechanism as $CrCl_3$ (Figure A.6). No sorbose peak was detected in HPLC chromatogram or ^{13}C NMR in NaOH, suggesting the sorbose formation is a trait of the MCl_3 via an intramolecular 1,5 hydride transfer.

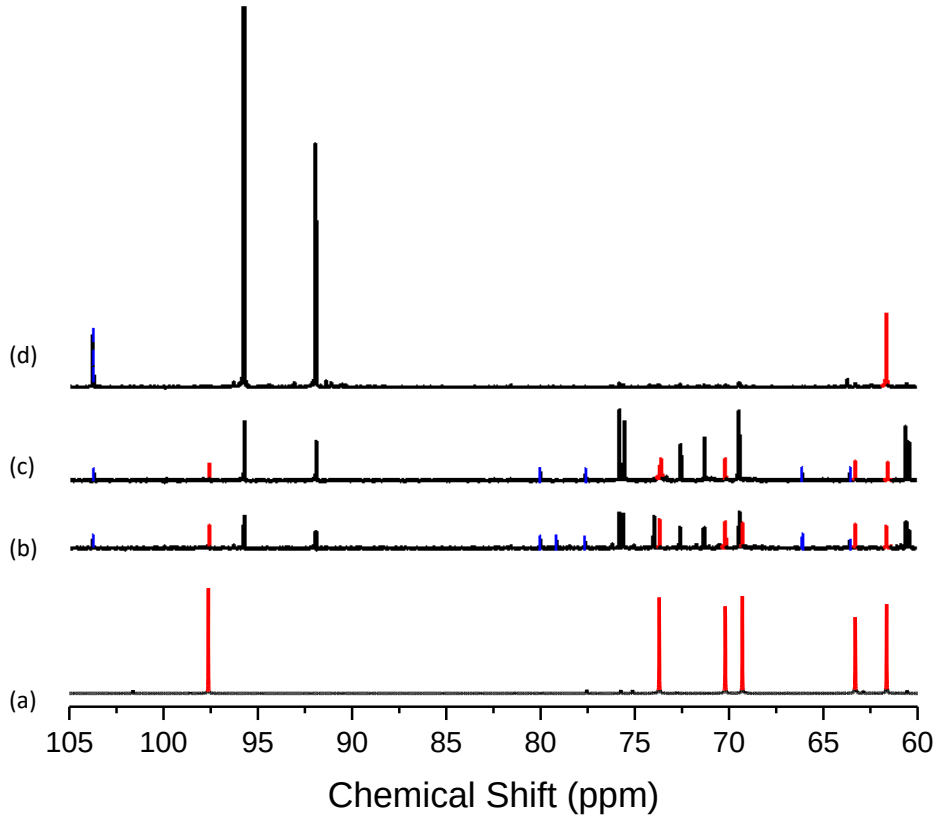

Figure 2.7. ^{13}C NMR spectra of (a) unlabeled sorbose and of the sugar fraction after reaction by $CrCl_3$ starting with (b) unlabeled glucose, (c) D2-glucose, (d) ^{13}C-C1 glucose. Glucose peaks are black, sorbose peaks are red, and peaks of the unknown compound are blue.

The resonance at δ = 103.8 ppm was assigned to an unidentified product, eluting the HPX 87P column at 14.7 min between glucose and sorbose. The compound is UV inactive. We constructed a ^{13}C NMR spectrum of this compound by mapping out the resonances that do not belong to glucose or sorbose. Accordingly, the compound gives rises to six carbon peaks at 103.8 ppm, 80 ppm, 79.2 ppm, 77.7 ppm, 66.1 ppm, and 63.6 ppm, suggesting it is a C6 compound. When ^{13}C-C1 glucose was

used, only a carbon resonance at δ = 103.8 ppm was detected as a labeled ^{13}C peak. When D2-glucose was used, the carbon peak at δ = 79.2 ppm was suppressed, indicating that a C-D bond formed. Based on the HPLC and ^{13}C NMR, this compound is probably a hexose. However, its ^{13}C NMR spectrum did not match with the spectra of any tested aldohexoses (galactose, idose, talose, altrose, allose) or ketohexoses (psicose, tagatose). Since D-hamamelose (2-C-hydroxymethyl-D-sorbose) was reported as a synthetic product from the Bilik reaction of fructose,[219] it is likely that the unknown compound is a branched chain hexose. A hexose in aqueous solution exists as an equilibrium mixture of tautomers.[218] Since there were only six detectable carbon peaks, this compound is likely to have a predominant cyclic form (similar to sorbose with 98% α-pyranose).

2.4 Conclusions

We have conducted isotopic tracing experiments coupled with NMR spectroscopy and liquid chromatography to elucidate the mechanisms of glucose interconversion by Lewis acid MCl_3 in aqueous phase. We systematically showed that the MCl_3 salts catalyze glucose isomerization to fructose via 1,2 hydride transfer, a mechanism characteristic of Lewis acid mediated isomerization. In contrast to the heterogeneous counterpart, Sn-BEA zeolite, the MCl_3 simultaneously facilitate glucose epimerization to mannose via both reverse 1,2 hydride transfer and the Bilik reaction with the former being the dominant pathway. The active species for hydride transfer with a bifunctional structure of Lewis acid metal center and a Brønsted OH group was postulated to also mediate the Bilik reaction. We propose that the extent to which the Bilik reaction occurs correlates with the effective ionic radius of the metal

aqua cation. Accordingly, the trivalent lanthanides have an optimum radius of around 1 Å and are more likely to mediate the Bilik reaction than the smaller cations of chromium (III) and the aluminum group. We also reported the formation of sorbose from the direct glucose isomerization via 1,5 hydride transfer, analogous to Ti-BEA. Another product, which appears as a branched chain C6 sugar, was also detected. Interestingly, transformations that were believed until now to be unique to heterogeneous Lewis acid catalysts have an analogue in counterpart homogeneous catalysts. However, the formation of multiple sugar interconversion products through different pathways suggests the less selective nature of the homogeneous metal salt catalysts. The higher flexibility, lack of confinement and the potentially different local environment of the active site could be reasons for the differences between homogeneous and heterogeneous catalysts, a topic that deserves further work.

Chapter 3

TANDEM LEWIS ACID /BRØNSTED ACID –CATALYZED CONVERSION OF CARBOHYDRATES TO 5-HYDROXYMETHYLFURFURAL USING ZEOLITE BETA

3.1 Introduction

Furans, such as furfural and 5-(hydroxymethyl)furfural (HMF), derived from lignocellulosic carbohydrates, are excellent platform chemicals for the production of fuel additives,[220] alkylated aromatics,[221] and organic solvents.[222] While furfural has been produced industrially from pentose sugars since 1921,[223] HMF production has not yet been commercialized at large scale[14] in part due to side reactions that render economics less attractive.[118]

HMF is typically produced by dehydrating fructose using a homogeneous Brønsted acid catalyst.[224] Identifying suitable heterogeneous catalysts has attracted attention due to simplified downstream separations. Many solid catalysts have been considered, including acidic carbons,[225] silicoaluminophosphates,[226] sulfonated carbonaceous TiO_2,[227] and zeolites.[140, 228] However, understanding of the underlying chemistry is poor because heterogeneous catalytic systems are more complicated than their homogeneous counterparts. Kruger et al. studied fructose dehydration in H-BEA-18 and identified several factors contributing to the dehydration chemistry that are absent from homogeneous catalysts, including the adsorption strength and the type of acid site, i.e., Brønsted or Lewis.[141]

While selectively converting fructose to HMF is an important scientific problem, glucose is far more naturally abundant than fructose, making it a more desirable substrate. However, the direct dehydration of glucose to HMF is slow and

gives low yields (see Yang *et al*.[229] for recent work and literature therein). Following the pioneering work of Davis and co-workers, it is now well established that Lewis acid zeolites, such as Sn-beta,[230] catalyze the isomerization of glucose to fructose. Additionally, Sn-beta can be combined with Brønsted acid catalysts for single pot conversion of glucose to HMF via the formation of fructose as an intermediate.[231] Similarly, Mazzota et al. found that a sulfonated carbon catalyst combined with Lewis-acidic TiO_2 can improve HMF yield from glucose.[227]

Tandem reactions in a single pot reactor have opened up new opportunities for the conversion of sugars, as recently reviewed in Caratzoulas et al.[232] Even though bifunctional solid catalysts, which contain both Lewis and Brønsted acid sites in a single material, can enable the direct conversion of glucose to HMF, the development and identification of optimal properties of such materials has not received much attention. Gallo *et al*. found recently that the H-BEA isomerizes xylose to xylulose and dehydrates xylulose to furfural.[15] Otomo et al. demonstrated that calcining H-BEA over 700 ºC or in steam over 500 ºC can increase the number of Lewis sites and ultimately lead to improved HMF yields from glucose.[233] Specifically, Kruger *et al*. studied fructose dehydration on H-BEA and found that when the zeolite was washed with HCl to remove the octahedrally coordinated Al atoms, there was no glucose formed. They concluded that the extra framework Al was the active Lewis acid site for isomerization. In addition, comparison of bifunctional catalysts to a physical mixture of Lewis and Brønsted solid acid catalysts or Lewis solid acid and homogeneous Brønsted acid catalysts is lacking.

Tandem reactions requiring different catalyst types have been of growing interest in biomass processing but their kinetics is generally poorly understood. For example, the kinetics of para-xylene formation via tandem Lewis-acid catalyzed cyclo-addition of dimethyl furan and ethylene followed by the Brønsted acid catalyzed dehydration of the resulting cycloadduct has recently been explored.[234] We showed that the former reaction is catalyzed homogeneously and the latter heterogeneously. When the density of Brønsted acid sites was varied (at fixed volume and thus at fixed Lewis acid 'site density'), two kinetic regimes were discovered: a linear regime, where the rate of para-xylene formation increases almost linearly with increasing Brønsted acid site concentration, followed by a plateau at high Brønsted acid site concentrations. The linear regime was unexpected given that the Lewis acid chemistry has a higher reaction barrier and is expected to be rate-controlling. Sensitivity analysis showed that the lack of sufficient Brønsted acid sites limits the rate of the overall tandem reactions and underscores that the rates of tandem reactions catalyzed by different catalysts or multifunctional catalysts is controlled by intrinsic rate constants, concentrations of participating species, and active site concentrations. We hypothesized that this may be a generic kinetic behavior of tandem reactions, though this has not yet been addressed. In addition, since most of reactants and products in this chemistry have negligible vapor pressure at reaction temperatures and stability issues at higher temperatures, the use of solvent is necessary. The significant effect of solvents on isomerization and dehydration chemistry has been well documented.[39, 138] In water, which is the solvent used in this work, a small fraction of the zeolite dissolves into aluminosilicate species that catalyzed fructose dehydration to HMF

homogeneously. The details of this homogeneous chemistry are described in our previous work.[139]

The selective production of HMF from glucose requires detailed understanding of the reaction kinetics of isomerization and dehydration reactions within the zeolite to identify optimal materials properties. The aim of the present work is to fill in this scientific gap. First, we present experimental adsorption and kinetic data in H-BEA-25. Next we build a model that (1) distinguishes homogeneous (Brønsted acid site dehydration chemistry) from heterogeneous (inside the zeolite) Brønsted and Lewis acid catalyzed glucose isomerization and fructose dehydration reactions and (2) accounts for the adsorption of multiple compounds inside the zeolite. To the best of our knowledge, this is the first kinetic model that explicitly considers the bifunctionality of Brønsted and Lewis acid sites in a zeolite for the conversion of glucose to HMF. We predict and contrast for the first time the kinetic regimes of both bifunctional Lewis/Brønsted solid acid catalysts, which is the main focus of this work, and physical mixtures of Lewis and Brønsted solid acid catalysts for tandem reactions and provide insights into the properties of catalysts that maximize the yield and the production rate of HMF. Comparison to hybrid heterogeneous Lewis acid/homogeneous Brønsted acid catalysts is also performed. Finally, we predict the optimal yield of HMF from glucose as an upper performance-bound and identify the factors controlling this yield.

3.2 Experimental Methods

3.2.1 Materials

Fructose 99% (Sigma Aldrich), HMF 98% (Sigma Aldrich), levulinic acid (LA) 98% (Sigma Aldrich liquid form), formic acid (FA) 88% (Fisher Scientific), hydrochloric acid 1 M (Sigma Aldrich), potassium chloride 98% (Merck) and distilled water were used for solution preparation. Commercial BEA zeolite from Zeolyst with SiO_2/Al_2O_3 ratio of 25 in ammonium form (NH_4-BEA-25) was calcined to generate the protonated form of the zeolite (H-BEA-25). The calcination program entailed heating the sample at 2 °C/min to 90 °C, holding for 1 h, heating at 2 °C/min to 450 °C, holding for 8 h, and cooling to room temperature.

Typical calcination introduces both Lewis and Brønsted acid sites.[235] For select experiments, the Lewis acidic octahedral aluminum sites were removed from H-BEA-25 using the method described by Hey et al.[236] 1 g of H-BEA-25 was added to a 20 ml glass vial containing 10 g of DI water, stirred at medium speed on a stir plate. The pH of the mixture was monitored using a glass electrode pH meter as 500 μL aliquots of 1.0 N HCl were added in 15 min intervals. Once the pH of the mixture reached between 0.97 and 1.03 and remained stable for at least 15 min, the vial was sealed and stirred for 16 hours. The solid was then filtered and rinsed with 60 mL of DI water four times to remove the free acid from the zeolite.

The zeolite micropore volume has been measured at 0.172 mL/g using N_2 sorption measurements.

3.2.2 Reaction kinetics

All reactions were performed in 20-mL glass vials. Each vial contained 2 mL of 10 wt% fructose or glucose in DI water or 2 wt% HMF in DI water and 0.25 g of H-BEA-25. Vials were weighed before and after the reaction to ensure that they did not leak during reaction. The vials were placed in a hot oil bath set to temperature, and a timer started immediately. The vials generally reached reaction temperature in less than 2 min after being placed in the oil bath. After reaction, vials were removed from the oil bath and quenched with cold water. Reaction times were chosen to achieve at least 10% conversion by the end of the reaction. Reaction solutions were analyzed using a Waters 2695 HPLC system with 2414 Refractive Index and 2998 Photodiode Array (UV) Detectors after filtering through a 0.22 μm syringe filter and diluting to a ratio of 0.3 g filtered solution to 0.7 g DI water. Analytes were separated on a BioRad Aminex HPX-87H column at 65 °C with 0.005 M H_2SO_4 mobile phase at 0.65 mL/min. Different temperatures between 110-140 ºC were investigated for each composition for a total of 11 different experimental conditions. Errors were estimated based on experiments performed for the HCl-washed H-BEA-25. The standard deviation for replicated experiments was 5-10% at most, and typically far lower for most of the data.

3.2.3 Adsorption isotherms

The procedure for measuring solute adsorption isotherms from aqueous solutions was the same as that described by Leon et al.[237] Ten different concentrations of fructose, HMF, LA, and FA were prepared in single solute aqueous solutions. The adsorption experiments were done in batch mode. 0.2 g of H-BEA-25 zeolite was

suspended in 1 mL of solution in a thermostatic water bath at the desired temperature for 5 hours to ensure that equilibrium was reached. The solution was then filtered with a 0.2 μm nylon membrane filter to obtain a clear liquid. The filtrate was analyzed using HPLC similarly to the reaction kinetics experiments. Each adsorption experiment was performed in triplicate.

3.2.4 Brønsted site density measurements

The Brønsted acid site density of H-BEA-25 zeolite was determined using the procedure of Kresnawahjuesa et al.[87] In summary, the total amount of propene formed from isopropylamine decomposition in the zeolite was determined. Isopropylamine decomposition is a Hoffman-elimination catalyzed by the Brønsted acid sites of the zeolite. Previous studies determined that a well-defined adsorption complex of one molecule of isopropylamine per Brønsted acid site precedes isopropylamine decomposition.[238] The amount of propene formed after complete isopropylamine decomposition is therefore equal to the number of Brønsted sites. A tubular flow reactor setup in conjunction with on-line gas chromatography (GC) analysis (Hewlett Packard 589 Series II equipped with dual FID/TCD detector) was used for these measurements. 2 mg of the zeolite was cleaned in the reactor furnace with helium flow at 500 ºC for 30 min, then cooled down to 100 ºC where the temperature was held constant for 30 min. During the 30 minutes hold at 100 ºC, a helium stream saturated with isopropylamine was fed through the reactor in order to saturate the Brønsted acid sites. The feed was switched to pure helium and the reactor temperature was then increased to 200 ºC and held for 90 min to remove isopropylamine that had not formed a complex with an adsorption site. Finally, the temperature was ramped up to 500 ºC

to desorb the decomposition products. During the desorption process, all gas products were trapped into liquid nitrogen cooled sampling loop. The amount of propene in the sample was then determined from the analysis of the gas chromatograph.

3.2.5 Computational methods

3.2.5.1 Adsorption

The numerical procedure for determining the parameters of the single-solute isotherms was outlined for H-BEA-18 elsewhere[237, 239] and here for H-BEA-25. Based on our previous findings, the adsorption isotherms of glucose and fructose in H-BEA are very similar.[237] Data and model performance are included in the SI (Figure B.3). The temperature dependent isotherm parameters, K and b, were fit to the van't Hoff equation as shown in Eq. (3.1 and (3.2. These relationships sufficiently describe the change in equilibrium adsorption loading with temperature (Figure B.4).

$$K = K_{298K} \cdot \exp\left[\frac{\delta H_K}{R}\left(\frac{1}{298K} - \frac{1}{T}\right)\right] \qquad (3.1)$$

$$b = b_{298K} \cdot \exp\left[\frac{\delta H_b}{R}\left(\frac{1}{298K} - \frac{1}{T}\right)\right] \qquad (3.2)$$

In Eq. (3.1 and Eq.(3.2, K_{298K} is the Henry constant at room temperature, δH_K is the heat of adsorption, R is the universal gas constant, T is the temperature, b_{298K} is the second isotherm parameter with a corresponding δH_b enthalpy change. The reactions produce a multicomponent mixture that contains fructose, glucose, HMF, FA and LA. To minimize the experimental effort on massive data collection of multicomponent systems, we proposed to model multicomponent adsorption using the ideal adsorbed solution theory (IAST), originally developed for adsorption of

multicomponent gases[240] and then extended to liquid mixtures,[241] using single-component experimental data.[237] The mathematical models have been outlined elsewhere.[241-242] Analytical expressions for determining the spreading pressure by integrating the isotherm equations were used whenever possible. Otherwise, numerical integration was performed.

3.2.5.2 Continuity equations

We assumed that the rate for reaching adsorption equilibrium is much faster than that of the reactions. As a result, the system can be modeled using a system of differential-algebraic Eq. (3.3 and (3.4. The species continuity in Eq. (3.3 includes reaction in both aqueous and adsorbed phases, while the adsorption isotherm relates the concentrations in both phases. Although including the activity coefficients in rate expressions would be more rigorous, we use concentrations because reagents are fairly dilute (at most 1 mole % of solute at 10 wt% glucose) and computing activities within zeolite pores is a generally an unsolved problem. This approach has been adopted in other studies in this system.[113, 221] The aqueous volume greatly exceeds the pore volume of the zeolite, so the aqueous volume is not expected to change with time.

$$\frac{dC_i}{dt} + \frac{m_{ads}}{V_{aq}}\frac{dq_i}{dt} = \frac{m_{ads}}{V_{aq}} r_i^{BEA} + r_i^{aq} \qquad (3.3)$$

Here C_i is the moles of component i per liter of aqueous phase, t is time, m_{ads} is the mass of zeolite in the reactor, V_{aq} is the volume of the aqueous phase, q_i is the moles of component i in the zeolite per gram of zeolite, r_i^{BEA} is the rate of consumption of component i in the zeolite (heterogeneous contribution), and r_i^{aq} is

the rate of consumption of component i in the aqueous phase (homogeneous contribution). The adsorption loading is given by Eq. (3.4:

$$q_i = f\left(C_{glu}, C_{fru}, C_{HMF}, C_{LA}, C_{FA}\right) \quad (3.4)$$

The function f in Eq. (3.4 is evaluated using Newton's method to solve the IAST equations.

3.2.5.3 Homogeneous reaction network

The pH of the aqueous phase of the zeolite suspension is lower than that of water due to the dissociation of the zeolite surface silanol groups. This homogeneous acidity may catalyze chemistry, which is accounted for using the rate laws and parameters outlined by Swift et al.[38, 243] These reactions include: fructose dehydration to HMF, fructose degradation to humins, HMF rehydration to FA/LA, HMF degradation to humins, and a second fructose degradation reaction that produces both humins and FA. The rates of these reactions are described by Eq. (3.5 -3.8.

$$r_{fru}^{aq} = -\left(\frac{k_1^{aq}\phi_f}{C_{H_2O}} + k_2^{aq} + k_5^{aq}\right) C_{fru} C_{H^+} \quad (3.5)$$

$$r_{HMF}^{aq} = k_1^{aq}\phi_f \left(\frac{C_{fru} C_{H^+}}{C_{H_2O}}\right) - \left(k_3^{aq} + k_4^{aq}\right) C_{HMF} C_{H^+} \quad (3.6)$$

$$r_{LA}^{aq} = k_3^{aq} C_{HMF} C_{H^+} \quad (3.7)$$

$$r_{FA}^{aq} = k_5^{aq} C_{fru} C_{H^+} + k_3^{aq} C_{HMF} C_{H^+} \quad (3.8)$$

Here k_j^{aq} is the rate constant of reaction j in the aqueous phase and ϕ_f is the fraction of fructose in the furanose form. The proton concentration in solution was fixed (pH = 3.46) based on the measured pH using mass titration at room temperature using the method of Noh and Schwartz[244] (Table B.2).

3.2.5.4 Heterogeneous reaction network

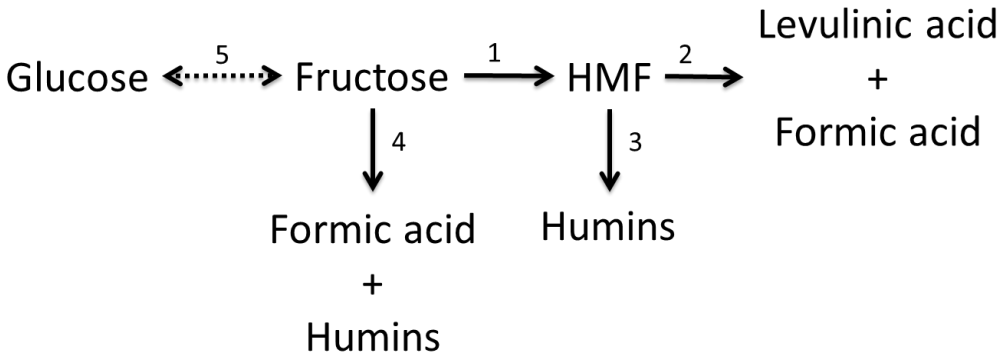

Figure 3.1. Reaction network inside H-BEA-25. Solid (dashed) lines indicate Brønsted (Lewis)-acid catalyzed reactions

The reaction network considered inside H-BEA is given in Figure 3.1. This network was postulated given the observed reaction products (glucose or fructose depending on substrate, HMF, FA, and LA). The formation of glucose from fructose and the converse arises from octahedrally coordinated Al acting as a Lewis acid site. Indeed, when these Lewis sites are removed from the catalyst, no glucose is observed (see also below).[141] Minor products, including glyceraldehyde, lactic acid, mannose, and furfural were observed in less than 1% of the overall carbon balance and were not explicitly considered in the reaction network. The rate equations for reactions within the zeolite are given in Eq.(3.9(3.13.

$$r_{fru}^{BEA} = \frac{n_{Al}}{\left(1+\phi_{Al_8:Al_4}\right)} \cdot \left[-\left(\frac{k_1}{q_{H_2O}} + k_4 + \phi_{Al_8:Al_4} \cdot \frac{k_5}{K_{FG}} \right) \cdot q_{fru} + \phi_{Al_8:Al_4} \cdot k_5 \cdot q_{Glu} \right] \quad (3.9)$$

$$r_{HMF}^{BEA} = \frac{n_{Al}}{1+\phi_{Al_8:Al_4}} \cdot \frac{k_1}{q_{H_2O}} \cdot q_{fru} - \frac{n_{Al}}{1+\phi_{Al_8:Al_4}} \cdot \left(k_2 + k_3\right) \cdot q_{HMF} \quad (3.10)$$

$$r_{LA}^{BEA} = \frac{n_{Al}}{1+\phi_{Al_8:Al_4}} \cdot k_2 \cdot q_{HMF} \quad (3.11)$$

$$r_{FA}^{BEA} = \frac{n_{Al}}{1+\phi_{Al_8:Al_4}} \cdot k_4 \cdot q_{fru} + \frac{n_{Al}}{1+\phi_{Al_8:Al_4}} \cdot k_2 \cdot q_{HMF} \quad (3.12)$$

$$r_{Glu}^{BEA} = n_{Al} \cdot \frac{\phi_{Al_8:Al_4}}{1+\phi_{Al_8:Al_4}} \frac{k_5}{K_{FG}} \cdot q_{Fru} - n_{Al} \cdot \frac{\phi_{Al_8:Al_4}}{1+\phi_{Al_8:Al_4}} \cdot k_5 \cdot q_{Glu} \quad (3.13)$$

Here n_{Al} is the moles of aluminum sites per gram of catalyst (mol/g) , $\phi_{Al_8:Al_4}$ is the ratio of Lewis acid sites to Brønsted acid sites (L:B), i.e., the ratio of octahedral to tetrahedral Al, k_j is the intrinsic rate constant of reaction j in the zeolite (either g/mol/min or 1/min), q_j is the real adsorption loading (mol/g), and K_{FG} is the equilibrium constant for glucose isomerization to fructose, calculated using the parameters in Rajabbeigi et al.[245] The estimated adsorption corresponds to the total uptake in the zeolite pores and not specifically to chemisorption to the active sites. Hydrophobic zeolites, which lack active sites, still adsorb HMF in significant quantities primarily through van der Waals interactions within the pore and entropic contributions due to the re-arrangements of the solvation cell. Since we cannot distinguish adsorption on individual sites, we take, what is known in the reaction engineering literature as, the *pseudo-homogeneous modeling approaching* within the pore. The number of Brønsted acid sites was measured at 0.61 mmol/g using isopropylamine TPD. The Lewis acid site density was measured using both solid state ^{27}Al NMR and FTIR in situ pyridine adsorption experiments as discussed in the Supplemental Information (section B.1). The determination of different acid sites is the subject of debate. Specifically, in pyridine adsorption experiment, the characteristic absorption band of Lewis acid site at wavenumber of 1453 cm^{-1} could arise from silanol groups, impurity alkali cations, or "true" Lewis acid sites as discussed in van Santen's book.[221] Therefore, the measured Lewis acid density from pyridine adsorption can be different from the number of octahedral coordinated Al, which we assigned to be the active site for glucose isomerization. In addition, the

Lewis to Brønsted acid ratio is determined through extinction coefficients for each of the adsorbed sites and can slightly change with different experimental instrument setups. Due to the controversy of the accuracy of using pyridine adsorption experiments to measure the ratio of Lewis to Brønsted acid site, we employ the results from ^{27}Al NMR measurements to determine the L:B ratio in the H-BEA-25 zeolite to be 0.3. Based on our model, the uncertainty in the characterization of L:B ratio translates into slightly different values of the pre-exponentials; importantly, the overall predictions do not change. Kruger et al. have previously investigated the effect of interactions of water with the zeolite crystals and have shown that catalytic performance of H-BEA-18 in aqueous solution does not change significantly after three use.[141, 246] Therefore, in this work we assume constant catalytic activity, while acknowledging that some loss of catalytic activity may occur at long times.

The complexity of this system necessitated simplifications regarding the reaction network (Figure 3.1), the pH variation during the course of reaction, and transport limitations. These have been assessed using sensitivity analysis, and it was found that the trends and model parameters presented below are robust to various model alterations (Figure B.5, Figure B.6 and Figure B.7).

3.2.5.5 Experimental data treatment

The vials used in reaction kinetic measurements were brought from reaction temperature to room temperature before concentrations were measured. As these vials cool, we expect the zeolite and solution to re-equilibrate as the adsorption isotherms are temperature-sensitive. We accounted for this lack of concentration measurements at reaction temperature by translating the aqueous concentration, measured at room

temperature, to expected aqueous concentrations at the reaction temperature using mass conservation and the isotherms, as shown in Eq.(3.14.

$$C_i\left(T=25^oC\right)+\frac{m_{ads}}{V_{aq}}q_i\left(T=25^oC\right)=C_i\left(T=T_{rxn}\right)+\frac{m_{ads}}{V_{aq}}q_i\left(T=T_{rxn}\right) \quad (3.14)$$

3.2.5.6 Parameter estimation procedure

Eqs (3.9)- (3.13) were solved using the Matlab *ode15s* differential-algebraic equation (DAE) solver. The experimental initial concentrations were used. The rate constants were fit using two adjustable parameters per rate constant, corresponding to the log of the rate constant at a reference temperature and the dimensionless activation energy. The parameterization is the same as for HCl-catalyzed fructose dehydration.[38] Finally, the sum of the squares of the differences between measured and predicted concentrations form the objective function that was minimized by using lsqnonlin is Matlab R2013b, which uses a trust region reflective algorithm.

3.3 Results and Discussion

3.3.1 Single-component isotherms

The estimated parameters for single-component adsorption isotherms are shown in Table 3.1. Experimental data and model predictions are included in Figure B.3. Interpretation of adsorption from solution is much more complicated than understanding adsorption from gas phase due to the interaction of solvent and solute with the solid phase, as well as the solvation effect on the solute. For example, a recent computational study of glucose transferring from aqueous solution to BEA zeolite

showed that the enthalpic effect is unfavorable and was compensated from a large entropic effect. The positive entropic contribution was attributed to the reconfiguration of the first coordination shell of water around glucose as it leaves the solvent.[246] The magnitude of these effects is expected to be different for each solute. Due to this complexity, the adsorption isotherms in our study were determined empirically. Accordingly, glucose and fructose adsorption followed the Henry isotherm since the adsorption loading showed linear dependence on the solute's concentration at low uptake. Redlich-Peterson (for HMF and LA) and Freundlich (for FA) isotherms described the experimental adsorption data better than the Langmuir isotherm. The estimated enthalpy changes of adsorption for the components ranged from 8.4 kJ/mol to 32.3 kJ/mol. These values are in the expected range and similar values have been observed by Leon et al.[237] The low apparent enthalpy change is the difference between the true heat of adsorption and the enthalpy of water solvation.[247] Independent molecular simulations illustrate these points and the contributions to the net adsorption enthalpies.[247-248]

Adsorption loadings in H-BEA-25 are higher than those previously reported in H-BEA-18.[237] This is expected since H-BEA-25 has a higher Si:Al ratio, corresponding to more hydrophobic pores than in H-BEA-18.We have performed adsorption isotherms of HMF in zeolite BEA with different Si : Al ratio. Decreasing Al content (increasing hydrophobicity of the zeolite) increases HMF saturation loading, without a pronounced effect on the enthalpy of adsorption.[227] The trend in adsorption loading is: HMF ~ LA > FA >> Fructose ~ Glucose. The strong adsorption

of HMF implies that HMF displaces fructose from the zeolite pores, highlighting the need for considering competitive adsorption.

Table 3.1. Fitted adsorption isotherm parameters for solutes in H-BEA-25.

Solute	Isotherm equation	Fitted value
Fructose Glucose*	$q = K \cdot C$	$K_{298K} = 0.2557\ L/g$ $\delta H = -20.14\ kJ/mol$
HMF	$q = \frac{K \cdot C}{1 + b \cdot C^n}$	$K_{298K} = 226.866\ L/g$ $\delta H_K = -32.21\ kJ/mol$ $b_{298K} = 197.85\ L/g$ $\delta H_b = -29.97\ kJ/mol$ $n = 0.8412$
LA	$q = \frac{K \cdot C}{1 + b \cdot C^n}$	$K_{298K} = 139.07\ L/g$ $\delta H_K = -29.09\ kJ/mol$ $b_{298K} = 107.05\ L/g$ $\delta H_b = -27.20\ kJ/mol$ $n = 0.8145$
FA	$q = K \cdot C^n$	$K_{298K} = 0.4664\ L/g$ $\delta H = -8.38\ kJ/mol$ $n = 0.7840$

* Glucose and fructose adsorption isotherms fall on the same line, as shown in Figure B.3.

3.3.2 Model assessment

Model predictions compared to experimental data for representative kinetic experiments in Figure 3.2 and a parity plot of all experimental data (Figure B.8) indicate that the model describes experimental trends at various conditions. Experiments using H-BEA-25 without any octahedral Al-sites were conducted to assess the predictive ability of the model. The octahedral Al sites were removed from the zeolite framework by washing with HCl while preserving the zeolite Brønsted acidity.[141, 236] As shown in Figure 3.2b, no glucose forms in these experiments, and the predicted concentration profiles (dashed lines) are in agreement with the experimental data (open symbols). This good agreement provides support that the model can describe the effects of altering the relative ratio of acid sites on performance discussed below.

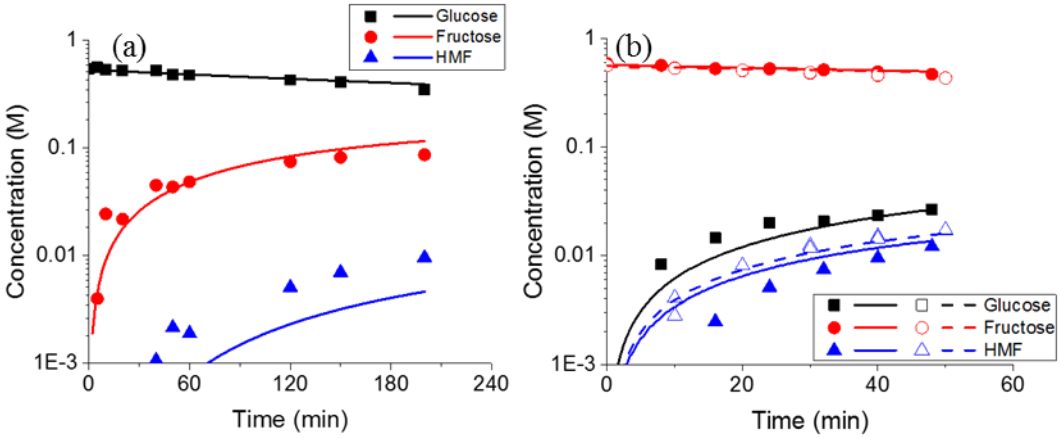

Figure 3.2. Comparison between model (solid lines) and experimental (closed symbols) concentration profiles of glucose, fructose, and HMF for experiments starting with 10 wt% glucose (a) or fructose (b) at 130 ºC with an H-BEA-25 loading of 125 g/l. Open symbols and dashed lines in (b) indicate experimental and predicted concentrations, respectively, for 10 wt% fructose dehydration using 125 g/L HCl-washed H-BEA-25. No glucose is formed in this case.

Next we turn into comparing model predictions to literature data in single phase and biphasic systems. The predicted selectivity of fructose dehydration to HMF is ~43% at 140 ºC, qualitatively consistent with the 30% reported experimentally by Ordomsky et al.[228] Removing HMF from the reactive phase using an organic extractant can reduce HMF loss.[113] Kruger et al. found an HMF selectivity from fructose of ~35% when an organic extracting phase is added to a mixture of H-BEA-18 and water at 130 ºC.[141] This finding is in qualitative agreement with simulations we performed here in a biphasic system (albeit H-BEA-25 was used here). When the Lewis sites of H-BEA-18 were experimentally removed, the selectivity of HMF from fructose increased to ~50%.[141] The corresponding model prediction of 59% is again in good agreement with the data.

Species partitioning between solution and zeolite phases and contribution of homogeneous chemistry

Here we address two topics that are hard to study via experiments alone. Simulations indicate that only a small fraction (up to 10%) of the chemistry proceeds homogeneously (Experimental data for model prediction

Figure B.10) under these conditions. The high zeolite loading used in our experiments (125 g/l) maximizes the contribution of the heterogeneous reactions to the overall reaction rate. This contribution is expected to vary with amounts of zeolite and solution, e.g., the less the zeolite, the more the contribution of the homogeneous chemistry.

A challenge in analyzing these experiments is the fact that significant portions of species remain adsorbed in the zeolite and that the adsorbed amounts are hard to

measure experimentally during reaction. Adsorption isotherms can relate the adsorbed concentrations to measurable concentrations in the aqueous phase to provide the overall concentration of each species in the system.

Typical experimentally measured (at room temperature) aqueous concentrations starting from fructose are shown in Figure 3.3 (closed symbols). We use adsorption isotherms to estimate the corresponding total concentration (adsorbed plus solution) profile of each component (open symbols in Figure 3.3). The total and solution concentrations of fructose and FA are very similar since they adsorb weakly in the zeolite; these compounds are primarily in the aqueous phase. On the other hand, very little HMF and LA are in solution due to their strong adsorption in the zeolite.

Recent work with homogeneous acids has shown that FA can be produced directly from fructose degradation[38] probably via a retro-aldol reaction.[229] As a result, the molar ratio of FA and LA was higher than 1 at low fructose conversions and then gradually decreased at higher conversions once the fraction of the HMF-derived FA becomes dominant. The data in Figure 3.3b show that FA is in excess of LA indicating that, as in homogeneous catalyzed reactions, the zeolite also catalyzes the direct conversion of fructose to FA.

Representative concentration profiles of the experiments using HMF as a substrate are shown in Figure 3.4. As expected, HMF rehydration produces equimolar amounts of FA and LA. However, an abrupt decrease in the HMF concentration in solution between the initial value and the one recorded at the first data point (10 min) is observed in Figure 3.4a, followed by a more gradual decrease thereafter. The total HMF concentration (open symbols in Figure 3.4a) does not exhibit the same rapid

decrease, indicating that the initial drop is primarily an effect of HMF adsorption. This conclusion is further corroborated by the absence of significant fractions of FA and LA at early reaction times. Since the HMF and LA are mainly adsorbed in the zeolite, the measured concentrations in solution are a poor indicator of their overall amount in the system and for estimating reaction rates. It is then not surprising that data in different labs cannot easily be reconciled. For example, differences in the amount of zeolites and/or solution-phase volume would result in different contributions of homogeneous and heterogeneous kinetics to the overall rates.

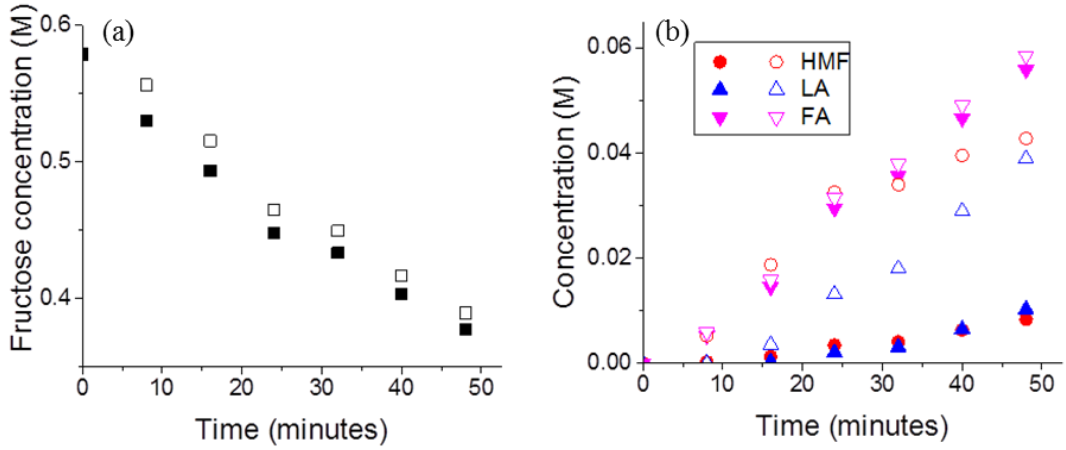

Figure 3.3. Measured concentration profiles in solution (closed symbols) and estimated total concentration (including aqueous and zeolite phase concentrations - see text; open symbols) starting with 10 wt% fructose at 140 ºC with 125 g/l of H-BEA-25. Accounting for the adsorbed amounts, especially for HMF and LA, is important for correct description of kinetics.

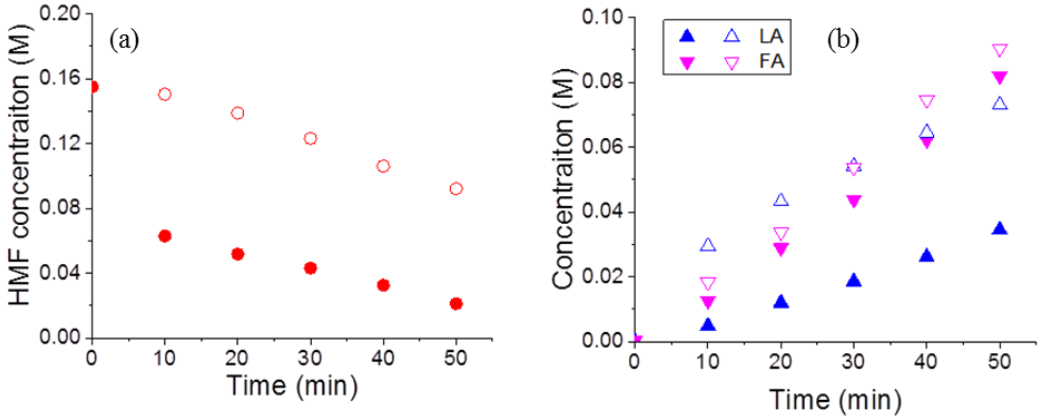

Figure 3.4. Aqueous species concentrations (closed symbols) and estimated total concentration (including aqueous and zeolite phase concentrations; open symbols) starting with 2 wt% HMF at 140 ºC with 125 g/l of H-BEA-25.

3.3.3 Kinetic parameters and comparison to other catalysts

Several prior studies have explored the reaction kinetics of zeolite catalyzed conversion of sugars to furans.[228, 249-251] Typically models describe rates as a function of solution concentrations[249] rather than those in the zeolite pores.[140] This approach lumps contributions from adsorption and homogeneously catalyzed reactions with heterogeneous catalysis, limiting the insights gained. One exception entails the work of Lourvanij and Rorrer who used a Langmuir-Hinshelwood model to estimate simultaneously adsorption and kinetics of glucose dehydration in H-Y, MCM-20, and MCM-41 catalysts.[252] Our work is the first to take input from single solute experimentally determined adsorption data for the construction of multicomponent isotherms and use this thermodynamic model to decouple homogeneous and heterogeneous reaction contributions using intrinsic (inside the zeolite) rather than bulk (solution) concentrations.

The estimated activation energies, rate constants at a reference temperature, and corresponding Arrhenius pre-exponentials are shown in Table 3.2. The activation energy of fructose dehydration (163 kJ/mol) is close to that in homogeneous catalysts (values between 130 and 160 kJ/mol[243, 253-254]), but lower than that reported by Lourvanij and Rorrer (205 kJ/mol) for H-Y zeolite.[252] This is not unexpected, as a different zeolite framework (faujasite vs. beta) and a different temperature range (130-190 ºC vs. 110-140 ºC) were considered and a rather limited number of data was employed in published work increasing the uncertainty in estimated parameters. The activation energy of fructose degradation to FA and humins (110 kJ/mol) also falls close to the 102 kJ/mol reported by Asghari and Yoshida[254] and 130 kJ/mol reported by both Swift et al. and Kuster et al.[243, 253] for homogeneously catalyzed fructose degradation to humins.

Table 3.2. Estimated parameters for the intrinsic reaction rates in zeolite beta.

Reaction	E_a, kJ/mol	$\ln(k_{398K})$[a]	$log_{10}(A_0)$ [a]
Fructose → HMF	142 ± 8	2.65 ± 0.10[b]	19.75[b]
HMF → FA+LA	111 ± 6	2.92 ± 0.03	15.78
HMF → Humins	145 ± 18	1.43 ± 0.35	19.63
Fructose → FA + Humins	79 ± 8	3.44 ± 0.16	11.88
Glucose →Fructose	113 ± 8	5.01 ± 0.06	17.06

[a] $\frac{g}{min \cdot mol}$ unless noted otherwise , [b] $\frac{1}{min}$

Glucose adsorbs weakly in the zeolite (Figure B.3), so the apparent activation energy obtained from an Arrhenius graph of initial rates (Figure B.15) is close to the intrinsic activation energy in Table 3.2 (117 kJ/mol) and in between those observed for Sn-BEA (~89 kJ/mol) and Ti-BEA (~155 kJ/mol),[68] as shown in Figure 3.5, indicating that octahedral Al sites catalyze the isomerization reaction effectively.

While direct dehydration of glucose to HMF is slow[229], the rate constant of isomerization is larger than that of fructose dehydration by more than one order of magnitude (Table 3.2), i.e., octahedral Al sites are efficient for isomerization, rationalizing why the concept of tandem reactions in a single pot works.

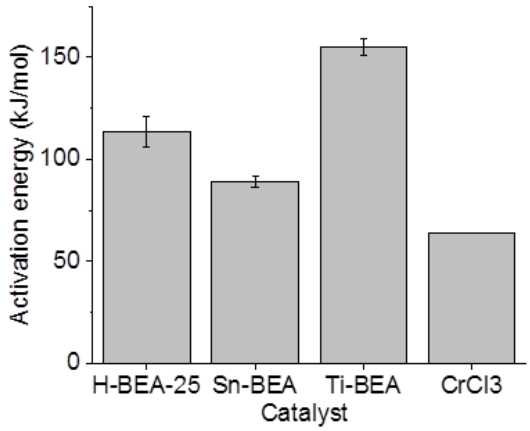

Figure 3.5. Apparent activation energy for glucose-fructose isomerization in Sn-BEA[68], Ti-BEA[68], homogeneous $CrCl_3$[106] and H-BEA (present work) based on glucose consumption at 110-130 ºC.

The zeolite catalyzed HMF degradation reactions have higher activation energies (124-179 kJ/mol) than the HCl catalyzed counterparts (60-110 kJ/mol),[243, 255] suggesting that confinement within the zeolite changes the energetics of HMF degradation. While the activation energies are high, so are the pre-exponential factors resulting to high rate constants, that eventually lead to significant HMF degradation. Furthermore, strong HMF adsorption accelerates its degradation in the zeolite.

The 'per-site' reactivity of HCl and H-BEA-25 can be compared directly by examining the rates of HMF and fructose consumption using the turnover frequency (TOF) of the catalysts (Figure 3.6). HCl converts nearly an order of magnitude more fructose per 'acid site in the reactor' per unit time than the zeolite. The number of

'active centers' is also different. In a 10 wt% fructose solution at 140 ºC, fructose loading in H-BEA-25 is 0.23 mmol/g. This is less than half the Brønsted site density in the zeolite measured experimentally (0.61 mmol/g). Under typical conditions of homogeneously catalyzed fructose dehydration, the concentration of the acid (i.e., HCl) is lower than that of fructose at those same conditions (i.e., 10 wt% fructose dehydration at pH~1 corresponds to 0.55 M fructose and 0.08 M HCl). Comparison between heterogeneous and homogeneous catalysts in this system should therefore be done with care, and intrinsic rate constants should be the preferred method.

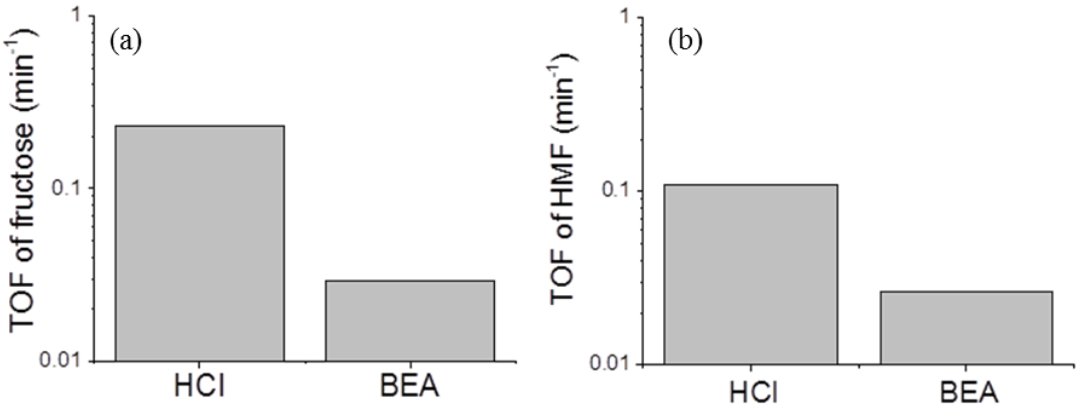

Figure 3.6.Turnover frequency (TOF), determined from experimental data after 30 min, of 10 wt% fructose (a) and 5 wt% HMF (b) in HCl (pH = 1.1) and H-BEA-25 (125 g/l) at 140 ºC.

3.3.3.1 Kinetic regimes

The tandem reactions of isomerization and dehydration require a balance between multiple rates to optimize HMF rate and yield. The rates are determined from intrinsic rate constants, the local concentrations around the active site, and the number of active sites. It has been demonstrated that by varying the post-synthesis calcination

procedure,[233] the ratio of Lewis to Brønsted acid sites can be adjusted. By adjusting this ratio, the relative rates of glucose isomerization to fructose and fructose dehydration to HMF can be altered. Therefore, it is interesting to study the effect of changing L:B ratio on the kinetic regimes. We have found (unpublished) that the HMF's enthalpy of adsorption remains fairly constant on BEA zeolites with different Si/Al ratio. Therefore, we believe that the largest contribution to the measured enthalpies of adsorption originates from the interaction with the zeolite pore rather than with the active sites.[227] As a result, the adsorption in the zeolite will be constant when changing the Lewis to Brønsted acid ratio. Herein, we explore the effect of L:B ratio on the kinetics of tandem reactions and the behavior of bifunctional materials, which are currently unknown. Figure 3.7(a-d) shows the predicted concentration profiles of glucose, fructose, HMF, and LA as a function of time for different Lewis to Brønsted acid site ratios in a single phase. Figure 3.7(e-f) shows the corresponding net reaction rates. The concentration of glucose decreases monotonically whereas those of fructose and HMF go through a maximum as a result of the competition between formation and consumption reactions. Initially, glucose is consumed faster with increasing L:B ratio since glucose isomerization is Lewis-acid catalyzed. Interestingly, at longer times (past the maximum in fructose concentration), the net rate of consumption of glucose is lower for higher densities of Lewis acid sites. This rather counterintuitive finding results from the fact that at high L:B ratios, there is an insufficient number of Brønsted acid sites to dehydrate fructose, and fructose accumulates in the reactor. As a consequence, the reverse isomerization reaction (fructose to glucose) becomes significant, reducing the net rate of glucose

consumption to be close to zero. Simple kinetic analysis[256] indicates that the ratio of concentrations of glucose and fructose is in quasi-steady state and at high L:B ratios, the isomerization reaction is close to equilibrium.

At low L:B ratios, the fructose production rate is low due to slow isomerization and fast dehydration due to having excess of Brønsted acid sites. Low L:B ratios limit fructose accumulation in the reactor and, consequently, the reverse isomerization reaction. Eventually, fructose is consumed via dehydration nearly as fast as it is produced leading to a low net rate (Figure 3.7f) and a slowly varying, low concentration (Figure 3.7b). As L:B increases, the glucose isomerization rate increases eventually leading to accumulation of fructose in the reactor. The high fructose concentration leads to faster rates of reverse isomerization (fructose to glucose) as well as dehydration to HMF and degradation to humins. These degradation reactions eventually become faster than the production of fructose from glucose isomerization despite the slower intrinsic kinetics (see rate constants in Table 3.2), causing fructose concentration to decrease rapidly. Figure 3.7c shows that the maximum HMF concentration increases with increasing L:B ratio. This is attributed to the decreasing number of Brønsted acid sites that catalyze HMF degradation (Figure 3.7f). Unlike fructose, whose concentration reaches a maximum at about the same time for various L:B ratios, the HMF concentration peaks at considerably longer times as L:B increases because HMF consumption reactions are limited by the lack of Brønsted acid sites. Finally, Figure 3.7d,h show the concentration and net rate of LA, respectively, vs. time. As expected, over typical time scales both the concentration and the rate of LA are optimized for intermediate L:B ratios.

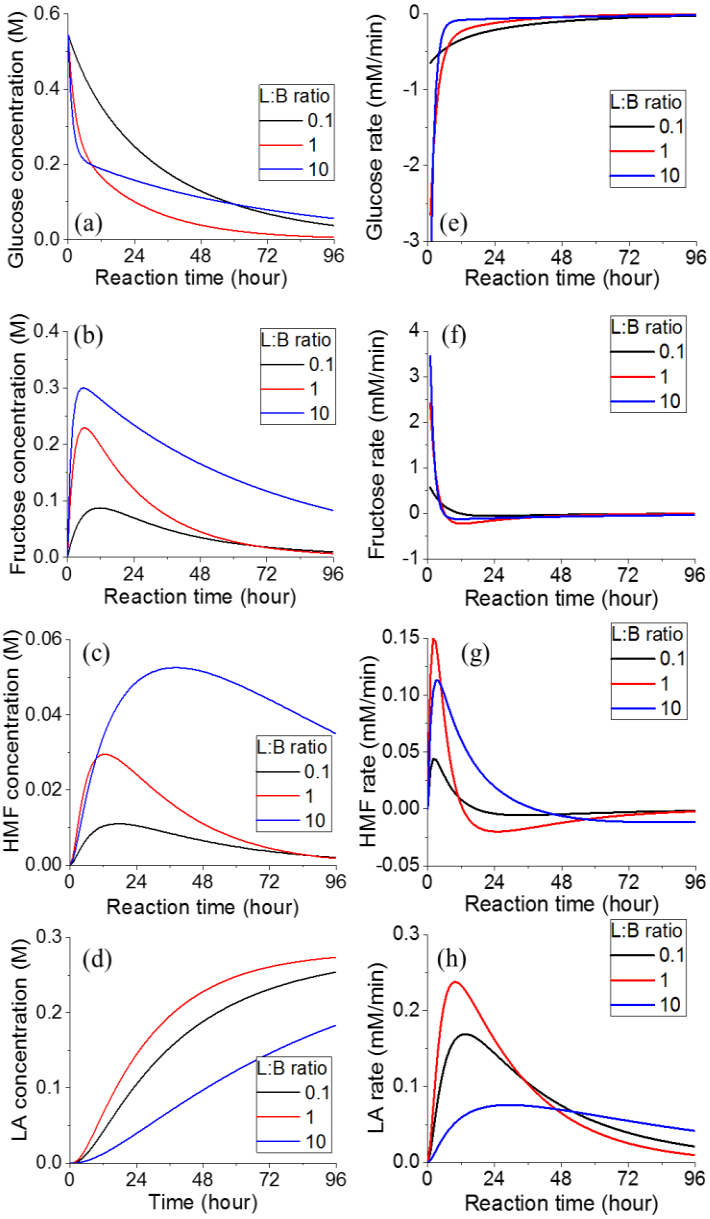

Figure 3.7. Predicted concentration profiles (a-d) and net reaction rates (e-h) of (a, e) glucose, (b, f) fructose, (c, g) HMF, and (d,h) LA at different L:B ratios. Conditions: 130 ºC, 125 g/L H-BEA-25, 1.2 mmol/g total sites, 10 wt% glucose.

The net rate of HMF production in Figure 3.7 is masked by dominant HMF degradation reactions. This is in contrast to our previous study where para-xylene does

not readily degrade. In order to draw a closer analogy to the para-xylene work, we consider the formation rate of HMF, rather than its net rate. As we show below, this case is relevant in biphasic systems. Figure 3.8a shows the formation rate of HMF as a function of the L:B ratio at different times. In all cases the HMF production rate exhibits a volcano relationship with an optimum L:B ratio of ~1, which indicates that at this L:B ratio, there is a balance between the rates of glucose isomerization to fructose and fructose dehydration to HMF. In order to rationalize the volcano relationship in Figure 3.8a, the normalized sensitivity coefficient (NSC) of HMF production rate with respect to the rate constants, defined as ($d \ln r_{HMF} / d \ln k_i$), was computed for different L:B ratios and is shown in Figure 3.9. On the left of the volcano curve, the isomerization reaction is rate-controlling. As L:B increases, the importance of isomerization decreases and eventually the Brønsted acid-catalyzed dehydration reaction becomes rate-determining step at high L:B ratios. At longer times, the rate of HMF formation becomes generally less sensitive to isomerization, because the reverse isomerization (fructose to glucose) becomes more prevalent. As the reverse isomerization becomes more important, the net rate of glucose consumption approaches zero (Figure 3.7e), even though the concentration of glucose in the aqueous phase is significant (Figure 3.7a).

This L:B ratio of ~1 falls well within the range produced by Otomo et al. (0.6 and 1.92),[233] indicating that it is feasible to experimentally tune the zeolite and improve the HMF rate. At that optimal ratio, HMF degradation reactions are also prevalent, reducing the net rate of HMF production (Figure 3.7f) and therefore the yield.

The bifunctional H-BEA system is different from that studied in the para-xylene work.[234] Here the total number of acid sites is fixed (determined by the zeolite Si/Al ratio) and as result, the concentration of one site cannot easily be changed arbitrarily while keeping the other constant. Furthermore, the first reaction (glucose isomerization) is heterogeneous rather than homogeneous. A system with closer resemblance to that studied in ref.[234] is a physical mixture of Lewis and Brønsted acid catalysts with properties those of the corresponding sites of H-BEA zeolite. When we simulated such a system and varied the Brønsted acid concentration alone (Figure 3.8b), a linear and a plateau regime are observed, as happens in the para-xylene chemistry. Thus, the multiple kinetics regimes appear to be a generic feature of tandem reactions catalyzed by multiple catalysts or multifunctional catalysts, as is the case here, and the shape depends on whether one can vary one site at the time or not.

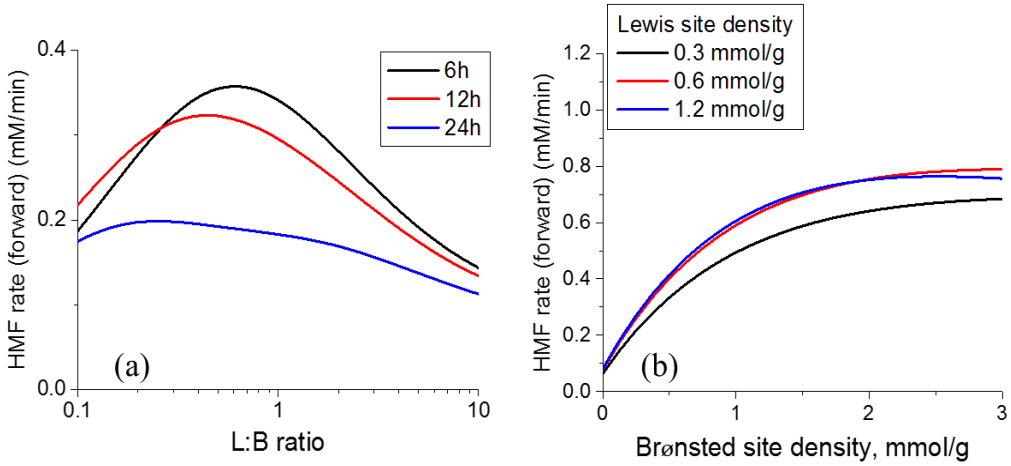

Figure 3.8. Predicted rate of HMF formation (forward) as a function of (a) Lewis to Brønsted acid site ratio (holding the total number of sites constant at 1.2 mmol/g) after 6, 12, and 24 hours and (b) Brønsted site density with Lewis site density held constant at 0.3, 0.6, and 1.2 mmol/g after 6 hours. Reaction starts with 10 wt% glucose at 130 ºC with 125 g/l of H-BEA.

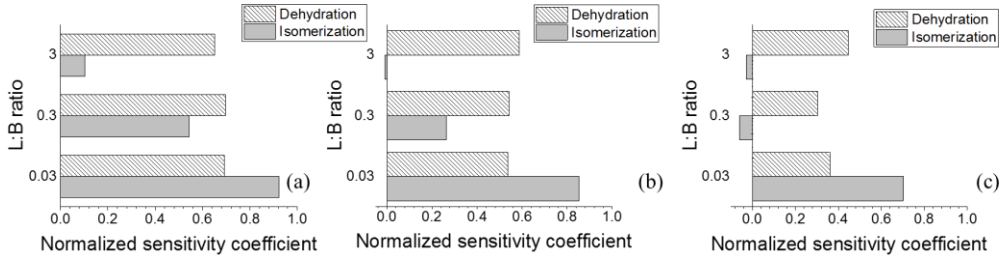

Figure 3.9. Normalized sensitivity coefficient of the forward HMF production rate for different L:B ratios after (a) 6 hours, (b) 12 hours, and (c) 24 hours. Conditions: 130 ºC, 125 g/L H-BEA-25, 1.2 mmol/g total sites, 10 wt% glucose.

3.3.3.2 Optimizing HMF yield in single phase and biphasic systems

Next we turn to the yield that is an economically important quantity. Figure 3.10a shows the HMF yield vs. L:B ratio at three different reaction times. Overall, the HMF yield is low. The highest HMF yield occurs at high L:B ratios and longer times because isomerization is fast leading to accumulation of fructose but the degradation reactions of fructose and HMF are slow due to unavailability of enough Brønsted acid sites. This is further corroborated in the sensitivity of HMF yield with respect to rate constants shown in Figure 3.10b. Accelerating the isomerization and dehydration increases the HMF yield. Conversely, humin formation from fructose and HMF and HMF rehydration have a negative impact on HMF yield. At short times, isomerization is important but at long times, where HMF yield is higher, HMF rehydration and humin formation reactions and fructose dehydration are key to improving HMF yield. Otomo et al. observed higher HMF yields from glucose when more Lewis sites were present in their H-BEA, in support of our findings.[233]

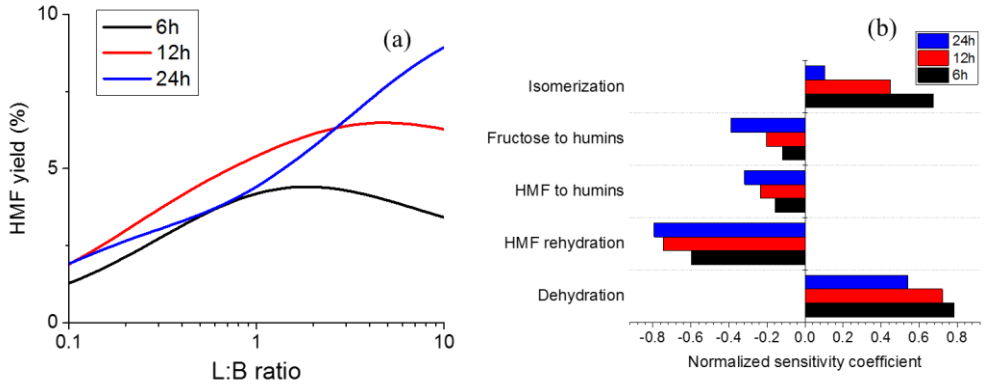

Figure 3.10. (a) HMF yield as a function of Lewis to Brønsted acid sites (L:B) ratio after 6, 12, and 24 hours and (b) corresponding normalized sensitivity coefficient of HMF yield for L:B = 1. Conditions: 130 ºC, 125 g/L H-BEA-25, 1.2 mmol/g total sites, 10 wt% glucose.

A common approach used experimentally to increase the HMF yield is to add an organic extractant that selectively removes HMF before it reacts.[257] Therefore, it is important to be able to predict the HMF yield and rate of formation in biphasic systems. Since we have previously developed models for the separation, the predictions should be reasonable. We simulate this in Figure 3.11 by considering extraction using a realistic organic solvent (partition coefficient = 2, $V_{org}/V_{aq} = 5$, similar to those used in previous work [258]) and an ideal solvent that is immiscible with water and extracts all HMF as it is being produced. The ideal solvent provides the optimal HMF yield, whose value is controlled from the humins formed from sugars. As it is well-known, our simulations indicate that extraction can considerably increase the HMF yield. Realistic extractors, such as those used in typical laboratory experiments, can lead only to moderate yields, whereas the ideal extractor can lead to (molar) yields approaching 60%. This indicates that developing a better separation scheme, e.g., by finding better extractants,[259] has the greatest potential for improving

the HMF yield. This is extremely important in the case of Brønsted acid zeolites since the typical use of inorganic salts for enhancing the partition coefficient[258] employed using HCl Brønsted acid is not a practical alternative (due to ion exchange reactions). In the actual biphasic system, higher yields occur for higher L:B ratios because HMF forms slowly and is extracted as soon as is formed, rather than being consumed by side reactions. Interestingly, the time for the optimal yield increases with increasing L:B ratio due to the low rate of dehydration of fructose. In the ideal extractor case, on the other hand, the same optimal yield is obtained at very long times (now shown) for all L:B ratios but intermediate L:B ratios give higher yields at shorter times and should be preferred.

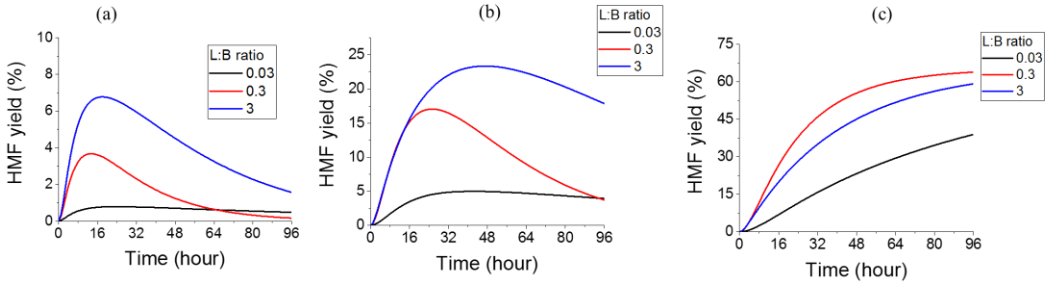

Figure 3.11. Predicted HMF yield in (a) aqueous single-phase solution, (b) a biphasic reactor (partition coefficient = 2, $V_{org}/V_{aq} = 5$) , and (c) an ideal biphasic reactor (all HMF extracted) at different L:B ratios. Conditions: 130 °C, 125 g/L H-BEA-25, 1.2 mmol/g total sites, 10 wt% glucose.

3.3.3.3 Identification of key materials' properties

The HMF yield shown in the biphasic reactor using the bifunctional H-BEA catalyst (Figure 3.11b) is lower compared to systems consisting of physical mixtures of catalysts, primarily when homogeneous HCl is involved as a Brønsted acid catalyst. For example, Nikolla et al. obtain a 53% molar yield of HMF in an experimental

biphasic reactor with Sn-BEA and HCl at 180 ºC.[231] Our results above indicate that the Lewis sites of Sn-BEA are more effective than those of H-BEA[245] (see also Figure 3.5), and HCl converts fructose to HMF faster than H-BEA (Figure 3.6). These findings along with the sensitivity analysis in Figure 3.10b provide insights into why H-BEA is not as an effective catalyst. In order to achieve high HMF yields, one needs to increase the rate of glucose isomerization and fructose dehydration, and thus the rate of HMF production, while reducing the rates of HMF degradation reactions. To better rationalize the differences among catalysts, we conduct 'numerical' experiments. Figure 3.12 shows the predicted maximum yield (with respect to time) of HMF from glucose in hypothetical catalysts in both a single-phase (Figure 3.12a) and a biphasic (Figure 3.12b) system. Rajabbeigi *et al*. recently published kinetic parameters for glucose-fructose isomerization in Sn-BEA based on aqueous concentrations.[245] The rate constants reported are between 11 and 7 times higher than those of the present study, depending on temperature. Since their study differs from ours in several important respects (temperature range, catalyst, adsorption), we assumed an increased rate constant by a factor of 10 would qualitatively capture differences in reactivity between Sn-BEA and H-BEA-25 without implying that the two studies are directly comparable. The HMF yield from a hypothesized zeolite BEA that could enhance the rate of isomerization of H-BEA by 10 times (BEA-L10) only marginally improved as shown in Figure 3.12. This is consistent with strong adsorption of HMF in H-BEA causing low HMF yields. Increasing HMF yield may be achieved either by reducing HMF adsorption strength, which would reduce its side-reactions or by increasing the strength of carbohydrate adsorption, which would

promote the desirable glucose isomerization and fructose dehydration reactions. Indeed, when the adsorption properties of H-BEA are modified so that HMF adsorbs as weakly as glucose/fructose or the glucose/fructose adsorb as strongly as HMF or both, the HMF yield increases considerably (the time needed to achieve maximum HMF yields varies as shown). Increasing sugar adsorption increases the rate of HMF production and yield, whereas weakening the HMF adsorption decreases the side reactions of HMF and thus improves the HMF selectivity (for a kinetic profile starting from fructose see Figure B.12). A mixture of zeolite with enhanced Lewis acid (BEA-L10) and HCl converts glucose to HMF faster and avoids the strong adsorption of HMF, leading to high yields, qualitatively consistent with experimental data.[231] Putting all these findings together, the bifunctional H-BEA is not as good a catalyst because it converts sugars slower due to being (1) a weaker Lewis acid catalyst than Sn-BEA and (2) a weaker Brønsted acid catalyst than HCl and (3) at the same time a strongly HMF-adsorbing material that promotes HMF side reactions. Identification of bifunctional materials (i.e., pore size, hydrophobicity) and/or a solvent that can promote sugar adsorption over HMF can make them viable. On the other hand, the H-BEA catalyst would be more suitable for converting glucose to levulinic acid directly, as this process would benefit from strong HMF adsorption and rehydration.

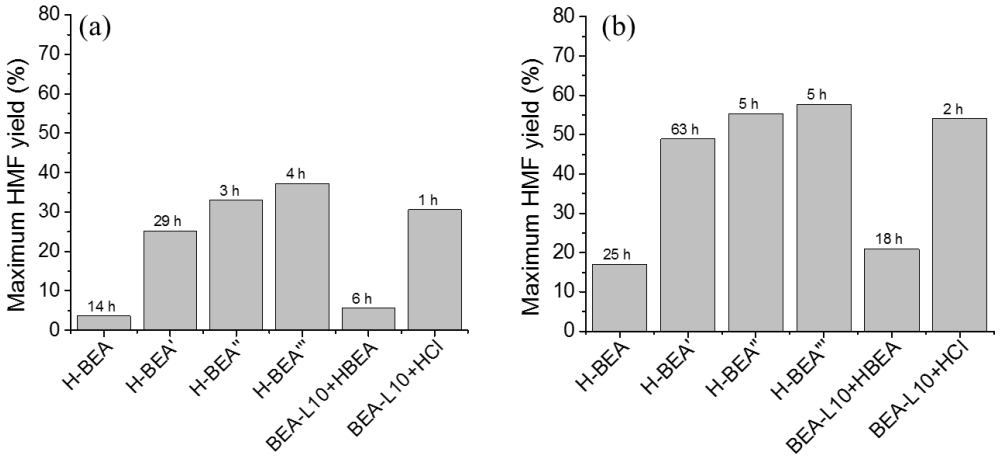

Figure 3.12. Predicted maximum HMF yield from glucose in (a) single phase and (b) biphasic (partition coefficient = 2, $V_{org}/V_{aq} = 5$) systems along with the time to reach that yield. Catalysts include the actual H-BEA, H-BEA with modified adsorption (H-BEA' has low HMF loadings, H-BEA'' has high glucose/fructose loadings, and H-BEA''' has increased glucose/fructose loading and lower HMF loadings), BEA-L10 combined with H-BEA or HCl.

3.4 Conclusions

The use of aluminosilicate zeolite BEA as a bifunctional catalyst for the conversion of glucose to HMF using tandem reactions has been investigated. We developed a model that accounts for multicomponent adsorption effects, homogeneous Brønsted acid catalyzed chemistry of fructose, and intrinsic heterogeneous Lewis acid catalyzed isomerization and Brønsted acid catalyzed fructose dehydration, HMF rehydration, and humin formation chemistry, the parameters of which were fitted to experimental data of this work. We show that the intrinsic reaction kinetics of fructose dehydration in H-BEA favor HMF formation. However, the relative strength of

carbohydrate vs. HMF adsorption, rather than intrinsic kinetics, causes slow fructose dehydration relative to homogeneous catalysts and low overall HMF yields due to strong HMF adsorption leading to side reactions. Using sensitivity analysis we show that strengthening fructose adsorption could increase HMF yield significantly, and HMF yields approaching those obtained using a combination of Sn-BEA and HCl can potentially be achieved. As far as H-BEA is concerned, despite its performance been modest in a single phase, it may be possible to attain high HMF yield using much better extraction.

We reveal that glucose conversion to HMF using tandem reactions exhibits two types of multiple kinetic regimes and this appears to be a generic feature of tandem reactions catalyzed by multiple or multifunctional catalysts. When a bifunctional catalyst with a fixed total number of acid sites is used (as in the case of aluminosilicate zeolites), the (forward) production HMF rate exhibits a volcano curve with increasing Lewis:Brønsted acid site ratio. In contrast, when the Brønsted and Lewis acid concentrations vary independently, a linear kinetic regime followed by a plateau form as the Brønsted acid concentration increases at fixed Lewis acid concentration.

Model predictions provide insights about the optimum catalyst properties under different reactor configurations. The HMF yield in a single aqueous phase is maximized when a catalyst with a high L:B ratio is used. When an ideal extracting phase is considered, then the maximum HMF yield approaches 60% at an optimum L:B ratio of ~1.

Chapter 4

ROLE OF LEWIS AND BRØNSTED ACIDITY IN METAL CHLORIDE CATALYSIS IN ORGANIC MEDIA: REDUCTIVE ETHERIFICATION OF FURANICS

4.1 Introduction

Research on renewable production of fuels has drawn significant attention due to rising concerns about climate change. Lignocellulosic biomass, the most natural abundant source of carbon, offers a green alternative to fuels without interfering with human-food consumption.[4] Biomass-derived furanyl ethers possess high cetane number, high energy density, and proven performance when blended with petroleum-derived diesel.[60, 150] Such ethers can be synthesized from 5-hydroxymethyl furfural (HMF),[260] a biomass derived platform chemical. HMF can be directly etherified by condensation with an alcohol to form 5-(alkoxymethyl)furfural (mono-ether)[61, 156, 159], or after hydrogenation of its carbonyl group followed by etherification to form 2,5-bis(alkoxymethyl)furan (di-ether), i.e., a reductive etherification route.[60, 151-152] The di-ether is higher grade fuel than the mono-ether owing to its higher stability and miscibility with commercial diesel.[60, 151] While acid-catalyzed etherification of HMF to a mono-ether with ion exchange resins,[60, 155, 261] heteropolyacids,[262] aluminosilicates,[159, 263] mineral acid,[60, 263] and metal salts[160-161, 185, 264-265] as catalysts has been studied quite extensively, literature on synthesis of the di-ether is limited. Bell and coworkers reported up to 60% yield to di-ether in a cascade reaction under H_2

pressure using a physical mixture of Pt/Al_2O_3 and Amberlyst-15.[60] More recently, Jae et al. and Lewis et al. independently investigated the use of metal-substituted BEA zeolites for the one-pot synthesis of the di-ether in 2-propanol or ethanol, without H_2 gas.[151-152] In this route, the Lewis acids are hypothesized to facilitate catalytic transfer hydrogenation of HMF by the Meerwein-Ponndorf-Verley (MPV) reduction in alcohol solvent that is also acting as a hydrogen donor. The product of the MPV reduction is sequentially etherified to the maximum of ca. 80% di-ether yield.[151-152] Di-ether formation was also reported over metal oxide catalysts.[158, 266] Evidently, reductive etherification of HMF is a promising process for production of di-ether on account of several advantages: single catalyst, no H_2 gas required, and one-pot reactor for process efficiency.

Besides metal substituted BEA zeolites, whose synthesis is still rather challenging, conventional homogeneous Lewis acid metal chlorides (e.g., $CrCl_3$, $AlCl_3$) have been shown to be effective for intramolecular MPV reduction of aldose to ketose (e.g., glucose isomerization).[47, 267-271] Mechanistic studies have revealed that the active-site structures of Sn-BEA and metal chlorides share striking similarities and facilitate the same catalytic pathways in aqueous solution.[46, 68, 135, 138, 230, 268-269] In the chelated transition state, characteristic of MPV reduction, the metal center coordinates the O1 and O2 atoms of the aldose (e.g., glucose) during an intramolecular hydride shift from the C2 to the C1 carbon. Because of the analogies between zeolites and metal salts for isomerization of glucose, one might speculate on the potential activity of metal salts for reductive etherification of HMF. In addition, metal salts offer

promising reusability as they are shown to be effectively recyclable after multiple runs without significant activity loss for glucose isomerization/dehydration to HMF.[193, 272]

Although metal salts have been demonstrated to be effective catalysts for direct etherification of HMF to mono-ether in alcohol solvent[185, 264-265], no di-ether production has been reported. Our group previously investigated catalysis of furfural hydrogenolysis by metal chlorides in 2-propanol, and observed formation of isopropyl furfuryl ether.[72] However, that work focused on synthesis of methyl furan and did not further explore the potential for reductive etherification.

Herein, we assess the catalytic activity of inexpensive, conventional Lewis acid metal chlorides for the tandem reductive etherification of HMF in 2-propanol, and reveal two main reaction pathways, depending on the metal cation. Furfuryl alcohol (FA) and furfural are employed as model compounds to further investigate each of the two pathways independently. By correlating the metal chloride speciation and reaction kinetics, we demonstrate that the metal chlorides actually play a bifunctional role in the reductive etherification of furanic compounds in organic media.

4.2 Experimental Methods

4.2.1 Materials

All chemicals and solvents were purchased from Sigma Aldrich and used without further modification. Reactants are HMF, furfural, and FA. The catalysts include $ZnCl_2$, $CrCl_3.6H_2O$, $FeCl_3.6H_2O$, $YbCl_3.6H_2O$, $DyCl_3.6H_2O$, $LaCl_3.7H_2O$, and $YCl_3.6H_2O$ as well as 0.1 M HCl in 2-propanol. Deuterated solvents for isotopic

labeling experiments are 2-propanol-d8 ($(CD_3)_2CDOD$) and 2-propanol-OD ($(CH_3)_2CHOD$).

4.2.2 Reductive etherification experiments

A typical experiment was carried out in a 100 mL Parr reactor vessel, consisting of 70 mL of 2-propanol solution of a metal salt and the reactant (HMF or furfural), sealed with 20 bar N_2. The reactor was heated to the desired temperature in a customized band heater, using a temperature controller. Samples were taken periodically and filtered for post reaction analysis.

4.2.3 Etherification kinetic experiments

Kinetic study of FA reactions was conducted in 5 mL thick walled glass vials, consisting of 2 mL of 2-propanol solution of 1 wt % FA and 5-20 mM catalyst ($CrCl_3$, YCl_3 or HCl). The reactor vials were heated to 90 °C, in a temperature controlled-aluminum block on a magnetic stir plate, and quenched in an ice bath at desired time points. The small glass reactors were used, instead of Parr reactor, because they require minimal heating time and to provide better data for the reaction kinetic model. This setup can only be used at low temperatures ($T \leq 120$ °C)

4.2.4 Product analysis

Products were identified with a gas chromatogram-mass spectrometer (GC-MS) system (Shimadzu QP 2010 Plus). Except for HMF, all quantifications were done in a GC (Agilent 7890 A), equipped with a HP-INNOWAX column, a flame ionization detector (FID) and a quantitative carbon detector (Polyarc^{TM}). The

Polyarc^{TM} reactor converts organic compounds to methane and gives a universal response in the FID to eliminate cumbersome calibrations.[273] Product concentrations were determined using the calibration curve for FA and carbon numbers of the product molecules. The method was verified by the collapse of calibration curves for various organic compounds with different carbon numbers (Figure C.1). HMF quantification was carried out with an Agilent 1200 Series high performance liquid chromatography (HPLC), equipped with a C-18 column (Agilent).

4.2.5 pH measurement

The pH of the solutions was measured with a glass pH electrode (Mettler Toledo InLab Science) and an Acumic basic AB 15 pH meter.

4.2.6 Spectroscopy techniques

Electrospray soft ionization mass spectra (ESI-MS) of the metal chloride solutions in 2-propanol were collected with a single quadrupole mass spectrometer (SQD2), using 2-propanol as mobile phase with the following parameters: capillary voltage 2.8 kV, extractor voltage 5 V, sample cone voltage, 20 V, source temperature, 363 K, desolvation temperature, 423 K, cone gas (N_2) flow, 40 L/h. X-ray absorption measurement (XAS) were performed at Cr K-edge (Z = 24, E_0 = 5989eV) in fluorescence mode, and Y K-edge (Z = 39, E_0 = 17038 eV) in transmission mode at Stanford Synchrotron Radiation Lightsource. Nuclear magnetic resonance ^{1}H NMR spectra of the post reaction solutions were recorded using a Bruker 400 MHz NMR spectrometer.

4.3 Results and Discussions

4.3.1 Catalytic activity of metal chlorides for reductive etherification of HMF

Various metal chlorides (MCl_x) were screened for HMF reaction in 2-propanol and exhibited a wide range of catalytic activity under the same reaction conditions (Figure 4.1). While $ZnCl_2$ and $LaCl_3$ showed little activity, other salts gave more than 60% HMF conversion. In all the experiments, low HMF initial concentration of 1 wt % was used to minimize self-condensation of HMF to heavy products[151] and enable focus on the mechanism of the main reaction. GCMS analysis revealed various products such as 5-(isopropoxymethyl)furfural **1** (mono-ether), 2,5-bis(hydroxymethyl)furan **2,** isopropyl levulinate **3**, 5-isopropoxymethylfurfuryl alcohol **4,** 2,5-bis(isopropoxymethyl)furan **5** (di-ether), 5-methyl furfural **6**, and 5-methyl furfural 2-(isopropoxymethyl) 5-methyl furan **7**. The observed products are similar to those of HMF reactions over Lewis acid zeolites (e.g., Sn-BEA) in alcohol solvents.[151-152] We postulate a reaction network of HMF reaction in 2-propanol solution of MCl_x, consisting of three major pathways (Figure 4.1). In pathway A, HMF etherification with 2-propanol forms **1**, which undergoes hydrolytic ring-opening to **3**. Pathway B proceeds via HMF transfer hydrogenation to **2**, followed by etherification to **4** and **5**. In pathway C, hydrogenolysis of HMF produces **6**, which is further reduced and etherified to **7**. Formation of hydrogenolysis products was also reported with solid Lewis acid Sn-BEA, presumably realized by in-situ H_2 generation and use.[151] Further investigation of the hydrogenolysis pathway is outside the scope of this work.

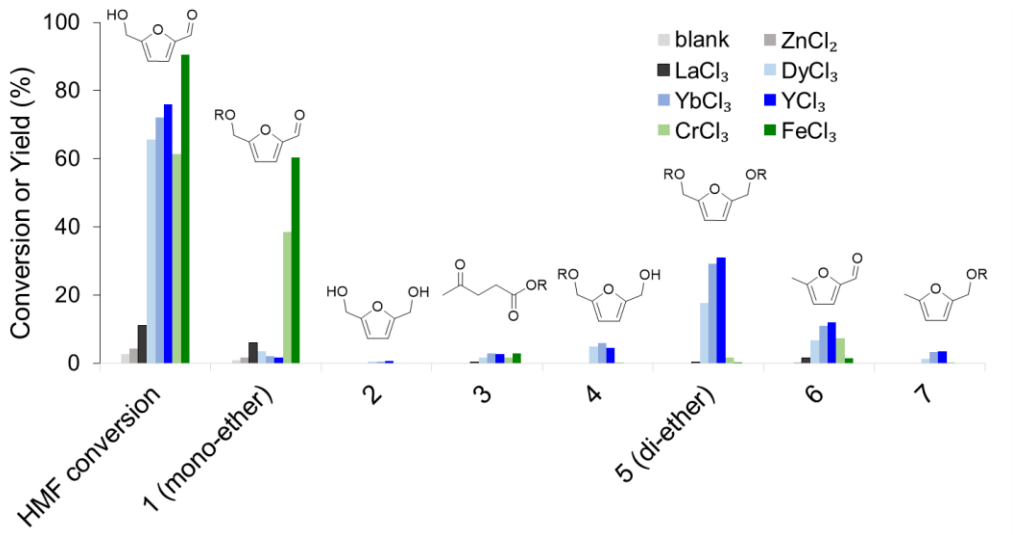

Figure 4.1: HMF conversion and product yields in 2-propanol catalyzed by variety of metal chlorides. Reaction conditions: 1 wt % HMF, 3 mM catalyst, 150 °C, 1 h reaction time. R represents an isopropyl group.

Among the tested catalysts, YCl_3 exhibited the highest activity for reductive etherification with approximately 35% yield to di-ether **5** without reaction-condition optimization. $DyCl_3$ and $YbCl_3$ also produced **5** as the major product at slightly lower yields. The post-reaction solutions turned dark brown due to significant polymerization. Nevertheless, our results demonstrate that some metal chlorides can be potential catalysts for one-pot reductive etherification of HMF to the di-ether. Noticeably, the product distribution significantly depends on the metal. While YCl_3, $YbCl_3$ and $DyCl_3$ favor reaction pathway B to the di-ether as stated, $CrCl_3$ and $FeCl_3$ selectively facilitate the direct etherification pathway A with up to 60% yield of the mono-ether **1**. The differences in activity and selectivity of MCl_3 for each pathway suggest the involvement of multiple catalytically active species and reaction mechanisms.

To untangle this complex reaction system, we used model compounds in order to study each reaction pathway independently: FA for direct etherification (pathway A); and furfural for reductive etherification (pathway B). $CrCl_3$ and YCl_3 were chosen as representative catalysts on account of their demonstrated chemoselectivity.

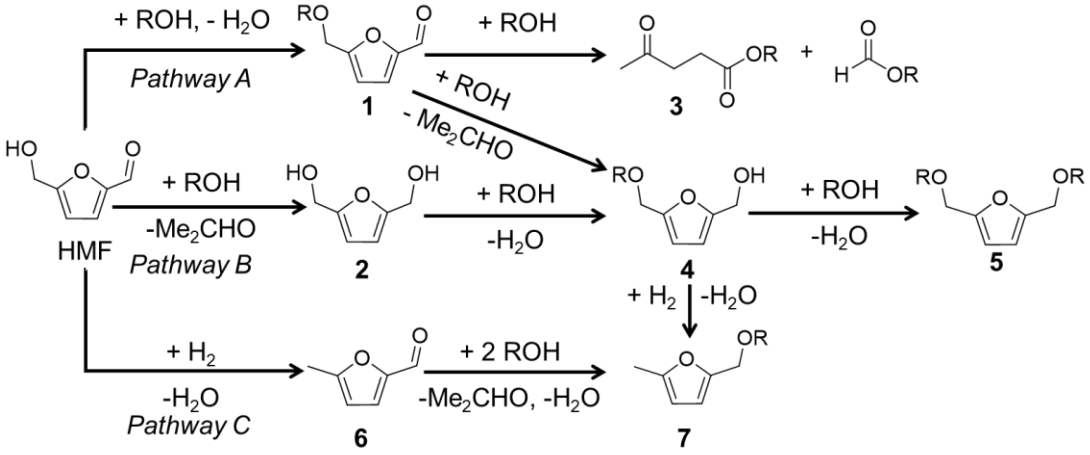

Figure 4.2. Proposed reaction network of HMF reactions by MCl_3 in 2-propanol. OR = $OCH(CH_3)_2$

4.3.2 Furfuryl alcohol (FA) etherification

4.3.2.1 Reaction network

First, we investigate the direct etherification of FA. Mirroring the reactivity trend of HMF reaction (pathway A), $CrCl_3$ is significantly more active than YCl_3, yielding 3.5 times as much ether (Figure C.2). The low pH of the 10 mM MCl_3 solution (1.23 for $CrCl_3$ and 1.91 for YCl_3) indicates that the solutions are acidic, likely due to protons released from MCl_3 alcoholysis.

$$MCl_x + (n+m)(ROH) \leftrightarrow MCl_{(x-n)}(OR)_n.(ROH)_m + nHCl \qquad (4.1)$$

Multiple studies have attributed the activity of metal salts in FA reactions to their induced Brønsted acidity; the FA conversion and product yields qualitatively correlate with the solution pH.[162, 274] However, the pH measurement in alcohol solvent does not provide the true acid concentration because it largely depends on the solvent.[203] Our attempts to experimentally measure the induced HCl concentration by acid-base titration were unsuccessful, possibly due to the base interfering with the MCl_3 speciation. Moreover, measurements at room temperature to quantify the Hammett acidity do not reflect the true induced Brønsted acidity at elevated temperatures. Thus, a quantitative relationship between the reactivity of metal salts and the induced Brønsted acidity has yet to be established. In addition, the catalytic role of the Lewis acidic metal chloride species itself remains elusive.

To deconvolute the Lewis and induced Brønsted acid contributions of MCl_3 solutions, herein we develop a simple reaction kinetic model of FA reaction in 2-propanol starting with the product speciation. Aside from isopropyl furfuryl ether (iPFE), isopropyl levulinate (iPL) was identified as another major product, which is also a value-added chemical, reported to form via FA alcoholyis.[162, 261, 274-277] Traces of 2-chloromethyl furan, α-angelica lactone, and dimerization products of furfuryl alcohol were observed in GC/GCMS analysis. The post reaction solutions turned yellowish, probably due to FA polymerization. A typical time-dependent concentration profile shows that iPFE and iPL initially form in parallel, consistent with published work on FA alcoholysis in ethanol by Maldonado and co-workers.[261] The authors also suggested that the two minor pathways to ethyl levulinate are through ethyl furfuryl ether and 4,5,5-triethoxypentan-2-one (TEP) as intermediates. However,

the corresponding 2-propanol analogue of TEP, 4,5,5-tri-isopropoxy-pentan-2-one (TIPP), was not observed during our reactions. Interestingly, when ethanol or 1-propanol was used as the solvent, at the same reaction conditions, the corresponding trialkoxypentanones were detected as major products (Figure C.3). The absence of TIPP suggests that the compound may not be stable in 2-propanol. As a result, we propose a FA reaction network, whereby iPL could form either directly from FA or via the iPFE intermediate (Figure 4.2, blue arrows).

To assess to role of induced Brønsted acidity, experiments were performed with HCl in the absence of MCl_3. Comparison of the selectivity for iPL and iPFE among $CrCl_3$, YCl_3, and HCl suggests that the FA reactions are not solely Brønsted acid catalyzed. The iPL to iPFE ratios for YCl_3 and $CrCl_3$ were higher than that for HCl, at the same FA conversion, indicating that FA etherification by MCl_3 was slightly more favored (Figure 4.4). Barbera et al. reported formation of furfuryl ether with either ZrO_2 (containing only Lewis acid sites) or sulfated ZrO_2 (containing both Lewis and Brønsted acid sites). Levulinate, on the other hand, was only observed in the presence of Brønsted acids (namely, after sulfation).[278] These important findings have been incorporated into our reaction network, where now FA etherification and side reactions can be facilitated by either the Lewis acid, MCl_3, or the induced Brønsted acid, HCl; while iPL formation pathways are catalyzed by HCl only (Figure 4.3, blue arrows).

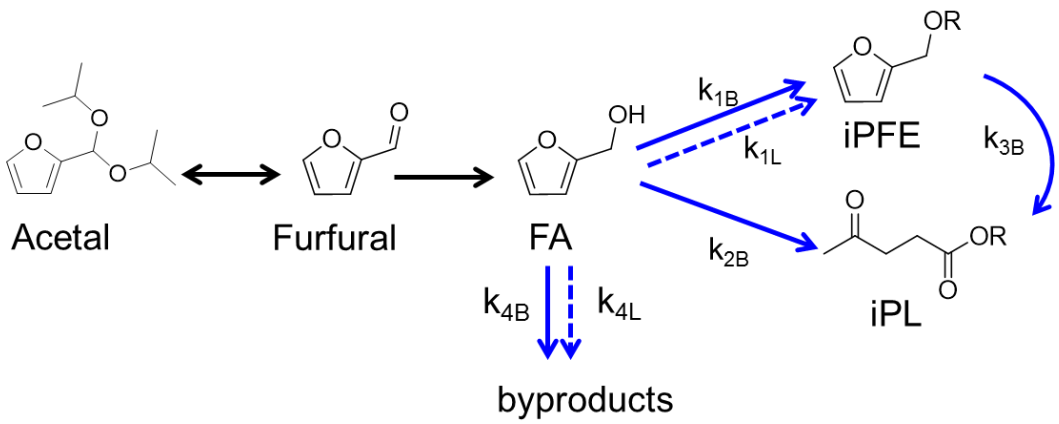

Figure 4.3. Proposed reaction network of furfural reductive etherification in 2-propanol. Furfuryl alcohol reaction network in blue arrows

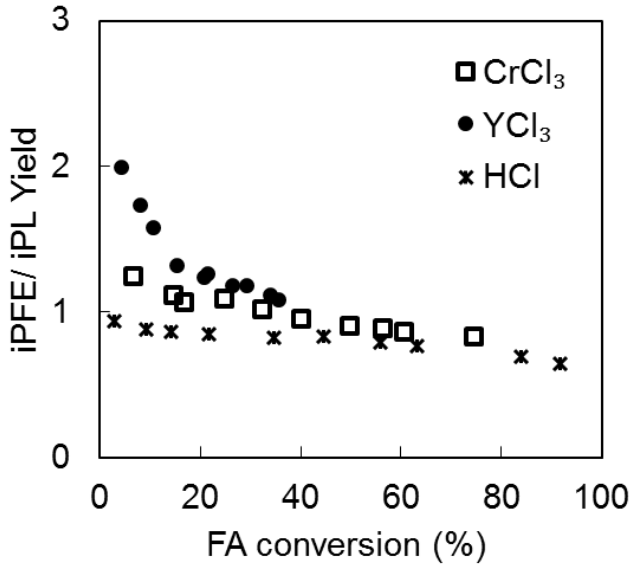

Figure 4.4: Selectivity to isopropyl furfuryl ether (iPFE) over isopropy levulinate (iPL) in $CrCl_3$, YCl_3, and HCl. Reaction conditions: 1 wt % furfuryl alcohol, 90 °C, 10 mM catalyst.

4.3.2.2 Kinetic model

Using the proposed reaction network, we developed a simple kinetic model to assess the intrinsic catalytic activity of MCl_3 solutions. Due to the lack of *in situ*

experimental methods to determine the acidity of MCl_3 solutions, the induced [HCl] was assumed to be a linear function of [MCl_3] within a rather small catalyst-concentration range (5-10 mM). (From the speciation equilibrium, one should expect a quadratic-like relationship between [HCl] and [MCl_3], which can be approximated as linear within a small range.) The assumed linearity is consistent with the linear correlation between [MCl_3] and [HCl] in aqueous solution predicted by the thermodynamic model OLI for various metal salts under similar reaction conditions (Figure C.4); the OLI model has been validated in past work.[267, 279]) The kinetic model assumes a perfectly mixed batch reactor and first-order dependence on the reactant and acid centers, as follows:

$$\frac{dC_{FA}}{dt} = -\left((k_{1B} + k_{2B} + k_{4B})[HCl] + (k_{1L} + k_{4L})[MCl_3]\right)C_{FA}$$

$$\frac{dC_{iPFE}}{dt} = (k_{1B}[HCl] + k_{1L}[MCl_3])C_{FA} - k_{3B}[HCl]C_{iPFE}$$

$$\frac{dC_{iPL}}{dt} = k_{2B}[HCl]C_{FA} + k_{3B}[HCl]C_{iPFE}$$

$$\frac{dC_{byproducts}}{dt} = (k_{4B}[HCl] + k_{4L}[MCl_3])C_{FA}$$

Induced acidity, $[HCl] = a[MCl_3] + b$

where k_{iB} is the rate constant of the i^{th} Brønsted acid catalyzed reaction (solid arrows, black square, Figure 4.3); k_{iL} is the rate constant of the i^{th} Lewis acid catalyzed reaction (dash arrows, black square, Figure 4.3); and *a* and *b* describe the induced [HCl]. The model parameters were regressed to the experimental concentration profiles of FA, iPFE, iPL, and byproducts (determined by carbon balance) using the *lsqnonlin* nonlinear fitting function in Matlab. The regression procedure was similar to that used in our earlier work on the tandem isomerization/dehydration of glucose by $CrCl_3$.[279] Specifically, the model rate constants were fitted in two stages. First, we

fitted the rate constants of the reactions catalyzed by HCl alone (Table 4.1). Then, we fitted the kinetic model for MCl_3, including the parameters *a* and *b* (Table 4.1).

Representative transient profiles of FA and of the products show good agreement between the model and the experimental data (Figure 4.5). Comparison of the rate constants reveals that the Brønsted acid is substantially more effective for FA etherification than the Lewis acid metal species, with k_{1B} being 18-fold and 60-fold higher than k_{1L} for $CrCl_3$ and YCl_3, respectively. A similar trend is observed for the side reactions. The superior reactivity of Brønsted acids for etherification has also been observed for solid acid catalysts. For example, Barbera *et al*. showed significant enhancement of ether formation after ZrO_2 sulfation.[278] Recently, Schwartz and co-workers reported orders of magnitude higher rates for etherification by Brønsted acids (H-zeolites) than Lewis acids (γ-Al_2O_3).[280] Additionally, our model predicts that the concentration of induced HCl in $CrCl_3$ solution is nearly an order of magnitude higher than in YCl_3 solution (Figure C.5). That is rationalized from the fact that Cr(III) is a stronger Lewis acid, making it easier for a solvated alcohol to lose a proton (alcoholyze) and produce a more acidic solution, similar to hydrolysis of the metal aqua cations.[200] Apparent rate constants (k_{1app}) were also determined to quantitate the overall observed reactivity (Figure 4.6). Clearly, *FA etherification by MCl_3 is primarily governed by the induced Brønsted acidity instead of the Lewis acidity*. Even though $CrCl_3$ is a more effective Lewis acid for etherification (higher k_{1L}) than YCl_3, the substantially higher ether formation-rate observed for $CrCl_3$ is mostly attributed to the higher concentration of induced HCl.

Table 4.1: Predicted rate constants of furfuryl alcohol (FA) reactions in Figure 4.3. Reaction conditions: 1 wt% FA, 90 °C, 5-10 mM MCl_3, 5-20 mM HCl.

Brønsted acid catalyzed rate constant k_B ($M^{-1}min^{-1}$)				Lewis acid catalyzed rate constant k_L ($M^{-1}min^{-1}$)				Induced [HCl] = a[MCl_3] + b			
				$CrCl_3$		YCl_3		$CrCl_3$		YCl_3	
k_{1B}	k_{2B}	k_{3B}	k_{4B}	k_{1L}	k_{4L}	k_{1L}	k_{4L}	a	b	a	b
0.34	0.38	0.11	0.07	0.019	3.4e-3	5.6e-3	5.3e-4	0.235	8.1e-4	0.0264	1.7e-4

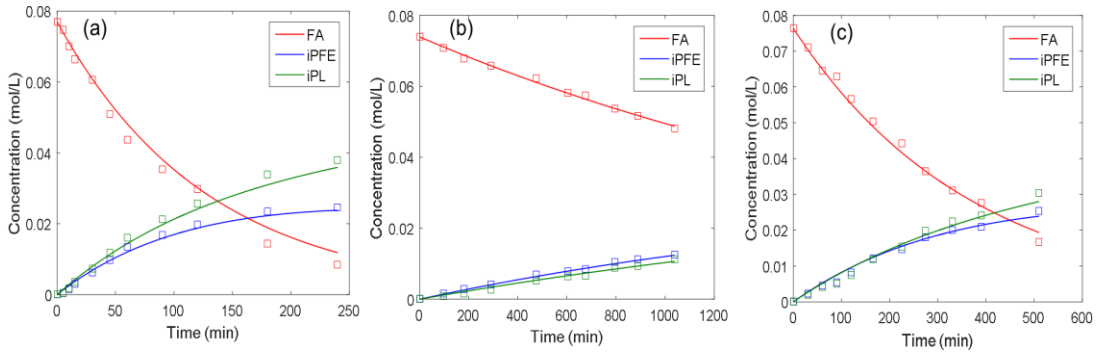

Figure 4.5: Experimental (symbols) and modeling (lines) concentration profiles of furfuryl alcohol (FA), isorpropyl furfuryl ether (iPFE) and isopropyl levulinate (iPL) in HCl (a), YCl_3 (b) and $CrCl_3$ (c). Reaction conditions: 1 wt % FA, 10 mM catalyst, 90 °C.

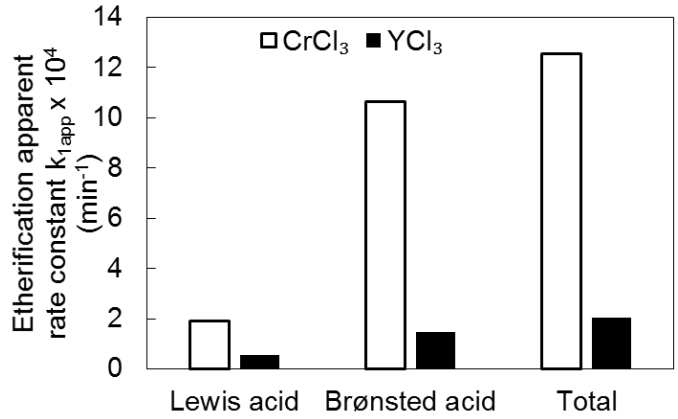

Figure 4.6: Apparent rate constant of furfuryl alcohol etherification $k_{1app} = k_1[catalyst]$ of 10 mM $CrCl_3$ and YCl_3.

4.3.3 Furfural reduction

4.3.3.1 Reaction mechanism

Furfural was employed to study the reduction pathway B, Figure 4.2. Isotopic tracing experiments in deuterated 2-propanol, in combination with GCMS analysis were carried out to investigate the furfural reduction mechanism by YCl_3 (Figure 4.7) and $CrCl_3$ (Figure C.6). When 2-propanol solvent is unlabeled (2-propanol-d0), the GCMS fragmentation of the FA product is the same as the FA standard, with the parent ion m/z = 98. However, in 2-propanol-d8 ($(CD_3)_2CDOD$) solvent, the parent ion of the FA product is m/z = 99. A unit shift in the spectrum of FA produced in 2-propanol-d8 indicates that one of the H atoms in the molecule has been replaced by a D, supportive of an intermolecular hydrogen transfer mechanism from 2-propanol to furfural. To examine the possibility of a dihydride mechanism, which usually occurs when catalysis involves a metal hydride,[281] 2-propanol-OD ($(CH_3)_2CHOD$)) was used as the solvent. The GCMS closely resembles that in 2-propanol-d0, suggesting that there was no H scrambling between O of 2-propanol and α-C of furfural. Consequently, we inferred that both $CrCl_3$ and YCl_3 facilitate furfural reduction via *an intermolecular hydrogen transfer (MPV) from α-C of 2-propanol to α-C of furfural*.

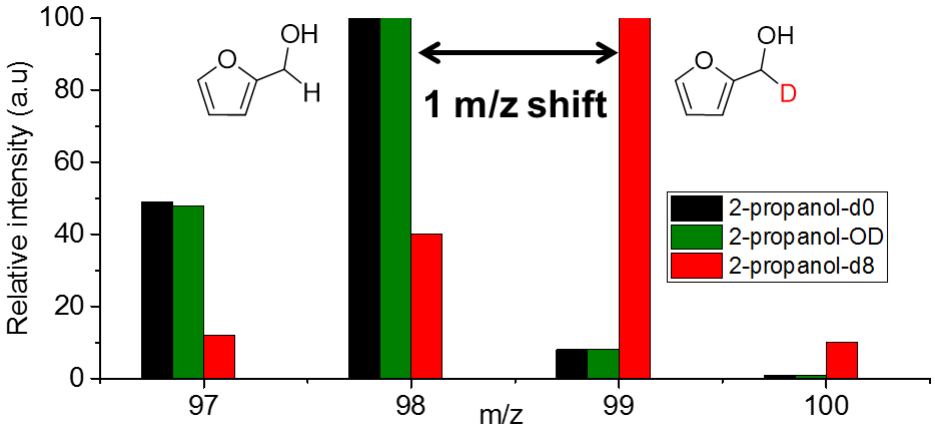

Figure 4.7: GCMS spectra of furfuryl alcohol product. Reaction conditions: 1 wt% furfural, 150 °C, 3 mM YCl_3, in 2-propanol-d0 (t= 30 min), 2-propanol-OD (t= 30 min), and 2-propanol-d8 (t= 1 h).

^{1}H NMR spectra of the post reaction mixtures in YCl_3 further support this conclusion by revealing the location of the replacing D (Figure 4.8). All three spectra in 2-propanol-d0, 2-propanol-OD and 2-propanol-d8 display the four distinguished peaks of FA at around 7.4 ppm (H_a) , 6.32 ppm (H_b), 6.27 ppm (H_c) and 4.54 ppm (H_d), where the first three peaks are assigned to the three H atoms on the furan ring, and the last peak belongs to H at α-C. The integrated peak ratio H_d : H_c is equal to 2 : 1, corresponding to the relative number of H giving rise to the resonances, in standard FA, and FA product in 2-propanol-d0 and 2-propanol-OD. However, in the ^{1}H NMR spectrum in 2-propanol-d8, the H_d: H_c peak ratio is 1:1, indicating that one of the H at the α-C was replaced by D. Primary kinetic isotope effect (k_H/k_D = 2.22) was observed when a 1: 1 by volume mixture of 2-propanol-d0 and 2-propanol-d8 was used as solvent, corresponding to H_d :H_c ratio of 1.31. Attempts to carry out the same ^{1}H NMR study for $CrCl_3$ were unsuccessful due to the paramagnetic nature of Cr, broadening the peaks and causing peak integration difficult. However, a mixture of unlabeled and

labeled FA was observed in the GCMS of FA produced in 1:1 mixture of 2-propanol by $CrCl_3$, resembling that by YCl_3 and suggesting a similar kinetic isotope effect (Figure C.7). Therefore, the intramolecular hydrogen transfer from α-C of 2-propanol to α-C of furfural is likely the rate determining step for furfural reduction by MCl_3.

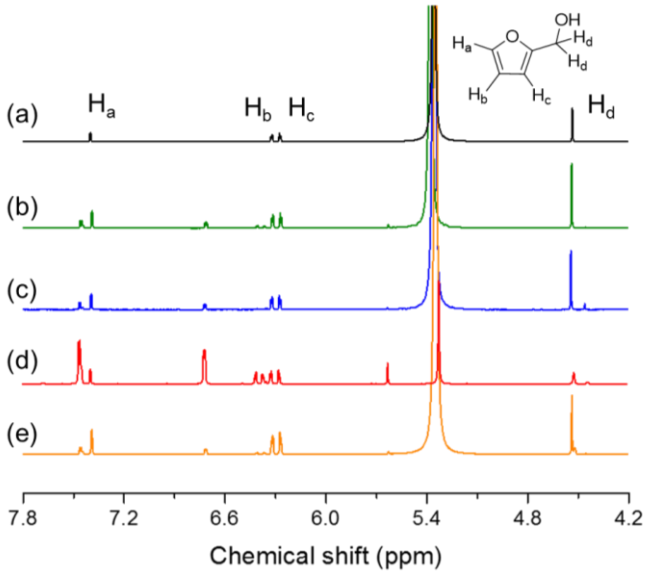

Figure 4.8: ^{1}H NMR spectra of furfuryl alcohol standard (a) and post reaction mixture of furfural reduction by YCl_3 in 2-propanol-d0 (b), 2-propanol-OD (c), 2-propanol-d8 (d) and 1:1 mixture of 2-propanol-d0 and 2-propanol-d8 (e).

4.3.3.2 Determination of catalytically active species

Besides FA, identifiable products in GC/GCMS analysis include iPFE and iPL, as well as trace amounts of the aldol condensation product of furfural and acetone. Noticeably, 2-furaldehyde di-isopropyl acetal was detected instantaneously after furfural and the catalyst solution were mixed, and decreased over the course of the reaction. It suggests that acetalization of furfural and 2-propanol is a fast and reversible reaction, pointing to the overall reaction network in Figure 4.3. Similarly to the observed activity trend for HMF, furfural reduction is considerably more favorable

in YCl_3, with nearly 10-fold higher FA yield than in $CrCl_3$ at the same reaction conditions (Figure C.8). Given the lower Brønsted acidity of YCl_3 solutions compared with $CrCl_3$ solutions, the higher YCl_3 reactivity for furfural reduction indicates that the reaction is catalyzed by Lewis acid metal species.

Alcoholysis of a metal chloride in 2-propanol forms metal isopropoxide cations, which are highly sensitive to moisture and may be hydrolyzed in the presence of water[282-283] in the $MCl_3.6H_2O$ solution. The alcoholyzed/hydrolyzed metal ions may also condense to form metal clusters.[284] The various metal species have been detected in ESI-MS and XAS of MCl_3 solution in 2-propanol (see Figure C.9 and Table C.1 for more details). Consequently, MCl_3 speciation is hypothesized to proceed via the following generalized steps of alcoholysis (Eq.4.1), hydrolysis (Eq.4.2), and oligomerization (Eq.4.3):

$$MCl_{(x-n)}(OR)_n.(ROH)_m + nH_2O \leftrightarrow MCl_{(x-n)}(OH)_n.(ROH)_m + nROH \quad (4.2)$$

$$MCl_{(x-n)}(OH)_n + MCl_{(x-m)}(OH)_m \rightarrow M_2Cl_{(2x-n-m)}(OH)_{(n+m-2)}O + H_2O \quad (4.3)$$

The various metal complexes possess different catalytic properties toward the reduction of furfural. Our previous studies on glucose isomerization by MCl_3 in aqueous solutions revealed $M(OH)^{2+}$ as the active species.[267-268]Adding excess HCl suppresses the hydrolyzed species, resulting in a drop of reactivity.[267] In a similar vein, here we investigated how adding HCl to MCl_3 solutions would influence activity toward furfural reduction. In the case of YCl_3, the furfural conversion and product yields drop monotonically with increasing [HCl] (Figure 4.9a). Interestingly, the $CrCl_3$ activity exhibits a maximum at increasing HCl concentration before dropping (Figure 4.9b). HCl partly prevents alcoholysis/hydrolysis of MCl_3 (R1 and R2), i.e.,

the formation of partially hydrolyzed metal cations. Because $CrCl_3$ is much more likely to be alcoholyzed/hydrolyzed than YCl_3, it is possible that hydrolyzed metal cations oligomerize (R3) due to their higher concentrations, thereby, reaching a maximum at an optimum [HCl]. Thus, we infer that the catalytically active species for furfural reduction are partially hydrolyzed metal cations. Computational studies of the mechanism of glucose isomerization by $CrCl_3$ have shown that the basic hydroxyl ligand on the metal center is essential, as it accepts a proton from the hydroxyl group at C2 carbon of glucose, which activates the intramolecular C2-C1 hydride shift at the Lewis acid metal center.[271] An analogous synergy might be drawn here for transfer hydrogenation of furfural. Overall, $CrCl_3$ and YCl_3 were shown to facilitate furfural reduction via the same intermolecular hydrogen transfer mechanism and have similar active species.

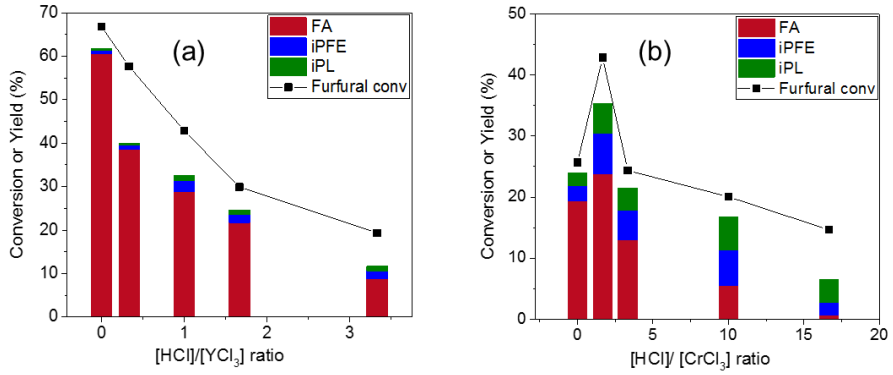

Figure 4.9: Effect of HCl addition on furfural conversion and product yields by YCl_3 (a) and $CrCl_3$ (b). Reaction conditions: 1 wt % furfural, 150 °C, 3 mM MCl_3, t= 30 min (YCl_3), t= 180 min ($CrCl_3$).

Experiments with varying temperature were conducted to determine the activation energy for furfural reduction by MCl_3. The rate constants were calculated

using the initial-rate approach, specifically from the initial linear part of the time-dependent profile of the total amount of product formation (FA, iPFE, iPL). A lower apparent activation energy was found for $CrCl_3$ than for YCl_3 (25.6 vs. 30 kcal/mol) despite its lower rate (see Arrhenius plots in Figure C.10). It should be noted that since the active species forms in-situ through metal salt alcoholysis/hydrolysis, its concentration is dependent on temperature. The higher apparent activation energy of YCl_3 could potentially be due to more hydrolyzed metal cations formation at higher temperatures. The intrinsic reactivity of $CrCl_3$ and YCl_3 should only be compared at the same active species concentration, which is currently challenging to determine at reaction temperatures.

4.4 Conclusions

We have evaluated the catalytic activity of various metal chlorides for the tandem reductive etherification of HMF in 2-propanol. Two main parallel reaction pathways were identified: direct etherification to mono-ether, favored by $CrCl_3$ and $FeCl_3$ (pathway A), and reductive etherification to di-ether, preferred by YCl_3, $YbCl_3$ and $DyCl_3$ (pathway B). To isolate each pathway, we employed model compounds: FA for pathway A and furfural for pathway B, with $CrCl_3$ and YCl_3 as representative catalysts. Through modeling of kinetic experiments, we quantified for the first time contributions from the Lewis acid metal species and from the induced Brønsted acidity, HCl, for FA etherification. The turnover frequency for etherification of FA by HCl is an order of magnitude higher than that by MCl_3, suggesting that the etherification activity over metal chlorides is governed by the induced Brønsted acidity. $CrCl_3$ favors etherification over YCl_3 owing to its higher ability to alcoholyze

and produce protons. On the other hand, furfural reduction (hydrogenation) is facilitated by Lewis acidic species. We carried out isotopic labeling experiments to investigate the mechanism of furfural reduction. GCMS and ^{1}H NMR analysis revealed that intermolecular hydrogen transfer from the α-C of 2-propanol to the α-C of furfural is the rate-determining step. Based on the correlation between the effect of HCl addition on the speciation of metal salts and on the MCl_3 activity for furfural reduction, we hypothesized that the catalytic active species for the transfer hydrogenation is a partially hydrolyzed metal cation, similar to the active species in glucose isomerization by MCl_3 in aqueous solution. The mechanistic understanding and methodology introduced in this work could provide insights into Lewis and Brønsted acid catalysis in organic media for other reactions.

Chapter 5

SYNERGY OF ACID-BASE SITES OF SUPPORTED ZIRCONIA FOR REDUCTIVE ETHERIFICATION OF BIOMASS-DERIVED FURAN DERIVATIVES

5.1 Introduction

It was shown in the previous chapter that metal chlorides possess multi-functional acid-base properties and can be effective for reductive etherification of 5-hydroxymethyl furfural (HMF) to 2,5-bis (alkoxymethyl) furan (BAMF). Specifically, the desirable catalyst needs a Lewis acid metal site with an adjacent hydroxyl group to facilitate transfer hydrogenation of HMF to 2,5-bis (hydroxymethyl) furan (BHMF), and either a Brønsted or a Lewis acid site to catalyze the subsequent etherification step to BAMF. The activity of homogeneous metal salts is difficult to control since the active species depend on the reaction conditions. Moreover, their catalyst separation and regeneration are challenging. Therefore, a solid catalyst with the desired acid-base properties could be superior. The metal substituted (Sn, Zr, Hf-) BEA zeolites have been shown to be very effective catalysts to HMF reductive etherification in alcohol solvent, yielding up to 80 % BAMF in either batch or continuous flow mode[151-152]. However, their currently complex and lengthy synthesis procedures prevent the process from scale-up. Luo *et al*. also observed BAMF production by some metal oxides (ZrO_2, TiO_2, and Al_2O_3) supported on SBA-15 although there was uncertainty in the reported product yield due to lack of calibration[158]. Among the metal oxides,

zirconia exhibited the highest BAMF selectivity. However when investigating ZrO_2/SBA-15 for HMF reaction in ethanol, Lanzafame *et al.* only detected the direct etherification product, 5-ethoxymethyl furfural[159]. The discrepancy between reported product selectivity over zirconia raises the question of the nature of the active sites. Herein, we assess quantitatively the activity and stability of ZrO_2 on a high surface area amorphous silica support for the reductive etherification of HMF in 2-propanol. In addition, the roles of the acid-base sites on the catalyst surface for etherification and transfer hydrogenation are elucidated by employing extensive catalyst characterization and by developing a structure-property relationship.

5.2 Experimental Methods

5.2.1 Catalyst synthesis and characterization

The ZrO_2 supported on SiO_2 catalysts (ZrO_2/SiO_2) were prepared by incipient wetness impregnation using zirconyl nitrate aqueous solution (Sigma Aldrich) and high surface area silica support (Alfa Aesar). The samples were air-dried overnight at room temperature, at 100 °C for 5 hours, and then calcined at 550 °C for 6 hours.

The specific surface area and pore volumes of the catalysts were measured by N_2 physisorption at 77 K using a Micromeritics ASAP 2020 instrument. Prior to the measurements, all the catalysts were degassed at 300 °C for 5 hours. The X-ray diffraction (XRD) spectra were recorded using a Bruker D8 diffractometer with a monochromatic Cu Kα radiation ($\lambda = 0.154$ nm) at 40 kV and 40 mA, operating in 2θ range of 5-80° at a scanning rate of 0.02°/s. Elemental analysis of the bulk materials was conducted with a high-power benchtop wavelength dispersive X-ray fluorescence

XRF (Rigaku). The X-ray photoelectron spectra (XPS) were obtained with a Thermo-Fisher K-alpha spectrometer, equipped with a monochromatic Al-Kα X ray source. Pyridine adsorption Fourier transform infrared (FTIR) spectra were recorded on an Agilent Cary 60 FTIR spectrometer, equipped with an MCT detector (128 scans at a spectral resolution of 2 cm^{-1}) in transmission mode. A catalyst sample was pressed into a self-standing disc, loaded in a custom made IR cell and degassed under vacuum (0.01 mTorr) at 450 °C for 1 hour prior to being cooled down to 50 °C. 100 mTorr of pyridine was introduced to the sample via a vacuum manifold and the sample was heated to 450 °C at a ramping rate of 2.5 °C/min. IR spectra were collected every 50 °C during the heating process. Temperature-programmed desorption (TPD) of CO_2 was carried out in a downward flow reactor connected with a quadrupole mass spectrometer (Pfeiffer Vacuum QMS 200). Catalyst pretreatment was conducted at 300 °C under inert He flow for 2 hours prior to introducing CO_2 (50 mL/min) at 25 °C for 30 minutes. The samples were purged with He for 1 hour to remove physiosorbed CO_2 before heated to 800 °C at the rate of 10 °C/min. Thermogravimetric analysis (TGA) was carried out in a TA instrument (Q600 HT) using 50 mL/min of air as the flowing gas on a [25-1200 °C] temperature range with a ramping rate of 10 K/min.

5.2.2 Catalytic reactions

The catalytic experiments were performed in a 100 mL Parr reactor under 20 bar of N_2 pressure, on a magnetic stir plate, heated by a custom-made band heater connected to a home-built PID temperature controller. In addition to the inlet/outlet gas port and pressure gauge, the Parr reactor was also equipped with a dip tube and a liquid sampling loop that was submerged in an ice bath to cool down the reaction

solution. The reactor vessel consisted of 0.1 M of reagent (HMF, furfural or furfuryl alcohol) in 70 mL of 2-propanol and 0.2 g of catalyst and was heated to the desired reaction temperature. The solution was sampled periodically. The post reaction solutions were filtered and analyzed with a gas chromatogram-mass spectrometer (GC-MS, Shimadzu QP 2010 Plus), using a HP-INNOWAX column (Agilent) for product identification. Product quantification was determined using a GC (Agilent 7890 A), equipped with a HP-INNOWAX column, a flame ionization detector (FID) and a quantitative carbon detector (Polyarc^{TM}). The Polyarc^{TM} consists of a micro-reactor to convert organic compounds to methane and gives a universal response in the FID to alleviate cumbersome calibrations. The quantification method has been laid out and verified in previous work.[285]

Catalyst stability test was conducted in a continuous up flow configuration in a ¼ inch tubular stainless steel reactor (Swagelok), and heated up to desired temperature using an oil bath. The catalyst bed consisted of 0.1 g catalyst loaded between glass wool plugs and 10 μM stainless steel filters (Swagelok) on either side. 0.1 M of HMF in 2-propanol in feed stream was introduced to the reactor by an HPLC pump (Alltech, 301 model) at 0.1 mL/min flow rate. The system was pressurized with nitrogen gas to 20 bar using an ultra-low flow precision back-pressure regulator (Equilibar, EB1ULF1). The effluent was sampled periodically and analyzed with the abovementioned GC and GCMS.

5.3 Results and Discussion

5.3.1 Catalytic performance assessment

The catalytic performance of the synthesized 7.5 wt % of ZrO_2 on support SiO_2 for HMF reductive etherification was compared with that of the commercial ZrO_2 at similar reaction conditions (Figure 5.1). Besides the di-ether as the major product (57% yield), GC detected products arising from hydrogenation, etherification and hydrogenolysis, similar to those previously observed in the reaction of HMF in 2-propanol by metal chlorides[285], including BHMF **1**, 5-(isopropoxymethyl)furfural **2**, 5-isopropoxymethylfurfuryl alcohol (PMFA) **3,** di-ether **5**, 5-methyl furfural **6**, and 5-methyl furfural 2-(isopropoxymethyl) 5-methyl furan **7** (see proposed reaction network in in Figure D.1). Isopropyl levulinate **4**, the ring-opening product of mono-ether, which forms in the presence of a Brønsted acid, was not detected. On the contrary, 5-hydroxylmethyl furfural diethyl acetal formed as the primary product over commercial ZrO_2 from the acetalization of HMF and 2-propanol; only traces of BHMF and no di-ether formed (see proposed reaction network in Figure D.2). The difference in product selectivity of the synthesized ZrO_2/SiO_2 and bulk ZrO_2 showed not only the superior activity of the supported catalyst toward reductive etherification but also the difference in their active sites.

Figure 5.1. Comparison of product distribution of HMF reaction in 2-propanol between YCl_3 (data from previous work[285]) (gray), commercial ZrO_2 (black), and the synthesized 7.5 wt% ZrO_2/SiO_2 (orange). Reaction conditions: 1 wt% HMF, HMF: metal molar ratio = 100:3 (100:10 in case of commercial ZrO_2, 150 °C, t= 3 h (1 h for YCl_3), 20 bar N_2.

The stability of the ZrO_2/SiO_2 was investigated in continuous flow mode (Figure 5.2) over 24 h of time of stream; the catalysts exhibited moderate deactivation. Specifically, the HMF conversion dropped from 90 to 60% while the di-ether yield decreased from 30 to 15%. TGA analysis of the spent catalyst showed 5% weight loss over the temperature range of 150-500 °C (Figure D.3). At the same time, the specific surface area of the spent catalyst was reduced by 10%, probably due to plugging by heavy byproducts. Interestingly, the increased BHMF-production over the course of reaction, at the expense of ethers, indicates that catalyst deactivation affects the etherification more than the hydrogenation. Similar observation was reported for the reductive etherification of HMF over Sn-BEA zeolite[152]. Other hydrogenolysis products were only observed in traces.

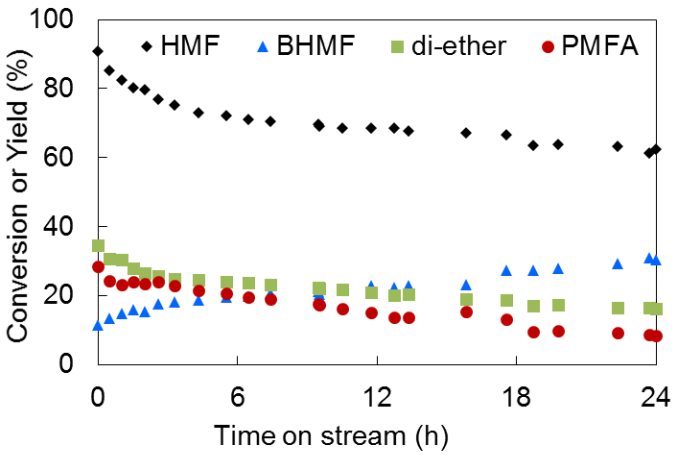

Figure 5.2. Concentration profile of HMF and major products in a continuous flow reactor containing 7.5 wt % ZrO_2/SiO_2. Reaction conditions: 1 wt % HMF in 2-propanol feed stream, 0.1 mL/min flow rate, 0.2 g catalyst, 150 °C, 20 bar.

5.3.2 Catalyst structure-activity relationship

Acid-base characteristics of the catalysts have been shown to play a crucial role on reductive etherification of HMF by homogeneous metal salts, zeolites and other metal oxides. Specifically, Lewis *et al*. proposed that Lewis acid metal site and hydroxyl group at the open sites of Sn-BEA is active for transfer hydrogenation and the silanol group is the responsible Brønsted acid for etherification[152]. Our previous work on metal chlorides similarly proposed that a Lewis acid-Brønsted base pair facilitates hydrogenation and either Lewis acid metal ions or the induced Brønsted acid can carry out etherification, with the latter being the primary active site[285]. Luo *et al*. investigated various metal oxides supported on silica and suggested at their Lewis acid and Brønsted acid sites are responsible for catalytic transfer hydrogenation and etherification, respectively[158]. To correlate the acid-base properties of the ZrO_2/SiO_2 to their observed reactivity for HMF reductive etherification, we first characterized the

catalyst acidity and basicity. The FTIR spectrum of pyridine adsorption on the catalyst at 50 °C revealed the type of acid sites and their density based on the adsorption band wavenumbers and intensity (Figure 5.3). The band at 1597 cm^{-1} disappeared after evacuation at 150 °C and is assigned to pyridine adsorbed on silica. The broad band at 1547 cm^{-1}, whose intensity was reduced at higher desorption temperature and vanished at 200 °C, corresponds to pyridine adsorption on Brønsted acid sites and is the signature of weak and low Brønsted acidity of the supported zirconia. The strong adsorption peak at 1445 cm^{-1}, characteristic for pyridine adsorption on Lewis acid sites, is still present at desorption temperature of 350 °C, suggesting a strong Lewis acidity. The differences in the binding energies of Zr $3d_{5/2}$, Si 2p and O 1s in the XPS spectra of the ZrO_2/SiO_2 from those of the silica support and pure zirconia samples reveal that the metal oxide-support interaction is responsible for the acid sites (Table D.1). For the synthesized ZrO_2/SiO_2 samples, the binding energies of O 1s and Zr $3d_{5/2}$ shift to lower and higher values compared to pure zirconia respectively, suggesting a higher electron density on O atoms and a higher positive charge on Zr, corresponding to the generation of Lewis acid sites. Compared to the pure silica support, the slightly lower binding energies of Si 2p and O 1s in ZrO_2/SiO_2 correlate to the formation of Brønsted acid sites. For basicity, CO_2 TPD on ZrO_2/SiO_2 was employed and the spectrum displayed the most significant CO_2 peak at low desorption temperature of 110 °C (Figure 5.4). The same desorption peak with much lower intensity was observed for the silica support and was assigned to bicarbonate adsorption mode on weak basic sites[93, 266, 286]. As a result, it is proposed that the ZrO_2/SiO_2 catalyst possesses a higher density of mostly weak basic sites than the support. The observed

creation of Lewis acid and Brønsted acid sites as well as the decrease in basicity of supported zirconia compared to bulk zirconia are in agreement with literature[287-289].

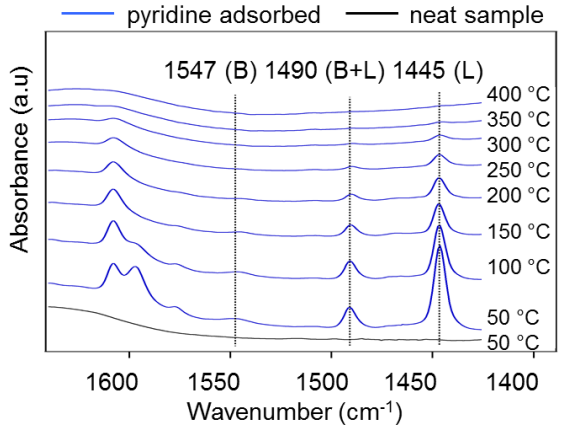

Figure 5.3. FTIR spectra on 7.5 wt% ZrO_2/SiO_2 before (black) and after pyridine adsorption (blue) and evacuated at different temperatures. (B): Brønsted acid peak, (L): Lewis acid peak.

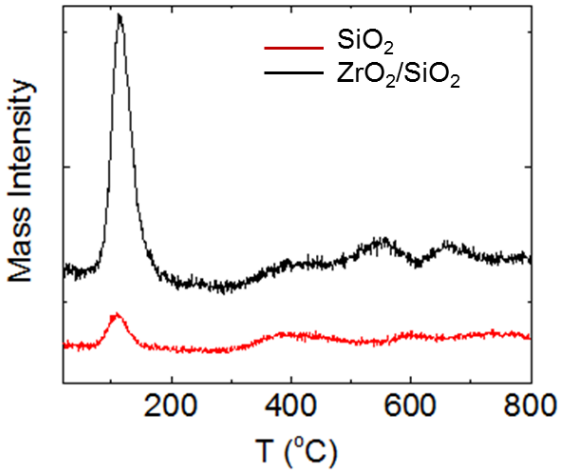

Figure 5.4. TPD of CO_2 on pure silica (red) and 7.5 wt% ZrO_2/SiO_2 samples.

In order to investigate the catalytic role of the characterized acid and basic sites of ZrO_2/SiO_2, we aim at adding different probe molecules that adsorb strongly on a specific site and study their effects on the rates of hydrogenation and etherification. To simplify complex analysis due to the multi-functionality of HMF, which contains both

hydroxyl and carbonyl groups, model compounds of a single functional group were employed, i.e., furfural for hydrogenation and furfuryl alcohol for etherification. The apparent rate constant was determined by the initial rate of reaction normalized by the initial concentration of reactant. When titrated with excess amount of pyridine or propionic acid, the rate of furfural hydrogenation to furfuryl alcohol reduced significantly by 3 and 14 times, respectively (Figure 5.5a). Similar rate-suppression was also observed when pyridine was added to the reaction starting with furfuryl alcohol. However, adding 2,6-di tertbutylpyridine (DTBD) did not alter the etherification rate (Figure 5.5b). While pyridine competitively absorbs on both Lewis and Brønsted acid sites, the steric hindrance of DTBD allows it to access Brønsted acid sites only[83]. Propionic acid has been shown to poison basic sites in metal oxides[290]. Therefore, the inhibitive effect by pyridine or propionic acid on hydrogenation suggests the synergy between the Lewis acid and basic sites on hydrogenation activity of the ZrO_2/SiO_2. For furfuryl alcohol, only pyridine addition slowed down the etherification to isopropyl furfuryl ether, indicating that the Lewis acid is primarily responsible for catalysis. Even though Brønsted acidity has been reported as active for etherification, the Brønsted acidity in the synthesized ZrO_2/SiO_2 is probably too weak and low to effectively carry out furfuryl alcohol etherification. It should be noted that surplus amount of titrants did not completely shut down the reactions, in contrast to what is usually observed in gas-phase reactions. This is probably because pyridine and propionic acid do not saturate all acid/basic sites, suggesting a solvation effect on the adsorption of the probe molecules to the catalyst in liquid phase. In fact, when measuring pyridine adsorption on zeolites in ethanol,

Gould *et al.* observed lower values than those in gas phase and attributed this to thermodynamics with competing solvation as a possible cause[291].

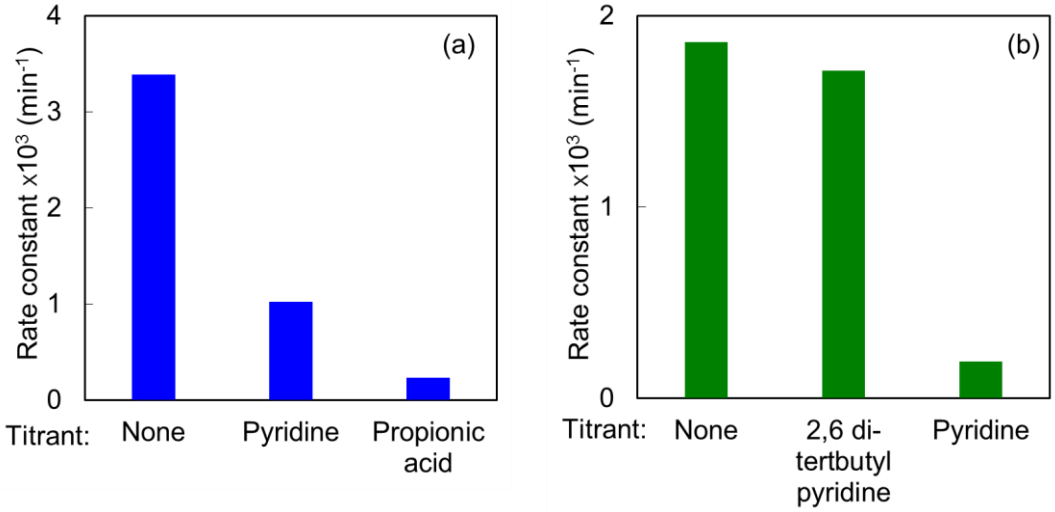

Figure 5.5. Effect of various titrants on the rate of furfural hydrogenation (a) and furfuryl alcohol etherification (b). Reaction conditions: 1 wt % furfural (or furfuryl alcohol), 7.5 wt % ZrO_2/SiO_2, reactant: metal molar ratio = 100:3, reactant: titrant molar ratio = 1:1, 110 °C for furfural (or 150 °C for furfuryl alcohol), 20 bar N_2.

5.3.3 Effect of zirconia loading

Silica supported catalysts with varied zirconia loading from 2 to 15 wt% were synthesized and tested for reductive etherification activity in order to determine the optimal ZrO_2 content. The bulk zirconia content was verified with XRF. We employed furfural hydrogenation and furfuryl alcohol etherification as representative reactions. Both the hydrogenation and etherification rate constants initially increased with increasing loading and then dropped at ZrO_2 loadings higher than 7.5 wt% (Figure 5.6). XRD spectra the ZrO_2/SiO_2 catalysts and pure silica support shared a broad peak at 23°, which was attributed to amorphous silica. For loadings of ZrO_2 of 7.5 wt% and higher, the crystallinity patterns display another broad band at 31° with increasing

intensity at higher ZrO_2 content. The additional diffraction peak is likely to be amorphous zirconia clusters (Figure D.4). At the same time, the specific BET surface area is reduced with increasing metal loading probably due to metal clusters forming that block the pores (Figure D.5). The surface zirconia content, determined by the relative intensity of Zr $3d_{5/2}$ photoelectrons in XPS measurement, deviated from the experimentally measured bulk zirconia content determined by XRF above 7.5 wt% ZrO_2 (Figure 5.7). If zirconia is atomically dispersed on the silica support, the surface and bulk zirconia content should have been the same. The deviation from the theoretical line for surface zirconia reveals that up to 5 wt%, ZrO_2 forms a monolayer on the silica support and at higher loadings, clusters form and plug the pores, in agreement with the XRD and BET data. Particles reduced the accessible surface area, leading to lower reaction rates at higher ZrO_2 loadings. Therefore, despite being effective, the current synthesis procedure does not seem to be optimal. Future work should consider experimenting with several synthesis variables such as precursor, type of support and impregnation method to maximize dispersion.

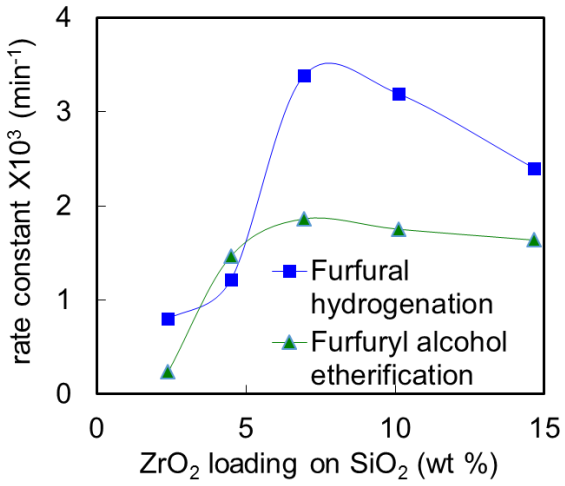

Figure 5.6. Effect of zirconia loading of ZrO_2/SiO_2 on the rate constant of furfural hydrogenation (■) and fufuryl alcohol etherification (▲).

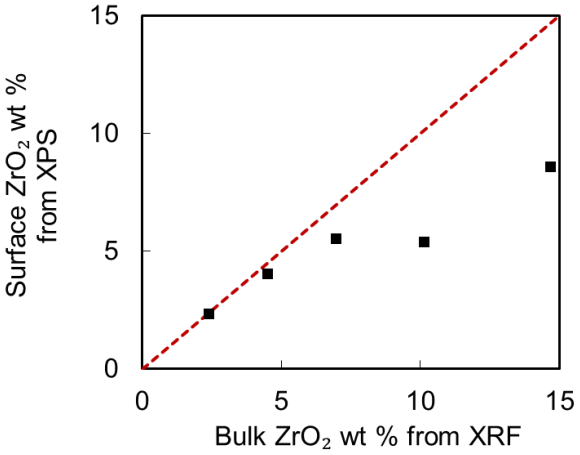

Figure 5.7. Comparison of the theoretical (---) and XPS-measured (■) ZrO_2 content on the surface and in the bulk of ZrO_2/SiO_2 vs. zirconia loading.

5.4 Conclusions

Zirconia-coated silica catalysts were synthesized using incipient wetness impregnation and exhibited high activity for reductive etherification of HMF giving up to 57% di-ether yield while possessing relatively good stability in a continuous flow

reaction. Kinetic studies and characterization showed that the superior catalytic performance of ZrO_2/SiO_2 is due to the synergy of its surface acid-base sites. Specifically, the interaction between the silica support and the zirconia creates Lewis acid and Brønsted acid sites compared to pure zirconia. The Lewis acid sites catalyze etherification and cooperate with the surface weak basic sites to facilitate transfer hydrogenation. Weak Brønsted acid sites were observed on the supported zirconia but do not appear catalytically responsible for etherification. Increasing the loading of zirconia coating lowers the metal oxide dispersion above a threshold that in turn reduces reactivity. Strategic tuning of the synthesis parameters may help optimizing the overall catalytic performance.

Chapter 6

PRODUCTION OF RENEWABLE OLEO-FURAN SURFACTANTS BY CROSS-KETONIZATION OF BIOMASS-DERIVED FURAN DERIVATIVES AND FATTY ACIDS

6.1 Introduction

The recent research focus on biomass conversion has significantly advanced the science and technology on valorizing the most naturally abundant renewable source of carbon to bio-chemicals. The oxygen content of biomass-derived building blocks can be leveraged to upgrade non-edible lignocellulose to valuable chemicals, such as plastics, rubber, lubricants, and detergents[63, 65, 292-296]. Specifically, the high functionality of furan derivatives has enabled innovative chemical routes to realize an economically viable bio-refinery. Promising paths include, but are not limited to, the synthesis of para-xylene from cycloaddition of dimethyl furan[65], butadiene via "dehydra-decyclization" of tetrahydrofuran[294], C_{33-45} hydrocarbon lubricants via a multi-step reaction of furfural[297]. Among the recent applications, synthesis of oleo-furan sulfonates (OFSs), which have been shown to possess excellent detergency, emerged as a potentially commercializable process[63]. OFS' structures includes a furan moiety as linker connecting a hydrophobic hydrocarbon chain with a sulfonate at the α carbon positions. Their surfactant properties were evaluated by critical micelle concentration (CMC), defined as the minimum surfactant concentration for micelle

formation, Kraft point (T_{Kraft}), below which surfactants form solid crystals, and their stability in hard water conditions. OFSs with linear alkyl chain exhibit lower CMC and T_{Kraft} than those of the petroleum-derived alkylbenzene sulfonate (LAS) analogues, indicating their enhanced surfactant performance. The furan moiety is hypothesized to improve surfactant solubility compared to benzene. Moreover, the OFS compounds could function in hard water conditions, i.e., in the presence of Ca^{2+}, much better than the LASs. Overall, OFS' production offers the advantage of (1) utilization of the cheap renewable woody feedstock, (2) enhanced detergency in cold water applications, and (3) improved stability in hard water, eliminating the need for the costly chelating agents compared to the conventional LAS. Preparation of OFSs proceeds by Friedel Crafts acylation of furan with a long chain C_8-C_{18} carboxylic (fatty) acid or fatty acid anhydride from vegetable oil as the initial step to form 2-alkoylfuran as the surfactant precursor, an optional hydrodeoxygenation step, followed by sulfonation. Among these steps, the C-C coupling reaction to form 2-alkoylfuran is considered as the bottleneck in the current routes. In the first route, furan is coupled with a fatty acid anhydride (e.g., lauric acid C_{12} anhydride) over a hierarchical porous Brønsted acid zeolite Al-SPP to yield up to 90% of the acylated furan (Figure 6.1, pathway A). Though selective, this pathway produces an equimolar amount of by-product lauric acid, which has a higher boiling point (~ 298 °C), rendering difficult the separation and recycle. The second route utilizes homogeneous trifuoroacetic anhydride to convert lauric acid feed to lauric anhydride, which then acylates furan in one pot Figure 6.1, pathway B). Similar to pathway A, this pathway generates a waste stream of corrosive trifluoroacetic acid.

Due to the disadvantages of the current methods, herein, we propose for the first time a new synthesis 2-alkoyl furan via cross ketonization of 2-furoic acid and lauric acid using heterogeneous catalysts (Figure 6.1, pathway C). The cross-ketonization strategy offers ease of separation and recyclability of solid catalysts and produces only water and carbon dioxide as byproducts, hence increases the operation efficiency.

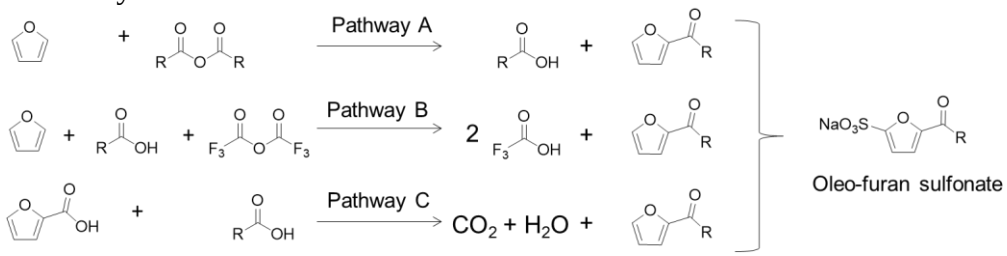

Figure 6.1. Various proposed pathways to produce oleo-furan sulfonate as bio-surfactant. R represents the n-$C_{11}H_{23}$ chain. Path C is the one developed herein.

Ketonization is an established C-C coupling reaction to prepare symmetrical dialkyl ketone or cyclic ketone from aliphatic acids. Common examples include ketonization of acetic acid to acetone[166, 298], and cyclization of adipic acid to cyclopentanone[298]. When two different carboxylic acids are used as the starting materials, a product mixture of self- and cross-ketonization can occur, reducing the selectivity to the desired cross-ketonization ketones[299]. Extensive research on the mechanism of surface catalyzed ketonization shows that the presence of α-hydrogen (α-H) in at least one of the carboxylic acid molecules is critical for the surface reaction to take place[168, 300]. The reaction rate monotonically increases with the number of α-H atoms in the absence of steric hindrance. For instance, the self-ketonization of propionic acid (with 2 α-H) occurs 10 times as fast as that of 2-methylpropanic acid (with 1 α-H)[299]. Accordingly, one may expect a much faster reaction rate for self-

ketonization of lauric acid (with 2-α-H) compared to that of cross-ketonization of lauric acid with 2-furoic acid (with no α-H), which makes the selective production of the desired cross-ketone product, 2-dodecanoyl furan, problematic. In addition, while most of the research on ketonization focuses on small molecules in the gas phase, the high boiling point of lauric acid requires reaction in the liquid phase. Therefore, the proposed cross-ketonization chemistry entails the following technical challenges of (1) kinetic limitation to high carbon yield via cross-ketonization, (2) lack of mechanistic insights, and (3) limited literature. In this report, we demonstrate for the first time the selective production of 2-dodecanoyl furan as a bio-surfactant precursor from biomass-derived 2-furoic acid and vegetable oil-derived lauric acid using Earth-abundant metal oxides. The reaction mechanism and catalytic active sites are elucidated to guide further research on catalyst design.

6.2 Experimental Methods

6.2.1 Materials

2-furoic acid and dodecanoic (lauric) acid are purchased from Sigma Aldrich. Solvent n-dodecane and dimethyl sulfoxide (DMSO) were acquired from Fisher Scientifics and used as are. Various metal oxides, including iron (II) oxide (FeO), iron (III) oxide (Fe_2O_3), and iron (II, III) oxide (Fe_3O_4), titanium oxide (TiO_2), zirconium oxide (ZrO_2), gamma aluminum oxide (γ-Al_2O_3), and cerium oxide (CeO_2) were obtained from Sigma Aldrich and used without further modification.

6.2.2 Catalytic reaction and analysis

A typical catalytic reaction was carried out in a 100 mL Parr reactor vessel, with a glass liner, containing 30 mL of n-dodecane solvent, 2-furoic acid and lauric acid as reactants, 0.2 gram metal oxide catalyst, under 20 bar N_2 pressure, with lauric acid as the limiting reagent. N-dodecane was chosen as the solvent due to its inertness, low vapor pressure and ability to solubilize lauric acid and the desired product. The reactor was heated up to desired temperature in a fitted band heater, using a house made PID controller, on a magnetic stir bar. After a designated time, the reactor was quenched in an ice bath and samples were filtered for analysis. Due to its low solubility in n-dodecane at room temperature, 2-furoic acid was extracted from the post-reaction solution by DMSO for further quantification. In recyclability experiments, the spent catalysts were collected, washed with cyclohexane and air-dried at room temperature overnight before used for the next catalytic experiment. Products were identified and quantified with a gas chromatogram-mass spectrometer (GC-MS) system (Agilent 7890B) and with a gas chromatogram-flame ionization detector (GC-FID) instrument, respectively. Both the GC-MS and GC-FID were equipped with a HP-1 column (Agilent). Calibration curves from commercial standards were used to quantify the concentrations of most of reactants and products. For 2-dodecanoyl furan where commercial standards are lacking, the product was quantified using the effective carbon number (ECN) method[301]. The ECN of 2-dodecanoyl furan was determined from the ECN of the commercially available 2-acetyl furan and hexane.

6.2.3 Catalyst characterization

Surface area and porosity of the iron oxide catalysts were determined from N_2 physisorption data at 77 K using the Micromeritics ASAP 2020 instrument. The crystallinity of the fresh and spent catalysts were measured by a Bruker D8 X-ray diffraction (XRD) instrument equipped with a monochromatic Cu Kα1 line ($\lambda = 0.154$ nm) at 40 kV and 40 mA, operating in 2θ range of 5-80° at a scanning rate of 0.02°/s. Temperature programmed reduction (TPR) by hydrogen was performed on a thermogravimetric analysis (TGA) instrument (TA Q600 HT) using 50 mL/min of 5% H_2 in N_2 as the flowing gas in the 25-1200 °C temperature range. In addition, H_2-TPR was also conducted in a downward flow reactor. X-ray photoelectron spectra (XPS) of the catalysts were collected on a Thermo-Fisher K-alpha XPS, equipped with Al-Kα X-ray monochromatic source with 400 μm spot size. The spent catalysts were handled in an air-free glovebox and transferred to a vacuum transfer module (Thermo Scientific) before XPS measurements to eliminate air exposure.

6.3 Results and Discussion

6.3.1 Catalytic activity of metal oxides for cross-ketonization of 2-furoic acid and lauric acid

Various metal oxides with high lattice energies, which have been shown to be active for surface-catalyzed ketonization, were screened for the reaction of 2-furoic acid and lauric acid in dodecane at 316 °C (Figure 6.2). GC-detected products included long chain ketones, 2-dodecanoyl furan and 12-tricosanone, and furan. While more than 40 % furan yield with respect to 2-furoic acid was observed over all the catalysts, ketones only formed over iron oxides (Fe_xO_y), ceria, and titania after 90 min

of reaction at 316 °C. Among these materials, iron oxides (Fe_xO_y) were the most active and selective towards 2-dodecanoyl furan formation. Specifically, up to 70% selectivity of 2-dodecanoyl furan with respect to lauric acid formed during 90 min of the reaction. FeO exhibited slightly higher activity than Fe_2O_3 and Fe_3O_4 per catalyst mass.

We proposed an overall reaction network by Fe_xO_y consisting of three main pathways: cross ketonization of 2-furoic acid and lauric acid to 2-dodecanoyl furan, self-ketonization of lauric acid to 12-tricosanone, and decarboxylation of 2-furoic acid to furan (Figure 6.3). The post-reaction solutions were yellowish and the total GC carbon balance for furoic acid was lower than 70 %, indicating formation of heavy organic deposit. No di-furfuryl ketone was detected as product of 2-furoic acid self-ketonization consistent with the critical role of α-H in the acid ketonization and the fact that the reaction takes place on the catalyst surface instead of in the bulk, which does not require an α-H and is often observed using alkali, alkaline earth, and rare earth metal oxides[164, 302]. Interestingly, the FeO solution turned reddish after reaction and upon exposure to air and contained iron species as measured with elemental XRF analysis (Table E.1). After filtering the spent FeO, fresh 2-furoic acid and lauric acid were added to the iron containing filtrate solution, and the reaction was performed at the same conditions as when FeO was employed. A 15% yield of 2-dodecanoyl furan formation was observed (Figure E.1), suggesting that homogeneous iron carboxylate forms in situ during the reaction over FeO and is active for cross-ketonization. No homogeneous iron species were detected in the case of Fe_2O_3 and Fe_3O_4 and their post-reaction filtrates exhibited no activity towards ketonization.

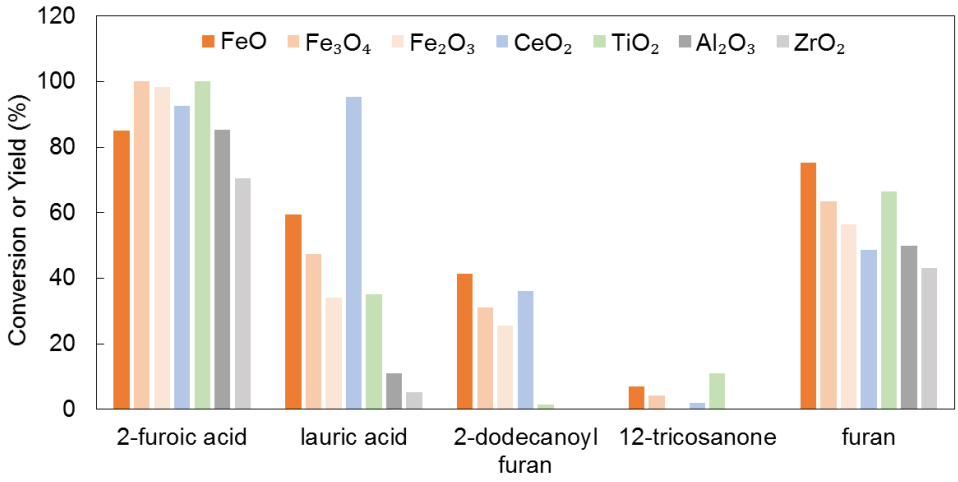

Figure 6.2. Activity of various commercial metal oxides for reaction of 2-furoic acid with lauric acid in n-dodecane. Reaction conditions: 0.05 M lauric acid, 0.25 M 2-furoic acid, 0.2 g catalyst, 316 °C, 90 min, 20 bar N_2.

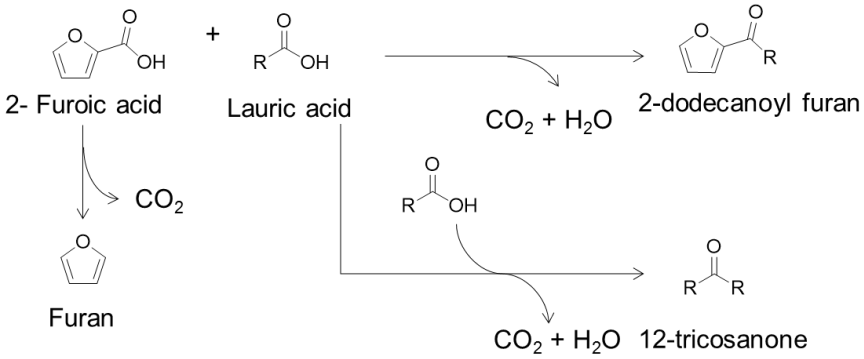

Figure 6.3. Proposed reaction network for reaction of 2-furoic acid and lauric acid in n-dodecane by iron oxide catalyst. R represents n-$C_{11}H_{23}$ group.

All three oxidation states of Fe_xO_y were tested for reusability up to 3 consecutive cycles (Figure 6.4). Due to the loss of catalyst during handling, approximately 10-20 wt % of fresh catalyst was added to the spent catalyst to keep the total catalyst amount constant for each cycle. Noticeably, no homogeneous iron carboxylates were observed in the last two cycles using spent FeO and the filtrate did not turn reddish. While the lauric acid conversion and 2-dodecanoyl furan yield over

FeO remained approximately the same for all 3 runs (within experimental error), the activity of the other Fe_xO_y catalysts increased in the second cycle, more noticeably so for Fe_2O_3, where the 2-dodecanoyl furan yield increased by 74%. In the third cycle, there was some deactivation observed for Fe_2O_3 although the overall activity was still higher than that of the first cycle. The unexpected reactivity enhancement of the spent catalysts required detailed characterization and is discussed in the following section.

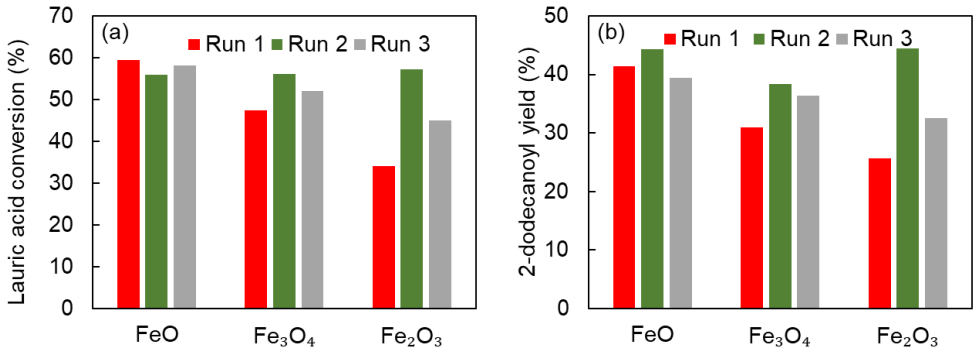

Figure 6.4. Lauric acid conversion (a) and 2-dodecanoyl furan yield (b) after three catalyst recycles in dodecane. Reaction conditions: 0.05 M lauric acid, 0.25 M 2-furoic acid, 0.2 g catalyst, 316 °C, 90 mins, 20 bar N_2

6.3.2 Determination of catalytic active sites from iron oxide characterization

The BET surface area and micropore volumes of the fresh iron oxides increased in the order of FeO < Fe_3O_4 < Fe_2O_3 and were overall very low, indicating that the materials are almost nonporous and the catalytic reactions take place mostly on their external surfaces (Table E.2). After the third reaction cycle, the surface area and pore volume substantially increased, remained unchanged, and slightly decreased for FeO, Fe_3O_4, and Fe_2O_3, respectively. The unexpected enhancement of surface area

by more than 2-orders of magnitude of FeO indicated significant alteration in morphology of the catalyst. XRD patterns of the fresh iron oxides displayed their expected polymorphs (Figure 6.5). The XRD patterns of γ-Fe_2O_3 (maghemite) in tetragonal system and Fe_3O_4 (magnetite) are not distinguishable because both oxides have the inverse spinel-type structure[303]. However, some maghemites contain other cations inserted at the octahedral Fe vacancy sites[304], giving rise to additional XRD peaks in the commercial fresh Fe_2O_3 of this work (matched with Maghemite-Q-00-02501402). After reaction, the spectrum of Fe_3O_4 remained unchanged, the aforementioned additional XRD peaks in the spent Fe_2O_3 disappear, and the diffraction pattern of the used FeO transforms to that of Fe_3O_4. In short, all Fe_xO_y catalysts display the crystallinity pattern of magnetite, suggesting reduction of Fe_2O_3 and oxidation of FeO during reaction. The same phenomenon was reported for iron oxides supported on silica after acetic acid ketonization by Bennet and co-workers[305]. The drastic change in surface area and porosity of the iron oxides may be attributed to their corresponding polymorph transformation.

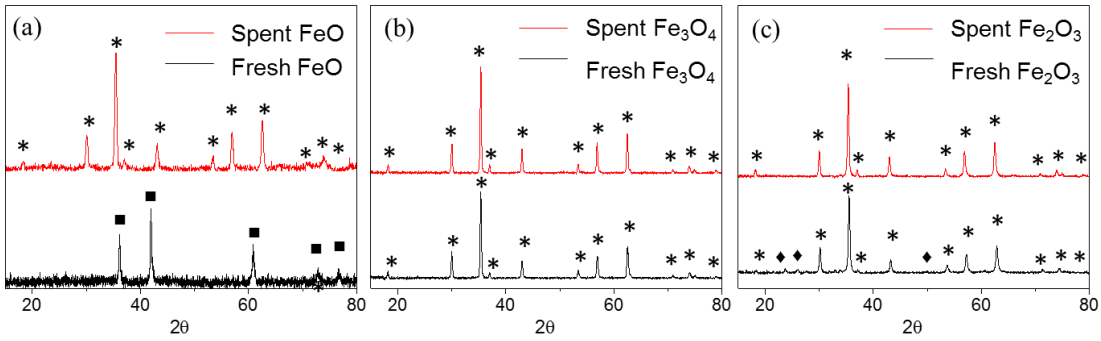

Figure 6.5. XRD pattern of the fresh and spent iron oxides FeO (a), Fe_3O_4(b), Fe_2O_3 (c) with assigned diffraction peaks for FeO (■), Fe_3O_4 or γ-Fe_2O_3 (*), and additional octahedral Fe cation peaks (♦).

To better understand the reduction of the Fe_xO_y, temperature-programmed reduction by H_2 coupled with thermal analysis were performed on the fresh iron oxides. Standard reduction Fe_2O_3 was postulated to take place via a 3-step mechanism: $Fe_2O_3 \rightarrow Fe_3O_4 \rightarrow FeO \rightarrow Fe$[306]. However, the TPR-TGA profiles of the commercial iron oxides indicate that the reduction mechanism is more complex and involves multiple convoluted steps, in agreement with literature[307-309] (Figure E.2). Specifically, partially reduction of Fe_2O_3 to Fe_3O_4 was observed in the [240-416 °C] temperature range. Total reduction to Fe^0 metal occurred at much higher temperatures, in the range of [416-743 °C]. Fe_3O_4 reduction took place at higher temperatures of [343- 457 °C] first and [457- 984 °C] for complete reduction to Fe^0. The cross-ketonization reaction temperature is 316 ºC, which is in the temperature range of Fe_2O_3 reduction to Fe_3O_4, resulting in the transformation of Fe_2O_3 to Fe_3O_4 after reaction observed by XRD. However, 316 ºC is lower than the reduction temperature of Fe_3O_4, explaining the stability in XRD pattern of the spent Fe_3O_4. Lastly, reduction of FeO was minimal for temperatures lower than about 600 °C. It is well documented that FeO is thermally unstable at temperatures lower than 570 °C and the disproportionation reaction of FeO to Fe metal and Fe_3O_4 takes place in the temperature range of [250-600 °C] without hydrogen consumption[308], explaining the observed oxidation of FeO to Fe_3O_4 after ketonization reaction. The metal Fe might have reacted with the acid reagents to generate homogeneous iron (II) carboxylates, which oxidized to iron (III) to turn reddish after exposure to air, and were active for cross-ketonization, as described in section 6.3.1. Other iron (II) salts, e.g., ferrocene (see Figure E.1), have been shown to be effective for cross-ketonization. No homogeneous iron carboxylates were observed

in the post-reaction filtrates of spent FeO in the last two reusability cycles since FeO had completely disproportionated after the first cycle. At the same time, no 2-dodecanoyl furan was detected when the filtrates were used as catalytic solutions for cross-ketonization.

In addition to XRD and H_2 TPR-TGA techniques, which only reveal crystal structure transformation of bulk iron oxides, we employed XPS to investigate the changes on the catalyst surfaces based on the binding energies of Fe 2p in fresh and spent catalyst. Interestingly, as shown in Figure 6.6a, the binding energy of Fe 2p photoelectrons of all the fresh iron oxide catalysts are the same at 711.0 eV for Fe $2p_{3/2}$ and 724.4 eV for Fe $2p_{1/2}$, in agreement with literature values for Fe^{3+}[310].The observed satellite peak at 719.4 eV, which is the characteristic of Fe_2O_3, complimentarily suggests the oxidation of Fe on the surface of the commercial magnetite and wustite, probably due to extended exposure to air. After the reaction, there are clear shifts in Fe $2p_{3/2}$ peaks of the used catalysts to 710.6 eV, a value in between Fe $2p_{3/2}$ binding energy of Fe_2O_3 (711.0 eV) and FeO (709.0 eV) (Figure 6.6b). A shoulder at 709.0 eV, assigned to Fe $2p_3$ of FeO, was observed in all XPS spectra of the spent catalysts. Therefore, the catalyst surfaces were reduced from Fe^{3+} to a mixture of Fe^{3+} and Fe^{2+} after reaction for all the Fe_xO_y catalysts. The disappearance of the satellite peaks in the spent catalysts provides further support that the catalyst surfaces contain Fe_3O_4. Therefore, the initially oxidized catalyst surfaces of all iron oxide catalysts are reduced to Fe_3O_4 during reaction, in agreement with the XRD result for the oxidation/reduction of bulk FeO/Fe_2O_3.

Interestingly, a closer look at the reaction evolution over Fe_3O_4 showed no 2-dodecanoyl furan production during the first 20 mins of the reaction prior to its rapid formation (Figure E.3). This induction period suggests that the surface of Fe_3O_4 transforms to the catalytically active form. To verify the hypothesis, reduction of the commercial Fe_3O_4 with H_2 at 316 °C for 30 mins in the dodecane solvent before using it for the cross-ketonization resulted in a material with much higher activity, i.e., 36% of 2-dodecanoyl furan yield (Figure 6.7) The XPS spectrum of Fe 2p of the pre-reduced Fe_3O_4 is similar to that of the spent Fe_3O_4 after a standard reaction experiment (Figure E.4). Specifically, the Fe $2p_{3/2}$ binding energy shifted to a lower value of 710.6 eV and there is a shoulder at 709 eV, assigned to Fe^{2+} $2p_{3/2}$. The absence of a satellite peak is a confirmation of the generation of Fe_3O_4 on the surface. The enhancement of Fe_3O_4 catalytic activity after H_2 pretreatment indicates that the newly formed Fe^{2+} sites on the catalyst surface are responsible for cross-ketonization. The ketonization activity improvement of Fe_2O_3 in the presence of H_2 has been reported for acetic acid ketonization[311-312]. We hypothesize that even though the reaction was operated under inert N_2, a reducing agent was produced during the initial time of the experiments to reduce the Fe^{3+} sites of the catalyst, explaining the induction period where no ketonization occurred. When the catalysts were pretreated with dodecane solution of 2-furoic acid or lauric acid individually at 316 °C for 30 mins prior to the catalytic reaction, similar catalytic activity to the case of H_2 pretreament was observed at 20 minutes (Figure 6.7). Interestingly, the increasing 2-dodecanoyl furan yield was also noted when the catalyst was pretreated with in dodecane solvent alone, although the effect was not as pronounced as in the cases with lauric acid, 2-furoic acid, or H_2 gas.

XPS measurements of all the pretreated Fe_3O_4 catalysts displayed the Fe 2p spectra of Fe_3O_4 instead of the oxidized surface of the fresh magnetite. After the pretreatments of the catalyst in dodecane at reaction conditions, traces of 2, 3, and 5-dodecanone was detected in GCMS suggested oxidization of dodecane. We propose that the solvent dodecane is partially dehydrogenated and subsequently oxidized to the corresponding ketone, releasing H_2 as a byproduct and a reduced-surface catalyst. The presence of lauric acid or 2-furoic acid in the pretreating dodecane solution probably promotes formation of reducing agents such as H_2 and CO via dehydrogenation/decarbonylation of the acid reactants. As a result, the cross-ketonization activity when the catalysts are pre-reduced with lauric acid or 2-furoic acid solution is higher than that with pure dodecane. In fact, iron-based oxides have been shown to be effective in dehydrogenation[313]. GCMS analysis of the gas products did not detect H_2, CO or CO_2 probably due to the negligible concentration in an inert N_2 filled in the reactor's headspace. Based on correlation of the enhancement in catalytic activity with the reduction of the catalyst surface, we propose that a reduced iron oxide surface is necessary to facilitate ketonization and Fe^{2+} is the catalytically active site. Figure shows a schematic illustration of the changes in oxidation state of the iron oxides after pretreatment and reactions.

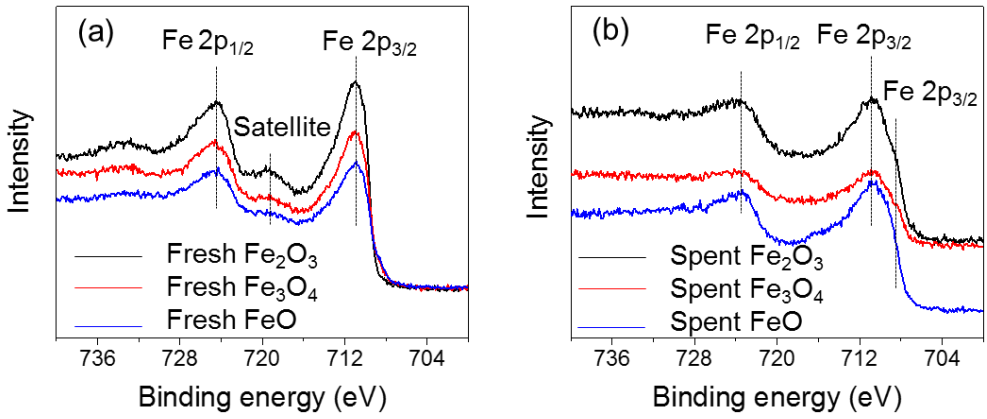

Figure 6.6. XPS spectra of Fe 2p on the iron oxide catalyst surfaces (a) before and (b) after cross-ketonization reaction.

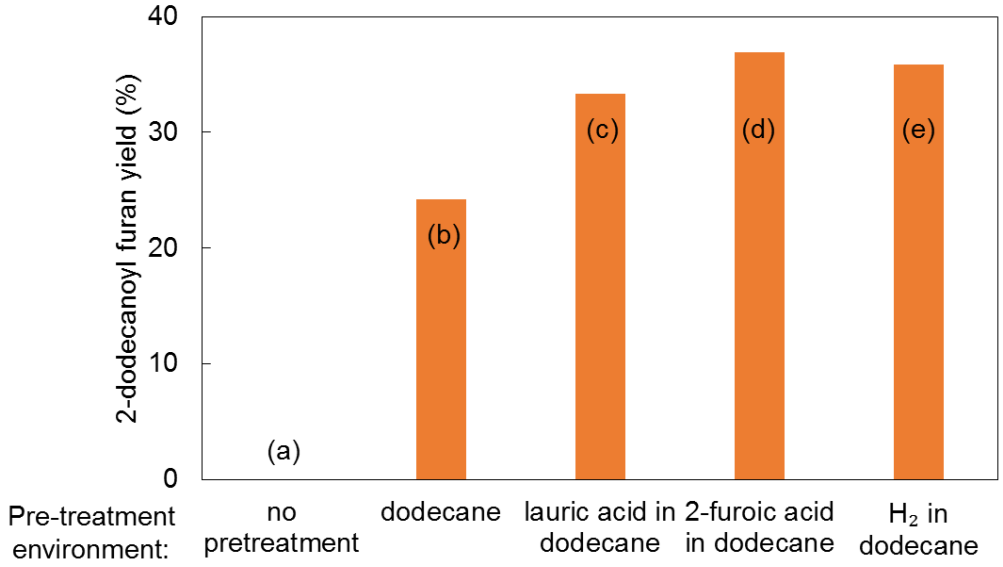

Figure 6.7. Comparison of cross-ketonization activity of Fe_3O_4 catalysts exposed to different pretreatment conditions: the catalyst was used as received (a) or was pre-treated in a dodecane solution of pure dodecane (b), 0.05 M lauric acid (c), 0.25 M 2-furoic acid (d), and 5 bar of H_2 (e). Pretreatment conditions: 316 °C, 30 mins, 0.2 g fresh Fe_3O_4. Reaction conditions: 0.05 M lauric acid, 0.25 M 2-furoic acid, 316 °C, 20 mins, 20 bars of N_2, 0.2 g pretreated Fe_3O_4.

6.3.3 Reaction mechanism:

Metal oxides have been proposed to facilitate surface-catalyzed ketonization via two possible mechanisms. A ketene ($R_2C=C=O$) is hypothesized to form via dehydration of the first carboxylic acid that contains an α-H, which then couples with the second adsorbed carboxylate to form the final ketone product[314-315]. Alternatively, many studies have provide evidence that a β-keto-acid, which has a ketone group at the β position of the carboxylic acid and can readily decarboxylate to form the ketone and CO_2, is the intermediate of ketonization[299-300, 316-317]. In this latter pathway, the α-H containing adsorbed carboxylate undergoes α-H abstraction by a surface metal site to form an enolate, which attacks the adjacent second adsorbed carboxylate to give a β-ketoacid intermediate. Accordingly, the carbonyl group of the ketone product is inherited from the parent carboxylic acid of ketene in the ketene-like mechanism or from the second adsorbed carboxylate in the β-keto acid mechanism. Since we have only one α-H containing carboxylic acid, i.e., lauric acid, in our system, isotopic labeling with lauric acid labeled ^{13}C at C_1 position was employed to distinguish between the two reaction paths. GCMS fragment patterns of the 12-tricosanone product show one unit shift to higher m/z ratio (Figure E.5a) compared to 12-tricosanone in the reaction with unlabeled lauric acid (Figure E.5b), suggesting the presence of a ^{13}C in the structure of self-ketonization of lauric acid. On the other hand, GCMS fragmentation of the cross-ketonization product is the same with standard 2-dodecanoyl furan, indicating that there is no ^{13}C incorporated into the structure of 2-dodecanoyl furan, and the carbonyl group comes from the 2- furoic acid parent (Figure E.5c). The results supported the β-keto acid intermediate acid mechanism. Consequently, we speculated a catalytic cycle pathway as illustrated in Figure 6.8.

Accordingly, the surface Lewis acid Fe^{2+} sites facilitate the initial adsorption of 2-furoic acid and lauric acid to their corresponding surface carboxylates prior to α-H abstraction from a basic oxygen site. C-C coupling between the adsorbed carboxylates generates the β-keto acid, which can be thermally decomposed to the final product, 2-dodecanoyl furan. It has been shown that coordinately unsaturated metal cations are necessary for surface carboxylate formation.[168, 171-172] As the density of the surface Fe^{2+} increases, so does the probability of two adjacent carboxylates co-existing to form the β-keto acid. Numerous studies have utilized metal doping on metal oxides, and/or catalyst pretreatment to create oxygen vacancies and unsaturated metal cations and ultimately increase ketonization activity[172-173, 299].

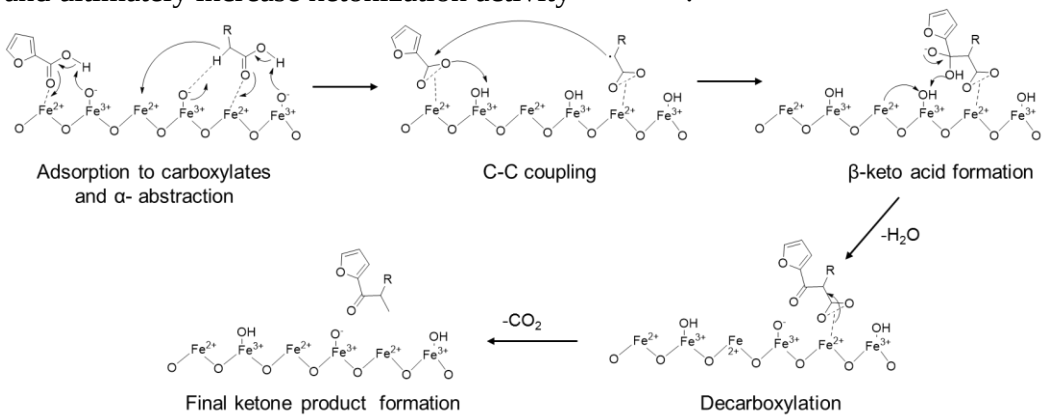

Figure 6.8. Postulated reaction mechanism of cross-ketonization of 2-furoic acid and lauric acid on Fe_3O_4.

6.4 Conclusion

An original method to produce surfactant precursor by cross-ketonization of biomass-derived furoic acid and vegetable oil-derived lauric acid to 2-dodecanoyl furan was proposed. The volatile byproducts and solid catalysts of the process can easily be separated from the desired product stream, providing certain advantages over

the previously proposed acylation process. Amongst the tested catalysts, Earth-abundant, commercially-available iron oxides were shown to be the most active and selective towards cross-ketonization. Detailed catalyst characterization, activity-structure relationships, and elucidation of reaction pathways provide insights into the catalytic active sites, reaction mechanism and stability of the catalysts. XRD and XPS on the fresh and spent catalysts combined reveal that all iron oxides transform during reaction to stable Fe_3O_4 (both bulk and surface phases). The presence of surface Fe^{2+} was hypothesized to be critical for the reaction to take place, owing to the enhancement in the reactivity of the pre-reduced catalyst surfaces. ^{13}C isotopic labeling supports the β-ketoacid intermediate pathway, where adjacently adsorbed laurate and furoate couple on the Fe^{2+} sites to form the corresponding β-ketoacid, which is then decarboxylated to 2-dodecanoyl furan. The iron oxide catalysts were reusable up to three consecutive cycles, with little or no deactivation. Insights into catalysis and reaction pathways can guide future work on process and catalyst design optimization for this new path to renewable surfactants.

Chapter 7

CONCLUSIONS AND OUTLOOK

This chapter provides an overview summary of accomplishments of the entire thesis and outlines future research directions.

7.1 Thesis Summary

The thesis focused on mechanistic understanding of the synergy between different acid and base sites of catalysts for facilitating the conversion of biomass-derived sugars and furanics to valuable chemicals and fuels. Herein, we applied a methodological approach to elucidate the catalytic active sites followed by revealing the reaction mechanism and deriving the reaction network and kinetics to ultimately optimize the catalyst and the process. Experimental catalyst characterization, coupled with titration method(s), unveiled structure-activity relationships of various catalytic active sites and catalyst performance. Isotopic labeling experiments in combination with spectroscopic analysis were instrumental to investigate reaction pathways. Finally, kinetic experiments and modeling studies mapped out the complex reaction networks to provide the key limitations of the catalysts and processes for subsequent optimization. Mechanistic investigations on commercially available catalysts were conducted to provide insights into design principles for more effective and commercially scalable catalysts.

A major part of the thesis centered on the production of 5-hydroxymethyl furfural (HMF), which is widely considered as one of the most valuable biomass building blocks. The two-step reaction of glucose isomerization and subsequent fructose dehydration to HMF was explored in aqueous solvent with both homogeneous metal chlorides and heterogeneous zeolites. Mechanistic studies put emphasis on glucose isomerization, which is the bottleneck of the process. We showed that the metal chlorides hydrolyze in water to form various metal ions and hydroniums, with the latter acting as Brønsted acid species for the second step of fructose dehydration. Catalyst solution titration with HCl and NaCl exposed the exclusive effect of H^+ on glucose isomerization and metal chlorides speciation. Specifically, both the rate of isomerization and the concentration of the partially hydrolyzed metal ions $M(OH)_x^{n+}$ are a function of H^+ addition and reach a maximum at the same intermediate concentration of HCl. This correlation provides further support for the previous hypothesis that the $M(OH)_x^{n+}$ are the active sites for glucose isomerization, regardless of the metal. Isotopic labeling experiments on ^{13}C labeled and deuterated glucose established that the active species acts as Lewis acid and Brønsted base pair to catalyze glucose isomerization via an intramolecular hydride transfer from C2 to C1 of glucose to fructose for all the studied metal chlorides. The hydroxyl group of the metal ions deprotonates the OH group of glucose prior to the formation of the six-member ring transition state at the Lewis acid metal center to facilitate the hydride transfer. The mechanism of glucose epimerization to mannose, however, follows two distinct pathways and depends on the metal. While water-sensitive metal salts, such as Cr, Al, Ga and In (III) chlorides, facilitate the epimerization via a reserve intramolecular

hydride transfer from fructose, water-tolerant lanthanide chlorides favor the Bilik mechanism to produce mannose directly from glucose via an intramolecular C1-C2 carbon shift of glucose. Overall, the study on homogeneous metal chlorides revealed the desirable features of an effective catalyst for the one-pot glucose conversion to HMF, which is the multi-functionality of Lewis acid-Brønsted base to catalyze glucose isomerization, and induced Brønsted acid for fructose dehydration. With this catalyst design principle, we found that the H-form zeolite beta (H-BEA) to be a potential catalyst with extra framework aluminum site as Lewis acid with an adjacent hydroxyl group as a base and the framework aluminum site as a Brønsted acid site. The density of Lewis-Brønsted acid site can be tuned with catalyst calcination of the commercial NH_4-BEA. The total acid sites can be varied with varying the Si/Al ratio. However, activity assessment of H-BEA showed unexpectedly low yield to HMF even though the zeolite exhibited the desirable catalytic sites as verified by ^{27}Al NMR and isopropyl amine decomposition. A kinetic model that integrated experimental kinetics and adsorption studies as well as catalyst characterization was developed for the first time to reveal the key limitations of the H-BEA zeolite. Preferential adsorption of the product HMF onto the zeolites from the aqueous solution, compared to the sugar reactants, was responsible for a low HMF yield. Strong adsorption of HMF in the zeolite's pores promotes its polymerization to coke and contributes to catalyst deactivation. A catalyst that increases the sugar adsorption onto the zeolites from the aqueous solution would be a strategy to enhance the zeolites' activity to the desired HMF. In this multifunctional Lewis/ Brønsted acid work, emphasis was also placed on understanding the interplay of the two catalysts in tandem reactions in series (glucose

to fructose and fructose to HMF) with parallel and series side reactions (sugars and HMF reactions to humins and rehydration of HMF) and how to balance the concentrations of the two catalysts.

The multi-functionality of metal chlorides was next explored in the tandem reductive etherification of HMF to 2,5-bis(isopropoxymethyl) furan (BAMF) as a potential biodiesel in alcohol solvent. Reduction and etherification activity were shown to depend largely on the metal. In order to decouple the interactions of the tandem reactions, each reaction was investigated individually with model compounds, namely furfural for reduction and furfuryl alcohol for etherification, respectively. Catalyst solution titration and isotopic labeling experiment methods, similar to those in the study of glucose isomerization, were employed and revealed that a partially hydrolyzed metal ion with Lewis acid metal site and an adjacent base site were responsible for catalyzing furfural reduction to furfuryl alcohol in 2-propanol via an intermolecular hydride transfer from α-C of 2-propanol to α-C of furfural. Kinetic modeling was leveraged as a key methodological innovation to bypass the challenge of measuring pH in organic solvents and unambiguously exposed the roles of Lewis acid metal ions and their induced Brønsted acid on etherification. While either the Lewis acid and Brønsted acid can be active for etherification, the latter was proven to be predominant. Whether the metal chloride favors reduction or etherification depends on their alcoholysis/hydrolysis degree in the alcohol solvent. The revelation of active species for each step of the reductive etherification of HMF to BAMF guided efforts to design and synthesize an effective multi-functional heterogeneous catalyst. Supported zirconia on high surface area silica, synthesized using incipient wetness

impregnation method, possessed the desired acid-base properties. Interaction between zirconia and the support creates stronger Lewis acid sites, weaker basic sites as well as additional Brønsted acid sites on the catalyst surface compared to the commercial bulk zirconia as characterized by spectroscopic techniques. The changes in the nature of acid-base sites were reflected with superior performance of ZrO_2/SiO_2 for reductive etherification of HMF. Catalyst poisoning with pyridine, 2,6-ditert butyl pyridine and propionic acid and their effect on the activity toward furfural reduction and furfuryl alcohol etherification confirmed the interplay of acid-base properties of the catalyst on reductive etherification.

In chapter 6, cross-ketonization of 2-furoic acid and lauric acid was proposed for the first time as a strategy to produce 2-dodecanoyl furan as the precursor for bio-surfactant oleo-furan sulfonates (OFS). OFS molecules were proven to exhibit excellent surfactant properties and endurance in hard water conditions without the need for additional chelates. The proposed cross-ketonization pathway provides the advantage of a clean byproduct separation compared to acylation. The commercial Earth abundant iron oxides were found active and selective to produce up to 57% yield of 2-dodecanoyl furan in dodecane solvent. While the commercial fresh iron oxides were oxidized to Fe^{3+} due to long exposure to air, phase transformations to Fe_3O_4 were observed for other iron oxide polymorphs by XRD and XPS analysis. Magnetite Fe_3O_4 was found to be the active and stable phase on the catalyst surface after reaction. An induction period, where no ketonization occured at the beginning of the experiments, suggested the in situ formation of the active sites. The Fe^{2+} site was revealed to be the

catalytic active site, and isotopic labeling experiments with ^{13}C labeled lauric acid suggested a reaction pathway via a β-ketoacid intermediate.

7.2 Outlook

7.2.1 Exploring synthesis methods to enhance the ZrO_2/SiO_2 catalyst activity for reductive etherification of HMF

Chapter 5 demonstrated that ZrO_2/SiO_2 is an active and stable catalyst for reductive etherification of HMF in 2-propanol. However, the catalyst performance can be improved by tuning the acid-base properties and dispersion by exploring different synthesis parameters including precursors, supports and synthesis procedure. Since Brønsted acid is substantially more effective than Lewis acid for etherification, it is desirable to increase the strength and density of the surface Brønsted acidity of the zirconia coated catalyst. Two types of Brønsted acids are generally postulated for a silica supported/mixed zirconia oxide systems: (1) the acidic OH of silanol groups that neighbor electronegative anions and (2) the labile proton which is created by the incorporation of zirconia into the tetrahedral structure of the silica support[288-289, 318-319]. While the former is often observed on the zirconia coated silica, such as the synthesized catalyst in our work[288-289, 319], the latter was detected in mixed oxides that exhibited stronger Brønsted acidity[110, 320]. As the result, co-precipitation[321-322] or sol gel[110, 320, 323] synthesis to develop the hetero linkage Si-O-Zr should probably be favored over impregnation for synthesis. In addition, the dispersion of surface zirconia may be maximized by changing the zirconia precursor. Literature reports that used a zirconyl nitrate solution created large ZrO_2 clusters on the surface while still exposing

silanol groups even at higher zirconia contents[324], consistent with our synthesized ZrO_2/SiO_2. To increase the dispersion to close to a theoretical monolayer, zirconium alkoxides were suggested as alternatives with their hydrolysis controlled by addition of acetylacetone. ZrO_2/SiO_2 synthesized with this method was shown to be highly dispersed on silica support to a maximum coverage.

7.2.2 Tailoring catalyst and process design towards 2-dodecanoyl furan production

Chapter 6 revealed Fe_3O_4 as an active and stable catalyst for cross-ketonization of 2-furoic acid and lauric acid. However, the commercial catalyst is nonporous and has very low surface area. Fe_3O_4 supported on a high surface area and thermally stable silica is expected to enhance the normalized activity per iron site. Fe_3O_4/SiO_2 has in fact been shown to be effective for acetic acid ketonization[305]. The ketonization rate can also be improved by increasing the surface acid density of the Fe_3O_4/SiO_2, which can be achieved by reducing the nanoparticle size of the synthesized catalyst[305]. In addition to enhancing cross-ketonization reactivity, mitigating decarboxylation of 2-furoic acid to furan, which appears to be the major side reaction, is crucial to tailor the carbon selectivity towards the desired 2-dodecanoyl furan. Mechanistic understanding of 2-furoic acid decarboxylation is limited and deserves deeper investigation. Experimental structure-activity study in combination with computational investigation may shed light on the catalytic site requirement for 2-furoic acid decarboxylation. Preliminary data showed that furan can be thermally produced at lower temperatures than cross-ketonization. Therefore, a kinetic study to derive the relevant kinetic

parameters of each reaction step of the reaction network would also be insightful and may enable optimization of reaction conditions.

7.2.3 Application of multi-functional acid-base catalysts toward the production of bio-fuels

With environmental concerns to reduce the dependence on petroleum feedstock for transportation fuels, research for new strategies to produce gasoline, diesel and jet fuels from biomass have been on the rise. Among the proposed strategies, ketonization is an efficient pathway for upgrading bio-oils since the chemistry does not only remove oxygen but also increases the C chain length of biomass-derived oxygenates. Despite being one of the oldest organic chemistries, ketonization of C2-C6 carboxylic acids, which make up > 30% of bio-oil, was only recently incorporated into the biomass valorization roadmap, in combination with subsequent aldol condensation and hydrodeoxygenation (HDO) to C9-C23 alkanes, which exhibit excellent diesel or jet fuel properties[5, 164, 325] (Figure 7.1). Shylesh *et al*. demonstrated this three-step process, including (1) a mixture of C5-C9 central ketones from cross ketonization of C3-C5 carboxylic acid over ZrO_2, (2) condensation of the ketones formed in step 1 to their respective dimer acyclic enones over Nb_2O_5, and (3) HDO of the enones to C1-C18 alkanes on a Pt-based catalyst[325]. Except for HDO which requires a metal catalyst, acid-base catalytic materials, especially inorganic metal oxides, have been widely applied for both ketonization and aldol condensation. Therefore, we envision the development of a multi-functional catalyst that can facilitate the one-pot ketonization and aldol condensation to long-chain oxygenates prior to the final HDO step. Mechanistic understanding on how the nature and strength

of the acid-base sites influence the ketonization and aldol condensation activity and product distribution will be crucial for developing an effective catalyst. In addition, catalyst activity and stability studies have only been conducted on model carboxylic acid compounds. The effect of impurities in bio-oil, such as water and alkalines, on catalyst performance should be investigated in order to apply the process to raw-bio-oils.

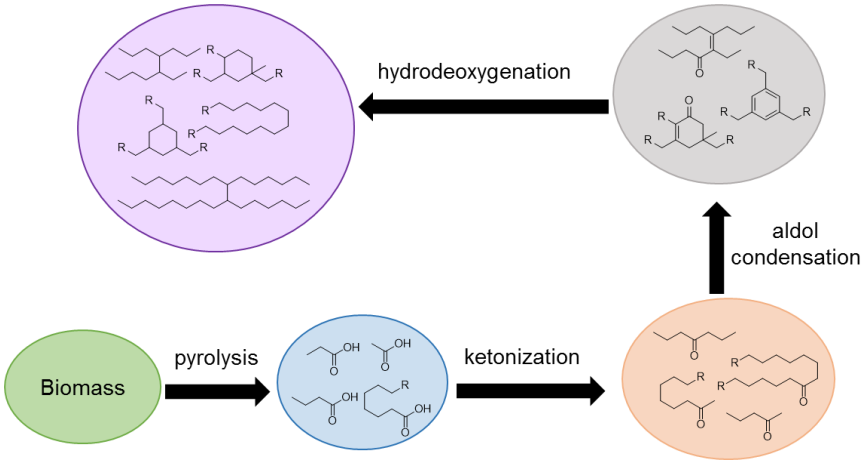

Figure 7.1. Proposed roadmap for converting biomass to bio-fuels. Adapted from Shylesh *et al.*[325]

REFERENCES

.

1. Solomon, S.; Plattner, G.-K.; Knutti, R.; Friedlingstein, P., *Proceedings of the National Academy of Sciences.* **2009**.
2. Caldeira, K.; Wickett, M. E., *Journal of Geophysical Research: Oceans.* **2005,** *110*.
3. Schmalensee, R.; Stoker, T. M.; Judson, R. A., *The Review of Economics and Statistics.* **1998,** *80*, 15-27.
4. Corma, A.; Iborra, S.; Velty, A., *Chemical Reviews.* **2007,** *107*, 2411-2502.
5. Huber, G. W.; Iborra, S.; Corma, A., *Chemical Reviews.* **2006,** *106*, 4044-4098.
6. Wettstein, S. G.; Alonso, D. M.; Gürbüz, E. I.; Dumesic, J. A., *Current Opinion in Chemical Engineering.* **2012,** *1*, 218-224.
7. McKendry, P., *Bioresource technology.* **2002,** *83*, 37-46.
8. Czernik, S.; Bridgwater, A. V., *Energy & Fuels.* **2004,** *18*, 590-598.
9. Amidon, T.; D. Wood, C.; M. Shupe, A.; Wang, Y.; Graves, M.; Liu, S., *Biorefinery: Conversion of Woody Biomass to Chemicals, Energy and Materials*. 2008; Vol. 2, p 100-120.
10. Aresta, M.; Dibenedetto, A.; Dumeignil, F., *Biorefinery: From Biomass to Chemicals and Fuels*. De Gruyter: 2012.
11. Herron, J. A.; Vann, T.; Duong, N.; Resasco, D. E.; Crossley, S.; Lobban, L. L.; Maravelias, C. T., *Energy Technology.* **2017,** *5*, 130-150.
12. Lynd, L. R.; Wyman, C.; Laser, M.; Johnson, D.; Landucci, R., *National Renewable Energy Laboratory, Golden, CO, Technical Report No. NREL/SR-510-35578.* **2005**.
13. Galkin, M. V.; Samec, J. S. M., *ChemSusChem.* **2016,** *9*, 1544-1558.
14. van Putten, R. J.; van der Waal, J. C.; de Jong, E.; Rasrendra, C. B.; Heeres, H. J.; de Vries, J. G., *Chemical Reviews.* **2013,** *113*, 1499-597.
15. Gallo, J.; Alonso, D.; Mellmer, M.; Yeap, J.; Wong, H.; Dumesic, J., *Topics in Catalysis.* **2013,** *56*, 1775-1781.
16. Alamillo, R.; Tucker, M.; Chia, M.; Pagán-Torres, Y.; Dumesic, J., *Green Chemistry.* **2012,** *14*, 1413-1419.
17. Duong, N.; Tan, Q.; Resasco, D. E., *Comptes Rendus Chimie.* **2018,** *21*, 155-163.
18. Jae, J.; Zheng, W.; Lobo, R. F.; Vlachos, D. G., *ChemSusChem.* **2013,** *6*, 1158-1162.
19. Gilkey, M. J.; Panagiotopoulou, P.; Mironenko, A. V.; Jenness, G. R.; Vlachos, D. G.; Xu, B., *ACS Catalysis.* **2015,** *5*, 3988-3994.

20. Chheda, J. N.; Dumesic, J. A., *Catalysis Today.* **2007,** *123*, 59-70.
21. Casanova, O.; Iborra, S.; Corma, A., *Journal of Catalysis.* **2010,** *275*, 236-242.
22. Ruppert, A. M.; Parvulescu, A. N.; Arias, M.; Hausoul, P. J. C.; Bruijnincx, P. C. A.; Gebbink, R. J. M. K.; Weckhuysen, B. M., *Journal of Catalysis.* **2009,** *268*, 251-259.
23. Gallezot, P., *ChemSusChem.* **2008,** *1*, 734-737.
24. Fernando, S.; Adhikari, S.; Chandrapal, C.; Murali, N., *Energy & Fuels.* **2006,** *20*, 1727-1737.
25. Mettler, M. S.; Vlachos, D. G.; Dauenhauer, P. J., *Energ Environ Sci.* **2012,** *5*, 7797-7809.
26. Climent, M. J.; Corma, A.; De Frutos, P.; Iborra, S.; Noy, M.; Velty, A.; Concepción, P., *Journal of Catalysis.* **2010,** *269*, 140-149.
27. Jin, F.; Enomoto, H., *Energ Environ Sci.* **2011,** *4*, 382-397.
28. Perego, C.; Bianchi, D., *Chemical Engineering Journal.* **2010,** *161*, 314-322.
29. Besson, M.; Gallezot, P.; Pinel, C., *Chemical Reviews.* **2014,** *114*, 1827-1870.
30. Antonakou, E.; Lappas, A.; Nilsen, M. H.; Bouzga, A.; Stöcker, M., *Fuel.* **2006,** *85*, 2202-2212.
31. Jae, J.; Tompsett, G. A.; Foster, A. J.; Hammond, K. D.; Auerbach, S. M.; Lobo, R. F.; Huber, G. W., *Journal of Catalysis.* **2011,** *279*, 257-268.
32. WEISZ, P. B.; HAAG, W. O.; RODEWALD, P. G., *Science.* **1979,** *206*, 57-58.
33. Idem, R. O.; Katikaneni, S. P. R.; Bakhshi, N. N., *Fuel Processing Technology.* **1997,** *51*, 101-125.
34. Kloetstra, K. R.; van Bekkum, H., *Journal of the Chemical Society, Chemical Communications.* **1995**, 1005-1006.
35. Bronsted, J. N., *Chemical Reviews.* **1928,** *5*, 231-338.
36. Jensen, W. B., *Chemical Reviews.* **1978,** *78*, 1-22.
37. Tanabe, K.; Hölderich, W. F., *Applied Catalysis A: General.* **1999,** *181*, 399-434.
38. Swift, T. D.; Bagia, C.; Choudhary, V.; Peklaris, G.; Nikolakis, V.; Vlachos, D. G., *ACS Catalysis.* **2014,** *4*, 259-267.
39. Chheda, J. N.; Rom?n-Leshkov, Y.; Dumesic, J. A., *Green Chemistry.* **2007,** *9*, 342.
40. Perego, C.; Bosetti, A., *Microporous and Mesoporous Materials.* **2011,** *144*, 28-39.
41. Adam, J.; Antonakou, E.; Lappas, A.; Stöcker, M.; Nilsen, M. H.; Bouzga, A.; Hustad, J. E.; Øye, G., *Microporous and Mesoporous Materials.* **2006,** *96*, 93-101.
42. Tian, J.; Wang, J.; Zhao, S.; Jiang, C.; Zhang, X.; Wang, X., *Cellulose.* **2010,** *17*, 587-594.
43. Palkovits, R.; Tajvidi, K.; Ruppert, A. M.; Procelewska, J., *Chemical Communications.* **2011,** *47*, 576-578.

44. Lu, Q.; Xiong, W.-M.; Li, W.-Z.; Guo, Q.-X.; Zhu, X.-F., *Bioresource technology.* **2009,** *100*, 4871-4876.
45. de Almeida, R. M.; Noda, L. K.; Gonçalves, N. S.; Meneghetti, S. M. P.; Meneghetti, M. R., *Applied Catalysis A: General.* **2008,** *347*, 100-105.
46. Nguyen, H.; Nikolakis, V.; Vlachos, D. G., *ACS Catalysis.* **2016,** *6*, 1497-1504.
47. Pagán-Torres, Y. J.; Wang, T.; Gallo, J. M. R.; Shanks, B. H.; Dumesic, J. A., *ACS Catalysis.* **2012,** *2*, 930-934.
48. Nakajima, K.; Baba, Y.; Noma, R.; Kitano, M.; N. Kondo, J.; Hayashi, S.; Hara, M., *J. Am. Chem. Soc.* **2011,** *133*, 4224-4227.
49. Nakajima, K.; Noma, R.; Kitano, M.; Hara, M., *The Journal of Physical Chemistry C.* **2013,** *117*, 16028-16033.
50. Corma, A.; Domine, M. E.; Valencia, S., *Journal of Catalysis.* **2003,** *215*, 294-304.
51. Ward, J. W., *Journal of Catalysis.* **1968,** *10*, 34-46.
52. Liu, C.; Carraher, J. M.; Swedberg, J. L.; Herndon, C. R.; Fleitman, C. N.; Tessonnier, J.-P., *ACS Catalysis.* **2014,** *4*, 4295-4298.
53. Mudge, L. K.; Weber, S. L.; Mitchell, D. H.; Sealock, L. J. J.; Robertus, R. J. *Investigations on catalyzed steam gasification of biomass*; PNL-3695 United States 10.2172/6565051 NTIS, PC A08/MF A01. PNNL English; ; Battelle Pacific Northwest Labs., Richland, WA (USA): 1981; p Medium: ED; Size: Pages: 162.
54. Gupta, R.; Lee, Y. Y., *Bioresource technology.* **2010,** *101*, 8185-8191.
55. Denmark, S. E.; Beutner, G. L., *Angewandte Chemie International Edition.* **2008,** *47*, 1560-1638.
56. Liu, X.; He, H.; Wang, Y.; Zhu, S.; Piao, X., *Fuel.* **2008,** *87*, 216-221.
57. Choudary, B. M.; Lakshmi Kantam, M.; Neeraja, V.; Koteswara Rao, K.; Figueras, F.; Delmotte, L., *Green Chemistry.* **2001,** *3*, 257-260.
58. Russbueldt, B. M. E.; Hoelderich, W. F., *Journal of Catalysis.* **2010,** *271*, 290-304.
59. Hattori, H., *Chemical Reviews.* **1995,** *95*, 537-558.
60. Balakrishnan, M.; Sacia, E. R.; Bell, A. T., *Green Chemistry.* **2012,** *14*, 1626.
61. Che, P.; Lu, F.; Zhang, J.; Huang, Y.; Nie, X.; Gao, J.; Xu, J., *Bioresource technology.* **2012,** *119*, 433-6.
62. Duong, N. N.; Wang, B.; Sooknoi, T.; Crossley, S. P.; Resasco, D. E., *ChemSusChem.* **2017,** *10*, 2823-2832.
63. Park, D. S.; Joseph, K. E.; Koehle, M.; Krumm, C.; Ren, L.; Damen, J. N.; Shete, M. H.; Lee, H. S.; Zuo, X.; Lee, B., *ACS central science.* **2016,** *2*, 820-824.
64. Williams, C. L.; Chang, C.-C.; Do, P.; Nikbin, N.; Caratzoulas, S.; Vlachos, D. G.; Lobo, R. F.; Fan, W.; Dauenhauer, P. J., *Acs Catalysis.* **2012,** *2*, 935-939.
65. Nikbin, N.; Feng, S.; Caratzoulas, S.; Vlachos, D. G., *The Journal of Physical Chemistry C.* **2014,** *118*, 24415-24424.

66. Sadula, S.; Oesterling, O.; Nardone, A.; Dinkelacker, B.; Saha, B., *Green Chemistry.* **2017,** *19*, 3888-3898.
67. Leipner, H.; Fischer, S.; Brendler, E.; Voigt, W., *Macromolecular Chemistry and Physics.* **2000,** *201*, 2041-2049.
68. Bermejo-Deval, R.; Assary, R. S.; Nikolla, E.; Moliner, M.; Román-Leshkov, Y.; Hwang, S.-J.; Palsdottir, A.; Silverman, D.; Lobo, R. F.; Curtiss, L. A.; Davis, M. E., *Proceedings of the National Academy of Sciences.* **2012,** *109*, 9727-9732.
69. Choudhary, V.; Pinar, A. B.; Lobo, R. F.; Vlachos, D. G.; Sandler, S. I., *ChemSusChem.* **2013,** *6*, 2369-2376.
70. Swift, T. D.; Nguyen, H.; Anderko, A.; Nikolakis, V.; Vlachos, D. G., *Green Chemistry.* **2015,** *17*, 4725-4735.
71. Orazov, M.; Davis, M. E., *Proceedings of the National Academy of Sciences.* **2015,** *112*, 11777-11782.
72. Panagiotopoulou, P.; Martin, N.; Vlachos, D. G., *ChemSusChem.* **2015,** *8*, 2046-54.
73. Macala, G. S.; Matson, T. D.; Johnson, C. L.; Lewis, R. S.; Iretskii, A. V.; Ford, P. C., *ChemSusChem: Chemistry & Sustainability Energy & Materials.* **2009,** *2*, 215-217.
74. Pandey, M. P.; Kim, C. S., *Chemical Engineering & Technology.* **2011,** *34*, 29-41.
75. West, R. M.; Liu, Z. Y.; Peter, M.; Gärtner, C. A.; Dumesic, J. A., *Journal of Molecular Catalysis A: Chemical.* **2008,** *296*, 18-27.
76. Hanson, R. M., *Journal of Chemical Education.* **2002,** *79*, 1486.
77. Rondinini, S., *Analytical and Bioanalytical Chemistry.* **2002,** *374*, 813-816.
78. Salomaa, P., *Acta chem. scand.* **1957,** *11*.
79. Gillespie, R.; Peel, T.; Robinson, E., *J. Am. Chem. Soc.* **1971,** *93*, 5083-5087.
80. Gorte, R., *Catalysis Letters.* **1999,** *62*, 1-13.
81. Cvetanović, R.; Amenomiya, Y., *Catalysis Reviews.* **1972,** *6*, 21-48.
82. Falconer, J. L.; Schwarz, J. A., *Catalysis Reviews Science and Engineering.* **1983,** *25*, 141-227.
83. Corma, A., *Chemical Reviews.* **1995,** *95*, 559-614.
84. Barthomeuf, D., Acidity and basicity in zeolites. In *Studies in Surface Science and Catalysis*, Elsevier: 1991; Vol. 65, pp 157-169.
85. Niwa, M.; Katada, N.; Sawa, M.; Murakami, Y., *The Journal of Physical Chemistry.* **1995,** *99*, 8812-8816.
86. Kapustin, G.; Brueva, T.; Klyachko, A.; Beran, S.; Wichterlova, B., *Applied catalysis.* **1988,** *42*, 239-246.
87. Kresnawahjuesa, O.; Gorte, R. J.; de Oliveira, D.; Lau, L. Y., *Catalysis Letters.* **2002,** *82*, 155-160.
88. Pereira, C.; Gorte, R., *Applied Catalysis A: General.* **1992,** *90*, 145-157.

89. Riseman, S. M.; Massoth, F. E.; Dhar, G. M.; Eyring, E. M., *The Journal of Physical Chemistry.* **1982,** *86*, 1760-1763.
90. Damyanova, S.; Centeno Ma Fau - Petrov, L.; Petrov L Fau - Grange, P.; Grange, P.
91. Emeis, C., *Journal of Catalysis.* **1993,** *141*, 347-354.
92. Miyata, H.; Moffat, J. B., *Journal of Catalysis.* **1980,** *62*, 357-366.
93. Lercher, J. A.; Gründling, C.; Eder-Mirth, G., *Catalysis Today.* **1996,** *27*, 353-376.
94. Jacobs, P. A.; Leuven, K., *Catalysis Reviews Science and Engineering.* **1982,** *24*, 415-440.
95. Fukuda, Y.; Tanabe, K., *Bulletin of the Chemical Society of Japan.* **1973,** *46*, 1616-1619.
96. Evans, J.; Whateley, T., *Transactions of the Faraday Society.* **1967,** *63*, 2769-2777.
97. Lavalley, J. C., *Catalysis Today.* **1996,** *27*, 377-401.
98. Binet, C.; Jadi, A.; Lamotte, J.; Lavalley, J., *Journal of the Chemical Society, Faraday Transactions.* **1996,** *92*, 123-129.
99. Goodsel, A. J.; Low, M.; Takezawa, N., *Environmental Science & Technology.* **1972,** *6*, 268-273.
100. Benesi, H.; Winquist, B., *Surface acidity of solid catalysts*. Academic Press: 1978.
101. Choudhary, V. R., *Zeolites.* **1987,** *7*, 272-276.
102. Benesi, H. A.; Winquist, B. H. C., Surface Acidity of Solid Catalysts. In *Advances in Catalysis*, Eley, D. D.; Pines, H.; Weisz, P. B., Eds. Academic Press: 1979; Vol. 27, pp 97-182.
103. Bakshi, K. R.; Gavalas, G. R., *Journal of Catalysis.* **1975,** *38*, 312-325.
104. Geilen, F. M.; vom Stein, T.; Engendahl, B.; Winterle, S.; Liauw, M. A.; Klankermayer, J.; Leitner, W., *Angewandte Chemie.* **2011,** *123*, 6963-6966.
105. Sun, J.; Zhu, K.; Gao, F.; Wang, C.; Liu, J.; Peden, C. H.; Wang, Y., *J. Am. Chem. Soc.* **2011,** *133*, 11096-11099.
106. Choudhary, V.; Mushrif, S. H.; Ho, C.; Anderko, A.; Nikolakis, V.; Marinkovic, N. S.; Frenkel, A. I.; Sandler, S. I.; Vlachos, D. G., *J. Am. Chem. Soc.* **2013,** *135*, 3997-4006.
107. Corma, A.; Hamid, S. B.; Iborra, S.; Velty, A., *ChemSusChem: Chemistry & Sustainability Energy & Materials.* **2008,** *1*, 85-90.
108. Centi, G.; van Santen, R. A., *Catalysis for renewables: from feedstock to energy production*. John Wiley & Sons: 2008.
109. Takagaki, A.; Ohara, M.; Nishimura, S.; Ebitani, K., *Chemical Communications.* **2009**, 6276-6278.
110. Tanabe, K.; Yamaguchi, T., *Catalysis Today.* **1994,** *20*, 185-197.

111. Holladay, J. E.; White, J. F.; Bozell, J. J.; Johnson, D. *Top value-added chemicals from biomass-Volume II—Results of screening for potential candidates from biorefinery lignin*; Pacific Northwest National Lab.(PNNL), Richland, WA (United States): 2007.
112. Mulder, G., *Journal für praktische Chemie.* **1840,** *21*, 321-370.
113. van Putten, R.-J.; van der Waal, J. C.; de Jong, E.; Rasrendra, C. B.; Heeres, H. J.; de Vries, J. G., *Chemical Reviews.* **2013,** *113*, 1499-1597.
114. Kuster, B., *Starch-Stärke.* **1990,** *42*, 314-321.
115. Musau, R. M.; Munavu, R. M., *Biomass.* **1987,** *13*, 67-74.
116. Wang, F.; Shi, A.-W.; Qin, X.-X.; Liu, C.-L.; Dong, W.-S., *Carbohydrate research.* **2011,** *346*, 982-985.
117. Seri, K.-i.; Inoue, Y.; Ishida, H., *Chemistry Letters.* **2000,** *29*, 22-23.
118. Torres, A. I.; Daoutidis, P.; Tsapatsis, M., *Energ Environ Sci.* **2010,** *3*, 1560-1572.
119. Michael McConnell, D. O., Sugar and Sweeteners Outlook. , Economic Research Service: July 18, 2018.
120. Yong, G.; Zhang, Y.; Ying, J. Y., *Angewandte Chemie International Edition.* **2008,** *47*, 9345-9348.
121. Newth, F., The formation of furan compounds from hexoses. In *Advances in carbohydrate chemistry*, Elsevier: 1951; Vol. 6, pp 83-106.
122. Feather, M. S.; Harris, J. F., Dehydration reactions of carbohydrates. In *Advances in carbohydrate chemistry and biochemistry*, Elsevier: 1973; Vol. 28, pp 161-224.
123. Moreau, C.; Durand, R.; Razigade, S.; Duhamet, J.; Faugeras, P.; Rivalier, P.; Ros, P.; Avignon, G., *Applied Catalysis, A: General.* **1996,** *145*, 211-224.
124. Antal Jr, M. J.; Mok, W. S.; Richards, G. N., *Carbohydrate research.* **1990,** *199*, 91-109.
125. Stütz, A. E., *Glycoscience: Epimerisation, Isomerisation and Rearrangement Reactions of Carbohydrates*. Springer Berlin Heidelberg: 2003.
126. Zhao, H.; Holladay, J. E.; Brown, H.; Zhang, Z. C., *Science.* **2007,** *316*, 1597-1600.
127. Ohara, M.; Takagaki, A.; Nishimura, S.; Ebitani, K., *Applied Catalysis A: General.* **2010,** *383*, 149-155.
128. Speck Jr, J. C., The lobry de Bruyn-Alberda van Ekenstein transformation. In *Advances in carbohydrate chemistry*, Elsevier: 1958; Vol. 13, pp 63-103.
129. Sowden, J. C.; Schaffer, R., *J. Am. Chem. Soc.* **1952,** *74*, 499-504.
130. Kooyman, C.; Vellenga, K.; De Wilt, H., *Carbohydrate Research.* **1977,** *54*, 33-44.
131. Fischer, H. O.; Taube, C.; Baer, E., *Berichte der deutschen chemischen Gesellschaft (A and B Series).* **1927,** *60*, 479-485.

132. Yu, S.; Kim, E.; Park, S.; Song, I. K.; Jung, J. C., *Catalysis Communications.* **2012,** *29*, 63-67.
133. Delidovich, I.; Palkovits, R., *ChemSusChem.* **2016,** *9*, 547-561.
134. Bhosale, S. H.; Rao, M. B.; Deshpande, V. V., *Microbiological reviews.* **1996,** *60*, 280-300.
135. Román-Leshkov, Y.; Moliner, M.; Labinger, J. A.; Davis, M. E., *Angewandte Chemie International Edition.* **2010,** *49*, 8954-8957.
136. Moliner, M.; Román-Leshkov, Y.; Davis, M. E., *Proceedings of the National Academy of Sciences.* **2010,** *107*, 6164-6168.
137. Pagan-Torres, Y. J.; Wang, T.; Gallo, J. M. R.; Shanks, B. H.; Dumesic, J. A., *Acs Catalysis.* **2012,** *2*, 930-934.
138. Bermejo-Deval, R.; Orazov, M.; Gounder, R.; Hwang, S.-J.; Davis, M. E., *ACS Catal.* **2014,** *4*, 2288-2297.
139. Kruger, J. S.; Nikolakis, V.; Vlachos, D. G., *Applied Catalysis A: General.* **2014,** *469*, 116-123.
140. Kruger, J. S.; Nikolakis, V.; Vlachos, D. G., *Current Opinion in Chemical Engineering.* **2012,** *1*, 312-320.
141. Kruger, J. S.; Choudhary, V.; Nikolakis, V.; Vlachos, D. G., *ACS Catalysis.* **2013,** *3*, 1279-1291.
142. Beers, A. E.; van Bokhoven, J. A.; De Lathouder, K.; Kapteijn, F.; Moulijn, J., *Journal of Catalysis.* **2003,** *218*, 239-248.
143. Kuster, B. F.; Temmink, H. M., *Carbohydrate research.* **1977,** *54*, 185-191.
144. Patil, S. K.; Lund, C. R., *Energy & Fuels.* **2011,** *25*, 4745-4755.
145. Horvat, J.; Klaić, B.; Metelko, B.; Šunjić, V., *Croatica Chemica Acta.* **1986,** *59*, 429-438.
146. Tsilomelekis, G.; Orella, M. J.; Lin, Z.; Cheng, Z.; Zheng, W.; Nikolakis, V.; Vlachos, D. G., *Green Chemistry.* **2016,** *18*, 1983-1993.
147. van Zandvoort, I.; Wang, Y.; Rasrendra, C. B.; van Eck, E. R.; Bruijnincx, P. C.; Heeres, H. J.; Weckhuysen, B. M., *ChemSusChem.* **2013,** *6*, 1745-1758.
148. .
149. Román-Leshkov, Y.; Barrett, C. J.; Liu, Z. Y.; Dumesic, J. A., *Nature.* **2007,** *447*, 982.
150. Mascal, M.; Nikitin, E. B., *Angewandte Chemie.* **2008,** *47*, 7924-6.
151. Jae, J.; Mahmoud, E.; Lobo, R. F.; Vlachos, D. G., *ChemCatChem.* **2014,** *6*, 508-513.
152. Lewis, J. D.; Van de Vyver, S.; Crisci, A. J.; Gunther, W. R.; Michaelis, V. K.; Griffin, R. G.; Roman-Leshkov, Y., *ChemSusChem.* **2014,** *7*, 2255-65.
153. Wang, D.; Astruc, D., *Chemical reviews.* **2015,** *115*, 6621-6686.
154. Gilkey, M. J.; Xu, B., *ACS catalysis.* **2016,** *6*, 1420-1436.
155. Sacia, E. R.; Balakrishnan, M.; Bell, A. T., *Journal of Catalysis.* **2014,** *313*, 70-79.

156. Raveendra, G.; Rajasekhar, A.; Srinivas, M.; Sai Prasad, P. S.; Lingaiah, N., *Applied Catalysis A: General.* **2016,** *520*, 105-113.
157. Liu, B.; Zhang, Z.; Huang, K., *Cellulose.* **2013,** *20*, 2081-2089.
158. Luo, J.; Yu, J.; Gorte, R. J.; Mahmoud, E.; Vlachos, D. G.; Smith, M. A., *Catal. Sci. Technol.* **2014,** *4*, 3074-3081.
159. Lanzafame, P.; Temi, D. M.; Perathoner, S.; Centi, G.; Macario, A.; Aloise, A.; Giordano, G., *Catalysis Today.* **2011,** *175*, 435-441.
160. Liu, B.; Zhang, Z.; Huang, K.; Fang, Z., *Fuel.* **2013,** *113*, 625-631.
161. Liu, J.; Tang, Y.; Wu, K.; Bi, C.; Cui, Q., *Carbohydr Res.* **2012,** *350*, 20-4.
162. Huang, Y.-B.; Yang, T.; Zhou, M.-C.; Pan, H.; Fu, Y., *Green Chem.* **2016,** *18*, 1516-1523.
163. Friedel, C., *Justus Liebigs Annalen der Chemie.* **1858,** *108*, 122-125.
164. Pham, T. N.; Sooknoi, T.; Crossley, S. P.; Resasco, D. E., *Acs Catalysis.* **2013,** *3*, 2456-2473.
165. Renz, M., *European journal of organic chemistry.* **2005,** *2005*, 979-988.
166. Gliński, M.; Kijeński, J.; Jakubowski, A., *Applied Catalysis A: General.* **1995,** *128*, 209-217.
167. Kim, K.; Barteau, M., *Journal of Catalysis.* **1990,** *125*, 353-375.
168. Pestman, R.; Koster, R.; Van Duijne, A.; Pieterse, J.; Ponec, V., *Journal of catalysis.* **1997,** *168*, 265-272.
169. Gumidyala, A.; Sooknoi, T.; Crossley, S., *Journal of Catalysis.* **2016,** *340*, 76-84.
170. Alotaibi, M. A.; Kozhevnikova, E. F.; Kozhevnikov, I. V., *Applied Catalysis A: General.* **2012,** *447*, 32-40.
171. Dooley, K. M.; Bhat, A. K.; Plaisance, C. P.; Roy, A. D., *Applied Catalysis A: General.* **2007,** *320*, 122-133.
172. Pham, T. N.; Shi, D.; Sooknoi, T.; Resasco, D. E., *Journal of catalysis.* **2012,** *295*, 169-178.
173. Fally, F.; Perrichon, V.; Vidal, H.; Kaspar, J.; Blanco, G.; Pintado, J.; Bernal, S.; Colon, G.; Daturi, M.; Lavalley, J., *Catalysis Today.* **2000,** *59*, 373-386.
174. Ilieva, L.; Pantaleo, G.; Ivanov, I.; Venezia, A.; Andreeva, D., *Applied Catalysis B: Environmental.* **2006,** *65*, 101-109.
175. Nikolla, E.; Román-Leshkov, Y.; Moliner, M.; Davis, M. E., *Acs Catalysis.* **2011,** *1*, 408-410.
176. Bermejo-Deval, R.; Assary, R. S.; Nikolla, E.; Moliner, M.; Román-Leshkov, Y.; Hwang, S.-J.; Palsdottir, A.; Silverman, D.; Lobo, R. F.; Curtiss, L. A., *Proceedings of the National Academy of Sciences.* **2012,** *109*, 9727-9732.
177. Gounder, R.; Davis, M. E., *ACS Catalysis.* **2013,** *3*, 1469-1476.
178. Bílik, V., *Chem. Zvesti*. **1972,** *26*, 183-186.
179. Gunther, W. R.; Wang, Y.; Ji, Y.; Michaelis, V. K.; Hunt, S. T.; Griffin, R. G.; Román-Leshkov, Y., *Nature communications.* **2012,** *3*, 1109.

180. Bermejo-Deval, R.; Gounder, R.; Davis, M. E., *Acs Catalysis.* **2012,** *2*, 2705-2713.
181. Rai, N.; Caratzoulas, S.; Vlachos, D. G., *ACS Catalysis.* **2013,** *3*, 2294-2298.
182. Sievers, C.; Musin, I.; Marzialetti, T.; Valenzuela Olarte, M. B.; Agrawal, P. K.; Jones, C. W., *ChemSusChem.* **2009,** *2*, 665-671.
183. Hu, S.; Zhang, Z.; Song, J.; Zhou, Y.; Han, B., *Green Chemistry.* **2009,** *11*, 1746-1749.
184. Binder, J.; Raines, R. A., *Soc.* **2009,** *131*, 1979-1985.
185. Dutta, S.; De, S.; Alam, M. I.; Abu-Omar, M. M.; Saha, B., *J Catal.* **2012,** *288*, 8-15.
186. Wang, T.; Glasper, J. A.; Shanks, B. H., *Applied Catalysis A: General.* **2015,** *498*, 214-221.
187. Tang, J.; Guo, X.; Zhu, L.; Hu, C., *ACS Catalysis.* **2015,** *5*, 5097-5103.
188. Caratzoulas, S.; Davis, M. E.; Gorte, R. J.; Gounder, R.; Lobo, R. F.; Nikolakis, V.; Sandler, S. I.; Snyder, M. A.; Tsapatsis, M.; Vlachos, D. G., *The Journal of Physical Chemistry C.* **2014,** *118*, 22815-22833.
189. Neuhaus, D.; Williamson, M. P., *The nuclear Overhauser effect in structural and conformational analysis*. VCH New York: 1989.
190. Braun, S.; Kalinowski, H.-O.; Berger, S., *100 and more basic NMR experiments*. VCH Weinheim: 1996.
191. Stewart, I. I., *Spectrochimica Acta Part B: Atomic Spectroscopy.* **1999,** *54*, 1649-1695.
192. Norton, A. M.; Nguyen, H.; Xiao, N. L.; Vlachos, D. G., *RSC Advances.* **2018,** *8*, 17101-17109.
193. Wang, T.; Pagán-Torres, Y. J.; Combs, E. J.; Dumesic, J. A.; Shanks, B. H., *Topics in Catalysis.* **2012,** *55*, 657-662.
194. Takasaki, Y., *Agricultural and Biological Chemistry.* **1966,** *30*, 1247-1253.
195. Isbell, H.; Frush, H.; Wade, C.; Hunter, C., *Carbohydrate Research.* **1969,** *9*, 163-175.
196. Kusin, A., *Berichte der deutschen chemischen Gesellschaft (A and B Series).* **1936,** *69*, 1041-1049.
197. Yanagihara, R.; Soeda, K.; Shiina, S.; Osanai, S.; Yoshikawa, S., *Bulletin of the Chemical Society of Japan.* **1993,** *66*, 2268-2272.
198. Angyal, S. J., *Carbohydrate research.* **1997,** *300*, 279-281.
199. Yamauchi, T.; Fukushima, K.; Yanagihara, R.; Osanai, S.; Yoshikawa, S., *Carbohydrate Research.* **1990,** *204*, 233-239.
200. Richens, D., *The chemistry of aqua ions: synthesis, structure, and reactivity: a tour through the periodic table of the elements. J*. Wiley, Chichester and New York: 1997.
201. Stütz, A. E., *Glycoscience: epimerisation, isomerisation and rearrangement reactions of carbohydrates*. Springer Science & Business Media: 2001; Vol. 215.

202. Tanase, T.; Shimizu, F.; Kuse, M.; Yano, S.; Hidai, M.; Yoshikawa, S., *Inorganic Chemistry.* **1988,** *27*, 4085-4094.
203. Takizawa, S.; Sugita, H.; Yano, S.; Yoshikawa, S., *J. Am. Chem. Soc.* **1980,** *102*, 7969-7971.
204. Shioi, H.; Yano, S.; Toriumi, K.; Ito, T.; Yoshikawa, S., *Journal of the Chemical Society, Chemical Communications.* **1983**, 201-202.
205. Osanai, S.; Inaba, K.; Yoshikawa, S., *Carbohydrate research.* **1991,** *209*, 289-295.
206. Rongère, P.; Morel-Desrosiers, N.; Morel, J.-P., *Journal of the Chemical Society, Faraday Transactions.* **1995,** *91*, 2771-2777.
207. Morel-Desrosiers, N.; Lhermet, C.; Morel, J.-P., *Journal of the Chemical Society, Faraday Transactions.* **1991,** *87*, 2173-2177.
208. Angyal, S. J., *Advances in carbohydrate chemistry and biochemistry.* **1989,** *47*, 1-43.
209. Whitfield, D. M.; Stojkovski, S.; Sarkar, B., *Coordination chemistry reviews.* **1993,** *122*, 171-225.
210. Israëli, Y.; Lhermet, C.; Morel, J.-P.; Morel-Desrosiers, N., *Carbohydrate research.* **1996,** *289*, 1-10.
211. Morel-Desrosiers, N.; Lhermet, C.; Morel, J.-P., *Journal of the Chemical Society, Faraday Transactions.* **1993,** *89*, 1223-1228.
212. Chethana, B.; Lee, D.; Mushrif, S. H., *Journal of Molecular Catalysis A: Chemical.* **2015,** *410*, 66-73.
213. Wasserman, E.; Rustad, J. R.; Xantheas, S. S., *The Journal of chemical physics.* **1997,** *106*, 9769-9780.
214. Clavaguéra, C.; Pollet, R.; Soudan, J.; Brenner, V.; Dognon, J., *The Journal of Physical Chemistry B.* **2005,** *109*, 7614-7616.
215. Lindqvist-Reis, P.; Munoz-Paez, A.; Díaz-Moreno, S.; Pattanaik, S.; Persson, I.; Sandström, M., *Inorganic chemistry.* **1998,** *37*, 6675-6683.
216. Cossy, C.; Barnes, A. C.; Enderby, J. E.; Merbach, A. E., *The Journal of Chemical Physics.* **1989,** *90*, 3254-3260.
217. Brand, S. K.; Labinger, J. A.; Davis, M. E., *ChemCatChem.* **2015**, n/a-n/a.
218. Bubb, W. A., *Concepts in Magnetic Resonance Part A.* **2003,** *19*, 1-19.
219. Hricoviniova, Z.; Lamba, D.; Hricovini, M., *Carbohydrate research.* **2005,** *340*, 455-458.
220. Roman-Leshkov, Y.; Barrett, C. J.; Liu, Z. Y.; Dumesic, J. A., *Nature.* **2007,** *447*, 982-5.
221. Williams, C. L.; Chang, C. C.; Do, P.; Nikbin, N.; Caratzoulas, S.; Vlachos, D. G.; Lobo, R. F.; Fan, W.; Dauenhauer, P. J., *ACS Catalysis.* **2012,** *2*, 935-939.
222. Tucker, M. H.; Alamillo, R.; Crisci, A. J.; Gonzalez, G. M.; Scott, S. L.; Dumesic, J. A., *ACS Sustain Chem Eng.* **2013,** *1*, 554-560.

223. Zeitsch, K. J., *The Chemistry and Technology of Furfural and its Many By-Products*. Elsevier Science: 2000.
224. Kuster, B. F. M., *Starch - Stärke.* **1990,** *42*, 314-321.
225. Wang, J. J.; Xu, W. J.; Ren, J. W.; Liu, X. H.; Lu, G. Z.; Wang, Y. Q., *Green Chemistry.* **2011,** *13*, 2678-2681.
226. Bhaumik, P.; Dhepe, P. L., *ACS Catalysis.* **2013,** *3*, 2299-2303.
227. Mazzotta, M. G.; Gupta, D.; Saha, B.; Patra, A. K.; Bhaumik, A.; Abu-Omar, M. M., *ChemSusChem.* **2014,** *7*, 2342-50.
228. Ordomsky, V. V.; van der Schaaf, J.; Schouten, J. C.; Nijhuis, T. A., *Journal of Catalysis.* **2012,** *287*, 68-75.
229. Yang, L.; Tsilomelekis, G.; Caratzoulas, S.; Vlachos, D. G., *ChemSusChem.* **2015**, n/a-n/a.
230. Moliner, M.; Román-Leshkov, Y.; Davis, M. E., *Proceedings of the National Academy of Sciences of the United States of America.* **2010,** *107*, 6164-6168.
231. Nikolla, E.; Román-Leshkov, Y.; Moliner, M.; Davis, M. E., *ACS Catalysis.* **2011,** *1*, 408-410.
232. Caratzoulas, S.; Davis, M. E.; Gorte, R. J.; Gounder, R.; Lobo, R. F.; Nikolakis, V.; Sandler, S. I.; Snyder, M. A.; Tsapatsis, M.; Vlachos, D. G., *Journal of Physical Chemistry C.* **2014**.
233. Otomo, R.; Yokoi, T.; Kondo, J. N.; Tatsumi, T., *Applied Catalysis, A: General.* **2014,** *470*, 318-326.
234. Patet, R. E.; Nikbin, N.; Williams, C. L.; Green, S. K.; Chang, C.-C.; Fan, W.; Caratzoulas, S.; Dauenhauer, P. J.; Vlachos, D. G., *ACS Catalysis.* **2015,** *5*, 2367-2375.
235. Kunkeler, P. J.; Zuurdeeg, B. J.; van der Waal, J. C.; van Bokhoven, J. A.; Koningsberger, D. C.; van Bekkum, H., *Journal of Catalysis.* **1998,** *180*, 234-244.
236. Hey, M. J.; Nock, A.; Rudham, R.; Appleyard, I. P.; Haines, G. A. J.; Harris, R. K., *J Chem Soc Farad T 1.* **1986,** *82*, 2817-2824.
237. Leon, M.; Swift, T. D.; Nikolakis, V.; Vlachos, D. G., *Langmuir : the ACS journal of surfaces and colloids.* **2013,** *29*, 6597-605.
238. Aronson, M.; Gorte, R.; Farneth, W. E., *Journal of Catalysis.* **1986,** *98*, 434-443.
239. Swift, T. D.; Bagia, C.; Nikolakis, V.; Vlachos, D. G.; Peklaris, G.; Dornath, P.; Fan, W., *AIChE Journal.* **2013,** *59*, 3378-3390.
240. Myers, A. L.; Prausnitz, J. M., *AIChE Journal.* **1965,** *11*, 121-+.
241. Radke, C. J.; Prausnitz, J. M., *AIChE Journal.* **1972,** *18*, 761-+.
242. Ranjan, R.; Thust, S.; Gounaris, C. E.; Woo, M.; Floudas, C. A.; Keitz, M.; Valentas, K. J.; Wei, J.; Tsapatsis, M., *Microporous and Mesoporous Materials.* **2009,** *122*, 143-148.
243. Swift, T. D.; Bagia, C.; Choudhary, V.; Peklaris, G.; Nikolakis, V.; Vlachos, D. G., *ACS Catalysis.* **2014,** *4*, 1320-1320.

244. Noh, J. S.; Schwarz, J. A., *Journal of Colloid and Interface Science.* **1989,** *130*, 157-164.
245. Rajabbeigi, N.; Torres, A. I.; Lew, C. M.; Elyassi, B.; Ren, L.; Wang, Z.; Je Cho, H.; Fan, W.; Daoutidis, P.; Tsapatsis, M., *Chemical Engineering Science.* **2014,** *116*, 235-242.
246. Bai, P.; Siepmann, J. I.; Deem, M. W., *AIChE Journal.* **2013,** *59*, 3523-3529.
247. Builes, S.; Sandler, S. I.; Xiong, R., *Langmuir : the ACS journal of surfaces and colloids.* **2013,** *29*, 10416-22.
248. Xiong, R.; Leon, M.; Nikolakis, V.; Sandler, S. I.; Vlachos, D. G., *ChemSusChem.* **2014,** *7*, 236-44.
249. Moreau, C.; Durand, R.; Pourcheron, C.; Razigade, S., *Industrial Crops and Products.* **1994,** *3*, 85-90.
250. Rac, V.; Rakić, V.; Stošić, D.; Otman, O.; Auroux, A., *Microporous and Mesoporous Materials.* **2014**.
251. Lourvanij, K.; Rorrer, G. L., *Industrial & Engineering Chemistry Research.* **1993,** *32*, 11-19.
252. Lourvanij, K.; Rorrer, G. L., *J Chem Technol Biot.* **1997,** *69*, 35-44.
253. Kuster, B. F. M.; Van Steen, H. J. C. D., *Starch - Stärke.* **1977,** *29*, 99-103.
254. Asghari, F. S.; Yoshida, H., *Industrial & Engineering Chemistry Research.* **2007,** *46*, 7703-7710.
255. Girisuta, B.; Janssen, L. P. B. M.; Heeres, H. J., *Green Chemistry.* **2006,** *8*, 701-709.
256. Salciccioli, M.; Stamatakis, M.; Caratzoulas, S.; Vlachos, D. G., *Chemical Engineering Science.* **2011,** *66*, 4319-4355.
257. Roman-Leshkov, Y.; Chheda, J. N.; Dumesic, J. A., *Science.* **2006,** *312*, 1933-7.
258. Román-Leshkov, Y.; Dumesic, J. A., *Topics in Catalysis.* **2009,** *52*, 297-303.
259. Xiong, R. C.; Miller, J.; Leon, M.; Nikolakis, V.; Sandler, S. I., *Chem. Eng. Sci.* **2015,** *126*, 169-176.
260. Bohre, A.; Dutta, S.; Saha, B.; Abu-Omar, M. M., *ACS Sustain Chem Eng.* **2015,** *3*, 1263-1277.
261. Gonzalez Maldonado, G. M.; Assary, R. S.; Dumesic, J.; Curtiss, L. A., *Energy Environ Sci.* **2012,** *5*, 8990-8997.
262. Wang, H.; Deng, T.; Wang, Y.; Qi, Y.; Hou, X.; Zhu, Y., *Bioresource technology.* **2013,** *136*, 394-400.
263. Arias, K. S.; Climent, M. J.; Corma, A.; Iborra, S., *ChemSusChem.* **2014,** *7*, 210-20.
264. Jia, X.; Ma, J.; Che, P.; Lu, F.; Miao, H.; Gao, J.; Xu, J., *Journal of Energy Chemistry.* **2013,** *22*, 93-97.
265. Zhou, X.; Zhang, Z.; Liu, B.; Zhou, Q.; Wang, S.; Deng, K., *Journal of Industrial and Engineering Chemistry.* **2014,** *20*, 644-649.

266. Hao, W.; Li, W.; Tang, X.; Zeng, X.; Sun, Y.; Liu, S.; Lin, L., *Green Chem.* **2016,** *18*, 1080-1088.
267. Choudhary, V.; Mushrif, S. H.; Ho, C.; Anderko, A.; Nikolakis, V.; Marinkovic, N. S.; Frenkel, A. I.; Sandler, S. I.; Vlachos, D. G., *Journal of the American Chemical Society.* **2013,** *135*, 3997-4006.
268. Choudhary, V.; Pinar, A. B.; Lobo, R. F.; Vlachos, D. G.; Sandler, S. I., *ChemSusChem.* **2013,** *6*, 2369-76.
269. Tang, J.; Guo, X.; Zhu, L.; Hu, C., *ACS Catalysis.* **2015,** *5*, 5097-5103.
270. Wang, T.; Pagán-Torres, Y. J.; Combs, E. J.; Dumesic, J. A.; Shanks, B. H., *Topics in Catalysis.* **2012,** *55*, 657-662.
271. Mushrif, S. H.; Varghese, J. J.; Vlachos, D. G., *Physical Chemistry Chemical Physics.* **2014,** *16*, 19564-19572.
272. Roy Goswami, S.; Dumont, M.-J.; Raghavan, V., *Industrial & Engineering Chemistry Research.* **2016,** *55*, 4473-4481.
273. Beach, C. A.; Krumm, C.; Spanjers, C. S.; Maduskar, S.; Jones, A. J.; Dauenhauer, P. J., *The Analyst.* **2016,** *141*, 1627-32.
274. Peng, L.; Gao, X.; Chen, K., *Fuel.* **2015,** *160*, 123-131.
275. Enumula, S. S.; Koppadi, K. S.; Babu Gurram, V. R.; Burri, D. R.; Rao Kamaraju, S. R., *Sustainable Energy Fuels.* **2017,** *1*, 644-651.
276. Zhang, Z.; Dong, K.; Zhao, Z. K., *ChemSusChem.* **2011,** *4*, 112-8.
277. Démolis, A.; Essayem, N.; Rataboul, F., *ACS Sustain Chem Eng.* **2014,** *2*, 1338-1352.
278. Barbera, K.; Lanzafame, P.; Pistone, A.; Millesi, S.; Malandrino, G.; Gulino, A.; Perathoner, S.; Centi, G., *Journal of Catalysis.* **2015,** *323*, 19-32.
279. Dallas Swift, T.; Nguyen, H.; Anderko, A.; Nikolakis, V.; Vlachos, D. G., *Green Chem.* **2015,** *17*, 4725-4735.
280. Meredith C. Allen, W. G., Thomas J. Schwartz, Functionalization of 5-hydroxymethylfurfural by selective
etherification. In *25th North American Catalysis Society Meeting*, Denver, CO, 2017.
281. Samec, J. S. M.; Backvall, J.-E.; Andersson, P. G.; Brandt, P., *Chemical Society Reviews.* **2006,** *35*, 237-248.
282. Bradley, D. C.; Mehrotra, R. C.; Rothwell, I. P.; Singh, A., 2 - Homometallic Alkoxides. In *Alkoxo and Aryloxo Derivatives of Metals*, Academic Press: London, 2001; pp 3-181.
283. Turova, N. Y.; Turevskaya, E. P.; Kessler, V. G.; Yanovskaya, M. I., General Synthetic Approaches. In *The Chemistry of Metal Alkoxides*, Springer US: Boston, MA, 2002; pp 11-30.
284. Rahaman, M. N., *Ceramic Processing and Sintering*. Taylor & Francis: 2003.
285. Nguyen, H.; Xiao, N.; Daniels, S.; Marcella, N.; Timoshenko, J.; Frenkel, A.; Vlachos, D. G., *ACS Catalysis.* **2017,** *7*, 7363-7370.

286. Bachiller-Baeza, B.; Rodriguez-Ramos, I.; Guerrero-Ruiz, A., *Langmuir : the ACS journal of surfaces and colloids.* **1998,** *14*, 3556-3564.
287. Damyanova, S.; Grange, P.; Delmon, B., *Journal of Catalysis.* **1997,** *168*, 421-430.
288. Yamaguchi, T.; Morita, T.; Salama, T. M.; Tanabe, K., *Catalysis Letters.* **1990,** *4*, 1-6.
289. Kawai, M.; Tsukada, M.; Tamaru, K., *Surface Science Letters.* **1981,** *111*, L716-L720.
290. Wang, S.; Iglesia, E., *Journal of Catalysis.* **2017,** *345*, 183-206.
291. Gould, N. S.; Xu, B., *Journal of Catalysis.* **2018,** *358*, 80-88.
292. Brandvold, T. A., Carbohydrate route to para-xylene and terephthalic acid. Google Patents: 2012.
293. Peters, M. W.; Taylor, J. D.; Manzer, L. E.; Henton, D. E., Methods of preparing renewable butadiene and renewable isoprene. Google Patents: 2010.
294. Abdelrahman, O. A.; Park, D. S.; Vinter, K. P.; Spanjers, C. S.; Ren, L.; Cho, H. J.; Vlachos, D. G.; Fan, W.; Tsapatsis, M.; Dauenhauer, P. J., *ACS Sustain Chem Eng.* **2017,** *5*, 3732-3736.
295. Balakrishnan, M.; Sacia, E. R.; Sreekumar, S.; Gunbas, G.; Gokhale, A. A.; Scown, C. D.; Toste, F. D.; Bell, A. T., *Proceedings of the National Academy of Sciences.* **2015,** *112*, 7645-7649.
296. Jadhav, D.; Grippo, A. M.; Shylesh, S.; Gokhale, A. A.; Redshaw, J.; Bell, A. T., *ChemSusChem.* **2017,** *10*, 2527-2533.
297. Balakrishnan, M.; Sacia, E. R.; Sreekumar, S.; Gunbas, G.; Gokhale, A. A.; Scown, C. D.; Toste, F. D.; Bell, A. T., *Proceedings of the National Academy of Sciences.* **2015**, 201508274.
298. Neunhoeffer, O.; Paschke, P., *Berichte der deutschen chemischen Gesellschaft (A and B Series).* **1939,** *72*, 919-929.
299. Nagashima, O.; Sato, S.; Takahashi, R.; Sodesawa, T., *Journal of Molecular Catalysis A: Chemical.* **2005,** *227*, 231-239.
300. Pulido, A.; Oliver-Tomas, B.; Renz, M.; Boronat, M.; Corma, A., *ChemSusChem.* **2013,** *6*, 141-151.
301. Scanlon, J. T.; Willis, D. E., *Journal of Chromatographic Science.* **1985,** *23*, 333-340.
302. Yamada, Y.; Segawa, M.; Sato, F.; Kojima, T.; Sato, S., *Journal of Molecular Catalysis A: Chemical.* **2011,** *346*, 79-86.
303. Jubb, A. M.; Allen, H. C., *ACS Applied Materials & Interfaces.* **2010,** *2*, 2804-2812.
304. Cornell, R. M.; Schwertmann, U., *The iron oxides: structure, properties, reactions, occurrences and uses*. John Wiley & Sons: 2003.
305. Bennett, J. A.; Parlett, C. M.; Isaacs, M. A.; Durndell, L. J.; Olivi, L.; Lee, A. F.; Wilson, K., *ChemCatChem.* **2017,** *9*, 1648-1654.

306. Nogueira, F. G. E.; Lopes, J. H.; Silva, A. C.; Lago, R. M.; Fabris, J. D.; Oliveira, L. C. A., *Applied Clay Science.* **2011,** *51*, 385-389.
307. Tiernan, M. J.; Barnes, P. A.; Parkes, G. M., *The Journal of Physical Chemistry B.* **2001,** *105*, 220-228.
308. Jóźwiak, W.; Kaczmarek, E.; Ignaczak, W.
309. Lin, H.-Y.; Chen, Y.-W.; Li, C., *Thermochimica Acta.* **2003,** *400*, 61-67.
310. Yamashita, T.; Hayes, P., *Applied surface science.* **2008,** *254*, 2441-2449.
311. Taimoor, A. A.; Favre-Reguillon, A.; Vanoye, L.; Pitault, I., *Catalysis Science & Technology.* **2012,** *2*, 359-363.
312. Karimi, E.; Gomez, A.; Kycia, S. W.; Schlaf, M., *Energy & Fuels.* **2010,** *24*, 2747-2757.
313. Mimura, N.; Takahara, I.; Saito, M.; Hattori, T.; Ohkuma, K.; Ando, M., *Catalysis Today.* **1998,** *45*, 61-64.
314. Hendren, T. S.; Dooley, K. M., *Catalysis today.* **2003,** *85*, 333-351.
315. Randery, S. D.; Warren, J. S.; Dooley, K. M., *Applied Catalysis A: General.* **2002,** *226*, 265-280.
316. Kuriacose, J.; Jewur, S., *Journal of Catalysis.* **1977,** *50*, 330-341.
317. Ignatchenko, A. V., *The Journal of Physical Chemistry C.* **2011,** *115*, 16012-16018.
318. Connell, G.; Dumesic, J., *Journal of catalysis.* **1987,** *105*, 285-298.
319. Bihuniak, P. P.; Condrate, R. A., *Journal of Non-Crystalline Solids.* **1981,** *44*, 331-343.
320. Miller, J. B.; Ko, E. I., *Journal of Catalysis.* **1996,** *159*, 58-68.
321. Toba, M.; Mizukami, F.; Niwa, S.-i.; Sano, T.; Maeda, K.; Annila, A.; Komppa, V., *Journal of molecular catalysis.* **1994,** *94*, 85-96.
322. Bosman, H.; Kruissink, E.; Vanderspoel, J.; Vandenbrink, F., *Journal of Catalysis.* **1994,** *148*, 660-672.
323. Soled, S.; McVicker, G., *Catalysis today.* **1992,** *14*, 189-194.
324. Dang, Z.; Anderson, B.; Amenomiya, Y.; Morrow, B., *The Journal of Physical Chemistry.* **1995,** *99*, 14437-14443.
325. Shylesh, S.; Gokhale, A. A.; Sun, K.; Grippo, A. M.; Jadhav, D.; Yeh, A.; Ho, C. R.; Bell, A. T., *Sustainable Energy & Fuels.* **2017,** *1*, 1805-1809.
326. Take, J.; Yamaguchi, T.; Miyamoto, K.; Ohyama, H.; Misono, M., Bronsted Site Population on External and on Internal Surface of Shape-Selective Catalysts. In *Studies in Surface Science and Catalysis*, Y. Murakami, A. I.; Ward, J. W., Eds. Elsevier: 1986; Vol. Volume 28, pp 495-502.
327. Netrabukkana, R.; Lourvanij, K.; Rorrer, G. L., *Industrial & Engineering Chemistry Research.* **1996,** *35*, 458-464.
328. Díaz-Moreno, S.; Muñoz-Páez, A.; Chaboy, J., *The Journal of Physical Chemistry A.* **2000,** *104*, 1278-1286.

329. Swift, T. D.; Nguyen, H.; Erdman, Z.; Kruger, J. S.; Nikolakis, V.; Vlachos, D. G., *Journal of Catalysis.* **2016,** *333*.

Appendix A

SUPPLEMENTARY INFORMATION FOR CHAPTER 2 MECHANISTIC INSIGHTS INTO LEWIS ACID METAL SALT-CATALYZED GLUCOSE CHEMISTRY IN AQUEOUS SOLUTION

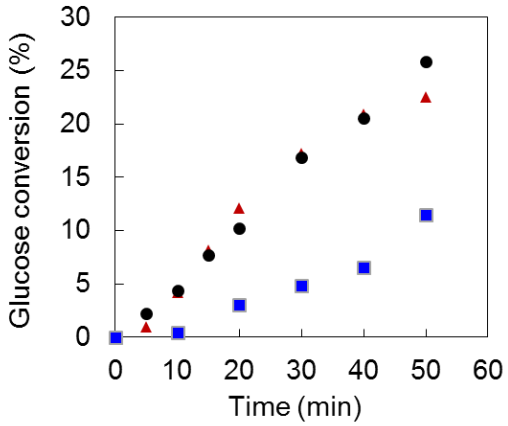

Figure A.1. Comparison of glucose conversion profile by $CrCl_3$ (●), $CrCl_3$ and NaCl (▲) and $CrCl_3$ and HCl (■). Reaction conditions: 1wt % glucose, 1.7 mM $CrCl_3$, 100 mM NaCl, 100 mM HCl, 140 °C.

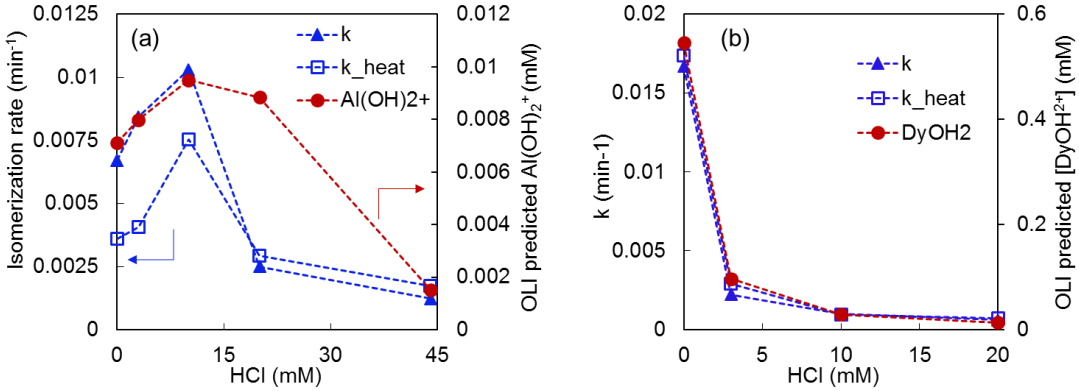

Figure A.2. The effect of HCl addition on the rate of isomerization with catalyst preheating (▲), without catalyst preheating (□) and concentration of MOH^{2+} predicted

by OLI (●) for 5 mM $AlCl_3$ (a) and 20 mM $DyCl_3$ (b). Reaction conditions: 1 wt % glucose, MCl_3, 140 °C, [0-44 mM] HCl.

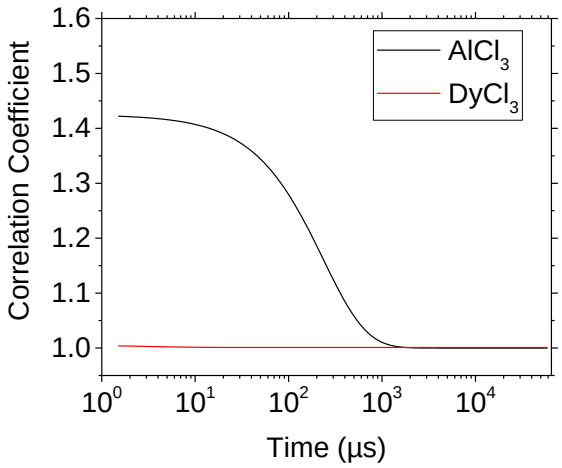

Figure A.3. Dynamic light scattering spectra of 5mM $AlCl_3$ and 20 mM $DyCl_3$ after heated up to 140 °C for 24 h.

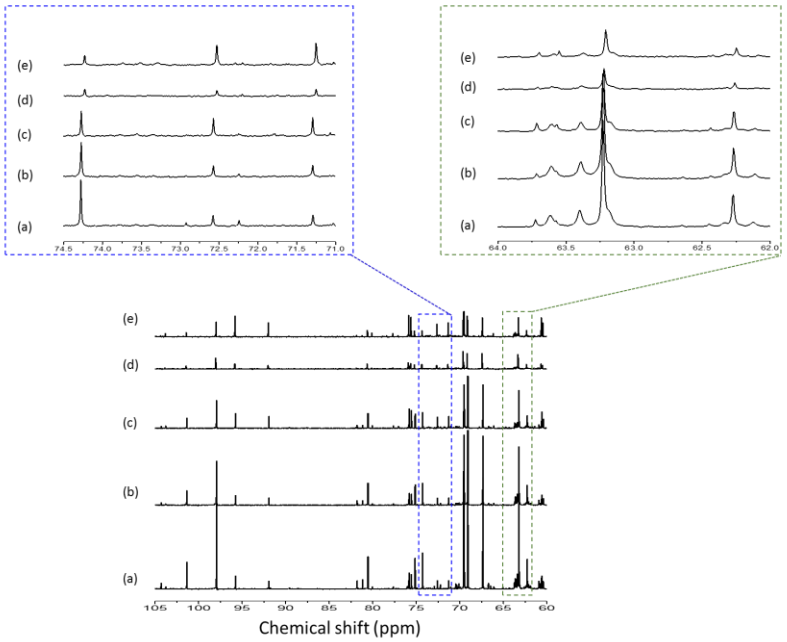

Figure A.4. Bottom: ^{13}C NMR spectra of sugar fraction after reaction from D2 glucose in (a) $GaCl_3$, (b) $InCl_3$, (c) $DyCl_3$, (d) $YbCl_3$, and (e) $LaCl_3$. Left blue box at top: magnification of the spectra in the C2 glucose region. Right green box at top: magnification of the spectra within the C1 fructose region.

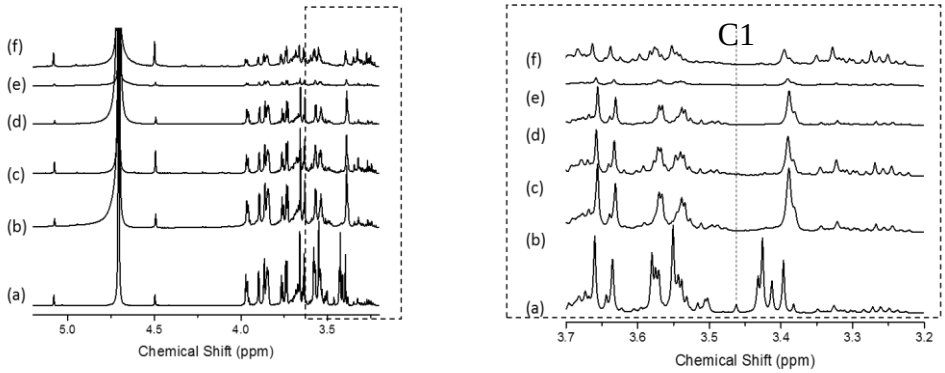

Figure A.5. Left: ^{1}H NMR of (a) a standard mixture of glucose and fructose, and sugar fraction after reaction from D2 glucose in (b) $GaCl_3$, (c) $InCl_3$, (d) $DyCl_3$, (e) $YbCl_3$, and (f) $LaCl_3$. Right: Magnification of the spectra in the region δ= 3.2-3.7 ppm.

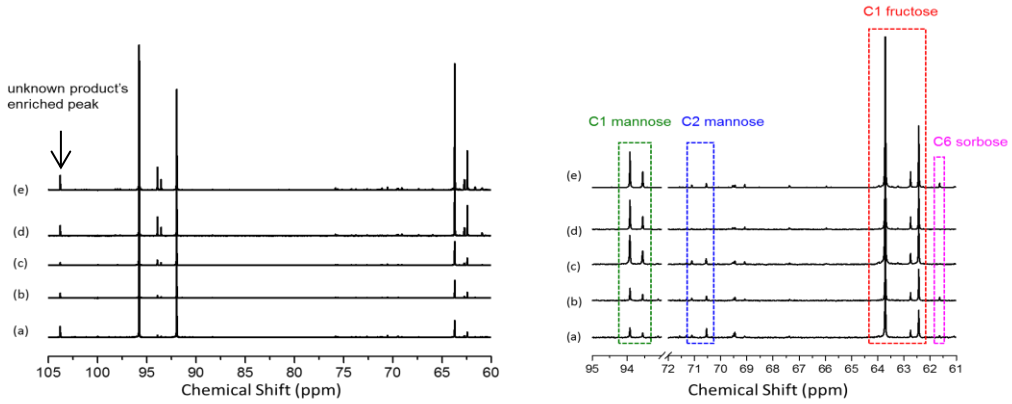

Figure A.6. Left: ^{13}C NMR spectra of the sugar fraction after reaction from ^{13}C-C1 glucose using (a) $LaCl_3$, (b) $DyCl_3$, (c) $GaCl_3$, (d) $InCl_3$, and (e) $AlCl_3$. Right: magnification of the spectra of the C1 mannose peaks (green box), the C2 mannose peaks (blue box), the C1 fructose peaks (red box), and the C6 sorbose peak (purple box).

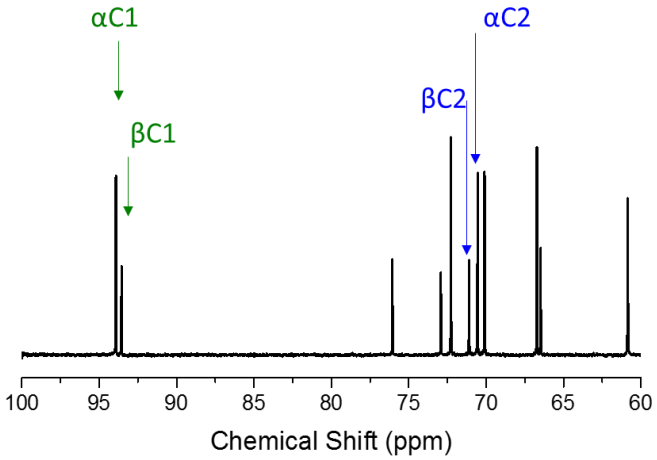

Figure A.7. ^{13}C NMR spectrum of an unlabeled mannose using quantitative ^{13}C NMR method.

Integration of the mannose peaks intensity in Figure S4:

$$\frac{C1}{C2} = \frac{\alpha C1 + \beta C1}{\alpha C2 + \beta C2} = \frac{11.93 + 5.21}{11.17 + 5.38} = 1.03$$

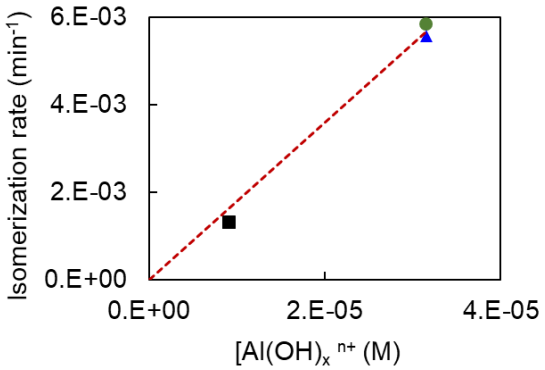

Figure A.8. Correlation between glucose isomerization rate with concentration of $Al(OH)_x^{m+}$ predicted by OLI. Reaction condition: 1wt % glucose, glucose: Al =11:1 molar ratio, 140 °C. Catalysts are $AlCl_3$ (●), $Al(NO_3)_3$ (▲) and $Al_2(SO_4)_3$ (■).

Appendix B

SUPPLEMENTARY INFORMATION FOR CHAPTER 3 TANDEM LEWIS ACID/BRØNSTED ACID-CATALYZED CONVERSION OF CARBOHYDRATES TO 5-HYDROXYMETHYLFURFURAL USING ZEOLITE BETA

B.1 Quantification of the Ratio of Lewis to Brønsted Acid Sites in H-BEa-25

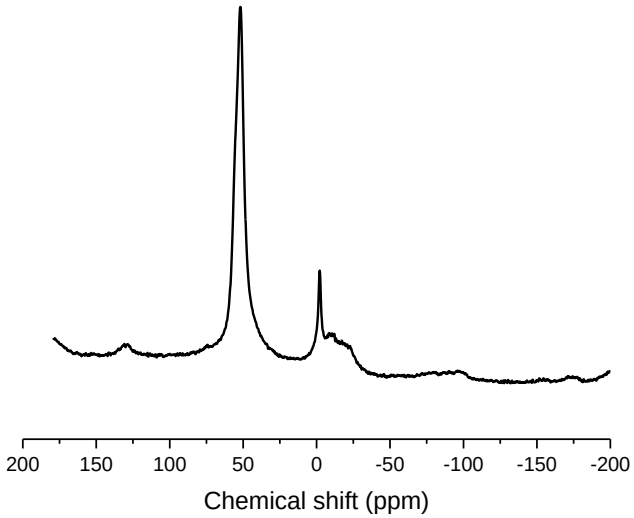

Figure B.1. ^{27}Al NMR spectrum of H-BEA-25 catalyst.

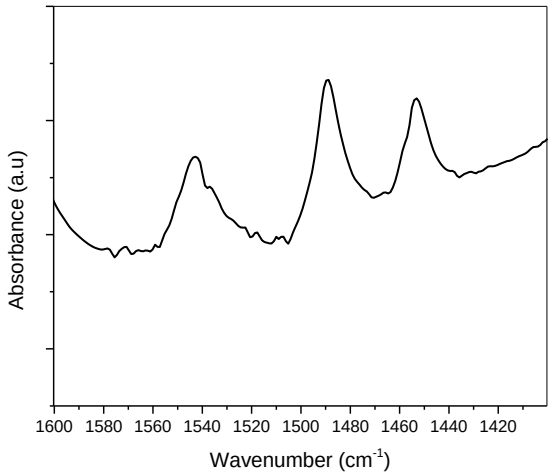

Figure B.2. FTIR spectra of pyridine adsorption of H-BEA-25.

Table B.1. Quantification of the ratio of Lewis to Brønsted acid site density

Entry	Method	Integrated peak ratio	Lewis/ Brønsted acid density
1	^{27}Al	0.3[a]	0.3
2	FTIR	0.62[b]	0.54[c]

(a) The ratio of integral peak area of octahedral Al to tetrahedral Al

(b) The ratio of integrated absorbance of Lewis acid band (1453 cm-1) to Brønsted acid band (1543 cm^{-1})

(c) The extinction coefficient values are 1.3 cm^{-1}/mmol for Brønsted acid site and 1.5 cm^{-1}/mmol for Lewis acid site.[326]

B.2 Adsorption

B.2.1 Single-component adsorption isotherms

This section compares the experimental observations of adsorption loadings with predictions using the isotherm equations and the fitted parameters shown in Table 3.1 of the manuscript.

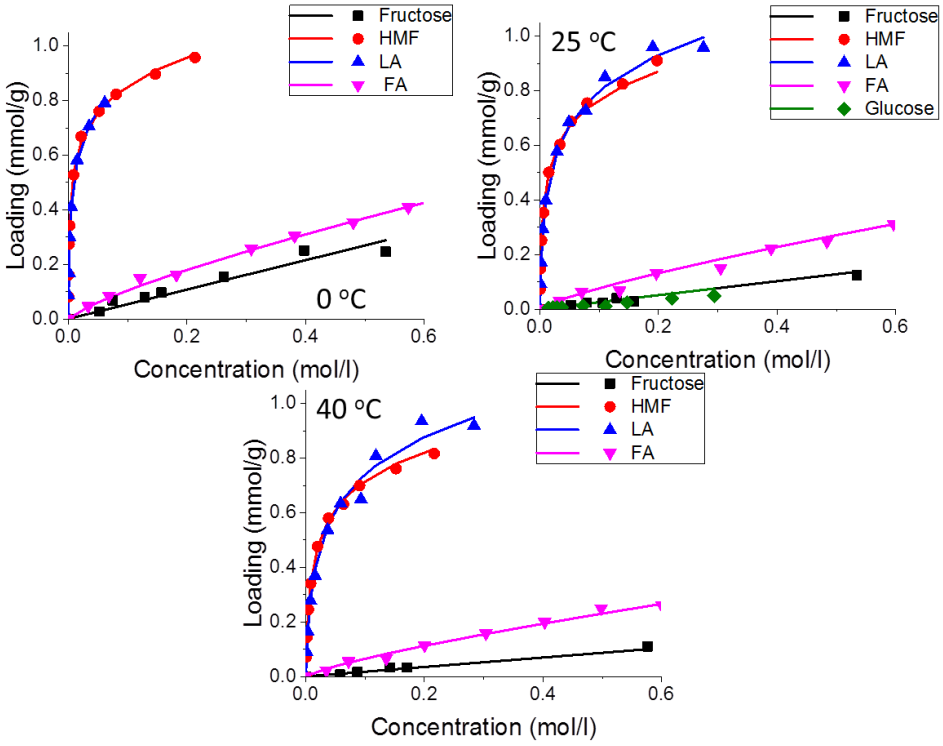

Figure B.3. Adsorption isotherms of fructose dehydration products in water on H-BEA-25. Experimental (points) and model predictions (lines) based on parameters shown in Table 3.1.

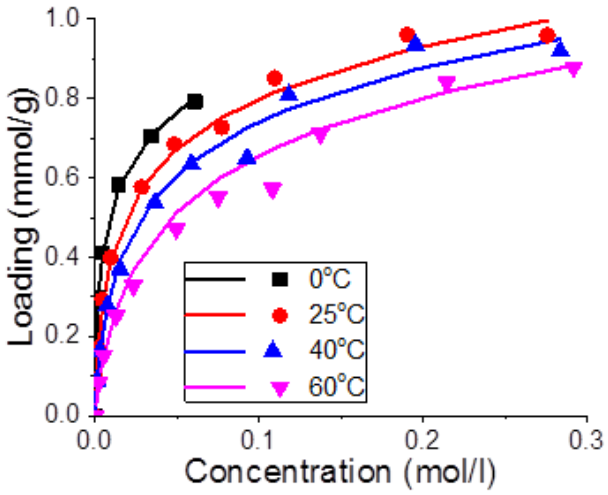

Figure B.4. Adsorption isotherm of LA on H-BEA-25 at various temperatures. Experimental (points) and model prediction (line) shown. Agreement between model predictions and observed isotherms indicates that the temperature-dependence of adsorption is captured by the model

B.2.2 Ideal adsorbed solution theory (IAST)

Ideal adsorbed solution theory (IAST) was originally devised to describe adsorption in gaseous mixtures, but has since been extended to a wide range of systems, including solution phase sorption. One key concept is the idea of spreading pressure:

$$\pi_i = \frac{RT}{A}\int_0^{c_i^0} \frac{q_i^0(c_i)}{c_i}\,dc_i \qquad (1)$$

Here q_i^0 is the single-component isotherm equation for component i as a function of its concentration c_i, R is the ideal gas constant, T is the absolute temperature, and A is the area of the solution-solid interface. When the system has reached equilibrium, the spreading pressures of the different components are equal. The single-component isotherm equations are given by Henry's law or the Redlich-

Peterson equation. For dilute solutions, the concentrations are related to the equivalent pure component concentration using the expression

$$C_i = z_i C_i^0 \tag{2}$$

Here, C_i is the concentration of species i in the mixture, C_i^0 denotes the concentration of solute i that adsorbs from a single solute ideal solution at the same temperature and spreading pressure as that of the mixture and z_i is the adsorbed phase mole fraction:

$$z_i = \frac{q_i}{\sum q_j} \tag{3}$$

Finally, it is assumed that there is no adsorbed area change on mixing:

$$\frac{1}{\sum q_j} = \sum \frac{z_i}{q_i^0} \tag{4}$$

This set of equations for the three adsorbing compounds HMF, LA, and FA yields a series of 12 equations and 12 variables (q_i, q_i^0, c_i, and c_i^0). These were solved using Newton's method with an initial guess corresponding to the multicomponent adsorbed concentrations being equal to the single component concentrations. A detailed accounting of the thermodynamic justification and assumptions is given by Myers and Prausnitz[240].

B.3 Sensitivity of Estimated Parameters

Zeolites in solution are known to have a buffering effect whereby they keep the pH close to that of their point of zero charge (pH^{pzc}) due to the (de)protonation of the surface hydroxyl groups. However, according to experiments, the pH of the solution decreases during the course of the reaction despite the buffering role of the zeolite[244].

Based on Table B.2, we do not expect the pH to be higher than 3.46. To assess the assumption of a constant pH, we re-estimated the parameters at a different constant pH of 3. The estimated parameters are robust (Figure B.5) with fructose degradation to FA having a lower fitted activation energy if the solution pH is assumed to be equal to 4. This finding agrees with prior work, which concluded that a zeolite-induced pH change in the aqueous phase had a negligible effect on the reaction rate[141].

Table B.2. Zeolite-induced pH change at different loadings. Procedure as implemented by Kruger et al.[141]

mass zeolite (g)	mass water (g)	zeolite:water mass ratio	log(mass ratio)	pH at 1 min.	pH at 2 min	pH at 3 min	Temp at 1 min (°C)	Temp at 3 min (°C)
0.0015	14.9947	0.00010	4.00	6.79	6.83	6.86	22.1	22.1
0.0149	14.9937	0.00099	3.00	4.96	4.94	4.93	21.9	21.9
0.1500	14.9969	0.01000	2.00	3.99	3.99	3.99	21.6	21.5
0.8440	8.4410	0.09999	1.00	3.46	3.46	3.47	21.5	22.0

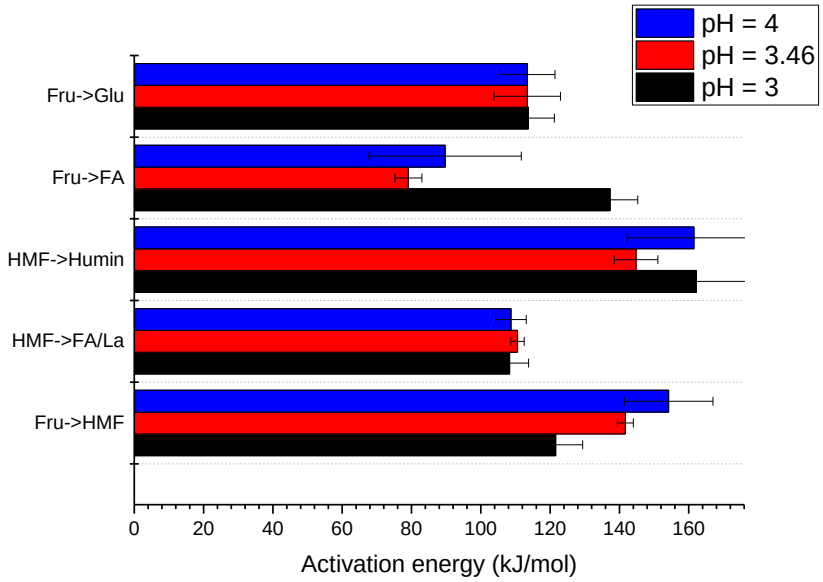

Figure B.5.Estimated parameters using different assumptions for homogeneous solution pH. Activation energies are in general agreement, indicating that the model is not sensitive to assumptions about the solution pH at reaction temperature.

The reaction network shown in Figure 3.1 asserts that humins form only from HMF and fructose via Brønsted acid catalyzed reactions. Paths leading to humin formation from glucose and Lewis acid catalyzed side reactions are probable, indicating that the rate constants of Reactions 3 and 4 may implicitly include contributions from additional paths. In order to investigate the effect of this assumption, we added a path for Lewis catalyzed humin formation from glucose or a direct Brønsted catalyzed humin formation path from fructose. Addition of these reactions has a slight effect on the estimated parameters of the other reactions, but resulted in large uncertainty of the humin formation reaction-parameters (Figure B.6) due to the lack of sufficient experimental data that quantify the carbon loss to humins from various paths. Given this finding, we decided to keep the reaction network as presented in the main paper.

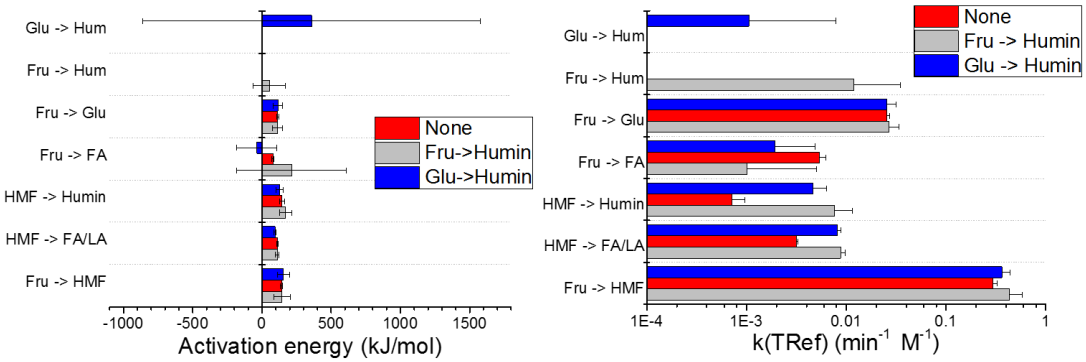

Figure B.6. Estimated parameters assuming additional humin formation reactions. The parameters associated with the non-humin formation reactions are rather insensitive to including these additional paths.

Internal diffusion can be considered significant if the Weisz modulus (Equation (5)) is greater than 0.1[123]. These diffusion limitations will be greatest when the concentration of reactant is the highest, i.e., at initial times. When fructose is used as a starting material, at 130 ºC, the sum of apparent rate constants is $k_F = 0.105$ min^{-1}. The particle radius estimated by sieving the powder is between 5-10 µm. Using the conservative $R_p = 10\ \mu m$ and an effective diffusivity $D_e = 1.77 * 10^{-9}\ cm^2/s$ (estimated based on glucose diffusion through faujasite at 30 ºC [327]), the Weisz modulus at initial time ($q_i = q_0$) is 0.11. Because$\Phi > 0.1$, minor internal diffusion limitations may be present. If particles have a smaller radius, diffusion limitations are not significant. Both HMF and glucose react more slowly than fructose ($k_H = 0.022$ min^{-1} and $k_G = 0.066$ min^{-1} for HMF and glucose, respectively) – for these compounds $\Phi_H = 0.023 < 0.1$ and $\Phi_G = 0.069 < 0.1$, so diffusion resistance can be assumed negligible for experiments starting with HMF or glucose.

$$\Phi = \frac{r_i \cdot R_p^2}{9 \cdot D_e \cdot q_0} = \frac{\left(k_i \cdot q_i\right) \cdot R_p^2}{9 \cdot D_e \cdot q_0} \quad (5)$$

The external transport limitations were examined by first writing out the mass balance in the zeolite and the bulk at initial times when glucose, the reactant, is the only species present:

$$\frac{dq}{dt} = \frac{3k_L}{r_p \rho_{BEA}}\left(C - C_S\right) - k_{BEA} q \tag{6}$$

$$\frac{dC}{dt} = -\frac{3k_L m_{BEA}}{r_p \rho_{BEA} V_{aq}}\left(C - C_S\right) - k_{aq} C \tag{7}$$

Here, q is the glucose loading in the zeolite, k_L is the mass transfer coefficient, r_p is the particle radius, ρ_{BEA} is the density of the zeolite, C is the aqueous concentration of glucose, C_S is the concentration of glucose on the zeolite surface, k_{BEA} is the apparent rate constant of glucose isomerization in the zeolite, m_{BEA}/V_{aq} is the mass of zeolite per reactor volume, and k_{aq} is the apparent rate constant of homogeneous glucose conversion. Glucose follows Henry's law adsorption, so the balance in eq 6 may be re-written:

$$\frac{dC_S}{dt} = \frac{3k_L}{r_p \rho_{BEA} K_{eq}}\left(C - C_S\right) - k_{BEA} C_S \tag{8}$$

Where K_{eq} is the Henry's law constant of glucose. After rescaling time by k_{BEA} and non-dimensionalizing, we have

$$\frac{dC_S}{d\tau} = \alpha\left(C - C_S\right) - C_S \tag{9}$$

$$\frac{dC}{d\tau} = -\alpha K_{eq}\frac{m_{BEA}}{V_{aq}}\left(C - C_S\right) - \frac{k_{aq}}{k_{BEA}} C \tag{10}$$

Where

$$\alpha = \frac{3k_L}{r_p \rho_{BEA} K_{eq} k_{BEA}} \tag{11}$$

If we define a new variable $w = C_S/C$, we have a new differential equation:

$$\frac{dw}{d\tau} = -w^2\alpha\frac{m_{BEA}}{V_{aq}}K_{eq} - \left(1+\alpha-\alpha\frac{m_{BEA}}{V_{aq}}K_{eq}-\frac{k_{aq}}{k_{BEA}}\right) \tag{12}$$

Using correlations, we estimate k_L is 0.33 m/s, $\rho_{BEA} = 1.2$ g/mL, $K_{eq} = 31$ mL/g and $r_p = 10$ μm which gives $\alpha \sim 3 \cdot 10^5$. Since $\alpha \gg 1$, we can re-write eq 12 as

$$\frac{dw}{d\tau} = -\alpha\frac{m_{BEA}}{V_{aq}}K_{eq}w^2 + \alpha\left(\frac{m_{BEA}}{V_{aq}}K_{eq}-1\right)w+\alpha \tag{13}$$

After adding the zeolite loading (125 g/L) and integrating, we solve for w:

$$w = 0.37 + 0.63\left[\frac{\tanh\left(2.42\alpha\tau\right)-0.587}{1-0.587\tanh\left(2.42\alpha\tau\right)}\right] \tag{14}$$

The profile of eq 14 is given in Figure B.7. Since $C_S/C \to 1$ at very short times, we conclude that $C \approx C_S$ over the course of the reaction and external transport is negligible.

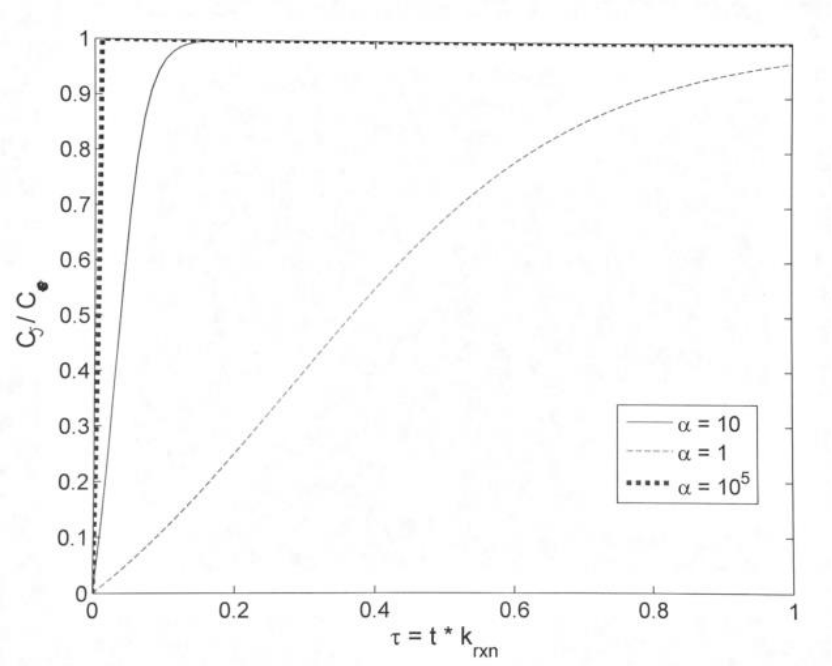

Figure B.7. $\boldsymbol{C_S/C}$ vs $\boldsymbol{\tau}$ for different values of $\boldsymbol{\alpha}$. As $\boldsymbol{\alpha}$ approaches the value used in the present work, $\boldsymbol{C_S/C \to 1}$ at very short times.

B.4 Reaction Kinetics

B.4.1 Kinetic parameters

The turnover frequency (TOF) can be calculated from experimental data using eq 15:

$$TOF = \frac{\left[C_0 - \left(C + \frac{m_{BEA}}{V_{reactor}} q \right) \right]}{n_{H^+} / V_{reactor} / t} \tag{15}$$

Here, C_o is the initial concentration, C is the concentration after reaction time t, n_{H+} is the number of Brønsted acid sites in the reactor, m_{BEA} is the total mass of the zeolite, $V_{reactor}$ is the volume of the solution, and q is the adsorption loading. 10 %w/v fructose solution at 140 ºC after 30 min of reaction using HCl or zeolite BEA has been used to calculate the TOF. The TOF of HCl (pH = 1.1) is 0.23 min^{-1} while that of H-BEA-25 (125 g/l) is 0.029 min^{-1}.

B.4.2 Parity plot

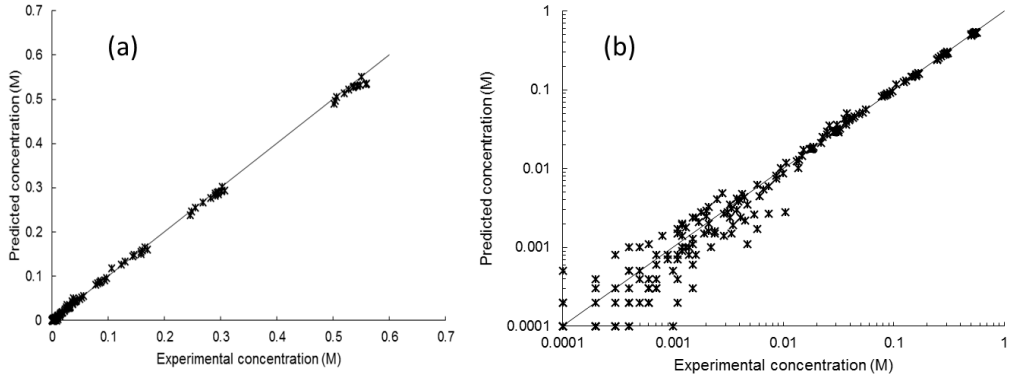

Figure B.8. Parity plot of model predictions and experimental observations indicating the quality of estimated kinetic parameters on both a linear (a) and logarithmic (b) scale.

B.4.3 Effect of catalyst loading

The kinetics of glucose dehydration with three different zeolite loadings at 130 ^{0}C was studied using the same experimental setup described in our manuscript. The zeolite loadings were 12.5 g/L, 50 g/L and 125 g/L, corresponding to aluminum to glucose molar ratio of 0.03, 0.1, and 0.3 respectively. As the catalyst concentration increased, the glucose conversion and product yields measured in the homogeneous phase increased, as shown in Figure B.9. This result is expected. However, the measured conversion did not increase linearly with the catalyst loading. This is likely due to the effect of adsorption, which should be taken into account in order to quantify the effect of catalyst loading. Figure B.9 also shows glucose conversion, and fructose and HMF yield as estimated from the model. The model prediction of glucose conversion and fructose yield are in reasonable agreement with the experimental data. The underestimation of HMF yield could partly due to the direct glucose dehydration to HMF at Brønsted acid sites that was not included in the model. Approximations in predicting multicomponent isotherm data may be another reason for the differences.

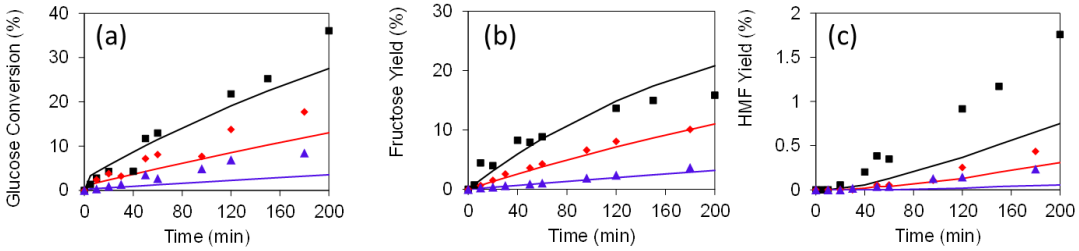

Figure B.9. Conversion of glucose (a) and yield of fructose (b), HMF (c) for reaction of 10 wt% glucose at 130 ^{o}C and zeolite loadings of 12.5 g/L (■), 50 g/L (◆) and 12.5 g/L (▲). Symbols are experimental data and lines are model predictions.

B.4.4 Prediction of fraction of reaction in the zeolite

Experimental data for model prediction

Figure B.10 shows that most of the chemistry (>90%) occurs in the zeolite. Virtually all HMF reactions occur in the zeolite, while some fructose reacts in the aqueous phase. So even though the zeolite has a lower TOF than the homogeneous acid, the proton concentration in the aqueous phase is not high enough to significantly catalyze dehydration chemistry. The zeolite therefore controls the reactivity of the system.

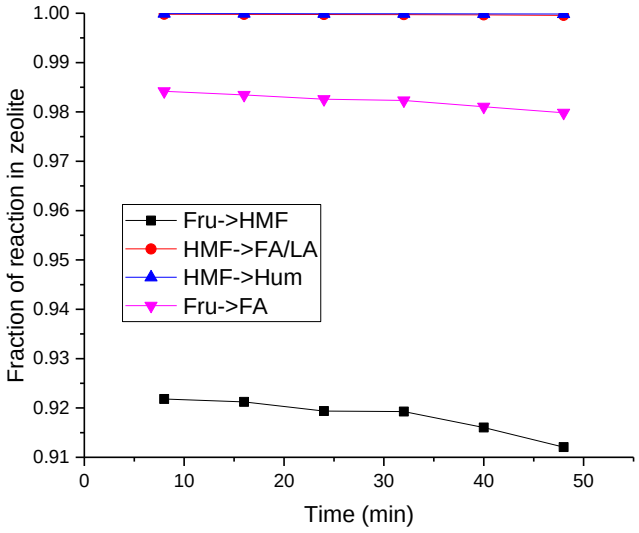

Figure B.10. Estimated fraction of reactions that occur in the zeolite starting with 10 %w/v fructose, 125 g/l H-BEA-25, at 130°C. pH estimated at 3.46. Fractions determined by the ratio: $\frac{r_{BEA}}{r_{BEA}+r_{H_2O}}$, where $\boldsymbol{r}$ is the rate normalized by reactor volume.

B.4.5 Experimental data for model prediction

This section provides the experimentally measured concentration profiles.

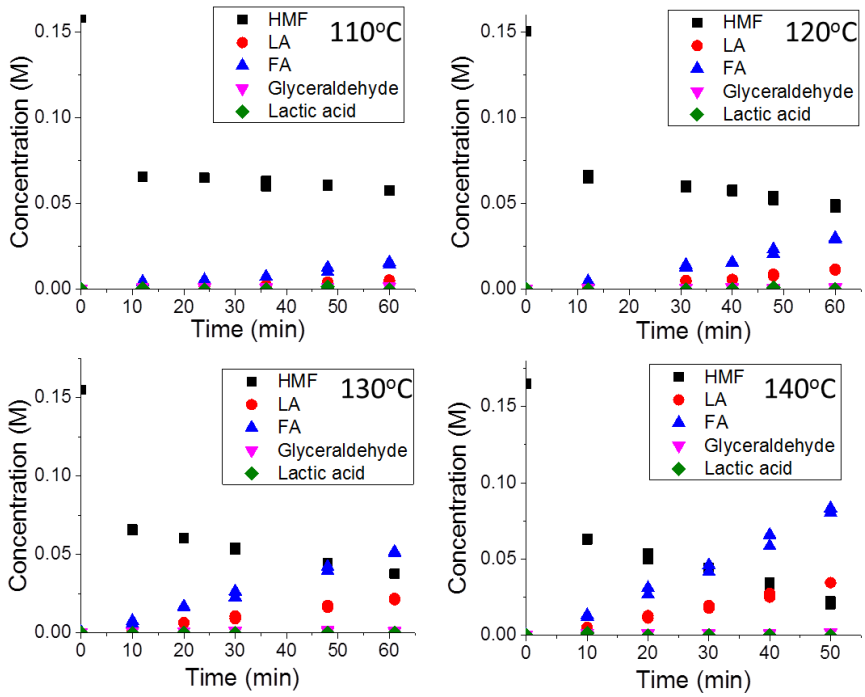

Figure B.11. Experimentally measured concentration profiles of HMF degradation in 125 g/l of H-BEA-25. Replicates shown as separate data points.

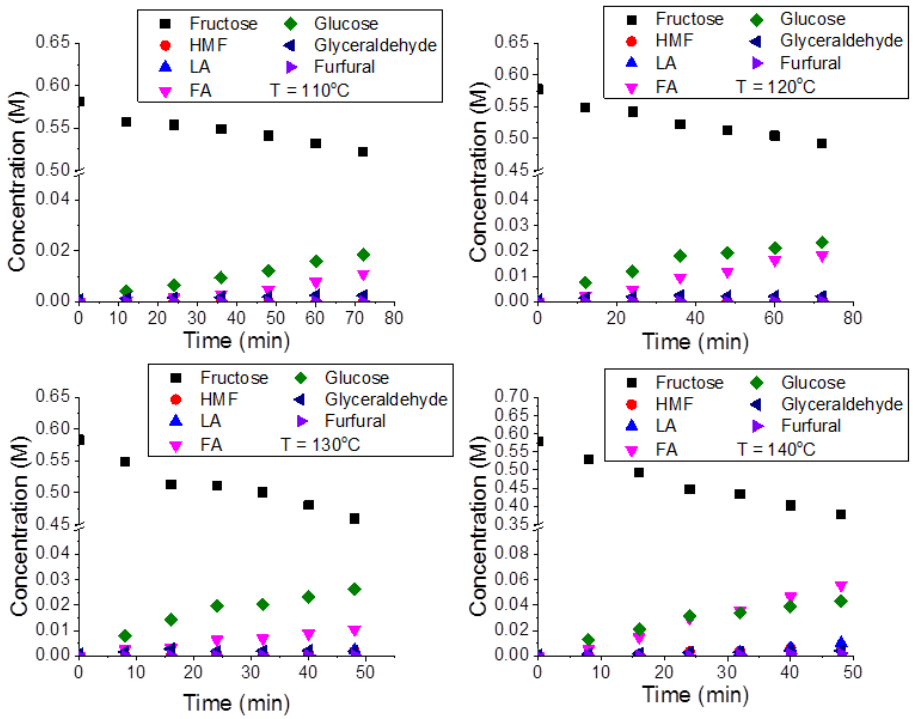

Figure B.12. Experimentally measured concentration profiles observed after fructose reaction in 125 g/l H-BEA-25 at different temperatures.

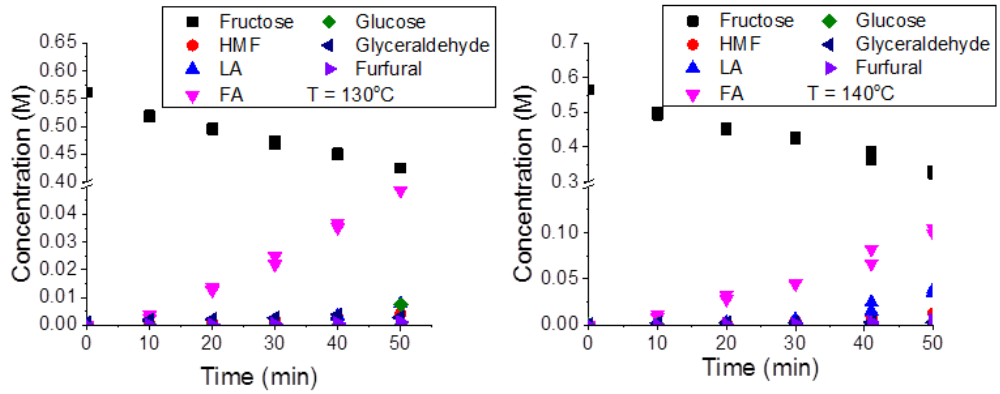

Figure B.13. Experimentally measured concentration profiles observed after fructose reaction in HCl-washed 125 g/l H-BEA-25 at different temperatures.

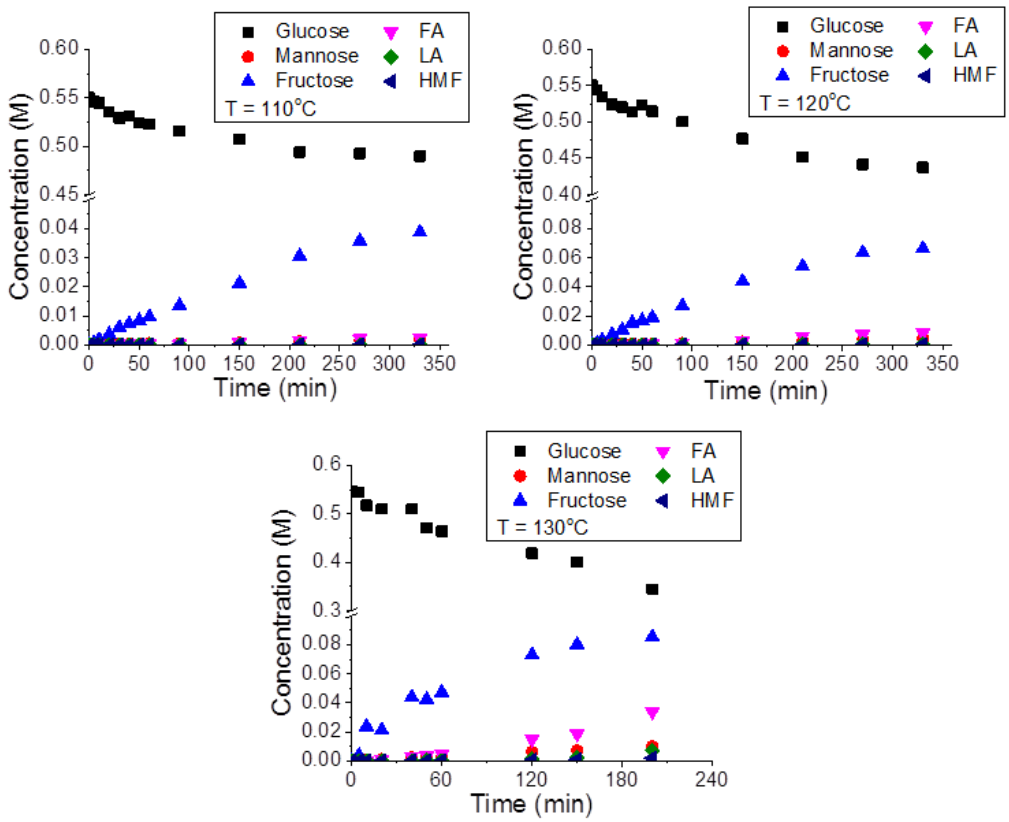

Figure B.14. Experimental observed concentration profiles after reaction of glucose with 125 g/l H-BEA-25 at various temperatures.

B.4.6 Arrhenius plot of apparent glucose consumption rates

Based on the kinetics shown in Figure B.14, an Arrhenius plot was used to estimate the apparent activation energy for glucose consumption in H-BEA-25.

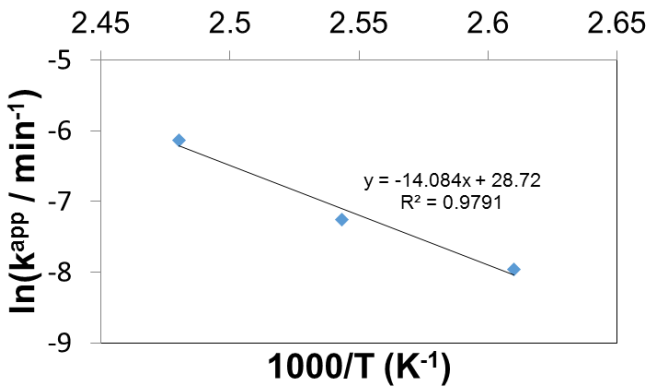

Figure B.15. Arrhenius plot based on apparent rates of glucose consumption.

Appendix C

SUPPLEMENTARY INFORMATION FOR CHAPTER 4
ROLE OF LEWIS AND BRØNSTED ACIDITY IN METAL CHLORIDE CATALYSIS IN ORGANIC MEDIA: REDUCTIVE ETHERIFICATION OF FURANICS

C.1 Polyarc™ Calibration Curve

$$concentration\ of\ A = \frac{slope\ \times Area\ of\ A}{carbon\ number\ of\ A}$$

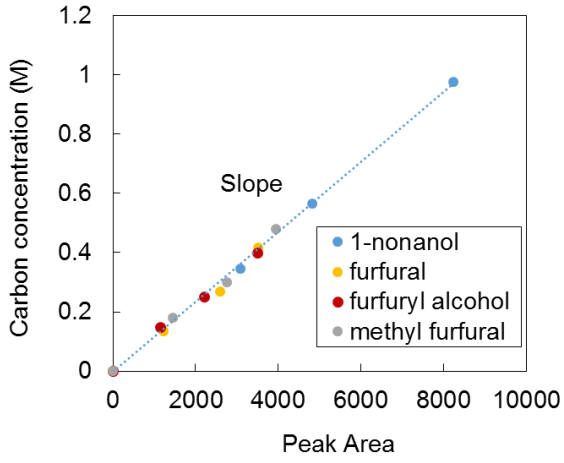

Figure C.1. Universal calibration curve of various compounds on the GC equipped with the PolyArc™.

C.2 Furfuryl Alcohol Reactivity with Select Catalysts

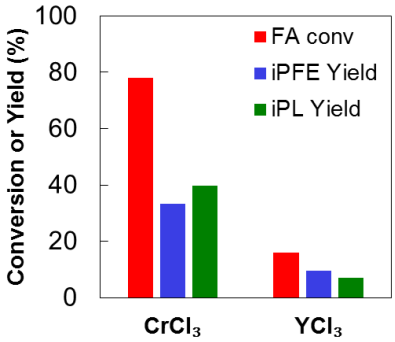

Figure C.2. Catalytic activity of $CrCl_3$ and YCl_3 in furfuryl alcohol reaction in 2-propanol. Reaction conditions: 1 wt % furfuryl alcohol, 90 °C, 10 mM MCl_3, t = 8 h.

C.3 GCMS Analysis of 4,5,5-Trialkoxypentan-2-one

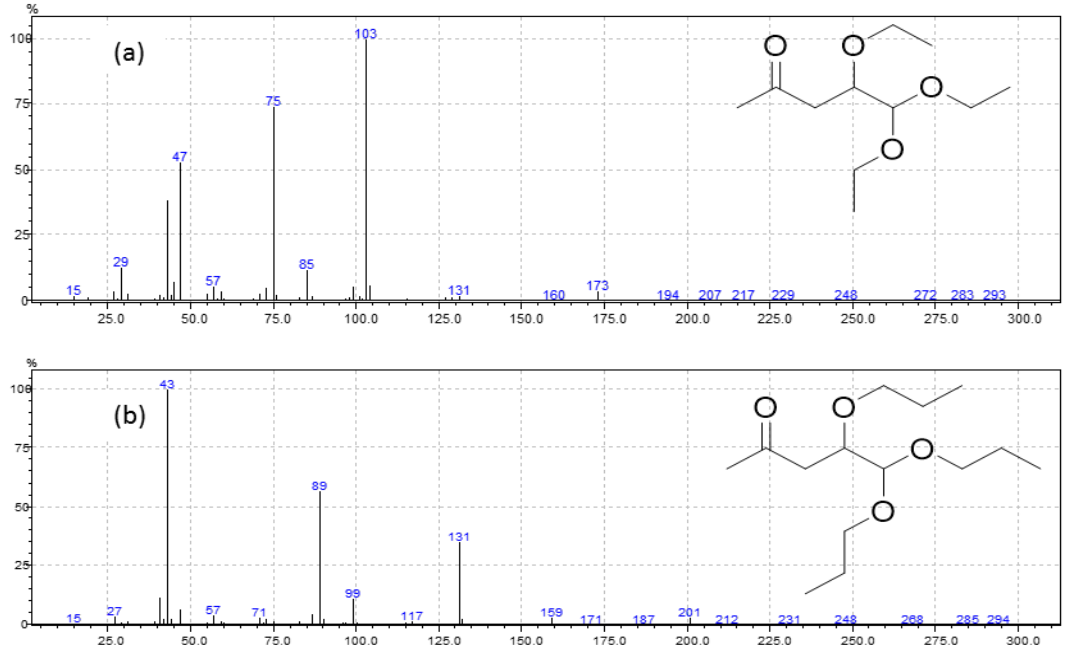

Figure C.3. GCMS spectra of 4,5,5-triethoxypentan-2-one (a) and 4,5,5-tripropoxypentane-2-one (b) produced from reaction of furfuryl alcohol in ethanol and 1-propanol respectively. Reaction conditions: 1 wt % furfuryl alcohol, 90 °C, t= 4 h.

C.4 OLI Prediction of Metal Salt Speciation

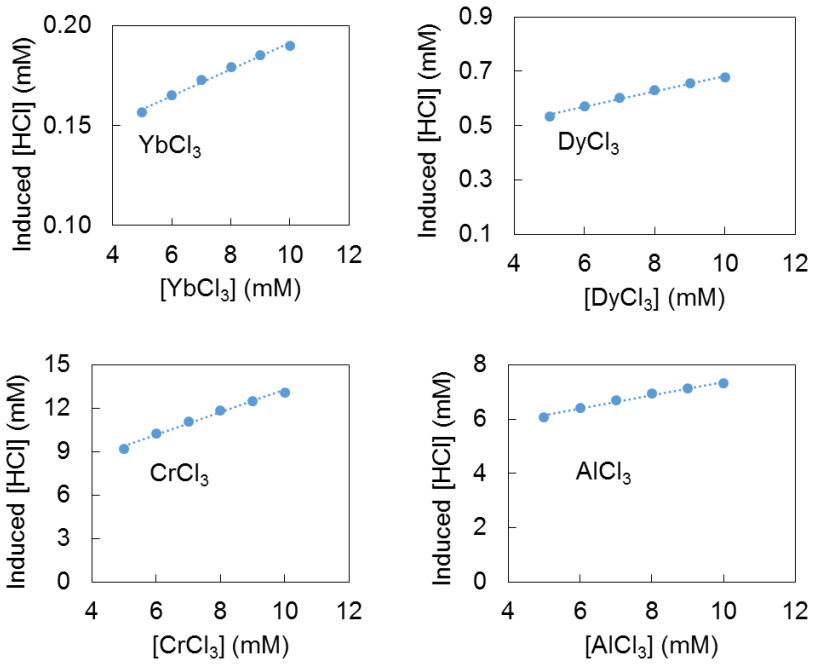

Figure C.4. Induced HCl concentration predicted by OLI for [5-10 mM] MCl_3 in aqueous solution at 100 °C showing a linear correlation between [HCl] and [MCl_3].

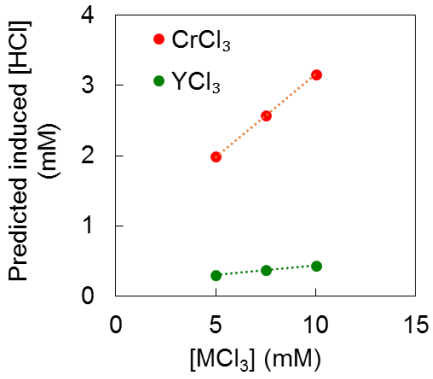

Figure C.5. Predicted induced HCl concentration of $CrCl_3$ and YCl_3 in 2-propanol using [5-10] mM MCl_3 at 90 °C.

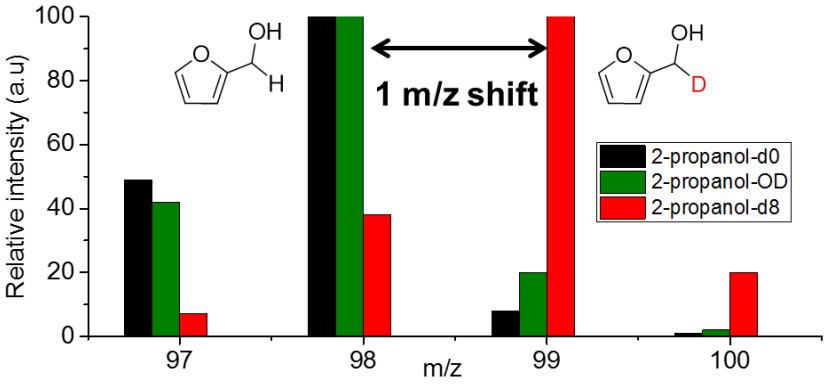

Figure C.6. GCMS spectra of furfuryl alcohol product over $CrCl_3$. Reaction conditions: 1 wt% furfural, 150 °C, 3 mM $CrCl_3$, in 2-propanol-d0 (t= 30 min), 2-propanol-OD (t= 30 min), 2-propanol-d8 (t= 1 h).

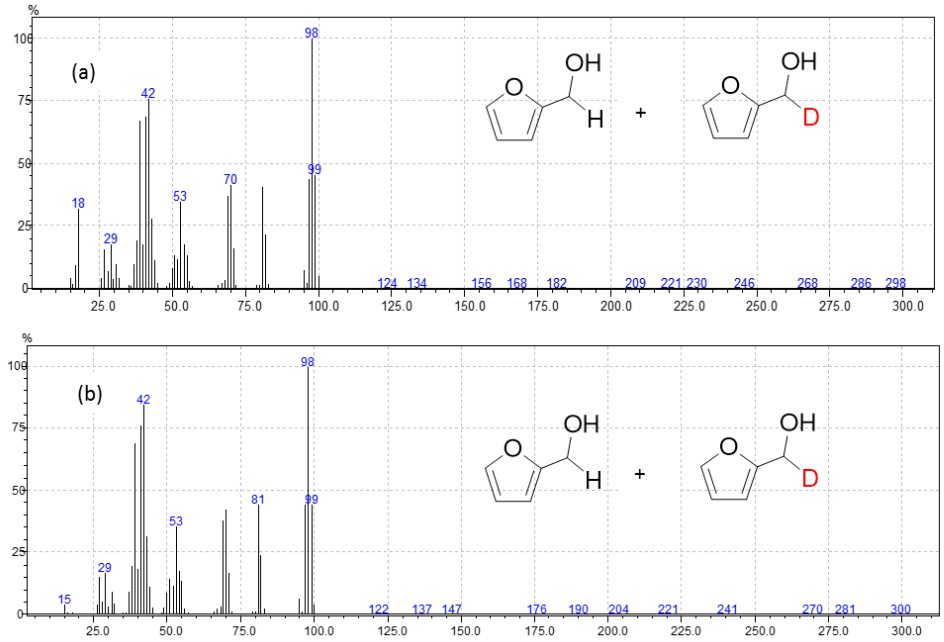

Figure C.7. : GCMS spectra of furfuryl alcohol product of furfural reduction by YCl_3 (a) and $CrCl_3$ (b) in 1:1 mixture of 2-propanol-d0 and 2-propanol-d8. Reaction conditions: 1 wt % furfural, 150 °C, t= 1 h.

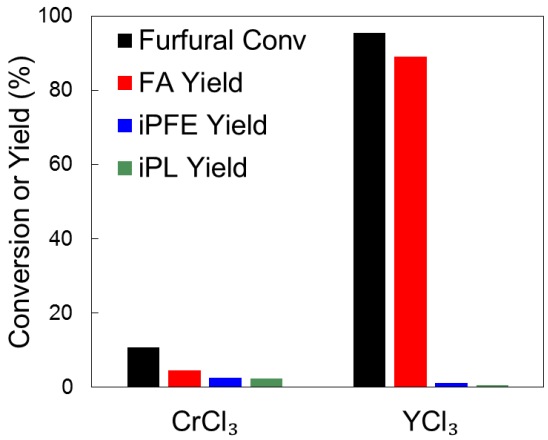

Figure C.8. Catalytic activity of $CrCl_3$ and YCl_3 for furfural reduction in 2-propanol. Reaction conditions: 1 wt % furfural, 150 °C, 3 mM MCl_3, t= 1 h

C.5 ESI-MS of Metal Chloride Solutions

Figure C.9 displays the ESI-MS spectra of YCl_3 and $CrCl_3$ in 2-propanol (ROH) solution with peak assignments to various metal complexes based on the m/z values. In the YCl_3 spectrum, the most dominant peak at m/z = 399 was assigned to the $[YCl_2(ROH)_4]^+$ metal cation and the lower peak at m/z = 423 matches either $Y[(OH)_2(ROH)_5]^+$ or $[YCl(OR)(ROH)_4]^+$. The $CrCl_3$ spectrum follows the same pattern with $[CrCl_2(ROH)_4]^+$ as the most abundant metal cation (m/z = 362), and $Cr(OH)_2(ROH)_4$ or $[CrCl(OR)(ROH)_3]^+$ (m/z = 326) presents at lower intensities. Peaks observed at higher m/z values (m/z > 500 or $CrCl_3$ and m/z > 600 for YCl_3) are probably the oligomer metal species produced via condensation of metal ions. In general, MCl_2^+ metal species, alcoholyed/hydrolyzed species such as $MCl(OR)^+$ and $M(OH)_2^+$, and oligomeric metal clusters were detected in the mass spectra of the metal chloride solutions in 2-propanol.

While ESI-MS is a common technique to identify species in solutions, the metal ion species may be modified during sampling by phenomena such as ligand loss, charge reduction, and condensation.[191] Loss of solvated ligand is evidently observed in ESI-MS spectra of the MCl_3 solutions by 60 m/z spacing between peaks, corresponding to the loss of a solvated 2-propanol. Charge reduction may occur to form hydrolyzed/ alcoholyzed metal ions, which may not originally exist in solution. However, since the pH values of the metal chloride solutions are lower than that of 2-propanol, alcoholysis must occur to some degree. The alcoholyzed/hydrolyzed metal ions may also oligomerize to form metal clusters although their intensity in the ESI-MS spectra may have been magnified via condensation with water vapor at some instrument interfaces.

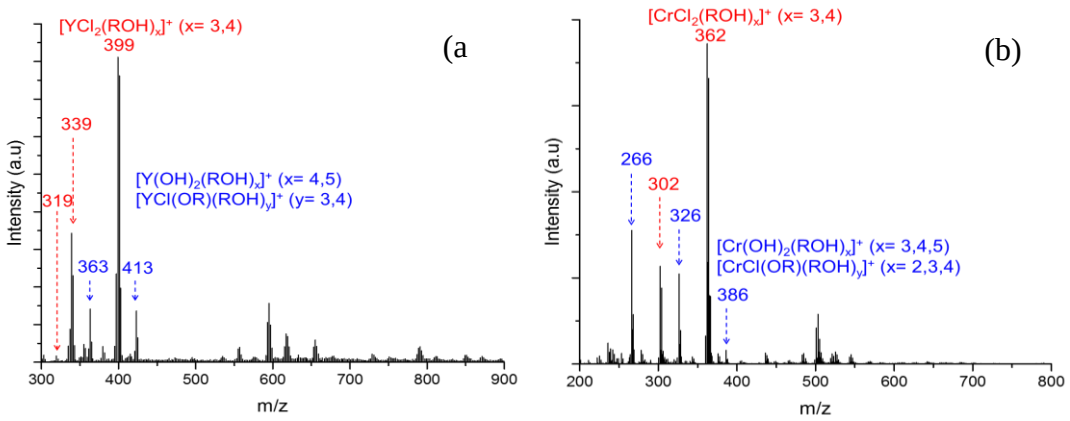

Figure C.9. ESI-MS spectra of 20 mM YCl_3 (a) and 20 mM $CrCl_3$ (b) in 2-propanol.

XAS of $CrCl_3$ and YCl_3 solution were also measured to give more insights to the coordination of the metal species (Table S1). The total coordination number (CN) of Cr might be underestimated due to the low resolution of the XAS spectra of $CrCl_3$. The CN of Y might be slightly overestimated as a systematic problem in

determination of CN for Y salt solutions, which is also acknowledged in literature.[328] Nevertheless, XAS data verified the alcohol and Cl coordination to the metal center observed in ESI-MS.

Table C.1. Coordination number (CN) and interatomic distance (R) obtained in fitting experimental XAS data of 20 mM YCl_3 and 20 mM $CrCl_3$ solution in 2-propanol.

Sample	Contribution	CN	R (Å)
YCl_3	Y-O	6.4 (9)	2.36 (1)
	Y-Cl	3 (1)	2.60 (1)
$CrCl_3$	Cr-O	2 (1)	2.0 (1)
	Cr-Cl	1 (1)	2.3 (1)

C.6 Apparent Activation Energy Analysis of Furfural Reduction

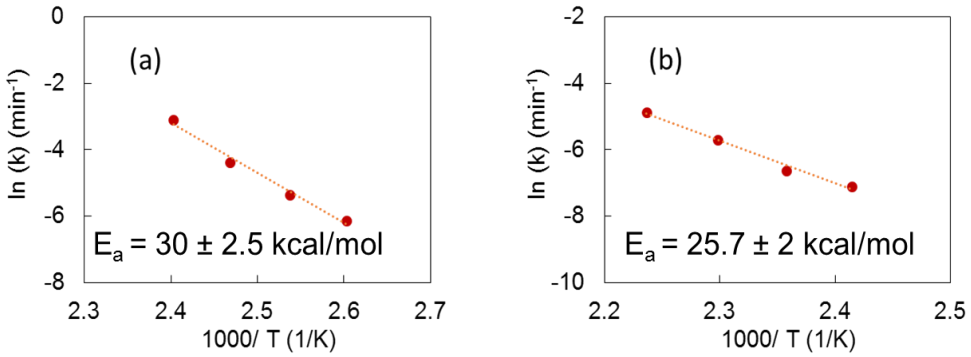

Figure C.10. Arrhenius graphs of furfural reduction in 2-propanol by YCl_3 (a) and $CrCl_3$ (b). Reaction conditions: 1 wt % furfural, 3 mM MCl_3.

Appendix D

SUPPLEMENTARY INFORMATION FOR CHAPTER 5 ON THE SYNERGY OF ACID-BASE SITES OF SUPPORTED ZIRCONIA FOR REDUCTIVE ETHERIFICATION OF BIOMASS-DERIVED FURAN DERIVATIVES

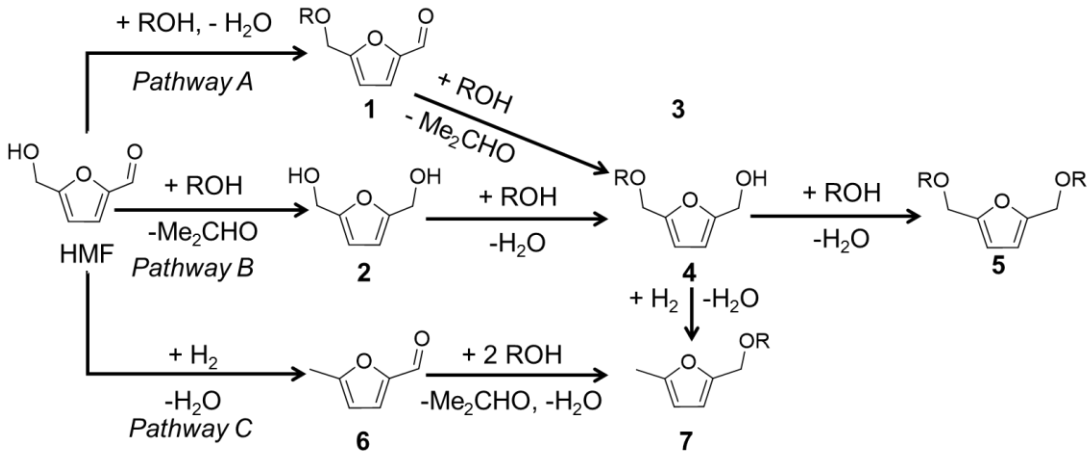

Figure D.1. Proposed reaction network of HMF reaction in 2-propanol by zirconia coated silica ZrO_2/SiO_2. R represents $(CH_3)_2CH$ group.

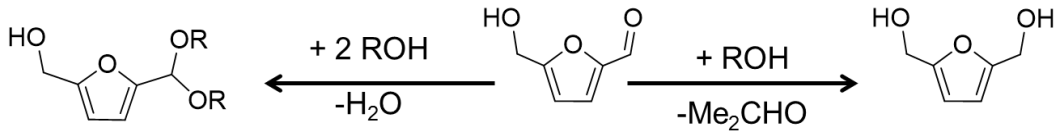

Figure D.2. Proposed reaction network of HMF reaction in 2-propanol by commercial bulk zirconia. R represents $(CH_3)_2CH$ group.

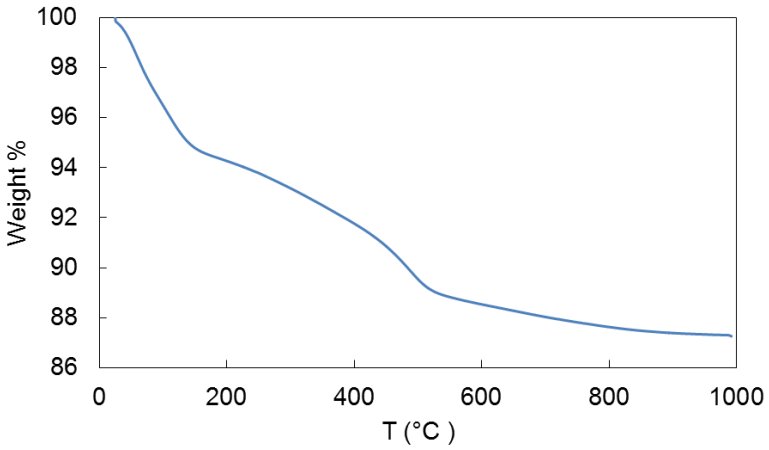

Figure D.3. Thermogravimetric analysis (TGA) of the spent 7.5 % ZrO_2/SiO_2 after stability experiment.

Table D.1. Binding energies of Zr $3d_{5/2}$, Si 2p and O 1s on the bulk ZrO_2, SiO_2, and the synthesized ZrO_2/SiO_2 with various zirconia content from XPS spectra.

ZrO_2 (wt %)	Binding Energy (eV)		
	Si 2p	Zr $3d_{5/2}$	O 1s
0	104.52	N/A	533.78
2	104.15	184.15	533.57
5	104.25	184.04	533.67
7.5	104.25	183.86	533.54
10	104.05	183.57	533.40
15	104.07	183.61	533.41
100	N/A	182.24	530.27

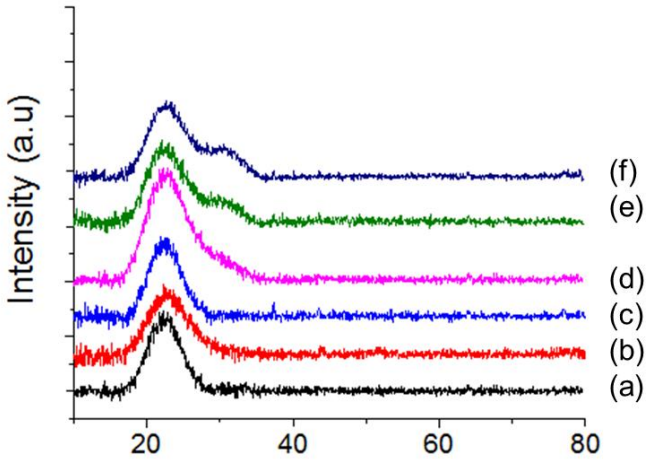

Figure D.4. XRD spectra of pure silica (a) and ZrO_2/SiO_2 with various zirconia content of 2.5 wt% (b), 5 wt% (b), 7.5 wt% (c), 10 wt% (d), 15 wt% (f).

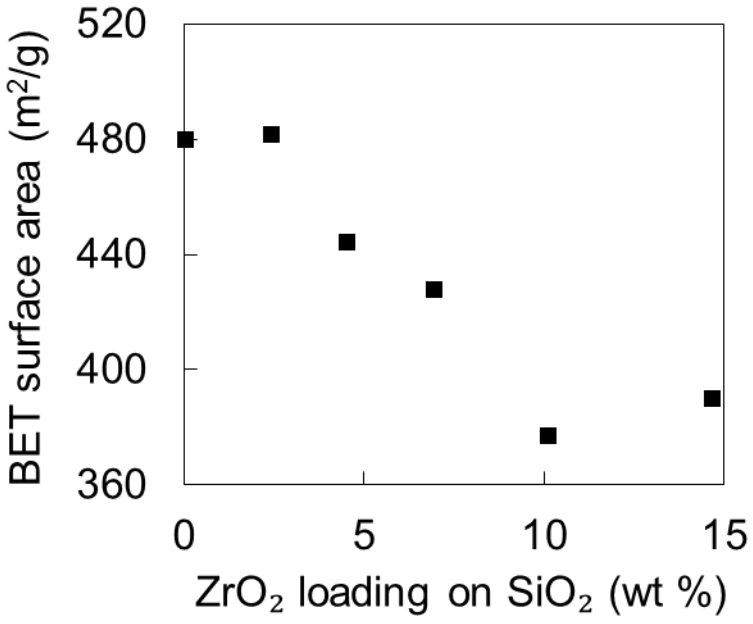

Figure D.5. BET surface area of ZrO_2/SiO_2 with various zirconia content.

Appendix E

SUPPLEMENTARY INFORMATION FOR CHAPTER 6 PRODUCTION OF RENEWABLE OLEO-FURAN SURFACTANTS BY CROSS-KETONIZATION OF BIOMASS-DERIVED FURAN DERIVATES AND FATTY ACIDS

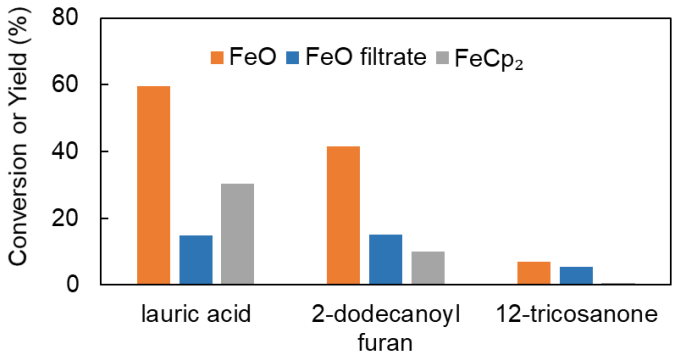

Figure E.1. Comparison of activity for cross-ketonization between FeO, its filtrate after reaction, and homogeneous ferrocene ($FeCp_2$). Reaction conditions: 0.05 M lauric acid, 0.25 M 2-furoic acid, 0.2 g FeO or $FeCp_2$, 316 °C, 90 mins.

Table E.1. Fe content in pure dodecane and post-reaction filtrates of iron oxides measured by XRF

Solution	Fe content
dodecane	0.0068
FeO filtrate	0.0656
Fe_3O_4 filtrate	0.0074
Fe_2O_3 filtrate	0 (N/A)

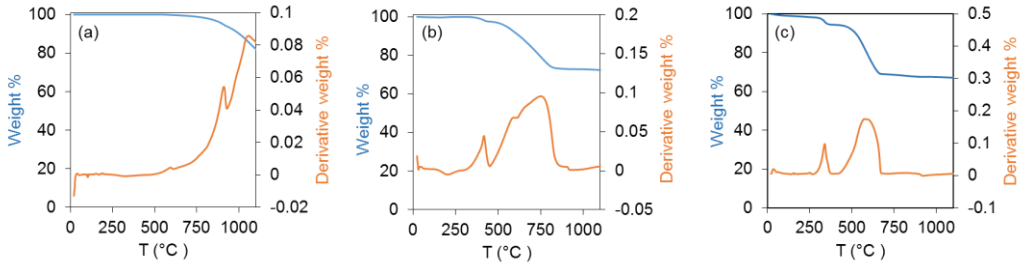

Figure E.2. H_2 TPR-TGA profiles of iron oxides: FeO (a), Fe_3O_4 (b), and Fe_2O_3 (c).

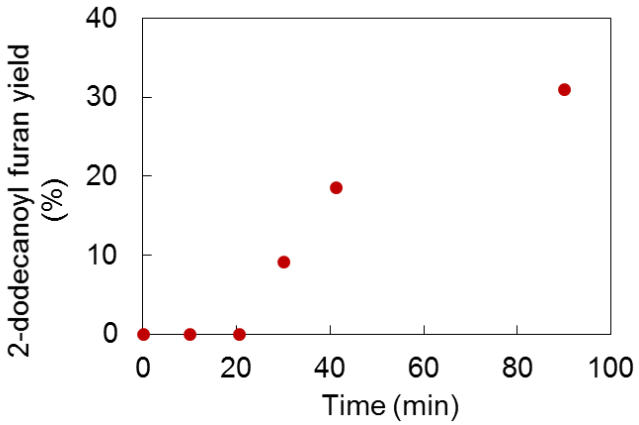

Figure E.3. Time evolution of 2-dodecanoyl furan formation by Fe_3O_4. Reaction conditions: 0.05 M lauric acid, 0.25 M 2-furoic acid, 0.2 g Fe_3O_4, 316 °C, 90 mins.

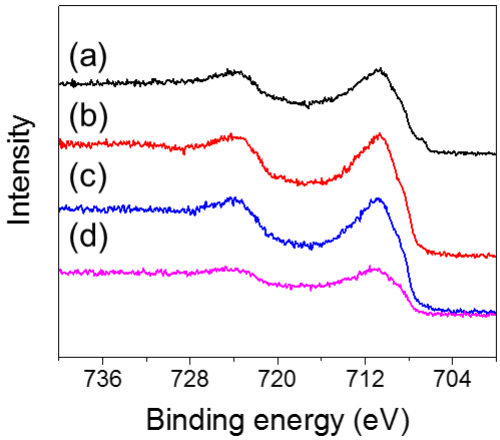

Figure E.4. XPS spectra of Fe $2p_{3/}$ of Fe_3O_4 catalyst pretreated in H_2 (a), pure dodecane (b), 0.05 M lauric acid in dodecane (c), and 0.25 M furoic acid in dodecane (d). Reaction conditions: 0.2 g Fe_3O_4, 316 °C, 30 mins.

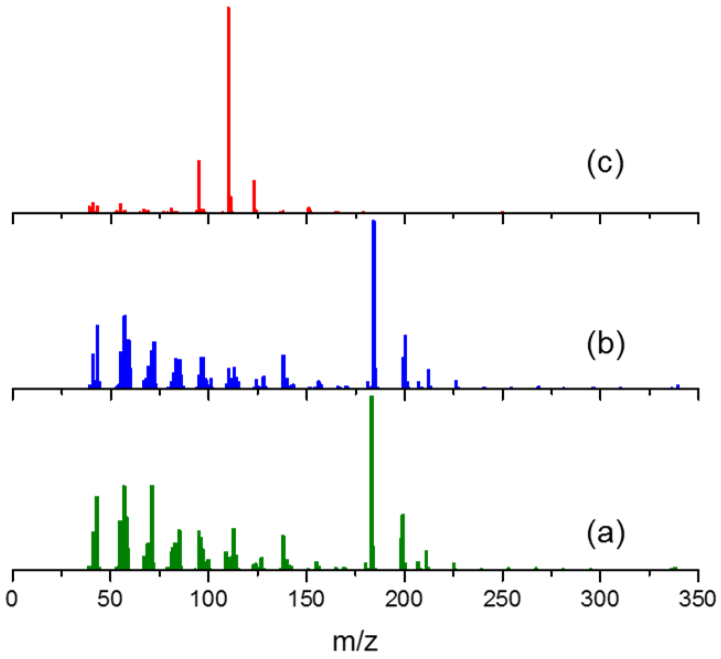

Figure E.5. GCMS spectra of (a) 12-tricosanone from reaction starting with unlabeled lauric, (b) 12-tricosanone from reaction starting with ^{13}C-C1 lauric acid, and (c) 2-dodecanoyl furan from reaction starting with^{13}C-C1 lauric acid.

Table E.2. BET surface areas and mircropore volumes of iron oxide catalysts before and after cross-ketonization reactions.

	Fresh catalyst			Spent catalyst		
	FeO	Fe_3O_4	Fe_2O_3	FeO	Fe_3O_4	Fe_2O_3
BET surface area (m^2/g)	0.11	8.75	34.28	18.73	9.10	17.70
Micropore volume (cm^3/g)	2.83 e-4	2.18e-2	7.58e-2	8.43e-2	2.29e-2	8.53e-2

Appendix F

PERMISSION

Chapter 2 was reproduced with permission from the American Chemical Society [46]

Chapter 3 was reproduced with permission from the Journal of Catalysis [329]

Chapter 4 was reproduced with permission from the American Chemical Society [285]

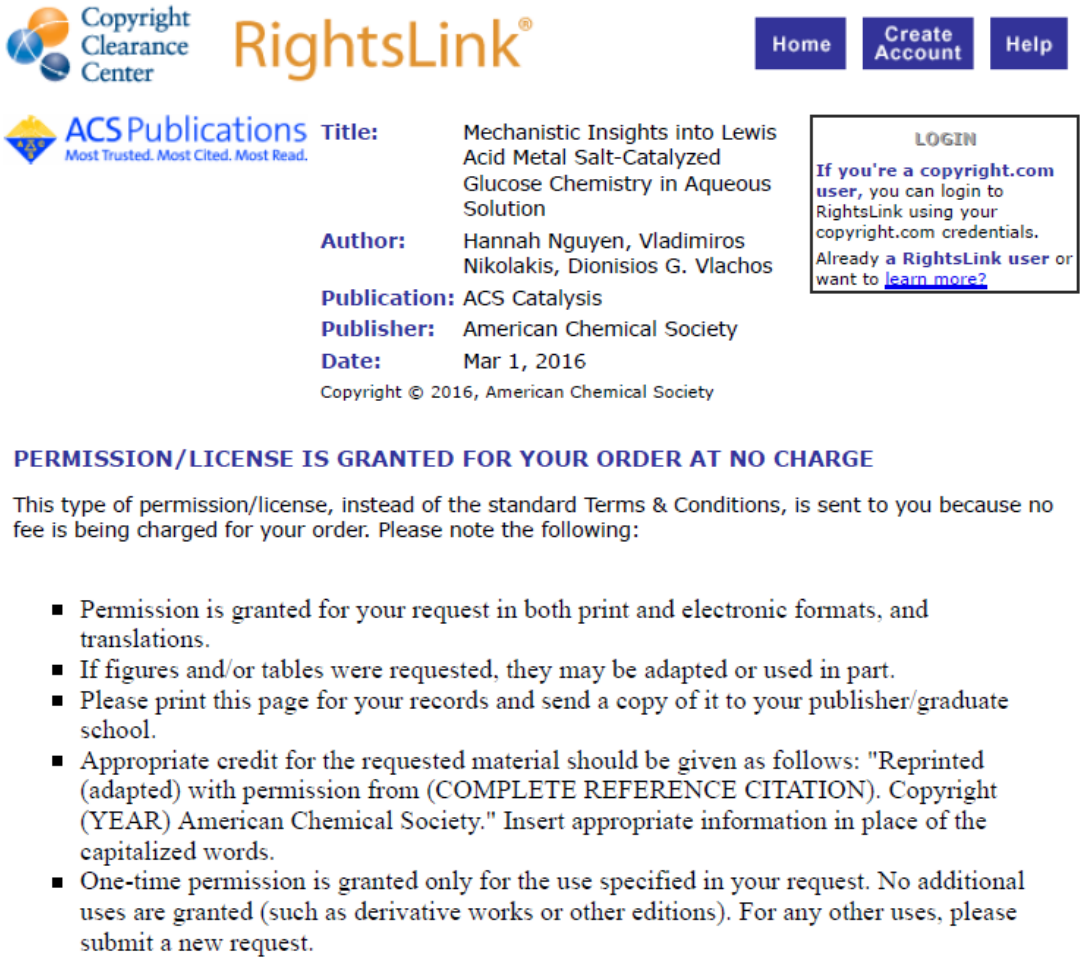

Copyright Clearance Center RightsLink®

Home | Create Account | Help

ACS Publications
Most Trusted. Most Cited. Most Read.

Title: Mechanistic Insights into Lewis Acid Metal Salt-Catalyzed Glucose Chemistry in Aqueous Solution

Author: Hannah Nguyen, Vladimiros Nikolakis, Dionisios G. Vlachos

Publication: ACS Catalysis

Publisher: American Chemical Society

Date: Mar 1, 2016

Copyright © 2016, American Chemical Society

LOGIN

If you're a copyright.com user, you can login to RightsLink using your copyright.com credentials.

Already **a RightsLink user** or want to learn more?

PERMISSION/LICENSE IS GRANTED FOR YOUR ORDER AT NO CHARGE

This type of permission/license, instead of the standard Terms & Conditions, is sent to you because no fee is being charged for your order. Please note the following:

- Permission is granted for your request in both print and electronic formats, and translations.
- If figures and/or tables were requested, they may be adapted or used in part.
- Please print this page for your records and send a copy of it to your publisher/graduate school.
- Appropriate credit for the requested material should be given as follows: "Reprinted (adapted) with permission from (COMPLETE REFERENCE CITATION). Copyright (YEAR) American Chemical Society." Insert appropriate information in place of the capitalized words.
- One-time permission is granted only for the use specified in your request. No additional uses are granted (such as derivative works or other editions). For any other uses, please submit a new request.

Figure F.1. Permission for Chapter 2

Copyright Clearance Center RightsLink®

Home | Create Account | Help

Title: Tandem Lewis acid/Brønsted acid-catalyzed conversion of carbohydrates to 5-hydroxymethylfurfural using zeolite beta

Author: T. Dallas Swift,Hannah Nguyen,Zachary Erdman,Jacob S. Kruger,Vladimiros Nikolakis,Dionisios G. Vlachos

Publication: Journal of Catalysis

Publisher: Elsevier

Date: January 2016

Copyright © 2015 Elsevier Inc. All rights reserved.

LOGIN

If you're a copyright.com user, you can login to RightsLink using your copyright.com credentials.

Already a RightsLink user or want to learn more?

Please note that, as the author of this Elsevier article, you retain the right to include it in a thesis or dissertation, provided it is not published commercially. Permission is not required, but please ensure that you reference the journal as the original source. For more information on this and on your other retained rights, please visit: https://www.elsevier.com/about/our-business/policies/copyright#Author-rights

Figure F.2. Permission for Chapter 3

Figure F.3. Permission for Chapter 4